UNICA

UNIVERSITÀ
DEGLI STUDI
DI CAGLIARI

Ph.D. DEGREE IN

Innovation Sciences and Technologies

Cycle XXXVI

TITLE OF THE Ph.D. THESIS

Nanoparticles from microalgae for environmental and biomedical applications

Scientific Disciplinary Sector(s)

CHIM/04, ING-IND/22, ING-IND/27, ING-IND/34

Ph.D. Student: Agnieszka Sidorowicz

Supervisor Prof. Giacomo Cao

Final exam. Academic Year 2022/2023
Thesis defence: February 2024 Session

Abstract

Microalgae, a group of organisms, have emerged as promising candidates for various applications due to the abundance of valuable metabolites combined with increased growth rate and biomass production. Nanoparticles derived from microalgae have exhibited substantial potential within the realm of biomedical and environmental applications. However, it is important to emphasize the need for further research aimed at addressing concerns surrounding kinetics, cellular viability, and yield, factors that affect the characteristics of the obtained nanoparticles. The utilization of diverse extraction techniques or synthesis conditions holds the potential to yield a spectrum of nanoparticles with distinctive properties, thereby presenting opportunities for versatile application across a multitude of sectors.

The investigation into the synthesis of silver nanoparticles, titanium dioxide nanoparticles, cobalt (II) hydroxide nanomaterials, and cobalt (II, III) oxide utilizing a methanolic extract *of S. platensis* has revealed their potential as innovative antifungal agents. The synthesis mechanism, characterized through Gas Chromatography-Mass Spectrometry (GCMS) and Fourier-Transform Infrared Spectroscopy (FTIR), proved the involvement of secondary metabolites, particularly amines. Diverse analytical techniques, including X-ray diffraction (XRD), Scanning Electron Microscopy (SEM), Thermogravimetric Analysis (TGA), and zeta potential measurements, have provided valuable insights into the properties of the synthesized nanomaterials. Among all the prepared structures, silver nanoparticles have demonstrated exceptional thermal stability and water dispersion properties. In tests conducted against various *Candida* species, it was observed that silver nanoparticles and cobalt (II) hydroxide nanomaterials exhibited potent antifungal activity at low minimum inhibitory concentration (MIC) values. Interestingly, exposure to light exhibited differential effects on MIC values, with a reduction observed for *C. krusei* and an increase for *C. albicans* and *C. glabrata*. These findings show the potential of nanomaterials synthesized using *S. platensis* extract in the development of effective antifungal agents in healthcare.

An additional application explored for nanomaterials synthesized using microalgae is related to their carbon monoxide oxidizing ability. The research has demonstrated the viability of extracts derived from microalgae species such as *S. platensis, C. vulgaris*, and *H. pluvialis* for the eco-friendly fabrication of nanoscale Co_3O_4 catalysts, each distinguished by unique characteristics. By changing the metabolic content of the extracts used for the synthesis and calcination temperatures, diverse Co_3O_4 catalysts were successfully obtained, exhibiting octahedral, nanosheet, and spherical morphologies, with structural defects and surface segregation of phosphorous and potassium. The introduction of phosphorous and potassium from the extracts increased the catalytic performance of Co_3O_4, especially when normalized against a specific surface area. In-depth investigations into the carbon monoxide oxidation mechanism revealed variances in oxygen mobility and carbonate formation. These novel findings hold considerable promise for the formulation of innovative synthesis methodologies aimed at producing highly efficient Co_3O_4 catalysts, contributing to more effective carbon monoxide oxidation and the sustainable synthesis of catalysts.

The catalytic properties of microalgae-derived nanoparticles were further investigated for the photocatalytic degradation of Brilliant Blue R dye, a commonly used laboratory dye for protein staining. The methanolic extract of *C. vulgaris* was employed for the successful synthesis of silver nanoparticles, with subsequent analysis of the impact of calcination on their properties. XRD analysis indicated that the products possessed a crystalline nature, initially consisting of Ag_2O and Ag phases with an average crystalline size of 16.07 nm prior to calcination. Post-calcination, these nanoparticles transformed into a pure Ag phase with a larger crystalline size of 24.61 nm. FTIR analysis highlighted the presence of capping functional groups on the silver nanoparticles, while SEM imagery revealed an irregular morphology and agglomeration post-calcination. EDX and TGA analyses further substantiated the involvement of metabolites in the organic coating. The UV-Vis analysis demonstrated changes in optical properties induced by calcination. Most importantly, the synthesized silver nanoparticles exhibited remarkable photocatalytic activity, achieving an 90.6% degradation efficiency when subjected to increased catalyst dosage during 90 minutes of visible light irradiation.

Utilizing a methanolic extract of *H. pluvialis*, silver nanoparticles were successfully synthesized, and their photocatalytic performance was assessed against Brilliant Blue R dye. XRD analysis affirmed the crystalline nature of the nanoparticles, initially comprising Ag_2O and Ag phases with a crystalline size of 14.27 nm prior to calcination. Following calcination, solely the Ag phase was observed, characterized by an increased crystalline size of 34.78 nm. Similar results to those observed in the case of silver nanoparticles derived from *C. vulgaris* were obtained through FTIR, SEM, EDX, and TGA analyses. Furthermore, UV-Vis analysis revealed changes in optical properties attributed to calcination. Obtained Ag nanoparticles demonstrated substantial photocatalytic activity, achieving a peak degradation efficiency of 65.9% with an elevated catalyst dosage during 90 minutes of visible light irradiation.

Additionally, silver nanoparticles from methanolic extract from *S. platensis* were investigated for photocatalytic Brilliant Blue R dye removal. XRD analysis revealed the presence of AgCl and Ag phases with a crystalline size of 13.02 nm prior to calcination, which transformed into pure Ag nanoparticles with an increased crystalline size of 24.35 nm post-calcination. FTIR analysis confirmed the involvement of metabolites from the extract in capping the silver nanoparticles. SEM images exhibited spherical or quasi-spherical morphologies with some agglomeration attributed to the calcination process. EDX and TGA analyses further provided evidence of metabolite involvement in the synthesis process. UV-Vis analysis demonstrated optical changes in the obtained nanoparticles. Synthesized silver nanoparticles exhibited photocatalytic activity, achieving a peak degradation efficiency of approximately 81.9% when used in increased catalyst dosage and alkaline conditions during 90 minutes of light irradiation. These findings demonstrate the potential of silver nanoparticles synthesized from microalgal extract for environmentally friendly and efficient photocatalytic applications, particularly in addressing water pollution concerns and the removal of organic dyes from wastewater.

Acknowledgements

I would like to express my sincere gratitude to the co-supervisor Prof. Alessandro Concas for his unwavering support and guidance throughout my doctoral research. Supervisors' expertise, constructive feedback, and encouragement have been instrumental in shaping the trajectory of my work.

To everyone who has been a part of this academic journey, I extend my deepest appreciation. Your involvement has left an indelible mark on this research.

Table of Contents

Chapter 1

Introduction

1.1 Microalgae

Microalgae are microscopic algae characterized by their small size, usually ranging from a few micrometers to a few hundred micrometers in diameter. Due to their size, observing microalgae requires specialized equipment for proper study. They can be found mainly in aquatic ecosystems such as freshwater and saltwater; however, they can also survive in terrestrial habitats. Despite their small size, microalgae play an important role in the environment due to their high photosynthetic efficiency compared to terrestrial plants, resulting in increased growth rates and biomass productivity [1]. Moreover, microalgae can be farmed without competing for arable land resources, thus alleviating the pressure of resource competition [2].

The use of microalgae dates back thousands of years, mainly as a food source for Chinese, Maya, and Aztec civilizations [3]. The first cultivation systems utilized eutrophic lakes or small natural basins for microalgae cultivation with favorable chemical composition, including high salinity, high pH, and high nutrient concentration [3]. However, to maximize biomass production on the industrial scale, artificial ponds and photobioreactors are used to prevent the invasion of competing microorganisms and optimize growth conditions.

In recent years, microalgae have gained more attention due to their unique metabolomic profile. The research on the cultivated microalgae revealed their high protein content, which could help feed the growing world population using more sustainable methods. Modifying medium composition, as well as growth conditions, can lead to variations in protein and lipid content [4]. Moreover, microalgae can be a source of vitamins and antioxidants, which can play an important role in maintaining homeostasis [5]. The microalgae species might also contain

essential fatty acids like gamma-linolenic acid (GLA) and alpha-linolenic acid (ALA), which have numerous health benefits [6].

The abundance of various metabolites present in microalgae allows them to be used as active ingredients in cosmetics. The cosmeceutical products based on microalgae can provide protection of skin properties and prevent bacterial or fungal infections [7]. In addition, the molecules from microalgae can be used as stabilizers, dyes, or thickening agents in the formulation process [7]. Further research is carried out to evaluate the potential metabolites that can be isolated from microalgae and to prevent side effects.

The increased lipid content of some microalgal species allows them to be utilized for the production of biofuels such as bio-oil, biodiesel, biogas, bioethanol, and bio-hydrogen [8]. Moreover, the adaptability of microalgae to grow in different habitats shows their potential for wastewater remediation with data estimating that 1 kg microalgae can fix about 9 g phosphorus and 63 g nitrogen from wastewater [9]. Both applications can be combined when microalgae are cultivated in wastewater and the biomass is further processed for high value products.

Extensive research and development efforts in the field of microalgae have led to the discovery of new applications and further optimization of existing ones. The results have demonstrated considerable promise across a variety of sectors, including but not limited to food, pharmaceuticals, cosmetics, and wastewater treatment. The continued exploration of microalgae is crucial for advancing sustainable and efficient practices in these fields. In addition, metabolites present in microalgae can be used to synthesize nanomaterials which might have many applications. Thus, the metabolomic composition of microalgae and the role of their metabolites in the synthesis process requires further attention. Among various microalgal species, the most studied are *Spirulina platensis*, *Chlorella vulgaris*, and *Haematococcus pluvialis* (Fig. 1).

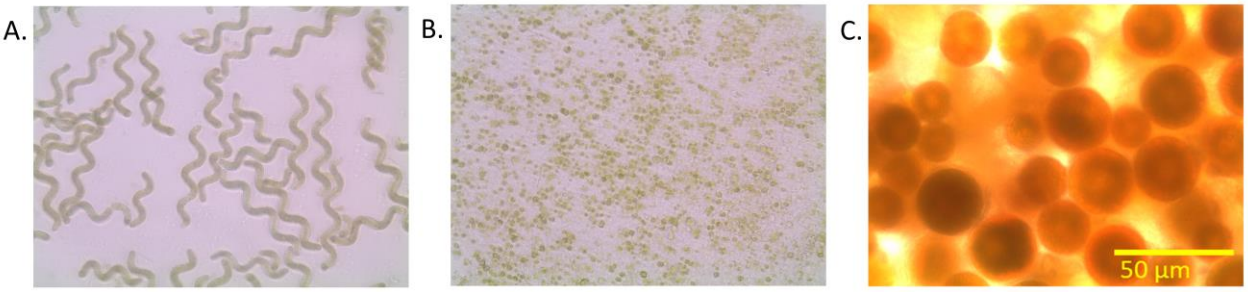

Figure 1 Optical microscopy of microalgae (A) *S. platensis*, (B) *C. vulgaris*, (C) *H. pluvialis*.

1.2 Spirulina platensis

S. platensis is one of the most common microalgae with characteristic spiral shape of its multicellular cylindrical filaments in an open helix ranging from 0.3 to 1.0 mm in length. The cells of *S. platensis* are surrounded by a cell wall, which contains peptidoglycan, lipopolysaccharides, and other structural components. The cellular wall plays a crucial role in safeguarding the filament and preserving its unique structure. The species belongs to the type *Cyanobacteria* and displays a distinctive blue-green color, thus it is commonly referred to as *Cyanobacteria* or blue-green microalgae. Unlike other microorganisms in this group, *S. platensis* does not form nitrogen-fixing heterocysts or resistant akinetes in its filaments [10,11].

S. platensis is commonly found in warm, alkaline, and brackish waters in temperatures between 30-35°C in tropical or subtropical regions. The microalga is also cultivated commercially with a typical productivity in open ponds in the range of 4 to 7 g/m^2/day, which in the open pond of 1750 m^2 results in weekly biomass production from 46.5 kg to 77 kg [12]. The cells float freely in water, due to the lack of flagella or cilia for movement.

Dried *S. platensis* contains a high protein content representing 70% of its weight. It is considered one of the richest protein sources of microbial origin and a potential substitute for conventional protein sources such as meat or soybean [13]. *S. platensis* also contains phycobiliproteins, with chromophores acting as a light receiver during photosynthesis linked to cysteine residues determining their spectroscopic characteristics [14]. One of the phycobiliproteins, phycocyanin, is used in food and cosmetics as a natural dye due to its blue color. It can also exhibit anti-inflammatory, antioxidant and anticancer properties [15].

Moreover, phycocyanin has ecological significance in detecting cyanobacteria bloom to indicate the number of the present microorganisms [16]. Although proteins from *S. platensis* are highly valuable, their main applications are limited due to the production costs and impairments with respect to their sensory characteristics.

Other than proteins, the commercial interest in *S. platensis* is related to its lipid content, constituting around 1-10% of dry weight. In total lipid content, *S. platensis* consists of 45% neutral lipids, 39% glycolipids, and 16% phospholipids [17]. Among various lipids, microalgae contains saturated and unsaturated fatty acids including gamma-linolenic acid (GLA) and alpha-linolenic acid (ALA), linoleic acid, oleic acid, and palmitic acid [18]. The molecules have been tested for their beneficial effect in the treatment of cancer and inflammatory pathologies [18]. It is worth noting that a combination of various metabolites may result in the synergistic effect providing a wider spectrum of action.

Other valuable components identified in S. platensis include chlorophyll, B-complex vitamins (such as B1, B2, B3, B6, and B12), vitamin E, vitamin K, minerals, (iron, calcium, magnesium, potassium, zinc) and phenolic compounds known for their antioxidant properties [19]. The health benefits from *S. platensis* are promising, however, more research is needed to fully understand the effect of the compounds in the human body.

1.3 Chlorella vulgaris

Other commonly studied microalga is *C. vulgaris*, typically spherical to ellipsoidal in shape with a diameter ranging from about 2 to 10 µm. The cells are surrounded by a rigid, thick cell wall made primarily of cellulose varying in thickness among different strains. In a heavy metal-induced stress conditions, *C. vulgaris* produces colorless, mucilaginous matrix acting as adsorbent to preventing the entrance of heavy metals into the cell [20]. *C. vulgaris* is a green alga belonging to the family *Chlorellaceae* containing a and b chlorophylls.

The typical habitat of *C. vulgaris* includes stagnant or slow-moving shallow freshwater in nutrient-rich environments preferably in slightly alkaline or neutral water conditions (pH 6.5 to 9.5). The growth rate is optimal within the range of 20°C to 30°C. The biomass productivity on

commercial scale was calculated around 1.14 g/m^2/day in outdoor cultures [21]. Similar to *S. platensis*, *C. vulgaris* is non-motile as it lacks flagella or cilia for movement.

Total protein content in *C. vulgaris* varies about 50% to 60% of its dry weight depending on growth conditions. Approximately 20% of the proteins are affixed to the cellular membrane, where they serve the purpose of maintaining structural integrity and facilitating transportation [22]. About half of the proteins are situated within the cell, while the remaining 30% are released into the extracellular medium [22]. The proteins are a source of all essential amino acids, making *C. vulgaris* a valuable plant-based protein supplement. However, due to the presence of rigid cellulose cell wall the disruption of algal cell wall is necessary to improve digestibility which can be achieved through mechanical or physical procedures, such as homogenization, sonication or enzymatic pre-treatments [23]. Further research is required to achieve optimal availability of the metabolites for human consumption.

Under optimal growth conditions, *C. vulgaris* has the potential to accumulate lipids ranging from 5% to 40% per unit of dry biomass. The produced lipids are mainly composed of glycolipids, phospholipids, neutral lipids, waxes, polar lipids, and fatty acids [22]. Under unfavorable growth conditions lipid content increases with accumulation of triacylglycerols (TAGs), making it a potential feedstock for biodiesel production [22]. In addition, *C. vulgaris* is used for extraction of fatty acids such as omega-3 and omega-6, which are important for human health [24]. Although resistant cell wall can possess a challenge in their accessibility, *C. vulgaris* contains antioxidants such as carotenoids and tocopherols preventing fatty acids from oxidation which is beneficial for their extraction [24].

The unique compound from *C. vulgaris* is *Chlorella* growth factor (CGF) which contains nucleic acids, amino acids, vitamins, and other nutrients [25]. When applied to *C. vulgaris* culture, it enhanced biomass and lipid production for a potential biodiesel production [26]. However, introduction of CGF into the diet of broiler chickens resulted in decreased growth in comparison with the dried *C. vulgaris* powder [27]. Thus, further studies are required to fully assess the impact of the metabolites on the diet.

1.4 Haematococcus pluvialis

Another edible microalga is *H. pluvialis*, green microalga with a spherical shape and diameter ranging from about 10 to 35 µm. The microalga has a complex life cycle with two main stages: green, when it possesses chloroplasts as well as two flagella, and red, which is triggered under stress conditions, when astaxanthin, a carotenoid pigment, is accumulated within the cell. The red cysts also have thick, multilayered cell walls which provide protection and resistance to *H. pluvialis* to survive unfavorable conditions. Additionally, the cells in the red stage are non-motile.

H. pluvialis can be found in nature in freshwater ponds, lakes, slow-moving rivers, streams, and wetlands. Due to its ability to transform into cysts, it can also survive periods of drought in rain pools and temporary ponds or in damp terrestrial environments. Controlled cultivation typically involves providing optimal conditions for its green stage and, after several days to a few weeks, triggering the production of astaxanthin by reducing nutrient supply with increasing light intensity in the induction phase [28]. The optimal temperature for growth is similar to other microalgae in a range of 25–30 °C.

The cells in the green stage have high protein content per dry weight of 29%–45% with carbohydrate content ranging from 15%–17%, and total lipids around 20% to 25% [29]. After transformation to red stage, the protein content decreases to 21-23%, carbohydrates increase to 41% while the lipid content ranges around 30% [29]. The significant changes in the cell composition show the adaptability of *H. pluvialis* to various conditions.

Commercially, *H. pluvialis* has gained immense attention in recent years for its ability to produce astaxanthin. In addition, *H. pluvialis* has the highest astaxanthin content of any natural source, making it a valuable resource to produce various health supplements and functional foods [30]. Astaxanthin is highly sought after in the pharmaceutical and nutraceutical industries due to its potential health benefits, including reducing inflammation, improving cardiovascular health, and boosting the immune system [31]. In the aquaculture industry, astaxanthin is added to the feed to enhance the coloration of fish and crustaceans, particularly salmon and shrimp

[31]. Besides astaxanthin, other carotenoids with antioxidant properties are extracted from *H. pluvialis* such as beta-carotene, canthaxanthin, and lutein [32].

The complex life cycle in response to stress conditions makes *H. pluvialis* a potential model organism to study cell responses including signals transduction and protection mechanisms which is believed to follow similar pathway as those observed in plants [33]. Moreover, the studies on astaxanthin synthesis site, encystement process, and correlation between astaxanthin esterification and deposition in the lipid globules might lead to further understanding of the molecular processes connected with carotenogenesis and production recombinant strains with increased carotenoid production [33,34].

1.5 Research objectives

Based on the abundance of the highly valuable metabolites in microalgal species and their applications in various sectors, *S. platensis*, *C. vulgaris*, and *H. pluvialis* were investigated for their application in nanotechnology.

The current research had following objectives:

1. State of the art literature review on the role of microalgal metabolites such as proteins, carbohydrates, and lipids during the synthesis of nanoparticles.
2. Literature review on the connection between the synthesis method and properties of the synthesized nanoparticles using microalgae.
3. Synthesis of Ag, TiO_2, $Co(OH)_2$, and Co_3O_4 nanomaterials using *S. platensis* methanolic extract and their characterization before and after calcination.
4. Description of the metabolites from *S. platensis* extract involved in the synthesis of Ag, TiO_2, $Co(OH)_2$, and Co_3O_4 nanomaterials using GC/MS technique.
5. Comparison of the antifungal activity against three *Candida spp*. of Ag, TiO_2, $Co(OH)_2$, and Co_3O_4 nanomaterials synthesized using methanolic *S. platensis* extract, in various concentrations of nanomaterials and in the presence or absence of light.
6. Synthesis of Co_3O_4 nanomaterials using methanolic extract of *S. platensis, C. vulgaris*, and *H. pluvialis* and their characterization in various calcination temperatures.

7. Comparison of the CO oxidation catalytic activity of Co_3O_4 nanomaterials synthesized using microalgal extract and commercially available Co_3O_4 nanomaterials.
8. Influence of the extract components (potassium and phosphorus) on the properties and activity of Co_3O_4 nanomaterials.
9. Synthesis of Ag nanoparticles using *S. platensis*, *C. vulgaris*, and *H. pluvialis* methanolic extract and their characterization before and after calcination.
10. Comparison of the photocatalytic activity against Brilliant Blue R dye in different light intensity, dye concentrations, catalyst loadings, pH, and before and after calcination.
11. Investigation of the photocatalytic mechanism of Ag NPs synthesized using microalgae against Brilliant Blue R dye.

1.6 Outline

Chapter 2 details the state-of-the-art literature review on the synthesis of nanoparticles using microalgae. The advantages and disadvantages of the usage of microalgae are discussed, as well as various approaches to the synthesis methods taking place inside or outside the cell. The main groups of the microalgal metabolites are characterized together with their main role during the synthesis. The biological applications of nanoparticles related to anticancer, sensing, drug delivery, immunomodulatory, antibacterial, and antifungal properties are connected with the properties of the synthesized nanoparticles used for the studies.

Chapter 3 describes the synthesis of Ag, TiO_2, $Co(OH)_2$ and Co_3O_4 nanomaterials using S. platensis methanolic extract for their antifungal activity. The involvement of metabolites from the extract was studied using GCMS and FTIR techniques while the nanomaterials were characterized by XRD, XRD, SEM, TGA and zeta potential. The effect of calcination and partial removal of organic content was studied. The products were applied against three different *Candida* species (*C. albicans, C. glabrata*, and *C. krusei*) in various concentrations and in the presence or absence of light. The results show the antifungal potential of nanomaterials synthesized using *S. platensis* extract.

Chapter 4 characterizes Co_3O_4 nanomaterials synthesized by three microalgae species *S. platensis, C. vulgaris*, and *H. pluvialis* and subjected to three different calcination temperatures.

The involvement of the extracts was studied using ATR-FTIR and UV-Vis techniques. The synthesized Co_3O_4 nanomaterials were characterized using XRD, BET, UV-Vis, SEM, TEM, EELS, XPS, and UATR-FTIR methods. The catalytic CO oxidation activity was measured in a continuous-flow reactor at room temperature, and the mechanisms were studied using in-situ DRIFTS, DSC, H_2-TPR, and O_2-TPD methods. The results revealed the prospects on the Co_3O_4 nanomaterials structural modifications by microalgal extract components.

Chapter 5 is dedicated to the synthesis of Ag nanoparticles using *S. platensis, C. vulgaris*, and *H. pluvialis* and the influence of calcination on their structure. The nanoparticles were characterized using XRD, FTIR, SEM, EDX, TGA, and UV-Vis techniques. The photocatalytic performance was studied against Brilliant Blue R dye in various conditions regarding light intensity, dye concentration, catalyst loading, pH or calcination process. The study focused on the mechanism of photocatalytic activity and optimization for the optimal dye removal.

Finally, chapter 6 is dedicated to conclusions.

1.7 References

1. A. Abdelfattah, S.S. Ali, H. Ramadan, E.I. El-Aswar, R. Eltawab, S.H. Ho, T. Elsamahy, S. Li, M.M. El-Sheekh, M. Schagerl, M. Kornaros, J. Sun, Microalgae-based wastewater treatment: Mechanisms, challenges, recent advances, and future prospects, Environ. Sci. Ecotechnology. 13 (2023) 100205. https://doi.org/10.1016/j.ese.2022.100205.

2. A. Mulgund, Increasing lipid accumulation in microalgae through environmental manipulation, metabolic and genetic engineering: a review in the energy NEXUS framework, Energy Nexus. 5 (2022) 100054. https://doi.org/10.1016/j.nexus.2022.100054.

3. I. Hamed, The Evolution and Versatility of Microalgal Biotechnology: A Review, Compr. Rev. Food Sci. Food Saf. 15 (2016) 1104–1123. https://doi.org/10.1111/1541-4337.12227.

4. M. Gantar, Z. Svirčev, Microalgae and cyanobacteria: Food for thought, J. Phycol. 44 (2008) 260–268. https://doi.org/10.1111/j.1529-8817.2008.00469.x.

5. A. Del Mondo, A. Smerilli, E. Sané, C. Sansone, C. Brunet, Challenging microalgal vitamins for human health, Microb. Cell Fact. 19 (2020) 1–23. https://doi.org/10.1186/s12934-020-01459-1.

6. A.K. Patel, A.S. Chauhan, P. Kumar, P. Michaud, V.K. Gupta, J.S. Chang, C.W. Chen, C. Di Dong, R.R. Singhania, Emerging prospects of microbial production of omega fatty acids: Recent updates, Bioresour. Technol. 360 (2022) 127534. https://doi.org/10.1016/j.biortech.2022.127534.

7. Ç. Yarkent, C. Gürlek, S.S. Oncel, Potential of microalgal compounds in trending natural cosmetics: A review, Sustain. Chem. Pharm. 17 (2020) 100304. https://doi.org/10.1016/j.scp.2020.100304.

8. S.S. Ali, S.G. Mastropetros, M. Schagerl, M. Sakarika, T. Elsamahy, M. El-Sheekh, J. Sun, M. Kornaros, Recent advances in wastewater microalgae-based biofuels production: A state-of-the-art review, Energy Reports. 8 (2022) 13253–13280. https://doi.org/10.1016/j.egyr.2022.09.143.

9. M. Han, C. Zhang, F. Li, S.H. Ho, Data-driven analysis on immobilized microalgae system: New upgrading trends for microalgal wastewater treatment, Sci. Total Environ. 852 (2022) 158514. https://doi.org/10.1016/j.scitotenv.2022.158514.

10. W. Raksajit, C. Maneeruttanarungroj, P. Mäenpää, K. Lehto, A. Incharoensakdi, Upregulation of Hox-hydrogenase gene expression by nutrient adjustment in the filamentous non-heterocystous cyanobacterium Arthrospira sp. PCC 8005, J. Appl. Phycol. 32 (2020) 3799–3807. https://doi.org/10.1007/s10811-020-02217-x.

11. Y.D. Perfiliev, A.K. Tambiev, M.A. Konnychev, A. V. Skalny, E.S. Lobakova, M.P. Kirpichnikov, Mössbauer spectroscopic study of transformations of iron species by the cyanobacterium Arthrospira platensis (formerly Spirulina platensis), J. Trace Elem. Med. Biol. 48 (2018) 105–110. https://doi.org/10.1016/j.jtemb.2018.02.030.

12. F. Delrue, E. Alaux, L. Moudjaoui, C. Gaignard, G. Fleury, A. Perilhou, P. Richaud, M. Petitjean, J.F. Sassi, Optimization of Arthrospira platensis (Spirulina) growth: From laboratory scale to pilot scale, Fermentation. 3 (2017) 59. https://doi.org/10.3390/fermentation3040059.

13. E.W. Becker, Micro-algae as a source of protein, Biotechnol. Adv. 25 (2007) 207–210. https://doi.org/10.1016/j.biotechadv.2006.11.002.

14. J. Dagnino-Leone, C.P. Figueroa, M.L. Castañeda, A.D. Youlton, A. Vallejos-Almirall, A. Agurto-Muñoz, J. Pavón Pérez, C. Agurto-Muñoz, Phycobiliproteins: Structural aspects, functional characteristics, and biotechnological perspectives, Comput. Struct. Biotechnol. J. 20 (2022) 1506–1527. https://doi.org/10.1016/j.csbj.2022.02.016.

15. A.L. Lupatini, L.M. Colla, C. Canan, E. Colla, Potential application of microalga Spirulina platensis as a protein source, J. Sci. Food Agric. 97 (2017) 724–732. https://doi.org/10.1002/jsfa.7987.

16. J. Wang, Z. Wang, Y. Cui, S. Yan, Dynamic monitoring of phycocyanin concentration in Chaohu Lake of China using Sentinel-3 images and its indication of cyanobacterial blooms, Ecol. Indic. 143 (2022) 109340. https://doi.org/10.1016/J.ECOLIND.2022.109340.

17. M.F. Ramadan, M.M.S. Asker, Z.K. Ibrahim, Functional bioactive compounds and biological activities of spirulina platensis lipids, Czech J. Food Sci. 26 (2008) 211–222. https://doi.org/10.17221/2567-cjfs.

18. L. Wang, B. Pan, J. Sheng, J. Xu, Q. Hu, Antioxidant activity of Spirulina platensis extracts by supercritical carbon dioxide extraction, Food Chem. 105 (2007) 36–41. https://doi.org/10.1016/J.FOODCHEM.2007.03.054.

19. B. Maddiboyina, H.K. Vanamamalai, H. Roy, Ramaiah, S. Gandhi, M. Kavisri, M. Moovendhan, Food and drug industry applications of microalgae Spirulina platensis: A review, J. Basic Microbiol. 63 (2023) 573–583. https://doi.org/10.1002/jobm.202200704.

20. N. Expósito, R. Carafa, V. Kumar, J. Sierra, M. Schuhmacher, G.G. Papiol, Performance of chlorella vulgaris exposed to heavy metal mixtures: Linking measured endpoints and mechanisms, Int. J. Environ. Res. Public Health. 18 (2021) 1–19. https://doi.org/10.3390/ijerph18031037.

21. T. Ainna Tunku Azmir Shah, L. Bee Gan, S. Zulkifly, H. Omar, A. Ismail, Bioeconomic study of Chlorella vulgaris in outdoor tank culture by using different types of fertilizer, (2014).

22. C. Safi, B. Zebib, O. Merah, P.Y. Pontalier, C. Vaca-Garcia, Morphology, composition, production, processing and applications of Chlorella vulgaris: A review, Renew. Sustain. Energy Rev. 35 (2014) 265–278. https://doi.org/10.1016/j.rser.2014.04.007.

23. M.P. Spínola, M.M. Costa, J.A.M. Prates, Enhancing Digestibility of Chlorella vulgaris Biomass in Monogastric Diets: Strategies and Insights, Animals. 13 (2023) 1017. https://doi.org/10.3390/ani13061017.

24. G. Canelli, L. Neutsch, R. Carpine, S. Tevere, F. Giuffrida, Z. Rohfritsch, F. Dionisi, C.J. Bolten, A. Mathys, Chlorella vulgaris in a heterotrophic bioprocess: Study of the lipid bioaccessibility and oxidative stability, Algal Res. 45 (2020) 101754. https://doi.org/10.1016/j.algal.2019.101754.

25. M.T. Ahmad, M. Shariff, F. Md. Yusoff, Y.M. Goh, S. Banerjee, Applications of microalga Chlorella vulgaris in aquaculture, Rev. Aquac. 12 (2020) 328–346. https://doi.org/10.1111/raq.12320.

26. A. Josephine, C. Niveditha, A. Radhika, A.B. Shali, T.S. Kumar, G. Dharani, R. Kirubagaran, Analytical evaluation of different carbon sources and growth stimulators on the biomass and lipid

production of Chlorella vulgaris - Implications for biofuels, Biomass and Bioenergy. 75 (2015) 170–179. https://doi.org/10.1016/j.biombioe.2015.02.016.

27. B.K. An, K.E. Kim, J.Y. Jeon, K.W. Lee, Effect of dried Chlorella vulgaris and Chlorella growth factor on growth performance, meat qualities and humoral immune responses in broiler chickens, Springerplus. 5 (2016) 1–7. https://doi.org/10.1186/s40064-016-2373-4.

28. S.N.H. Oslan, N.F. Shoparwe, A.H. Yusoff, A.A. Rahim, C.S. Chang, J.S. Tan, S.N. Oslan, K. Arumugam, A. Bin Ariff, A.Z. Sulaiman, M.S. Mohamed, A review on haematococcus pluvialis bioprocess optimization of green and red stage culture conditions for the production of natural astaxanthin, Biomolecules. 11 (2021) 1–15. https://doi.org/10.3390/biom11020256.

29. M. Mularczyk, I. Michalak, K. Marycz, Astaxanthin and other nutrients from haematococcus pluvialis—Multifunctional applications, Mar. Drugs. 18 (2020) 459. https://doi.org/10.3390/md18090459.

30. R. Le-Feuvre, P. Moraga-Suazo, J. Gonzalez, S.S. Martin, V. Henríquez, A. Donoso, C. Agurto-Muñoz, Biotechnology applied to Haematococcus pluvialis Fotow: challenges and prospects for the enhancement of astaxanthin accumulation, J. Appl. Phycol. 32 (2020) 3831–3852. https://doi.org/10.1007/S10811-020-02231-Z/TABLES/4.

31. S.N.H. Oslan, J.S. Tan, S.N. Oslan, P. Matanjun, R.A.M. Mokhtar, R. Shapawi, N. Huda, Haematococcus pluvialis as a potential source of astaxanthin with diverse applications in industrial sectors: Current research and future directions, Molecules. 26 (2021) 6470. https://doi.org/10.3390/molecules26216470.

32. P. Casella, A. Iovine, S. Mehariya, T. Marino, D. Musmarra, A. Molino, Smart Method for Carotenoids Characterization in Haematococcus pluvialis Red Phase and Evaluation of Astaxanthin Thermal Stability, Antioxidants 2020, Vol. 9, Page 422. 9 (2020) 422. https://doi.org/10.3390/ANTIOX9050422.

33. S. Boussiba, Carotenogenesis in the green alga Haematococcus pluvialis: Cellular physiology and stress response, Physiol. Plant. 108 (2000) 111–117. https://doi.org/10.1034/j.1399-3054.2000.108002111.x.

34. Y. Ren, J. Deng, J. Huang, Z. Wu, L. Yi, Y. Bi, F. Chen, Using green alga Haematococcus pluvialis for astaxanthin and lipid co-production: Advances and outlook, Bioresour. Technol. 340 (2021) 125736. https://doi.org/10.1016/j.biortech.2021.125736.

Chapter 2

Nanoparticles from microalgae and their biomedical applications

Adapted from:

Nanoparticles from Microalgae and Their Biomedical Applications

Agnieszka Sidorowicz, Giacomo Fais, Mattia Casula, Massimiliano Borselli, Giuseppe Giannaccare, Antonio Mario Locci, Nicola Lai, Roberto Orrù , Giacomo Cao, and Alessandro Concas

Marine Drugs, vol. 21, no. 6, p. 352, Jun. 2023, doi: 10.3390/md21060352.

2.1 Introduction

The increasing human population and life expectancy are causing a change in the leading cause of death, such as heart conditions, cancer, or pulmonary diseases [1]. The shift is pushing the healthcare system to find new solutions to these problems; however, hospitals can be a source of nosocomial infections which are especially dangerous for immunocompromised patients. Another major issue is microbial antibiotic resistance due to antibiotics abuse which can lead to the emergence of life-threatening diseases [2].

New promising solutions are introduced by recent developments in nanotechnology which are focused on the manipulation of matter having characteristic size lower than 100 nm in at least one dimension. The prevailing quantum effect at such scale can give rise to multiple applications of the products. The prepared materials at the nanoscale might have different features than their bulk equivalents which show the potential for obtaining various properties even within the same element. Several methods are used to synthesize nanoparticles (NPs) such as physical, chemical, or biological routes. Among them, great attention is being paid to biological synthesis due to its low toxicity and biocompatibility, which are crucial for biomedical applications.

One group of organisms used for biological synthesis is microalgae due to their rapid increase in biomass, the independence on arable land, and the abundance of valuable metabolites [3]. Moreover, microalgae can be cultivated also in the wastewater independently from seasonal breaks which is an important economical aspect [4]. The bioactive substances derived from the secondary metabolism such as proteins, polysaccharides, lipids, vitamins, and pigments have displayed their great potential for many applications [5] The identified compounds are mainly used for their nutritional value; however, they can participate in the synthesis of various NPs used for biomedical applications.

Although the use of metabolites in the synthesis of various NPs can result in obtaining highly valuable materials, the mechanism behind it is still unclear [6,7]. In this review, the state of the art related to the participation of microalgal compounds in NPs synthesis is analyzed considering the location of the process (intra- or extracellular). Moreover, recent biomedical applications are taken into account to show the potential of microalgae to be applied in medicine. The recent advancements in the synthesis of NPs using microalgae have been summarized connecting their synthesis method with resulted performance. Therefore, the work can provide future prospects for the optimization of the synthesis of highly valuable materials using microalgae.

2.2 Biological synthesis

2.2.1 Microalgal metabolites

Microalgae are single-celled, photosynthetic organisms found in both marine and freshwater ecosystems. The classification of these organisms is based on the properties such as pigmentation, photosynthetic membrane organization, chemical nature of the photosynthetic storage products, or morphological features [6]. The groups are poly-phyletic and highly diverse, with both procaryotic and eucaryotic organisms. The most abundant microalgae are *Cyanophyceae* (blue-green algae), *Bacillariophyceae* (including the diatoms) and *Chlorophyceae* (green algae), with 50,000 estimated existing species, out of which 30,000 species were investigated [6]. Microalgae produce a variety of substances, including proteins, carbohydrates, lipids, nucleic acids, vitamins, and minerals [8–10]. The cellular content of each group varies depending on the specific strain and their physiological reactions to biotic and/or abiotic factors

such as light intensity, photoperiod, temperature, medium composition, and growth phase [11,12]. The typical compounds reported so far participating in the synthesis of nanoparticles are proteins, carbohydrates, and lipids.

The main mechanism involved in the biosynthesis of NPs deals with different metabolites of microalgae that can reduce precursor metal ions into a zerovalent state (Fig. 2).

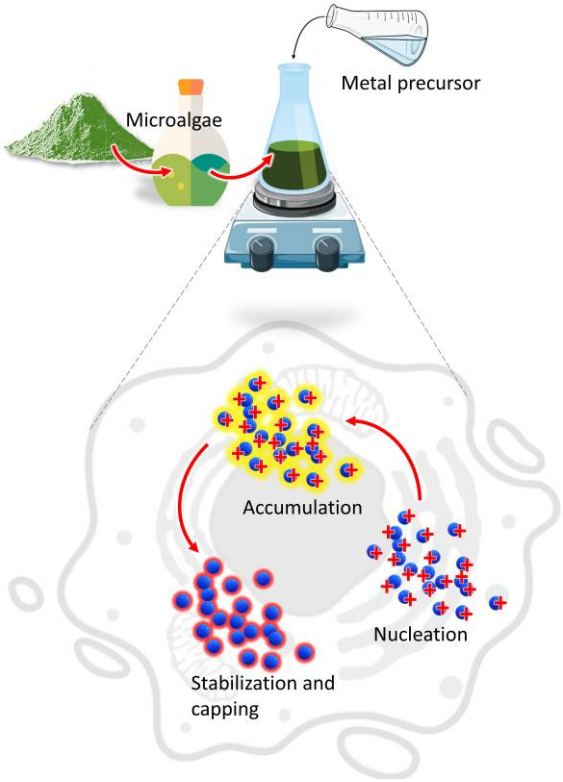

Figure 2 Mechanism of NPs synthesis by microalgae.

The process involves (i) the activation phase, when the metal ion is reduced, and nucleation occurs, followed by (ii) the growth phase, with an amalgamation of formed unit cells into crystallites which is concluded in (iii) the termination phase, where NPs having different shapes and sizes are thermodynamically stable [13]. Other factors such as temperature, pH, or metal ion concentration could affect the synthesis process; however, the participation of microalgae metabolites is crucial to understand the connection between the synthesis procedure and the properties of the obtained product [14,15]. Moreover, during microalgae cultivation sunlight and carbon dioxide can be acquired from the surroundings while the nutrients could be converted

from the wastewater to form biomass which provides the new routes for economic sustainability [16].

2.2.2 Proteins

Proteins are an important component in the structure and metabolism of micro-algae. They are an integral part of the cellular membrane and light-harvesting complex as well as they participate as enzymes in numerous catalytic reactions [17,18]. Several species of microalgae are studied due to their high protein content ranging from 42-70% in some cyanobacteria and up to 58% for *Chlorella vulgaris* dry weight [19,20].

The involvement of proteins in the synthesis of nanoparticles is usually investigated using Fourier Transform Infrared Spectroscopy (FTIR) based techniques. The reduction role of the proteins is demonstrated during the oxidation of −CHO to −COOH group, while NH_2 groups usually play capping functions through residual amino acids such as cysteine, tyrosine, and tryptophan [21]. In the study by Chokshi et al., the spectra between prepared extract of *Acutodesmus dimorphus* and prepared Ag NPs were compared, showing the role of amide linkage in the stabilization of Ag NPs by peptides and proteins [22]. The obtained NPs were spherical with 2-20 nm in size. Moreover, the overlapping peaks between the extract and the product suggest their coating properties to ensure their stabilization and prevent agglomeration. The surface of NPs might be further modified by sulfonated polysaccharides with proteins that provide a link between nanoparticles and coating molecules [21]. Proteins also possess a strong affinity to bind to metal ions that act as reducing agents [21]. Similar findings have been reported for AgCl NPs from Chlorella vulgaris and Ti NPs from marine microalgae *Phaeodactylum tricornutum* [23,24]. Although the exact mechanism of the synthesis is unknown, the statistical experimental design approach has been studied by using response surface methodology for future large-scale production.

2.2.3 Carbohydrates

Similar to proteins, carbohydrates display both structural and metabolic properties. Mono-, and oligosaccharides can be found attached to proteins or lipids, forming glycoproteins or glycolipids, while polysaccharides are the major structural component of the cell wall [25]. Moreover,

glucose and starch-like energy storage products are obtained during photosynthesis as the primary carbon-containing molecules in microalgae [26]. Cyanophytes were reported to accumulate glycogen, while other species form semi-amylopectin [27]. Two glucose polymers, amylopectin, and amylose are starch component of *Chlorophyta*, however, *Rhodophyta* synthesize a carbohydrate polymer known as floridean starch [10,28]. Diatoms produce chrysolaminarin composed of β(1,3) and β(1,6) linked glucose units which can accumulate around 7% of their total carbon content in the optimal conditions and up to 80% under strong nutrient depletions [29,30].

Carbohydrates are rich in reducing groups, such as hydroxy and carboxy, which can bind and reduce metal atoms, thereby acting as reducing agents. Moreover, due to the supramolecular interactions by inter and intra-molecular hydrogen bonding, they can stabilize formed nanoparticles and prevent further agglomeration, acting as cap-ping agents [16,31]. The potential of secretory carbohydrates from *C. vulgaris* was tested by the removal of biomass from the culture and used for the synthesis of FeOOH NPs [32]. The synthesis process using carbohydrates was compared with chemical route with sodium hydroxide acting as a precipitating agent. The carbohydrates were reported to be involved in the nucleation process by chelation of iron ions to prevent monotonic nucleation and limit nuclei size, which is further controlled in the growth phase to inhibit large particle formation. The secretory carbohydrates were described mainly for their reducing properties rather than being capping agents. The obtained NPs were spherical with size range 8-17 nm.

The exopolysaccharides from *Botryococcus braunii* and *Chlorella pyrenoidosa* were also tested for the synthesis of Ag NPs [33]. The polysaccharides performed both reducing and capping functions, and were bound to the Ag NPs surface through carboxy and hydroxy groups. Similar size range was reported of 5-15 nm. In a study by Jakhu et al., Au NPs synthesized from *Chlorella* polysaccharides were compared with Au NPs synthesized using citrate to compare their properties [34]. Both products exhibited a controlled size range; however, AuNPs from polysaccharides were stable in the pH range 2-12 while citrate-Au NPs were stable only at basic pH values. The NPs synthesized using polysaccharides were significantly bigger than citrate with

size ranges 30-40 nm and 10-15 nm respectively. Furthermore, citrate-Au NPs were forming agglomerates in a 30-fold lower concentration of NaCl, further proving the stabilization of the surface of Au NPs by microalgal polysaccharides.

2.2.4 Lipids

Secondary to polysaccharide, lipids function as energy reservoirs as well as structural components of the cell membranes. In microalgae, lipids are mainly composed of (i) neural lipids such as free fatty acids, acylglycerols, and carotenoids, and (ii) polar lipids, including phospholipids and galactolipids [35]. The polar lipids fraction can significantly increase during exponential growth; however, during stationary phase when the nutrient availability is limited under stress conditions, they can produce tri-acylglycerols [36]. The fatty acid content is composed of a mixture of C16 and C18 saturated and unsaturated fatty acids with longer carbon-chains including omega fatty acids. Saturated fats are stored in neutral lipid bodies while unsaturated are connected with polar lipids in membranes maintaining membrane fluidity under fluctuating cultivation conditions [37,38]. The overall lipid fraction can represent up to 20-50% of the dry biomass, depending on the microalgal species and cultivation conditions such as nutrient availability, salinity, light intensity, and growth phase [39]. During the nutrient depletion, the neutral lipid and polysaccharide content can increase at the expense of proteins [40]. Lipids receive the greatest attention for extraction followed by pro-duction of biodiesel whereas polyunsaturated fatty acids are used for their nutraceutical value.

In contrast to water, which is commonly used for the synthesis, the involvement of lipids requires the usage of different solvents. Kashyap et al. utilized ethanolic extract to synthesize Ag/AgCl NPs from *Chlorella sp., Lyngbya putealis, Oocystis sp*., and *Scenedesmus vacuolatus* [41]. During the optimization process, *Oocystis sp* did not manage to produce NPs while Chlorella sp extract resulted in the synthesis of Ag/AgCl NPs of the smallest size. The study highlighted the role of lipids and proteins along with the hydroxy group stretching movements in the Ag/AgCl NPs formation with the size range 10-20 nm. In a study by Gusain et al., lipids and carbohydrates were extracted separately from *Acutodesmus obliquus* and used for the synthesis of carbon dots by the microwave thermal method [42]. The products had size range of 1.2-11 nm. The carbon

source did not alter the fluorescence behavior; however, the exact interactions during synthesis were not studied. The optical properties changed with the addition of acetone which demonstrated the potential of using different solvent for the synthesis. The role of lipids is hypothesized mainly as capping agents.

2.2.5 Intracellular synthesis

Depending on the location where NPs are formed, the corresponding synthesis can be divided into intracellular or extracellular routes. During the former one, live cultures are exposed to the metal precursor, and charged metal ions are transported by negatively charged sites of cell wall [43]. The trapped ions undergo reduction and form NPs of various sizes and morphologies inside the cell, which require various steps of purification from biomass.

In a study by Li et al., *Chromochloris zofingiensis* culture was used to prepare Au NPs [44]. The cells after synthesis were characterized showing a peak characteristic for Au NPs in the UV-vis spectrum, which was also confirmed by transmission and scanning electron microscopy findings. The proposed mechanism involves chelation by negatively charged functional groups in the cell wall such as −COOH, −OH, and $-OSO_3H$ followed by diffusion into the cytosol and reduction by electrons generated from photosynthetic electron transport using enzymes. Other species with different cell wall structures were also investigated for the synthesis mechanism. Instead, *Euglena gracilis* species cell wall possesses a glycoprotein-containing pellicle that allowed metal ions to easily penetrate the cell. On the contrary, the marine microalga *Nitzschia laevis* is composed of rigid cell wall containing amorphous hydrated porous silica frustule acting as a barrier to reduce ion diffusion into the cells. In addition, Raman spectroscopy was explored as a tool to identify and quantify biomass components in microalgae.

The effect of Ag/AgCl NPs synthesis on chlorophyll and lipid accumulation was studied on freshwater microalgae Scenedesmus sp., showing decrease of 20-35% after 120 h [45]. However, the cells treated with 0.5 mM AgNO3 showed 75.86% increase in palmitic acid due to the stress induced by Ag/AgCl NPs. Thus, the cells were able to synthesize Ag/AgCl NPs and improve the quality of biodiesel production. Intracellular synthesis was also used to obtain CdSe quantum dots from *C. pyrenoidosa* and *S. obliquus* [46]. First, selenium ions were introduced to the culture

to generate selenium precursors within photosynthetic electron transport system and after 12 h were combined with cadmium ions to form CdSe quantum dots. The algal cells were damaged during the process probably because of precursors reducing enzymatic activity and cell vitality. The intracellular synthesis process requires proper optimization to ensure high yield while maintaining a low toxicity profile.

2.2.6 Extracellular synthesis

The extracellular synthesis utilizes either the secreted molecules such as polysaccharides or involves processing of the biomass to produce extract which is utilized for synthesis of NPs [47]. This route is considered more convenient as NPs are easily purified from the solution. In addition, it allows for further modification of metabolites participating in the synthesis by varying adopted solvents, concentration, time, or pH [48,49].

The cell-free filtrate from freshwater microalgae *S. obliquus* culture with different nitrogen sources were used to extracellularly synthesize Ag NPs [50]. The study concentrated on the activity of reductases, nitrogen and sulfate, on Ag NPs synthesis depending on the composition of the medium. The enzymes are conjugated with electron donor and act as reducing agents. Moreover, the activity influenced not only the yield but also the properties or the obtained Ag NPs especially their size. Consequently, their size inversely correlated antimicrobial activity which demonstrates the importance of metabolites during the synthesis.

The cell-free *C. vulgaris* culture was investigated for different factors affecting Ag NPs synthesis including time, extract/precursor ratio, temperature, pH, precursor molarity, and incubation conditions [51]. The optimal conditions were maximum incubation time (24 h), silver nitrate/extract ratio (8:2), 37 °C, pH 12, 3 mM silver nitrate, and shaking. The study shows the potential of varying multiple factors during the synthesis of NPs, which might result in products with different properties. In a study by Shalaby et al., algal biomass was processed to obtain an extract which provided metabolites implicated in the synthesis of iron oxide NPs [52]. The synthesis was perfected by varying the ratio of precursor to extract, and the product with the highest absorbance was selected for further application.

2.3 Biomedical applications of microalgal NPs

The synthesis route free from toxic waste as well as economical and environmentally-friendly aspects show great potential of NPs synthesized from marine and fresh-water microalgae for a variety of applications (Fig. 3). Presence of naturally occurring biomolecules improves their biocompatibility in comparison with other synthesis routes, and thus, can be used for biomedical applications. In addition, the growth parameters and metabolites content can be easily altered to obtain a variation in the morphology of NPs for diverse utilization.

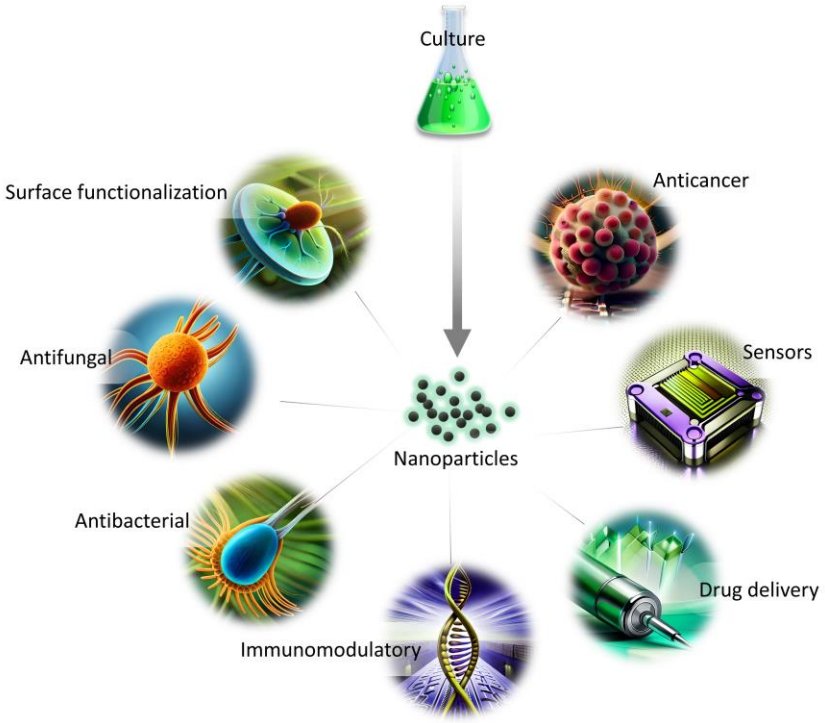

Figure 3 Applications of NPs from microalgae in biomedical fields.

The major drawback connected with the synthesis of NPs using a biological approach is their possible wide size distribution or heterogenous morphology. Thus, the obtained product might be difficult to assess in the context of molecular interactions within tissues or organs. The reason behind the differences might be connected with the complexity of molecules participating in the synthesis which reduce the metal ions with varying efficiency. However, the effect can be minimized by utilizing selected classes of secondary metabolites which can also improve the knowledge of their role in the synthesis. Currently, the lack of understanding behind the synthesis mechanism and the long-term effects of NPs are also limiting factors in the biological approach.

2.3.1 Anticancer activity

The anticancer activity of NPs synthesized from microalgae has been extensively investigated. The general mechanism associated with anticancer activities of NPs is related to ROS generation (Fig. 4). In a recent study by Hamida et al., Ag NPs were synthesized using freshwater strain *Coelastrella aeroterrestrica* and their anticancerous activity against four malignant cell lines was compared with chemically synthesized Ag NPs and the anticancer drug 5-fluorouracil [53]. The results showed the highest antiproliferative activity of microalgal Ag NPs against MCF-7, MDA, HCT-116, and HepG2 cell lines with low toxicity against non-cancerous cell lines, compared to the other tested. The activity was attributed to its small size, high stability, less agglomeration, and the surface chemistry. However, the mechanistic pathway inside the cancer cell and the pharmacokinetic nature of Ag NPs have yet to be explored.

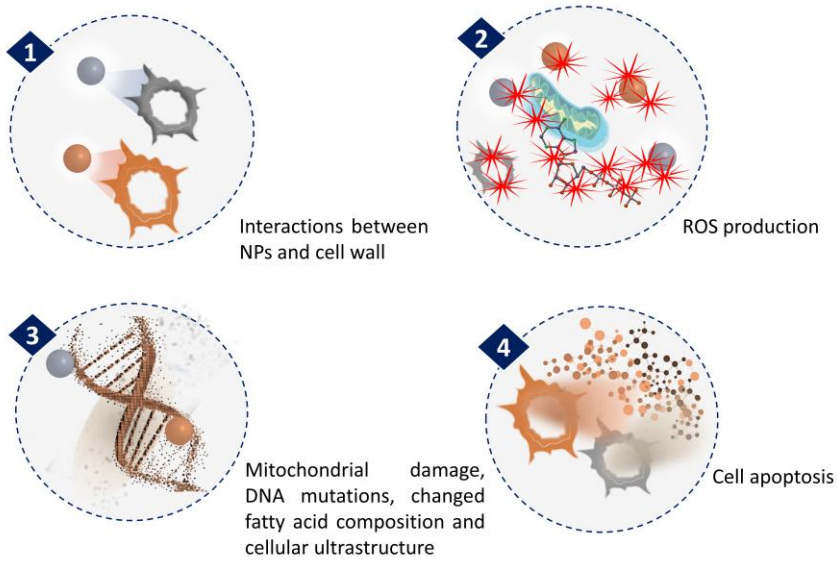

Figure 4 Mechanism of NPs anticancer activity through ROS generation.

The influence of various nanocomposites (NCs) synthesized from microalgae on cancer cell lines was also tested. In two separate studies, *S. obliquus* extract was used to conjugate Ag NPs with PtFe2O4 NPs ($PtFe_2O_4$@Ag) and $GaFe_2O_4$ NPs ($GaFe_2O4$@Ag) [54,55]. The cytotoxic properties of $PtFe_2O_4$@Ag NCs were related to cross-linking be-tween Pt and DNA to disrupt transcription and replication as well as reactive oxygen species (ROS) generation, lipid peroxidation and enhanced glutathione (GSH) degradation by Ag NPs. Similarly, Ga in $GaFe_2O_4$@Ag NCs can alter iron metabolism, resulting in the appearance of chromatin fragmentation and apoptotic bodies that

induce cell apoptosis. The prepared $PtFe_2O_4$@Ag NCs displayed a more prominent anti-cancerous activity than the $GaFe_2O_4$@Ag NCs; however, it was lower than cisplatin, a gastric cancer medication used as a control. Furthermore, $MgFe_2O_4$@Ag NCs were synthesized using extract of *C. vulgaris* showing anticancer activity through a similar apoptotic pathway [56]. The role of MgO in the NCs was attributed to enhancement of the magnetic properties and disruption of the cell membrane. Further studies are needed to enhance NCs activity and describe their effects in various cancerous and non-cancerous cell lines. Other reported NPs synthesized using microalgae tested for anticancer activity are presented in Tab. 1.

Table 1 Anticancer activity of NPs synthesized from microalgae.

Types of NPs	Microalgae Species Used	General Environment	Size and Morphology of NPs	Tested cancerous cell lines	Ref.
Silver NPs (Ag NPs)	*Arthrospira platensis*	marine, freshwater	2.23–14.68 nm, spherical	A549, HCT, Hep2 and WISH	[58]
Copper NPs (CuO NPs)	*Arthrospira platensis*	marine, freshwater	3.75–12.4 nm, spherical	A549, HCT, Hep2 and WISH	[58]
Silver NPs (Ag NPs)	*Arthrospira platensis*	marine, freshwater	30 nm, spherical	A-549, MCF-7	[59]
Au/cellulose nanocomposite	*Chlorella vulgaris*	freshwater	113-203 nm, spherical	A-549	[60]
Gold NPs (Au NPs)	*Dunaliella salina*	marine	22.4 nm, spherical	MCF-7	[61]
Carbon quantum dots	*Pectinodesmu sp.*	freshwater	67 nm, spherical	HCC 1954, HCT 116	[62]

Types of NPs	Microalgae Species Used	General Environment	Size and Morphology of NPs	Tested cancerous cell lines	Ref.
Silver NPs (Ag NPs)	*Trichodesmium erythraeum*	marine	26.5 nm, cubical	MCF-7, He La	[63]
Silver NPs (Ag_2O/|AgO NPs)	*Oscillatoria sp*	Freshwater	4.42–48.97 nm, quasi-spherical	CaCo-2, HeLa	[64]

Microalgae can serve as a source of valuable compounds that not only take part in the synthesis of anticancer drugs but also exhibit anticancer properties themselves. However, their proper action requires maintaining their structure which could be damaged due to the chemical or physical factors. In a study by İnan et al., the marine microalga *C. variabilis* and *C. pyrenoidosa* oil extracts were encapsulated into NPs using electrospraying technique [57]. Encapsulated oil extracts showed higher biocompatibility, while only *C. variabilis* oil extract showed improved anticancer properties com-pared to the non-encapsulated form. The activity changed in the dose-dependent manner with observed changes in the morphology of the cells. The research on optimizing encapsulation techniques could lead to the development of novel anticancer drugs of microalgal origin.

2.3.2 Biomedical sensor

Algal-synthesized NPs have shown the potential to be utilized for detection of dopamine, which plays an essential role in renal, central nervous, cardiovascular, and hormonal regulation. Moreover, it acts as neurotransmitter in reward and movement regulation in the brain and its abnormal concentrations can cause neurological disorders. The study by Huang et al. utilized ethanolic extract of the marine microalga *Spirulina* to synthesize Au NPs with 11-14 nm in size

for dopamine detection [65]. The proteins and polysaccharides from the extract participated in the synthesis as reducing and capping agents with abundance of -OH and -COOH groups on the Au NPs sur-face. The interactions between functional groups of dopamine cause changes in Au NPs surface allowing dopamine to be adsorbed thus forming additional hydrogen, ester, and amide bonds with other neighboring Au NPs. In that way, dopamine can act as a linkage between Au NPs with a new enhanced plasmon resonance absorption peak changing the color of the solution from wine red to blue-black. The set-up was tested to evaluate selectivity and anti-interference showing specificity in the presence of various components such as amino acids, salts, and glucose. However, when the Ca^{2+} content was above 200 µM, it could form complexes with the oxygen of –COOH group causing Au NPs aggregation, which can be thus prevented by keeping Ca^{2+} concentration at lower levels. When tested in human urine, the method was proven to be accurate and precise with a simple detection protocol.

Another compound that could be detected by NPs synthesized by microalgae is atropine, a tropane alkaloid used to treat low heart rate (bradycardia), overdose of cholinergic drugs and cholinergic poisoning, as well as to help reduce saliva, mucus, or other secretions during a surgery [66]. The marine microalga *S. platensis* biomass was used in a process to obtain Ag NPs on their surface as a coating material with an average size of 59 nm. The product was placed on the electrode with and without binder to test its properties. The results revealed high electrocatalytic activity in atropine de-termination with response fluctuation by change in pH value. The selectivity, stability, and reproducibility test proved the potential of the material as a stable sensor. In addition, the performance was confirmed by using atropine sulfate ampoule and water as real samples further elaborating the high accuracy and recovery rate of the prepared electrode.

In addition to neurotransmitters or pharmaceuticals, the glucose level can also be monitored by NPs from microalgae [67]. The biomass of *C. vulgaris* was processed using the hydrothermal method, acid hydrolysis assisted by ultrasonics, and was followed by hydrothermal method to obtain carbon dots. After each hydrothermal treatment, the carbon dots were collected to compare their synthesis method with properties. Acidic hydrolysis was considered crucial to

degrade starch and cellulose to reduce sugars to increase yield and prevent interactions between Fe^{2+} and residual –NH groups on the surface. In addition, low pH helped to prevent quenching during fluorescence response of carbon dots. The sensing mechanism was tested for Fe^{3+} and H_2O_2 and then applied to determine the glucose level in blood samples based on the reaction of the glucose oxidase enzyme and the quenching of fluorescence under optimized conditions. The results revealed high sensitivity and selectivity of the sensor obtained with potential use in diagnostics.

2.3.3 Drug delivery

Targeted drug delivery is a strategy to selectively administer pharmaceuticals into specific area to maximize its efficacy while avoiding side effects. In a study by Wang et al., microrobots were prepared for drug loading, targeted delivery, and chemo-photothermal therapy [68]. First, *S. platensis* cells were used as a template for core–shell-structured Pd@Au NPs synthesis by electroless deposition to act as photo-thermal conversion agents to allow laser-triggered degradation to release the drug. Additionally, Fe_3O_4 NPs were deposited on the surface via a sol–gel process for the magnetic actuation of the material. The anticancer drug doxorubicin was loaded on the prepared structure to allow their chemotherapeutic effect. The obtained micro-robots exhibited significant propulsion under a magnetic field and can be structurally disassembled into individual components under laser irradiation to be used for pH- and laser-triggered drug release. Moreover, Au and Fe_3O_4 NPs can be utilized as CT and MR imaging contrast agents, demonstrating the real-time monitoring of the treatment. Considering their small size, the authors suggest their oral administration for gastrointestinal cancer therapy.

Doxorubicin-loaded microrobots were also synthesized using the marine microalga *Thalassiosira weissflogii* as a template to substitute mesoporous silica NPs [69]. The magnetic Fe_3O_4 NPs were adhered to the template surface for the magnetic actuation properties. Using an external magnetic field, the movement of microrobots can be controlled in trajectories by changing the frequency, allowing microrobots to move through channels of various diameters. The clustering behavior enables the micro-robots to carry high-load to the target position with subsequent

release in a pH-sensitive manner. The microrobots were tested on MCF-7 human breast cancer cells demonstrating their efficiency. Further studies in vivo are required to test their application.

In addition, the marine microalga *T. weissflogii* was utilized in a separate study as a template for the delivery of curcumin-loaded drugs for anticancer and antibacterial properties [70]. The nanoporous architecture of *T. weissflogii* frustules provided a cage-like structure for curcumin adsorption which was stabilized by interactions of functional groups. The potential of *T. weissflogii* to be used for drug delivery systems shows its future application for the treatment of a wide range of diseases.

Microalgae can act not only as a template for drug delivery but can also be a source of valuable molecules that display therapeutic activities. Freshwater microalgae *Botryococcus braunii* and *Microcystis aeruginosa* oil, rich in polyunsaturated fatty acids, were loaded into NP electrosprayed with alginate/polyvinylidene (PVA) and tested for antibacterial activity with stabilized release [71]. The encapsulation protected bio-active and antioxidant properties of the oil which shows the potential for their storage and use for commercial application.

2.3.4 Immunomodulatory action

The study by Chandrarathna et al. investigated the effect of pectin, a polysaccharide isolated from marine strain *Spirulina maxima* [72]. The nano form of the compound was obtained through sonication to avoid possible modifications from the addition of chemicals. The material was tested on the mice model in comparison with non-sonicated pectin, with an average particle size of 64.11 nm and 152.90 nm for sonicated and original pectin, respectively. The results revealed increased weight gain in the nano-pectin-treated mice due to the improved digestibility and availability of nutrients with the small particle size. In addition, small particle size provided a higher surface area for microbial growth in the intestines than the original longer pectin molecules. The mice treated with nano-pectin displayed an increased density of goblet cells in the gut barrier which blocks the access of pathogenic microbes to the gut epithelium as well as showed higher expression of intestinal alkaline phosphatases, which provide an anti-inflammatory effect. It was assumed that in order to better understand the interactions between pectin and gut microbiome long-term studies are required.

The immunomodulatory effect of nano-pectin from *S. maxima* was also tested in zebrafish both in vitro and in vivo [73]. The low toxicity of nano-pectin was hypothesized to be due to the morphological properties as well as the surface functionalization. In addition, the transcriptional analysis of immune related genes was performed to further describe the immunomodulatory action. The results showed increased expression of cytokines and antioxidants that participate in the innate immune response. Al-together, nano-pectin was crucial for stress-tolerance and anti-inflammatory actions on the molecular level for disease resistance. Although the wound healing activity was not remarkable, nano-pectin was hypothesized to engage immune system during the process. The studies on mice and zebrafish show the potential of nano-pectin to regulate the immune system response in different organisms; however, further investigations are required to understand the underlying mechanisms behind those actions.

Polysaccharides from a different marine species, *Arthrospira fusiformis*, were also tested for the synthesis of Ag NPs and their immunomodulatory properties [74]. The prepared material was tested in vitro on *Pseudomonas aeruginosa* as well as in vivo on *P. aeruginosa* infected rat models. The Ag NPs were on average around 10 nm in size with homogenous distribution. The findings showed a strong antibacterial effect due to the breakage of the outer membrane *of P. aeruginosa*, affecting cell permeability with the disruptions created called “pits” that lead to cell lysis, as investigated by in vitro studies. The algal coating was suggested to interact with human serum protein by slightly reducing its concentration resulting in increased cellular uptake and intracellularly killing of bacteria. Moreover, Ag NPs used as wound dressing of *P. aeruginosa* infected areas enhanced the wound healing by cytokine modulation and reducing of the inflammation. The proposed mechanism involves liberation of Ag^{+} from Ag NPs and their sequestration by H_2S–synthesizing enzymes in the macrophage resulting in formation of Ag_2S and lowering the inflammation. After 7 days of treatment the tissue structure in rats was restored, which shows the potential of Ag NPs from algae for future treatments which should be assessed during clinical trials.

2.3.5 Antibacterial activity

Antibiotic resistance can be counted among the worst threats to human health worldwide. Overuse of antibiotics leads to the emergence of multidrug bacterial strains, which are difficult to target using currently available medicaments. Therefore, as an alternative, the use of NPs has been proposed as novel antibacterial agents with superior bactericidal activity. The NPs obtained can alter the cell wall and membrane, penetrate the cytosol, and generate reactive oxygen species (ROS), leading to further damage to enzymes, lipids, and DNA [75]. The biomolecules on the NPs surface can enhance the antibacterial activity, while their exact role is not well understood. The activity targets both Gram-positive and Gram-negative bacteria including multidrug susceptible as well as multidrug resistant strains [76]. However, the antibacterial activity can vary between different tested bacterial strains of the same species probably due to the horizontal gene transfer [77]. As a result, bacteria may acquire genome is-lands encoding enzymes responsible for antimicrobial resistance to NPs. The role of NPs synthesis and morphology on their activity is presented in Tab. 2. The antibacterial activity was mainly tested using Ag NPs, however, other NPs such as Au NPs or ZnO NPs are also studied for their properties. Moreover, different microalgal species used for the synthesis result in various morphologies of the prepared NPs which further signifies the potential of microalgae to obtain antibacterial agents.

Table 2 Antibacterial activity of NPs synthesized from microalgae.

Types of NPs	Microalgae Species Used	General Environment	Size and Morphology of NPs	Bacteria Species Tested	Ref.
Gold NPs (AuNPs)	*Arthrospira platensis*	marine, freshwater	5 nm, spherical	*S. aureus, B. subtilis*	[77]
Gold NPs (AuNPs)	*Neodesmus pupukensis (MG257914)*	freshwater	5-34 nm, circular	*Pseudomonas sp, Serratia marcescens*	[78]
Silver NPs (AgNPs)	*Chlorococcum humicola (IMMTCC-17)*	freshwater	2-16 nm, spherical	*E. coli (ATCC-1105)*	[79]

Types of NPs	Microalgae Species Used	General Environment	Size and Morphology of NPs	Bacteria Species Tested	Ref.
Silver NPs (AgNPs)	*Scenedesmus sp. (IMMTCC-25)*	marine, freshwater	5-10 nm, spherical	*S. cutans, E. coli*	[80]
Silver NPs (AgNPs)	*Chlorella vulgaris sp.*	freshwater, terrestrial	7 nm, spherical	*S. aureus, E. coli*	[81]
Silver NPs (AgNPs)	*Chroococcus minutus*	freshwater	crystalline	*E. coli, S. aureus, P. aeruginosa,*	[82]
Silver NPs (AgNPs)	*Oscillatoria limnetica*	freshwater	3.30-17.97 nm, spherical/ anisotropic	*E. coli, B. cereus*	[83]
Silver NPs (AgNPs)	*Oscillatoria princeps*	marine, brackish, freshwater,	3.30-17.97 nm, spherical	*S. aureus, S. pyogenes, E. coli,*	[84]
Silver NPs (AgNPs)	*Anabaena sp. 66-2, Cylindrospermopsis sp. USC-CRB3, Synechocystis sp. 48-3, B. braunii,*	marine, brackish, freshwater	13-25 nm, spherical/ elongated	*B. megaterium, E. coli, B. subtilis, M. luteus, P. aeruginosa, S. aureus*	[85]
Silver NPs (AgNPs)	*Chlorella pyrenoidosa NCIM 2738*	freshwater	8 nm, irregular	*K. pneumoniae, A. hydrophila, Acenetobacter sp., S. aureus*	[86]
Silver NPs (AgNPs)	*Chlorella vulgaris sp. (C. vulgaris)*	freshwater	1,6-34,4 nm, spherical	*Staphilococcus Aureus, Klebsiella Pneumonia*	[23]
Silver NPs (AgNPs)	*Neodesmus pupukensis (MG257914)*	freshwater	52-179 nm, spherical	*Pseudomonas aeruginosa, E. coli, K. Pneumoniae, S. marcescens*	[78]
Silver NPs (AgNPs)	*Spirogyra varians*	freshwater	17.6 nm, spherical	*B. cereus, P. aeruginosa and Klebsiella, S. aureus, L.*	[87]

Types of NPs	Microalgae Species Used	General Environment	Size and Morphology of NPs	Bacteria Species Tested	Ref.
				monocytogenes, *E. coli*	
Silver NPs (AgNPs)	*Coelastrella aeroterrestrica*	freshwater	14.5 nm, hexagonal	*Staphylococcus aureus*, *Streptococcus pyogenes*, *Bacillus subtilis*, *Escherichia coli*, *Pseudomonas aeruginosa*	[53]
Silver NPs (AgNPs)	*Limnothrix sp. 37-2-1*	freshwater	31.86 nm, elongated	*B. megaterium*, *E. coli*, *B. subtilis*, *M. luteus*, *P. aeruginosa*, *S. aureus*	[85]
Silver NPs (AgNPs)	*Anabaena* sp. 66-2	brackish	24.13 nm, irregular	*B. megaterium*, *E. coli*, *B. subtilis*, *M. luteus*, *P. aeruginosa*, *S. aureus*	[85]
Silver NPs (AgNPs)	*Synechocystis* sp. 48-3	marine, brackish	14.64 nm, irregular	*B. megaterium*, *E. coli*, *B. subtilis*, *M. luteus*, *P. aeruginosa*, *S. aureus*	[85]
Silver NPs (AgNPs)	*Botryococcus braunii*	freshwater	15.67 nm, spherical	*B. megaterium*, *E. coli*, *B. subtilis*, *M. luteus*, *P. aeruginosa*, *S. aureus*	[85]

Types of NPs	Microalgae Species Used	General Environment	Size and Morphology of NPs	Bacteria Species Tested	Ref.
Silver NPs (AgNPs)	*Coelastrum* sp. 143-1	freshwater	19.28 nm, spherical	*B. megaterium, E. coli, B. subtilis, M. luteus, P. aeruginosa, S. aureus*	[85]
Silver NPs (AgNPs)	*Limnothrix* sp. 37-2-1	freshwater	25.65 nm, spherical and elongated	*B. megaterium, E. coli, B. subtilis, M. luteus, P. aeruginosa, S. aureus*	[85]
Silver NPs (AgNPs)	*Arthrospira platensis*	marine, freshwater	13.85 nm, spherical	*B. megaterium, E. coli, B. subtilis, M. luteus, P. aeruginosa, S. aureus*	[85]
Zinc oxide NPs (ZnO)	*Chlorella vulgaris sp. (C. vulgaris)*	freshwater	150 nm crystalline structure/21 nm rod-like appearance	*Staphylococcus aureus , Enterococcus faecalis, Escherichia coli, Pseudomonas aeruginosa*	[88]
Zinc oxide NPs (ZnO)	*Arthrospira platensis*	marine, freshwater	30.0-55.0 nm, spherical	*Bacillus subtilis, Staphylo coccus aureus, Pseudom onas aeruginosa, Esch erichia coli*	[89]

2.3.6 Antifungal activity

Emerging resistance to antifungal drugs with their limited availability becomes a growing public health concern, leading to an increase in fungal infections. Moreover, fungal infections can

rapidly spread in hospitals, especially between immunocompromised patients [90]. Therefore, increasing attention is being paid to satisfy the need to develop new and effective antifungal agents. So far, NPs have demonstrated excellent fungicidal activity against several fungal species, as shown in Table 3. The antifungal activity was studied for a variety of NPs, including Au NPs, Fe_3O_4 NPs, Ag NPs or $Co(OH)_2$ nanoflakes with various size ranges and morphologies. In addition, microalgae can contain molecules with fungicidal activity and if they also participate in the synthesis as reducing or capping agents, it would offer synergistic antifungal action [91].

Table 3 Antifungal activity of NPs synthesized from microalgae.

Types of NPs	Microalgae Species Used	General Environment	Size and Morphology of NPs	Species of Fungi Tested	Ref.
Cobalt hydroxide NPs ($Co(OH)_2$ NMs)	*Arthrospira platensis*	marine, freshwater	3.52 nm, nanoflake	*C. albicans, C. glabrata, C. krusei.*	[92]
Cobalt oxide NPs (Co_3O_4 NMs)	*Arthrospira platensis*	marine, freshwater	13.28 nm, nanoflake	*C. albicans, C. glabrata, C. krusei.*	[92]
Gold NPs (AuNPs)	*Neodesmus pupukensis (MG257914)*	freshwater	5-34 nm, circular shape	*A. niger, A. fumigatus, A. flavus, F. solani C. albicans*	[78]
Gold NPs (AuNPs)	*Chlorella sorokiniana*	freshwater	20 - 40 nm, spherical	*C. tropicalis, C. glabrata, and C. albicans*	[93]
Gold NPs (AuNPs)	*Chlorella Vulgaris*	freshwater	2 - 10 nm, spherical	*C. albicans*	[94]
Iron oxide NPs (Fe_3O_4-NPs)	*Chlorella K01*	freshwater	50 – 100 nm, spherical	*Fusarium oxysporum, Fusarium tricinctum, Fusarium maniliforme, Rhizoctonia solani, and Phythium sp.*	[95]

Types of NPs	Microalgae Species Used	General Environment	Size and Morphology of NPs	Species of Fungi Tested	Ref.
Silver NPs (AgNPs)	*Arthrospira platensis*	marine, freshwater	9.72 nm (before calcination) / 26.01 nm (after calcination), oval-shaped	*C. albicans, C. glabrata, C. krusei.*	[92]
Titanium dioxide NPs (TIO_2 NPs)	*Arthrospira platensis*	marine, freshwater	4.81 nm (before calcination) / 4.62 nm (after calcination), spherical-shaped	*C. albicans, C. glabrata, C. krusei.*	[92]
Zinc oxide NPs (ZnO)	*Arthrospira platensis*	marine, freshwater	≈30.0 to 55.0 nm, spherical	*C. albicans*	[89]

2.3.7 Functionalization to reduce toxicity

Microalgae are also a source of valuable compounds which can be further stabilized on the NPs surface. The study by Torrez-Diaz et al. proposed a method to stabilize *Chlorella* freshwater microalgae peptide (VECYGPNRPQF) on the Au NPs surface [96]. The NPs of Au were obtained through the chemical method of citrate reduction, and then peptide solution was added to the flask. The average product size was 15 nm in diameter and spherical in size with high stability after removing stabilizing agents and centrifuge runs. Peptide-functionalized Au NPs showed almost three times higher antioxidant activity than non-functionalized Au NPs, as well as decreased marine ecosystem toxicity, which could be linked with increased stability of functionalized Au NPs. The effect of the peptide on the marine organisms was hypothesized as either adaptation or usage as a nutrient in the stressful environment.

In a study by Rudi et al. Ag NPs from the commercial source were functionalized by adding to the culture of marine microalgae *S. platensis* and extraction from the biomass [97]. The product was spherical with 8-20 nm in size and administered to rats in comparison to PEG-Ag NPs. The greater concentration of silver was observed in the liver, however, the presence of silver in the brain tissues confirms the ability of Ag NPs to penetrate the blood-brain barrier. The *Spirulina*-functionalized Ag NPs were excreted from all organs except the brain while non-modified PEG-Ag NPs were also present in the liver. However, in a study by El-Deeb et al., upon treatment, the level of liver enzymes ALT and AST increased, while the concentration of urea and albumin remained normal, suggesting the interactions between Ag NPs mainly in the liver. The complexity of interactions between NPs and various organs should be assessed in a long-term study to understand the underlying molecular mechanisms.

The Se NPs synthesized using different amount of marine microalgae *S. platensis* polysaccharide extract were tested to assess their cytotoxicity against several cancer cell lines [98]. Increased concentration of polysaccharides decreased size of the prepared Se NPs to 20–50 nm with more homogeneous size distribution than without added polysaccharides. Moreover, Se NPs prepared from S. platensis polysaccharides were stable for at least 3 months with almost 9-fold increase in uptake by the cells. Subsequently, enhanced uptake improved the anti-cancer activity through apoptosis induction. In addition, the material showed selectivity between cancer and normal cell lines also displaying the potential for cancer chemoprevention.

In a separate study, Se NPs were functionalized with different amount of phycocyanin, pigment purified from marine microalgae *Spirulina sp*., against insulinoma cells [99]. The phycocyanin showed a similar tendency for the size and size distribution of Se NPs as that of polysaccharides; however, increasing the phycocyanin content in-creased the shell diameter surrounding Se NPs. Thus, the phycocyanin dosage was optimized, as smaller NPs are up-taken easily due to their larger surface area. The functionalized Se NPs showed protective action against intracellular ROS overproduction, mitochondria fragmentation, and activation of enzymes leading to cell apoptosis, induced by palmitic acid. The cytoprotective activity of functionalized Se NPs show their potential against diseases related to pancreatic islet damage.

2.4 Conclusions and future prospectives

Undoubtedly, microalgae serve as excellent candidates for the synthesis of a variety of NPs due to their rich content of secondary metabolites acting as capping and reducing agents. However, the process can suffer from several limitations such as low yield, the need for optimization of conditions, or the amount of time to complete the synthesis. The exact mechanism involving the action of metabolites is needed to describe NPs production. The wide range of NPs synthesized from microalgae applied in the biomedical sector shows the potential of the metabolites to influence the physicochemical properties of NPs. Further research is required to address the issues of kinetics, cell viability, and yield with their effect on the properties of NPs synthesized by conventional methods and by using microalgae.

As far as the future implications are concerned, it can be assumed that the alteration of synthesis conditions might also lead to extending the knowledge of the role of metabolites on the obtained NPs. Various species of microalgae and precursors can be tested for their application in the biomedical field. Moreover, diverse techniques applied in the extract preparation, targeting certain classes of metabolites might explain their role in the synthesis. Therefore, future studies on the synthesis of NPs using microalgae can lead not only to the optimization of the process but also to the conceptual understanding of the connection between synthesis, properties, and activity of NPs.

2.5 References

1. Ritchie, H.; Roser, M. Causes of Death, Our World in Data Available online: https://ourworldindata.org/causes-of-death (accessed on 16 April 2023).

2. Inda-Díaz, J.S.; Lund, D.; Parras-Moltó, M.; Johnning, A.; Bengtsson-Palme, J.; Kristiansson, E. Latent Antibiotic Resistance Genes Are Abundant, Diverse, and Mobile in Human, Animal, and Environmental Microbiomes. Microbiome 2023, 11, 44, doi:10.1186/s40168-023-01479-0.

3. Santiago-Díaz, P.; Rico, M.; Rivero, A.; Santana-Casiano, M. Bioactive Metabolites of Microalgae from Canary Islands for Functional Food and Feed Uses. Chem. Biodivers. 2022, 19, e202200230, doi:10.1002/CBDV.202200230.

4. Ray, A.; Nayak, M.; Ghosh, A. A Review on Co-Culturing of Microalgae: A Greener Strategy towards Sustainable Biofuels Production. Sci. Total Environ. 2022, 802, 149765, doi:10.1016/J.SCITOTENV.2021.149765.

5. Ibrahim, T.N.B.T.; Feisal, N.A.S.; Kamaludin, N.H.; Cheah, W.Y.; How, V.; Bhatnagar, A.; Ma, Z.; Show, P.L. Biological Active Metabolites from Microalgae for Healthcare and Pharmaceutical Industries: A Comprehensive Review. Bioresour. Technol. 2023, 372, 128661, doi:10.1016/j.biortech.2023.128661.

6. Cai, Y.; Lim, H.R.; Khoo, K.S.; Ng, H.-S.; Cai, Y.; Wang, J.; Tak-Yee Chan, A.; Show, P.L. An Integration Study of Microalgae Bioactive Retention: From Microalgae Biomass to Microalgae Bioactives Nanoparticle. Food Chem. Toxicol. 2021, 158, 112607, doi:10.1016/j.fct.2021.112607.

7. Maqbool, Q.; Yigit, N.; Stöger-Pollach, M.; Ruello, M.L.; Tittarelli, F.; Rupprechter, G. Operando Monitoring of a Room Temperature Nanocomposite Methanol Sensor. Catal. Sci. Technol. 2022, doi:10.1039/D2CY01395A.

8. Soru, S.; Malavasi, V.; Caboni, P.; Concas, A.; Cao, G. Behavior of the Extremophile Green Alga Coccomyxa Melkonianii SCCA 048 in Terms of Lipids Production and Morphology at Different PH Values. Extremophiles 2019, 23, 79–89, doi:10.1007/s00792-018-1062-3.

9. Soru, S.; Malavasi, V.; Concas, A.; Caboni, P.; Cao, G. A Novel Investigation of the Growth and Lipid Production of the Extremophile Microalga Coccomyxa Melkonianii SCCA 048 under the Effect of Different Cultivation Conditions: Experiments and Modeling. Chem. Eng. J. 2019, 377, 120589, doi:https://doi.org/10.1016/j.cej.2018.12.049.

10. Tsvetanova, F.; Yankov, D. Bioactive Compounds from Red Microalgae with Therapeutic and Nutritional Value. Microorg. 2022, Vol. 10, Page 2290 2022, 10, 2290, doi:10.3390/MICROORGANISMS10112290.

11. Gao, P.; Guo, L.; Gao, M.; Zhao, Y.; Jin, C.; She, Z. Regulation of Carbon Source Metabolism in Mixotrophic Microalgae Cultivation in Response to Light Intensity Variation. J. Environ. Manage. 2022, 302, 114095, doi:10.1016/J.JENVMAN.2021.114095.

12. Udayan, A.; Pandey, A.K.; Sirohi, R.; Sreekumar, N.; Sang, B.I.; Sim, S.J.; Kim, S.H.; Pandey, A. Production of Microalgae with High Lipid Content and Their Potential as Sources of Nutraceuticals. Phytochem. Rev. 2021 2022, 1–28, doi:10.1007/S11101-021-09784-Y.

13. Khan, F.; Shahid, A.; Zhu, H.; Wang, N.; Javed, M.R.; Ahmad, N.; Xu, J.; Alam, M.A.; Mehmood, M.A. Prospects of Algae-Based Green Synthesis of Nanoparticles for Environmental Applications. Chemosphere 2022, 293, 133571, doi:10.1016/J.CHEMOSPHERE.2022.133571.

14. Dinc, S.K.; Vural, O.A.; Kayhan, F.E.; San Keskin, N.O. Facile Biogenic Selenium Nanoparticle Synthesis, Characterization and Effects on Oxidative Stress Generated by UV in Microalgae. Particuology 2022, 70, 30–42, doi:10.1016/J.PARTIC.2021.12.005.

15. Alishah Aratboni, H.; Rafiei, N.; Mehdizadeh Allaf, M.; Abedini, S.; Naseema Rasheed, R.; Seif, A.; Barati, B.; Wang, S.; Morones-Ramírez, J.R. Nanotechnology: An Outstanding Tool for Increasing and Better Exploitation of Microalgae Valuable Compounds. Algal Res. 2023, 71, 103019, doi:10.1016/J.ALGAL.2023.103019.

16. Chan, S.S.; Low, S.S.; Chew, K.W.; Ling, T.C.; Rinklebe, J.; Juan, J.C.; Ng, E.P.; Show, P.L. Prospects and Environmental Sustainability of Phyconanotechnology: A Review on Algae-

Mediated Metal Nanoparticles Synthesis and Mechanism. Environ. Res. 2022, 212, 113140, doi:10.1016/J.ENVRES.2022.113140.

17. Zittelli, G.C.; Lauceri, R.; Faraloni, C.; Margarita, A.; Benavides, S.; Torzillo, G. Valuable Pigments from Microalgae: Phycobiliproteins, Primary Carotenoids, and Fucoxanthin. Photochem. Photobiol. Sci. 2023 2023, 1, 1–57, doi:10.1007/S43630-023-00407-3.

18. Kumar, R.; Hegde, A.S.; Sharma, K.; Parmar, P.; Srivatsan, V. Microalgae as a Sustainable Source of Edible Proteins and Bioactive Peptides – Current Trends and Future Prospects. Food Res. Int. 2022, 157, 111338, doi:10.1016/J.FOODRES.2022.111338.

19. Yucetepe, A. A Combination of Osmotic Shock and Ultrasound Pre-Treatments and the Use of Enzyme for Extraction of Proteins from Chlorella Vulgaris Microalgae: Optimization of Extraction Conditions by RSM. J. Food Meas. Charact. 2022, 16, 1516–1527, doi:10.1007/s11694-021-01258-1.

20. García-Gómez, C.; Márquez-Reyes, J.M.; Vidales-Contreras, J.A.; Nápoles-Armenta, J.; Luna-Maldonado, A.I. The Use of Microalgae and Cyanobacteria for Wastewater Treatment and the Sustainable Production of Biomass. Omi. Environ. Eng. Microbiol. Syst. 2022, 269–282, doi:10.1201/9781003247883-13.

21. Shankar, P.D.; Shobana, S.; Karuppusamy, I.; Pugazhendhi, A.; Ramkumar, V.S.; Arvindnarayan, S.; Kumar, G. A Review on the Biosynthesis of Metallic Nanoparticles (Gold and Silver) Using Bio-Components of Microalgae: Formation Mechanism and Applications. Enzyme Microb. Technol. 2016, 95, 28–44, doi:10.1016/J.ENZMICTEC.2016.10.015.

22. Chokshi, K.; Pancha, I.; Ghosh, T.; Paliwal, C.; Maurya, R.; Ghosh, A.; Mishra, S. Green Synthesis, Characterization and Antioxidant Potential of Silver Nanoparticles Biosynthesized from de-Oiled Biomass of Thermotolerant Oleaginous Microalgae Acutodesmus Dimorphus. RSC Adv. 2016, 6, 72269–72274, doi:10.1039/C6RA15322D.

23. da Silva Ferreira, V.; ConzFerreira, M.E.; Lima, L.M.T.R.; Frasés, S.; de Souza, W.; Sant'Anna, C. Green Production of Microalgae-Based Silver Chloride Nanoparticles with Antimicrobial

Activity against Pathogenic Bacteria. Enzyme Microb. Technol. 2017, 97, 114–121, doi:10.1016/J.ENZMICTEC.2016.10.018.

24. Caliskan, G.; Mutaf, T.; Agba, H.C.; Elibol, M. Green Synthesis and Characterization of Titanium Nanoparticles Using Microalga, Phaeodactylum Tricornutum. Geomicrobiol. J. 2022, 39, 83–96, doi:10.1080/01490451.2021.2008549.

25. Gouda, M.; Tadda, M.A.; Zhao, Y.; Farmanullah, F.; Chu, B.; Li, X.; He, Y. Microalgae Bioactive Carbohydrates as a Novel Sustainable and Eco-Friendly Source of Prebiotics: Emerging Health Functionality and Recent Technologies for Extraction and Detection. Front. Nutr. 2022, 9, 391, doi:10.3389/fnut.2022.806692.

26. Ran, W.; Wang, H.; Liu, Y.; Qi, M.; Xiang, Q.; Yao, C.; Zhang, Y.; Lan, X. Storage of Starch and Lipids in Microalgae: Biosynthesis and Manipulation by Nutrients. Bioresour. Technol. 2019, 291, 121894, doi:10.1016/J.BIORTECH.2019.121894.

27. Kaur, A.; Taggar, M.S.; Kalia, A.; Singh, M. Nitrate-Induced Carbohydrate Accumulation in Chlorella Sorokiniana and Its Potential for Ethanol Production. Bioenergy Res. 2022, 15, 253–263, doi:10.1007/s12155-021-10292-2.

28. Manning, S.R.; Perri, K.A.; Blackwell, K. Bioactive Polysaccharides from Microalgae. Polysaccharides Microb. Orig. 2022, 625–648, doi:10.1007/978-3-030-42215-8_37.

29. Jensen, E.L.; Yangüez, K.; Carrière, F.; Gontero, B. Storage Compound Accumulation in Diatoms as Response to Elevated CO2 Concentration. Biol. 2020, Vol. 9, Page 5 2019, 9, 5, doi:10.3390/BIOLOGY9010005.

30. Wang, F.; Yang, R.; Guo, Y.; Zhang, C. Isolation, Characterization and Immunomodulatory Activity Evaluation of Chrysolaminarin from the Filamentous Microalga Tribonema Aequale. Mar. Drugs 2023, Vol. 21, Page 13 2022, 21, 13, doi:10.3390/MD21010013.

31. Abadi, B.; Hosseinalipour, S.; Nikzad, S.; Pourshaikhali, S.; Fathalipour-Rayeni, H.; Shafiei, G.; Adeli-Sardou, M.; Shakibaie, M.; Forootanfar, H. Capping Agents for Selenium Nanoparticles in Biomedical Applications. J. Clust. Sci. 2022 2022, 1, 1–22, doi:10.1007/S10876-022-02341-3.

32. Ghanbariasad, A.; Taghizadeh, S.M.; Show, P.L.; Nomanbhay, S.; Berenjian, A.; Ghasemi, Y.; Ebrahiminezhad, A. Controlled Synthesis of Iron Oxyhydroxide (FeOOH) Nanoparticles Using Secretory Compounds from Chlorella Vulgaris Microalgae. Bioengineered 2019, 10, 390, doi:10.1080/21655979.2019.1661692.

33. Navarro Gallón, S.M.; Alpaslan, E.; Wang, M.; Larese-Casanova, P.; Londoño, M.E.; Atehortúa, L.; Pavón, J.J.; Webster, T.J. Characterization and Study of the Antibacterial Mechanisms of Silver Nanoparticles Prepared with Microalgal Exopolysaccharides. Mater. Sci. Eng. C 2019, 99, 685–695, doi:10.1016/J.MSEC.2019.01.134.

34. Jakhu, S.; Sharma, Y.; Sharma, K.; Vaid, K.; Dhar, H.; Kumar, V.; Singh, R.P.; Shekh, A.; Kumar, G. Production and Characterization of Microalgal Exopolysaccharide as a Reducing and Stabilizing Agent for Green Synthesis of Gold-Nanoparticle: A Case Study with a Chlorella Sp. from Himalayan High-Altitude Psychrophilic Habitat. J. Appl. Phycol. 2021, 33, 3899–3914, doi:10.1007/s10811-021-02580-3.

35. Jiménez Callejón, M.J.; Robles Medina, A.; Macías Sánchez, M.D.; González Moreno, P.A.; Navarro López, E.; Esteban Cerdán, L.; Molina Grima, E. Supercritical Fluid Extraction and Pressurized Liquid Extraction Processes Applied to Eicosapentaenoic Acid-Rich Polar Lipid Recovery from the Microalga Nannochloropsis Sp. Algal Res. 2022, 61, 102586, doi:10.1016/J.ALGAL.2021.102586.

36. Khoo, K.S.; Ahmad, I.; Chew, K.W.; Iwamoto, K.; Bhatnagar, A.; Show, P.L. Enhanced Microalgal Lipid Production for Biofuel Using Different Strategies Including Genetic Modification of Microalgae: A Review. Prog. Energy Combust. Sci. 2023, 96, 101071, doi:10.1016/J.PECS.2023.101071.

37. Vrana, I.; Bakija Alempijević, S.; Novosel, N.; Ivošević DeNardis, N.; Žigon, D.; Ogrinc, N.; Gašparović, B. Hyposalinity Induces Significant Polar Lipid Remodeling in the Marine Microalga Dunaliella Tertiolecta (Chlorophyceae). J. Appl. Phycol. 2022, 34, 1457–1470, doi:10.1007/s10811-022-02745-8.

38. Zheng, G.; Gu, F.; Cui, Y.; Lu, L.; Hu, X.; Wang, L.; Wang, Y. A Microfluidic Droplet Array Demonstrating High-Throughput Screening in Individual Lipid-Producing Microalgae. Anal. Chim. Acta 2022, 1227, 340322, doi:10.1016/J.ACA.2022.340322.

39. Karimi, K.; Saidi, | Majid; Moradi, P.; Ali, |; Najafabadi, T. Biodiesel Production from Nannochloropsis Microalgal Biomass-Derived Oil: An Experimental and Theoretical Study Using the RSM-CCD Approach. Can. J. Chem. Eng. 2023, doi:10.1002/CJCE.24863.

40. Kafil, M.; Berninger, F.; Koutra, E.; Kornaros, M. Utilization of the Microalga Scenedesmus Quadricauda for Hexavalent Chromium Bioremediation and Biodiesel Production. Bioresour. Technol. 2022, 346, 126665, doi:10.1016/J.BIORTECH.2021.126665.

41. Kashyap, M.; Samadhiya, K.; Ghosh, A.; Anand, V.; Shirage, P.M.; Bala, K. Screening of Microalgae for Biosynthesis and Optimization of Ag/AgCl Nano Hybrids Having Antibacterial Effect. RSC Adv. 2019, 9, 25583–25591, doi:10.1039/C9RA04451E.

42. Gusain, D.; Renuka, N.; Guldhe, A.; Bux, F. Use of Microalgal Lipids and Carbohydrates for the Synthesis of Carbon Dots via Hydrothermal Microwave Treatment. Inorg. Chem. Commun. 2021, 134, 109021, doi:10.1016/J.INOCHE.2021.109021.

43. Algal, M.; Alprol, A.E.; Tageldein Mansour, A.; El-Beltagi, H.S.; Ashour, M. Algal Extracts for Green Synthesis of Zinc Oxide Nanoparticles: Promising Approach for Algae Bioremediation. Mater. 2023, Vol. 16, Page 2819 2023, 16, 2819, doi:10.3390/MA16072819.

44. Li, X.; Mao, X.; Xie, W.; Liu, B.; Chen, F. Intracellular Biosynthesis of Gold Nanoparticles for Monitoring Microalgal Biomass via Surface-Enhanced Raman Spectroscopy. ACS Sustain. Chem. Eng. 2022, 10, 4872–4880, doi:10.1021/acssuschemeng.1c07432.

45. Kashyap, M.; Samadhiya, K.; Ghosh, A.; Anand, V.; Lee, H.; Sawamoto, N.; Ogura, A.; Ohshita, Y.; Shirage, P.M.; Bala, K. Synthesis, Characterization and Application of Intracellular Ag/AgCl Nanohybrids Biosynthesized in Scenedesmus Sp. as Neutral Lipid Inducer and Antibacterial Agent. Environ. Res. 2021, 201, 111499, doi:10.1016/J.ENVRES.2021.111499.

46. Zhang, Z.; Chen, J.; Yang, Q.; Lan, K.; Yan, Z.; Chen, J. Eco-Friendly Intracellular Microalgae Synthesis of Fluorescent CdSe QDs as a Sensitive Nanoprobe for Determination of Imatinib. Sensors Actuators B Chem. 2018, 263, 625–633, doi:10.1016/J.SNB.2018.02.169.

47. Yilmaz Öztürk, B. Intracellular and Extracellular Green Synthesis of Silver Nanoparticles Using Desmodesmus Sp.: Their Antibacterial and Antifungal Effects. Caryologia 2019, 72, 29–43, doi:10.13128/CAYOLOGIA-249.

48. Hardiningtyas, S.D.; Putri, F.A.; Setyaningsih, I. Antibacterial Activity of Ethanolic Spirulina Platensis Extract-Water Soluble Chitosan Nanoparticles. IOP Conf. Ser. Earth Environ. Sci. 2022, 1033, 012053, doi:10.1088/1755-1315/1033/1/012053.

49. Muthusamy, G.; Thangasamy, S.; Raja, M.; Chinnappan, S.; Kandasamy, S. Biosynthesis of Silver Nanoparticles from Spirulina Microalgae and Its Antibacterial Activity. Environ. Sci. Pollut. Res. 2017, 24, 19459–19464, doi:10.1007/s11356-017-9772-0.

50. Darwesh, O.M.; Matter, I.A.; Eida, M.F.; Moawad, H.; Oh, Y.K. Influence of Nitrogen Source and Growth Phase on Extracellular Biosynthesis of Silver Nanoparticles Using Cultural Filtrates of Scenedesmus Obliquus. Appl. Sci. 2019, Vol. 9, Page 1465 2019, 9, 1465, doi:10.3390/APP9071465.

51. Rajkumar, R.; Ezhumalai, G.; Gnanadesigan, M. A Green Approach for the Synthesis of Silver Nanoparticles by Chlorella Vulgaris and Its Application in Photocatalytic Dye Degradation Activity. Environ. Technol. Innov. 2021, 21, 101282, doi:10.1016/J.ETI.2020.101282.

52. Shalaby, S.M.; Madkour, F.F.; El-Kassas, H.Y.; Mohamed, A.A.; Elgarahy, A.M. Green Synthesis of Recyclable Iron Oxide Nanoparticles Using Spirulina Platensis Microalgae for Adsorptive Removal of Cationic and Anionic Dyes. Environ. Sci. Pollut. Res. 2021, 28, 65549–65572, doi:10.1007/s11356-021-15544-4.

53. Hamida, R.S.; Ali, M.A.; Almohawes, Z.N.; Alahdal, H.; Momenah, M.A.; Bin-Meferij, M.M. Green Synthesis of Hexagonal Silver Nanoparticles Using a Novel Microalgae Coelastrella Aeroterrestrica Strain BA_Chlo4 and Resulting Anticancer, Antibacterial, and Antioxidant

Activities. Pharm. 2022, Vol. 14, Page 2002 2022, 14, 2002, doi:10.3390/PHARMACEUTICS14102002.

54. Fani, A.; Varmazyar, S.; Akbari, F.; Garfami, M.; Mohaghegh, R.; Balkhi, S.; Mojdehi, S.R.; Tabassi, N.R.; Hosseinpour, T.; Ghanbari, Z.; et al. Green Synthesis of a Novel PtFe2O4@Ag Nanocomposite: Implications for Cytotoxicity, Gene Expression and Anti-Cancer Studies in Gastric Cancer Cell Line. J. Clust. Sci. 2023, 34, 535–546, doi:10.1007/s10876-022-02244-3.

55. Sharif, A.P.; Habibi, K.; Bijarpas, Z. kohanrooz; Tolami, H.F.; Alkinani, T.A.; Jameh, M.; Dehkaei, A.A.; Monhaser, S.K.; Daemi, H.B.; Mahmoudi, A.; et al. Cytotoxic Effect of a Novel GaFe2O4@Ag Nanocomposite Synthesized by Scenedesmus Obliquus on Gastric Cancer Cell Line and Evaluation of BAX, Bcl-2 and CASP8 Genes Expression. J. Clust. Sci. 2022, 34, 1065–1075, doi:10.1007/s10876-022-02288-5.

56. Kardan, M.; Pouraei, A.; Jaahbin, N.; Ghasemipour, T.; Mehraban, F.; Jahani Sayyad Noveiri, M.; Hedayati, M.; Salehzadeh, A. Cytotoxicity of Bio-Synthesized MgFe2O4@Ag Nanocomposite on Gastric Cancer Cell Line and Evaluation Its Effect on Bax, P53 and Bcl-2 Genes Expression. J. Clust. Sci. 2022, 33, 1579–1588, doi:10.1007/s10876-021-02087-4.

57. İnan, B.; Mutlu, B.; Karaca, G.A.; Koç, R.Ç.; Özçimen, D. Bioprospecting Antarctic Microalgae as Anticancer Agent against PC-3 and AGS Cell Lines. Biochem. Eng. J. 2023, 195, 108900, doi:10.1016/J.BEJ.2023.108900.

58. Doman, K.M.; Gharieb, M.M.; Abd El-Monem, A.M.; Morsi, H.H. Synthesis of Silver and Copper Nanoparticle Using Spirulina Platensis and Evaluation of Their Anticancer Activity. https://doi.org/10.1080/09603123.2022.2163987 2023, doi:10.1080/09603123.2022.2163987.

59. Soror, A.F.S.; Ahmed, M.W.; Hassan, A.E.A.; Alharbi, M.; Alsubhi, N.H.; Al-Quwaie, D.A.; Alrefaei, G.I.; Binothman, N.; Aljadani, M.; Qahl, S.H.; et al. Evaluation of Green Silver Nanoparticles Fabricated by Spirulina Platensis Phycocyanin as Anticancer and Antimicrobial Agents. Life 2022, Vol. 12, Page 1493 2022, 12, 1493, doi:10.3390/LIFE12101493.

60. Hamouda, R.A.; Abd El Maksoud, A.I.; Wageed, M.; Alotaibi, A.S.; Elebeedy, D.; Khalil, H.; Hassan, A.; Abdella, A. Characterization and Anticancer Activity of Biosynthesized Au/Cellulose Nanocomposite from Chlorella Vulgaris. Polym. 2021, Vol. 13, Page 3340 2021, 13, 3340, doi:10.3390/POLYM13193340.

61. Singh, A.K.; Tiwari, R.; Singh, V.K.; Singh, P.; Khadim, S.R.; Singh, U.; Laxmi; Srivastava, V.; Hasan, S.H.; Asthana, R.K. Green Synthesis of Gold Nanoparticles from Dunaliella Salina, Its Characterization and in Vitro Anticancer Activity on Breast Cancer Cell Line. J. Drug Deliv. Sci. Technol. 2019, 51, 164–176, doi:10.1016/J.JDDST.2019.02.023.

62. Amjad, M.; Iqbal, M.; Faisal, A.; Junjua, A.M.; Hussain, I.; Hussain, S.Z.; Ghramh, H.A.; Khan, K.A.; Janjua, H.A. Hydrothermal Synthesis of Carbon Nanodots from Bovine Gelatin and PHM3 Microalgae Strain for Anticancer and Bioimaging Applications. Nanoscale Adv. 2019, 1, 2924–2936, doi:10.1039/C9NA00164F.

63. Sathishkumar, R.S.; Sundaramanickam, A.; Srinath, R.; Ramesh, T.; Saranya, K.; Meena, M.; Surya, P. Green Synthesis of Silver Nanoparticles by Bloom Forming Marine Microalgae Trichodesmium Erythraeum and Its Applications in Antioxidant, Drug-Resistant Bacteria, and Cytotoxicity Activity. J. Saudi Chem. Soc. 2019, 23, 1180–1191, doi:10.1016/J.JSCS.2019.07.008.

64. El-Sheekh, M.M.; Hassan, L.H.S.; Morsi, H.H. Assessment of the in Vitro Anticancer Activities of Cyanobacteria Mediated Silver Oxide and Gold Nanoparticles in Human Colon CaCo-2 and Cervical HeLa Cells. Environ. Nanotechnology, Monit. Manag. 2021, 16, 100556, doi:10.1016/J.ENMM.2021.100556.

65. Huang, G.; Chen, X.; Li, N.; Xie, T.; Guo, Y.; Fu, Y.; Jiao, T. A Convenient Synthesis of Gold Nanoparticles in Spirulina Extract for Rapid Visual Detection of Dopamine in Human Urine. Colloids Surfaces A Physicochem. Eng. Asp. 2022, 650, 129675, doi:10.1016/J.COLSURFA.2022.129675.

66. Ameen, F.; Hamidian, Y.; Mostafazadeh, R.; Darabi, R.; Erk, N.; Islam, M.A.; Orfali, R. A Novel Atropine Electrochemical Sensor Based on Silver Nano Particle-Coated Spirulina Platensis

Multicellular Blue-Green Microalga. Chemosphere 2023, 324, 138180, doi:10.1016/J.CHEMOSPHERE.2023.138180.

67. Jafari, S.M.; Masoum, S.; Tafreshi, S.A.H. A Microlagal-Based Carbonaceous Sensor for Enzymatic Determination of Glucose in Blood Serum. J. Ind. Eng. Chem. 2021, 101, 195–204, doi:10.1016/J.JIEC.2021.06.012.

68. Wang, X.; Cai, J.; Sun, L.; Zhang, S.; Gong, D.; Li, X.; Yue, S.; Feng, L.; Zhang, D. Facile Fabrication of Magnetic Microrobots Based on Spirulina Templates for Targeted Delivery and Synergistic Chemo-Photothermal Therapy. ACS Appl. Mater. Interfaces 2019, 11, 4745–4756, doi:10.1021/acsami.8b15586.

69. Li, M.; Wu, J.; Lin, D.; Yang, J.; Jiao, N.; Wang, Y.; Liu, L. A Diatom-Based Biohybrid Microrobot with a High Drug-Loading Capacity and PH-Sensitive Drug Release for Target Therapy. Acta Biomater. 2022, 154, 443–453, doi:10.1016/J.ACTBIO.2022.10.019.

70. Saxena, A.; Dutta, A.; Kapoor, N.; Kumar, A.; Tiwari, A. Envisaging Marine Diatom Thalassiosira Weissflogii as a “SMART” Drug Delivery System for Insoluble Drugs. J. Drug Deliv. Sci. Technol. 2022, 68, 102983, doi:10.1016/J.JDDST.2021.102983.

71. İnan, B.; Özçimen, D. Preparation and Characterization of Microalgal Oil Loaded Alginate/Poly (Vinyl Alcohol) Electrosprayed Nanoparticles. Food Bioprod. Process. 2021, 129, 105–114, doi:10.1016/J.FBP.2021.07.008.

72. Chandrarathna, H.P.S.U.; Liyanage, T.D.; Edirisinghe, S.L.; Dananjaya, S.H.S.; Thulshan, E.H.T.; Nikapitiya, C.; Oh, C.; Kang, D.H.; de Zoysa, M. Marine Microalgae, Spirulina Maxima-Derived Modified Pectin and Modified Pectin Nanoparticles Modulate the Gut Microbiota and Trigger Immune Responses in Mice. Mar. Drugs 2020, Vol. 18, Page 175 2020, 18, 175, doi:10.3390/MD18030175.

73. Rajapaksha, D.C.; Edirisinghe, S.L.; Nikapitiya, C.; Dananjaya, S.H.S.; Kwun, H.J.; Kim, C.H.; Oh, C.; Kang, D.H.; De Zoysa, M. Spirulina Maxima Derived Pectin Nanoparticles Enhance the

Immunomodulation, Stress Tolerance, and Wound Healing in Zebrafish. Mar. Drugs 2020, Vol. 18, Page 556 2020, 18, 556, doi:10.3390/MD18110556.

74. El-Deeb, N.M.; Abo-Eleneen, M.A.; Al-Madboly, L.A.; Sharaf, M.M.; Othman, S.S.; Ibrahim, O.M.; Mubarak, M.S. Biogenically Synthesized Polysaccharides-Capped Silver Nanoparticles: Immunomodulatory and Antibacterial Potentialities Against Resistant Pseudomonas Aeruginosa. Front. Bioeng. Biotechnol. 2020, 8, 643, doi:10.3389/fbioe.2020.00643.

75. Roy, A.; Bulut, O.; Some, S.; Mandal, A.K.; Yilmaz, M.D. Green Synthesis of Silver Nanoparticles: Biomolecule-Nanoparticle Organizations Targeting Antimicrobial Activity. RSC Adv. 2019, 9, 2673–2702, doi:10.1039/C8RA08982E.

76. Khalid, M.; Khalid, N.; Ahmed, I.; Hanif, R.; Ismail, M.; Janjua, H.A. Comparative Studies of Three Novel Freshwater Microalgae Strains for Synthesis of Silver Nanoparticles: Insights of Characterization, Antibacterial, Cytotoxicity and Antiviral Activities. J. Appl. Phycol. 2017, 29, 1851–1863, doi:10.1007/s10811-017-1071-0.

77. Suganya, K.S.U.; Govindaraju, K.; Kumar, V.G.; Dhas, T.S.; Karthick, V.; Singaravelu, G.; Elanchezhiyan, M. Size Controlled Biogenic Silver Nanoparticles as Antibacterial Agent against Isolates from HIV Infected Patients. Spectrochim. Acta Part A Mol. Biomol. Spectrosc. 2015, 144, 266–272, doi:10.1016/J.SAA.2015.02.074.

78. Omomowo, I.O.; Adenigba, V.O.; Ogunsona, S.B.; Adeyinka, G.C.; Oluyide, O.O.; Adedayo, A.A.; Fatukasi, B.A. Antimicrobial and Antioxidant Activities of Algal-Mediated Silver and Gold Nanoparticles. IOP Conf. Ser. Mater. Sci. Eng. 2020, 805, 012010, doi:10.1088/1757-899X/805/1/012010.

79. Jena, J.; Pradhan, N.; Prasad Dash, B.; Behari Sukla, L.; kumar Panda Affiliations, P. Biosynthesis and Characterization of Silver Nanoparticles Using Microalga Chlorococcum Humicola and Its Antibacterial Activity. Int. J. Nanomater. Biostructures 2013, 3, 1–8.

80. Jena, J.; Pradhan, N.; Nayak, R.R.; Dash, B.P.; Sukla, L.B.; Panda, P.K.; Mishra, B.K. Microalga Scenedesmus Sp.: A Potential Low-Cost Green Machine for Silver Nanoparticle Synthesis. J. Microbiol. Biotechnol. 2014, 24, 522–533, doi:10.4014/jmb.1306.06014.

81. Ebrahiminezhad, A.; Bagheri, M.; Taghizadeh, S.M.; Berenjian, A.; Ghasemi, Y. Biomimetic Synthesis of Silver Nanoparticles Using Microalgal Secretory Carbohydrates as a Novel Anticancer and Antimicrobial. Adv. Nat. Sci. Nanosci. Nanotechnol. 2016, 7, 015018, doi:10.1088/2043-6262/7/1/015018.

82. Sahoo, C.R.; Maharana, S.; Mandhata, C.P.; Bishoyi, A.K.; Paidesetty, S.K.; Padhy, R.N. Biogenic Silver Nanoparticle Synthesis with Cyanobacterium Chroococcus Minutus Isolated from Baliharachandi Sea-Mouth, Odisha, and in Vitro Antibacterial Activity. Saudi J. Biol. Sci. 2020, 27, 1580–1586, doi:10.1016/J.SJBS.2020.03.020.

83. Hamouda, R.A.; Hussein, M.H.; Abo-elmagd, R.A.; Bawazir, S.S. Synthesis and Biological Characterization of Silver Nanoparticles Derived from the Cyanobacterium Oscillatoria Limnetica. Sci. Reports 2019 91 2019, 9, 1–17, doi:10.1038/s41598-019-49444-y.

84. Bishoyi, A.K.; Sahoo, C.R.; Sahoo, A.P.; Padhy, R.N. Bio-Synthesis of Silver Nanoparticles with the Brackish Water Blue-Green Alga Oscillatoria Princeps and Antibacterial Assessment. Appl. Nanosci. 2021, 11, 389–398, doi:10.1007/s13204-020-01593-7.

85. Patel, V.; Berthold, D.; Puranik, P.; Gantar, M. Screening of Cyanobacteria and Microalgae for Their Ability to Synthesize Silver Nanoparticles with Antibacterial Activity. Biotechnol. Reports 2015, 5, 112–119, doi:10.1016/J.BTRE.2014.12.001.

86. Aziz, N.; Faraz, M.; Pandey, R.; Shakir, M.; Fatma, T.; Varma, A.; Barman, I.; Prasad, R. Facile Algae-Derived Route to Biogenic Silver Nanoparticles: Synthesis, Antibacterial, and Photocatalytic Properties. Langmuir 2015, 31, 11605–11612, doi:10.1021/acs.langmuir.5b03081.

87. Salari, Z.; Danafar, F.; Dabaghi, S.; Ataei, S.A. Sustainable Synthesis of Silver Nanoparticles Using Macroalgae Spirogyra Varians and Analysis of Their Antibacterial Activity. J. Saudi Chem. Soc. 2016, 20, 459–464, doi:10.1016/J.JSCS.2014.10.004.

88. Taghizadeh, S.M.; Lal, N.; Ebrahiminezhad, A.; Moeini, F.; Seifan, M.; Ghasemi, Y.; Berenjian, A. Green and Economic Fabrication of Zinc Oxide (ZnO) Nanorods as a Broadband UV Blocker and Antimicrobial Agent. Nanomater. 2020, Vol. 10, Page 530 2020, 10, 530, doi:10.3390/NANO10030530.

89. El-Belely, E.F.; Farag, M.M.S.; Said, H.A.; Amin, A.S.; Azab, E.; Gobouri, A.A.; Fouda, A. Green Synthesis of Zinc Oxide Nanoparticles (ZnO-NPs) Using Arthrospira Platensis (Class: Cyanophyceae) and Evaluation of Their Biomedical Activities. Nanomater. 2021, Vol. 11, Page 95 2021, 11, 95, doi:10.3390/NANO11010095.

90. Martins-Santana, L.; Rezende, C.P.; Rossi, A.; Martinez-Rossi, N.M.; Almeida, F. Addressing Microbial Resistance Worldwide: Challenges over Controlling Life-Threatening Fungal Infections. Pathog. 2023, Vol. 12, Page 293 2023, 12, 293, doi:10.3390/PATHOGENS12020293.

91. Scaglioni, P.T.; Pagnussatt, F.A.; Lemos, A.C.; Nicolli, C.P.; Del Ponte, E.M.; Badiale-Furlong, E. Nannochloropsis Sp. and Spirulina Sp. as a Source of Antifungal Compounds to Mitigate Contamination by Fusarium Graminearum Species Complex. Curr. Microbiol. 2019, 76, 930–938.

92. Sidorowicz, A.; Margarita, V.; Fais, G.; Pantaleo, A.; Manca, A.; Concas, A.; Rappelli, P.; Fiori, P.L.; Cao, G. Characterization of Nanomaterials Synthesized from Spirulina Platensis Extract and Their Potential Antifungal Activity. PLoS One 2022, 17, e0274753, doi:10.1371/JOURNAL.PONE.0274753.

93. Gürsoy, N.; Yilmaz Öztürk, B.; Dağ, İ. Synthesis of Intracellular and Extracellular Gold Nanoparticles with a Green Machine and Its Antifungal Activity. Turkish J. Biol. 2021, 45, 196–213, doi:10.3906/biy-2010-64.

94. Annamalai, J.; Nallamuthu, T. Characterization of Biosynthesized Gold Nanoparticles from Aqueous Extract of Chlorella Vulgaris and Their Anti-Pathogenic Properties. Appl. Nanosci. 2015, 5, 603–607, doi:10.1007/s13204-014-0353-y.

95. Win, T.T.; Khan, S.; Bo, B.; Zada, S.; Fu, P.C. Green Synthesis and Characterization of Fe3O4 Nanoparticles Using Chlorella-K01 Extract for Potential Enhancement of Plant Growth Stimulating and Antifungal Activity. Sci. Reports 2021 111 2021, 11, 1–11, doi:10.1038/s41598-021-01538-2.

96. Torres-Díaz, M.; Abreu-Takemura, C.; Díaz-Vázquez, L.M. Microalgae Peptide-Stabilized Gold Nanoparticles as a Versatile Material for Biomedical Applications. Life 2022, 12, 831, doi:10.3390/life12060831.

97. Rudi, L.; Zinicovscaia, I.; Cepoi, L.; Chiriac, T.; Peshkova, A.; Cepoi, A.; Grozdov, D. Accumulation and Effect of Silver Nanoparticles Functionalized with Spirulina Platensis on Rats. Nanomaterials 2021, 11, 2992, doi:10.3390/NANO11112992/S1.

98. Liu, C.; Fu, Y.; Li, C.E.; Chen, T.; Li, X. Phycocyanin-Functionalized Selenium Nanoparticles Reverse Palmitic Acid-Induced Pancreatic β Cell Apoptosis by Enhancing Cellular Uptake and Blocking Reactive Oxygen Species (ROS)-Mediated Mitochondria Dysfunction. J. Agric. Food Chem. 2017, 65, 4405–4413, doi:10.1021/acs.jafc.7b00896.

99. Yang, F.; Tang, Q.; Zhong, X.; Bai, Y.; Chen, T.; Zhang, Y.; Li, Y.; Zheng, W. Surface Decoration by Spirulina Polysaccharide Enhances the Cellular Uptake and Anticancer Efficacy of Selenium Nanoparticles. Int. J. Nanomedicine 2012, 7, 835–844, doi:10.2147/IJN.S28278.

Chapter 3

Characterization of nanomaterials synthesized from *Spirulina platensis* extract and their potential antifungal activity

Adapted from:

Characterization of nanomaterials synthesized from *Spirulina platensis* extract and their potential antifungal activity

Agnieszka Sidorowicz¶, Valentina Margarita¶, Giacomo Fais, Antonella Pantaleo, Alessia Manca, Alessandro Concas, Paola Rappelli, Pier Luigi Fiori, and Giacomo Cao

PLoS One, vol. 17, no. 9, p. e0274753, Sep. 2022, doi: 10.1371/JOURNAL.PONE.0274753.

3.1 Introduction

In the last two decades, the number of fungal infections significantly increased due to a higher prevalence of immunocompromised patients, broad-spectrum use of antibiotics, and growing need for hyperalimentation in hospitals [1]. One of the most common fungal infections is candidemia, caused by *Candida spp*, responsible for 15% of nosocomial infections, with an estimated mortality of 47% [2]. In addition, the risk of infection increases when surgical and mechanical devices are used, such as endotracheal tubes, drains, or urinary catheters [3]. Other potential risk factors include lack of, or inadequate, hygiene-environment of healthcare workers and duration of stay in the intensive care unit for more than 7 days [4,5].

Currently, treatment of fungal infections is based on polyenes, azoles, or echinocandins, which demonstrate strong fungicidal activity but can also cause adverse side effects or trigger several additional medications [6]. Moreover, such products could be poorly tolerated or could show a narrow spectrum of activity [7]. Recently, polyenes, azoles, and echinocandins have displayed an increase in Candida resistance due to their general and long-term use [8,9].

As for new fungicidal agents, significant attention has been given to nanomaterials (NMs) owing to their wide range of applications. Synthesized nanostructures have a size range of 1 – 100 nm in at least one dimension and altered physicochemical properties compared with bulk material including increased surface to volume ratio, high reactivity, altered magnetic and optical properties. Commonly obtained antimicrobial nanoparticles (NPs) include Ag NPs [10], ZnO NPs [11], CuO NPs [12], TiO_2 NPs [13], and Au NPs [14]. However, albeit showing strong antimicrobial activity, most of the synthesized NMs cannot be employed due to their low biocompatibility, especially when synthesized using chemical methods [15, 16, 17]. In this regard, green synthesis routes have been shown to be effective, simple, and affordable to produce biocompatible NMs [18]. Specifically, the techniques based on the use of extracts from blue-green algae seem quite promising [19].

It should be noticed that several works have investigated the synthesis of silver nanoparticles (Ag NPs), including the so called “allotropic silver” form [20], and their applications. In particular, Ismail and colleagues studied antioxidant, antiviral and antimicrobial activity of Ag NPs synthesized using phycobiliprotein extract of *S. platensis* [21]. The results showed the great potential of *S. platensis* extract as a tool to synthesize biocompatible Ag NPs to be used in the biomedical field.

Along with Ag NP, titanium dioxide NPs (TiO_2 NPs) are materials of great significance, mainly used for the photodegradation of several environmental contaminants [22,23]. Moreover, low toxicity and good biocompatibility of TiO_2 NPs find their applications in the biomedical field, such as bone tissue engineering, targeted drug delivery systems, or antibacterial devices for prevention and treatment of infections [24,25,26].

Recently, cobalt hydroxide ($Co(OH)_2$ NMs) and cobalt oxide nanomaterials (Co_3O_4 NMs) have been tested for biological as well as magnetic and catalytic applications [27]. Currently, to the best of our knowledge no reports are available on the synthesis of cobalt nanomaterials using Spirulina extract. Although Anwar et al describe the use of $Co(OH)_2$ NPs therapy against *Acanthamoeba castellani* infections, antimicrobial properties of green-synthesized $Co(OH)_2$ NMs have not been studied so far [28]. It is also worth mentioning that the photoactivity of NMs for a degradation of organic pollutants has been also investigated [29].

In our study, *S. platensis* extract has been used to synthesize six types of NMs: Ag NPs (before and after calcination), TiO_2 NPs (before and after calcination), $Co(OH)_2$ NMs, and Co_3O_4 NMs, in different concentrations with the presence of absence of light for their antifungal activity against *Candida albicans, C. glabrata*, and *C. krusei*. The participation of secondary metabolites from the extract was assessed and the characterization of the NMs was carried out with the aim of fully understanding the nanomaterials properties along with their antifungal activity.

3.2 Materials and methods

Unialgal culture of cyanobacterium S. platensis was obtained from the operating plant of TOLO Green located in Arborea (Sardinia, Italy) and cultivated in modified Zarrouk's Medium for enhanced biomass production [30]. The medium was prepared according to the composition in Table 1 while K_2SO_4 and $MgSO_4$ were added aseptically after setting pH to 9 and autoclaving the resulting solution under high pressure at 121°C for 20 min. It should be noted that the trace metal solution Zarrouk medium had the following composition: H_3BO_3 2860 mg/L, $ZnSO_4 \cdot 7\ H_2O$ 222 mg/L, $MnCl_2 \cdot 4\ H_2O$ 1810 mg/L, $CuSO_4 \cdot 5\ H_2O$ 79 mg/L while the trace metal solution Modified Zarrouk Medium was characterized by the following composition: EDTA 250 mg/L, H_3BO_3 57 mg/L, $ZnSO_4 \cdot 7\ H_2O$ 110 mg/L, $MnCl_2 \cdot 4\ H_2O$ 25.3 mg/L, $CoCl_2 \cdot 6\ H_2O$ 8.05 mg/L, $CuSO_4 \cdot 5\ H_2O$ 7.85 mg/L, $Mo_7O2_4(NH_4)_6 \cdot 4\ H_2O$ 5.5 mg/L.

The culture was cultivated in aerated photobioreactor (Medinlab™, Italy) under continuous illumination of white and blue LED lamps (Nicrew®) that ensured a photosynthetic photon flux density (PPFD) of 30 µmol $m^{-2}\ s^{-1}$. A picture of the entire process to obtain nanomaterials *from S. platensis* extract is reported in Fig 5. The temperature of the environment was set to 25°C. The

initial optical density at a wavelength of 750 nm (OD_{750}) was equal to 0.05 and increased to 0.4 after 14 days of cultivation. Then, the culture was centrifuged at 4°C under 1500 RPM (Heraeus® Megafuge® 1.0R) and the residue was dried at room temperature for 7 days. Next, the dried residue was weighted, and 5 g of biomass were added to 300 mL of methanol (Merck® LiChrosolv® hypergrade). The flask was sonicated for 30 min (Soltec® Sonica® 2400 ETH S3) and stirred at 250 RPM (IKA® RH Digital Magnetic Stirrer) for additional 30 min. To remove the biomass, the suspension was filtered using standard filtration paper (Whatman®) and then evaporated using rotary evaporator (BUCHI Rotavapor™ R-210 Rotary Evaporator System) to remove about 70% of methanol. The concentrated extract was then diluted to the final volume of 600 mL and divided in three equal aliquots to be used for the synthesis.

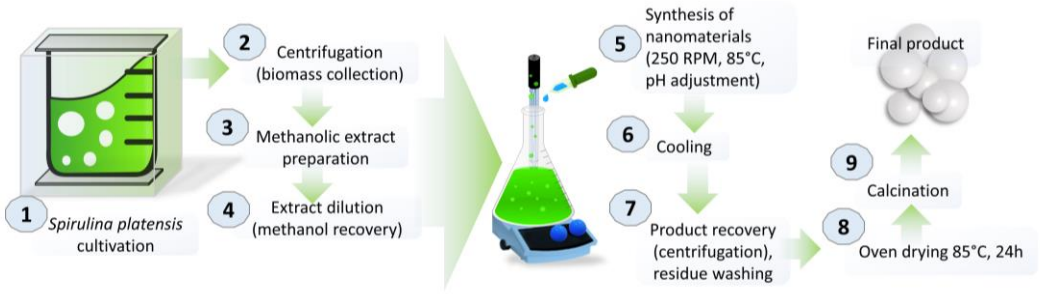

Figure 5 Preparation of nanomaterials from *S. platensis.*

3.2.1 Synthesis of nanostructures

The prepared extract was heated to 85°C and stirred at 250 RPM (IKA® RH Digital Magnetic Stirrer) and then a 2 ml sample was taken and labelled as “before the synthesis”. Subsequently, metal salts in powder were added to the extract to obtain 0.1 M solution of silver nitrate (Carlo Erba®), cobalt (II) chloride hexahydrate (Carlo Erba®) and titanium (IV) oxysulfate - sulfuric acid hydrate (AlfaAesar®) (3.40 g, 4.76 g and 5.56 g respectably). Next, after 15 min, the pH was raised by 3-4 points (for silver and cobalt salts up to 8, for titanium up to 4) using 1.25 M NaOH. After the salt has been added, the reaction (with stirring and heating) takes place for 1.5 h since it is quenched by removing from heat source for about 30 min. Subsequently, the resulting solution was centrifuged at 8°C using 4000 RPM (Heraeus® Megafuge® 1.0R) and the obtained supernatant was withdrawn and labelled as “after the synthesis”, while the residue was

repeatedly washed with MiliQ H_2O (Millipore®, Milan, Italy) in subsequent centrifugation cycles. Finally, the residue was dried at 80°C for 24 h and then ground using mortar and pestle to obtain two equal parts. One part was stored in Eppendorf tube in absence of light and the other one was calcined in muffle furnace (Gelman Instrument®) for 3 h at different temperatures (150°C for silver, 400°C for titanium and 450°C for cobalt). After calcination, the samples were stored under the same conditions as the samples before calcination.

3.2.2 Materials characterization

To investigate the influence of operating conditions such as pH and elevated temperature, an additional experiment was performed (mimicking reaction). The extract was heated to 85°C and stirred at 250 RPM (IKA® RH Digital Magnetic Stirrer). Then, a 1.25 M HCl solution was added to obtain the same pH as the flasks used during the synthesis process previously mentioned (5 for silver and cobalt, 0 for titanium). Subsequently, after 15 min pH was raised using a solution 1.25 M NaOH to the same values reached during the synthesis process (8 for silver and cobalt, 4 for titanium). Since the moment of adding diluted acid, the reaction continued for 1.5 h and then was left to cool down (the exact protocol as synthesis of nanomaterials). At the end point, the samples from mimicking reactions were taken from both flasks and labelled for GCMS sample preparation.

During sample preparation, 400 µl of the liquid samples taken before the synthesis, after mimicking reaction occurs and the synthesis of Ag NPs as well as TiO2 NPs were dried under nitrogen flow. Then, they were derivatized with 100 µL of methoxyamine hydrochloride/pyridine solution (Sigma Aldrich, Milano, Italy) (Sigma Aldrich, Milano, Italy). The samples were vortexed and incubated for 17 h. Subsequently, 100 µL of NO-bis (trimethylsilyl) trifluoroacetamide (BSTFA) (Sigma Aldrich, Milano, Italy) was added and samples were vortexed. Next, 800 µL of 20 ppm 2-dodecanone/hexane (Sigma Aldrich, Milano, Italy) solution was mixed with the liquids. At the end of the preparation step, the samples were filtered with 0.45 µm syringe filter (Sigma Aldrich, Milano, Italy). The sample after cobalt synthesis (prepared separately to avoid precipitation), once transferred to glass vial (400 µl), was dried under nitrogen flow, then 200 µL

of BSTFA was added. The sample was finally vortexed, mixed with 800 µL of 20 ppm 2-dodecanone/hexane and filtered to avoid precipitation.

After derivatization, samples were injected in a Hewlett Packard 6850 Gas Chromatograph, 5973 mass selective detector (Agilent Technologies, Palo Alto, CA), using helium as carrier gas at 1.0 mL/min flow. 1 µL of each sample was injected in the split-less mode and resolved on a 30 m × 0.25 mm × 0.25 µm DB-5MS column (Agilent Technologies, Palo Alto, CA). Inlet, interface, and ion source temperatures were 250, 250 and 230°C, respectively. The starting temperature of the oven was set to 50°C while the final one was led to 230 °C using a heating rate of 5°C/min for 36 min and then the sample was kept at a constant temperature for 2 min. Electron impact mass spectra were recorded from 50 to 550 m/z at 70 eV. The identification of metabolites was performed by mass spectra comparison with analytical standards using the NIST14 library database of the National Institute of Standards and Technology (Gaithersburg, MD).

The Fourier transform infrared spectroscopy (FTIR) was performed using Nicolet™ iS™ 10 FTIR Spectrometer (Thermo Fisher Scientific®, Madison, Wisconsin, USA) in the range 400-4000 cm^{-1}.

X-Ray Diffraction (XRD) analysis of the prepared nanostructures was carried out using X-Ray Diffractometer (Phillips®, PW1830/00, Nederlands and Rigaku SmartLab® with graphite monochromator in the diffracted beam). The scanning was performed at 40 kV and 30 mA using CuKα (λ =1.54 Å) radiation with a diffraction angle between 12° and 90° using 0.1° interval within 10 s. Diffraction pattern from each sample was analysed with HighScore Plus (v 3.0) and Maud™ (v. 2.99) software as well as Crystallography Open Database (COD, October 2014). Crystallite size was estimated after baseline correction using the well-known Debye-Scherrer's formula.

Scanning Electron Microscopy (SEM) analysis was carried out using Hitachi S4000 FEG HRSEM (Hitachi Ltd., Tokyo, Japan) operated at 20 kV. Image acquisitions were obtained by Quartz PCI software (Quartz Imaging Corporation, Vancouver, Canada). The samples were coated with 2 nm of platinum to enhance the contrast. EDX analysis results were acquired using UltraDry EDX Detector (Thermo Fisher Scientific®, Madison, Wisconsin, USA), and NSS3 software (Thermo Fisher Scientific®, Madison, Wisconsin, USA). The image analysis was performed by ImageJ 1.52a software.

Thermogravimetric Analysis (TGA) was performed using Differential Thermal Analyzer TG/DSC (NETZSCH® STA 409 PC) in a temperature range 25 – 1000°C and a heating rate of 10°C/min with air flow 100 mL/min.

Zeta potential measurement was performed using Zetasizer® Helix (Malvern Panalytical Ltd., UK). Before the measurement, the samples were sonicated using a suitable bath (Branson Ultrasonics™ 1210, USA) for 20 min. The results were analysed using Zetasizer® Software (Malvern Panalytical Ltd., UK).

3.2.3 Antifungal study

Three *Candida* species were used in this work: *C. albicans*, *C. glabrata* and *C. krusei*. All microbial strains were previously isolated from vaginal swabs of patients with fungal infection and collected from the laboratory of Microbiology of University of Sassari (Italy).

Clinical isolates were characterized using mass spectrometry identification techniques (MALDI-TOF). The strains were stored at -80°C until use; microbial strains were thawed in Luria Bertani (LB) Medium (Merck) and were grown overnight at 37°C under shaking (180 RPM). After 24 h, the growth of each isolate was assessed spectrophotometrically at 600 nm.

Antifungal activity of nanomaterials was assessed by microdilution method, using 48 wells plates. Nanomaterials were suspended in 1 ml of Phosphate Buffer Saline (PBS) 1X (Merck) sterile, vortexed and sonicated 1 min three times to remove debris that could interfere with assay. Serial two-fold dilutions of each nanomaterial, ranging from 100 µg/ml to 6 µg/ml, were performed in PBS 1x in the rows of a 48 wells-plates.

C. albicans, C. glabrata and *C. krusei* were seeded at 5 × 104 cell/well and incubated at 37°C and 5% CO2 in the various concentrations of nanomaterials and extract before the synthesis for 48 h in the presence or absence of light. *Candida spp.* in LB broth added with amphotericin B (16 µg/ml) [31] was used as positive control while strains in LB broth were used as negative control. LB broth was used as blank.

After 48 hours of incubation, the plates were microscopically observed and the minimum inhibitory concentration (MIC), defined as the lowest drug concentration that inhibit the visible

growth of a microorganism at the end of the incubation period, was detected [32]. To determinate whether the nanomaterial concentration could inhibit the growth of fungi, the entire volumes of wells with the highest inoculum were seeded in LB agar plates (100 µL aliquots/plate) which were incubated at 37°C for 48 hours. The nanomaterial was evaluated to be fungicidal when it was able to kill ≥99.9% of the final inoculum. Moreover, the effect of light on viability of microorganisms was evaluated by studying the growth of *Candida* species under light exposition.

The experiments were carried out in triplicate. The significance was calculated using Student's t-test and difference were considered significant at $p< 0.05$.

3.3 Results and discussion

S. platensis is a well-known source of various nutrients which are used as food supplements worldwide. Moreover, extracted secondary metabolites can play an important role not only in human nutrition but also for the synthesis of nanomaterials. By comparing the composition of extracts before synthesis, mimicking and after synthesis it can be inferred that in all cases amines such as methylamine, diethanolamine, and ethanamine are clearly involved in the synthesis of NPs. The observed results agree with the existing literature. Amines have been used in the past for nanoparticle synthesis using chemical synthesis route [33]. Recently, they are also used to synthesize and functionalize nanoclusters and could play a role in obtaining their ultrasmall size [34, 35]. Diethanolamine was used for the synthesis of silver and titanium-based nanoparticles working as a reaction controlling agent to form homogeneous precipitates and in case of silver decreased its size more efficiently than monoethanolamine used during the reaction [36, 37]. The study highlighted the important role of hydroxyl groups present in diethanolamine which can act as reducing agents. In additions, when studying the synthesis mechanism using amines of cobalt oxide nanomaterials, it was observed that initially three-dimensional (3D) nanoparticles are formed from the precursor solution and then they start transforming into 2D nanosheets at critical size of 3.0-4.4 nm [38]. Moreover, the authors proved the interactions of cobalt oxide with $-NH_2$ group using methylamine model. Most probably amines during the synthesis acted as reducing agents (Fig. 6) that provide electrons to metal ions facilitating the formation of metal

NPs as well as the attachment of other secondary metabolites which act as stabilizing (capping) agents that hinder the surface reaction of newly formed NPs with compounds in the surrounding environment.

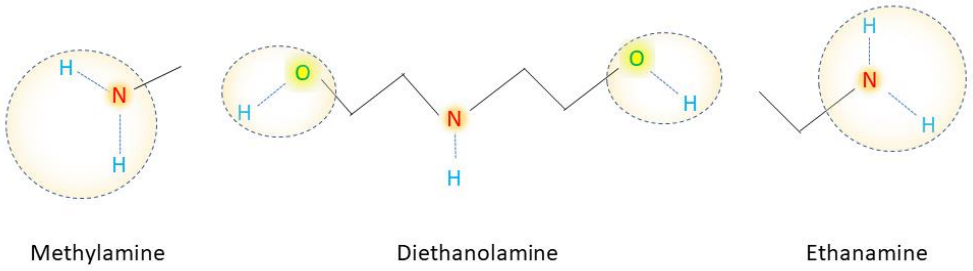

Figure 6 Main functional groups in methylamine, diethanolamine, and ethanamine, respectively participating in the reduction of metal ions into nanomaterials.

During the Ag NPs synthesis in addition to amines, ethyl mandelate, propylene glycol, butanedioic acid, L-glutamic acid derivative, and glyceryl-glycoside derivative were utilized. Although the role of ethyl mandelate was not studied before, it may act as a capping agent. The properties of propylene glycol were studied mainly as an emollient in Ag NPs loaded hydrogels to increase their stability [39]. Butanedioic acid on the surface of Ag NPs was tested for sensitive quantification of melamine [40] and, in the present study it was probably attached to the amine ligands. Although the involvement of L-glutamic acid derivatives in the Ag NPs synthesis was not empirically verified, due to its antioxidant properties, it can be reasonably assumed that it plays a key role in the further reduction of silver metal ions into silver NPs. Similar role can be attributed to glyceryl-glycoside derivative, which was reported to undergo hydrolysis and oxidation during the formation of Ag NPs [41]. Interestingly, during the reaction, concentration of the glyceryl-glycoside derivative isomer is increasing as well as of 2-methylpentan-2-ol while the exact mechanism of their action is unknown.

The important role of proteins present in the *S. platensis* extract for the synthesis of Ag NPs was investigated by Ameen et al [42]. In addition to polysaccharides from *S. platensis* extract, Attia et al utilized gamma radiation to synthesize Ag NPs [43]. The product was successfully used against *Erwinia amylovora*, Gram-negative bacteria, which caused fire blight infection on trees. Results

showed that both proteins and polysaccharides from *S. platensis* on the surface of Ag NPs have prominent antimicrobial effects.

Compared with mimicking reaction, in the TiO_2 NPs synthesis, lactic acid and lactose were utilized apart from amines. Beyond acting act as an acid catalyst and electron donor, lactic acid was reported to mediate surface interactions of nuclei favouring the coalescence of nanoparticles formed at the beginning of the synthesis, during hydrolysis and condensation [44]. The study described binding of the Ti(IV) ions by a donor-acceptor bond, which transfers the electrons and reduces its partial positive charge. Therefore, Ti(IV) ions' reactivity and equilibrium constant (during heating) of hydrolysis and condensation are reduced with lactic acid acting as a capping ligand further mediating formation of nanoparticles. While the involvement of lactose during TiO_2 NPs was not described so far, owning to its reducing properties, it may participate as a reducing agent. Similarly, to the Ag NPs synthesis, there is also a contribution of glyceryl-glycoside derivatives and 2-methylpentan-2-ol in addition to increasing concentration of glycerol.

So far, *S. platensis* was used to synthesize TiO_2 NPs while TiO_2 was added directly to the culture, and the product was retrieved after one week [45]. The authors observed nanoparticles' penetration into the *Spirulina* cells, thus resulting in a notch-like structure with consequent cell damage. The antimicrobial application of TiO_2 NPs was foreseen, however not tested, and the effects of *S. platensis* metabolites on TiO_2 NPs formation remained unknown.

Additional secondary metabolites were observed to be utilized during $Co(OH)_2$ NMs synthesis such as amines, ethyl mandelate, 1,4-bis(trimethylsilyl) benzene, nonane, ethylene glycol, propylene glycol, lactic acid, glycerol, butanedioic acid, L-glutamic acid derivative, glyceryl-glycoside derivatives, and lactose. The role of ethyl mandelate, propylene glycol, lactic acid, butanedioic acid, L-glutamic acid derivative, glyceryl-glycoside derivative and lactose is probably similar to their action during synthesis of Ag NPs and TiO_2 NPs. Ethylene glycol and glycerol may act as stabilizing agents comparably with propylene glycol. The exact role of 1,4-bis(trimethylsilyl)benzene and nonane is unknown. Interestingly, the sample after synthesis also consisted of propylamine and retinal, however, description of their involvement requires further studies.

The synthesis of cobalt-based nanocatalysts has been investigated so far using levulinic acid, gallic acid, starch, and metal-organic substrates to evaluate their catalytic activity towards dyes [46]. In addition, Co_3O_4 NMs prepared by using *Geranium wallichianum* and *Populus ciliate* plants leaves extract showed antimicrobial properties [47,48]. In such investigation, the involvement of stigmasterol, ursolic acid, β-sitosterol, β-sitosterol galactoside, and herniarin in the Co_3O_4 NMs synthesis was assumed albeit no experiments have been conducted to elucidate the corresponding mechanism.

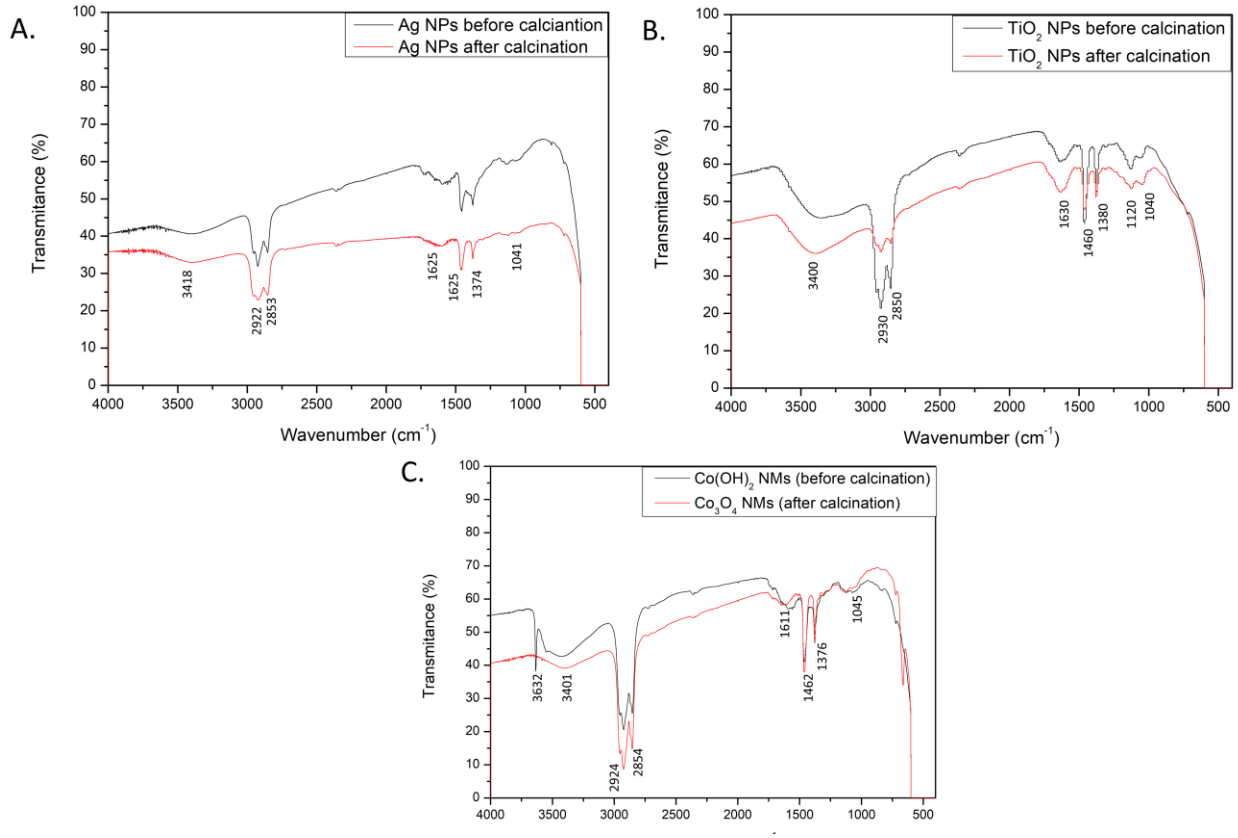

Figure 7 FTIR spectra of the prepared nanomaterials (A) Ag NPs before and after calcination, (B) TiO_2 NPs before and after calcination, (C) $Co(OH)_2$ NMs and Co_3O_4 NMs.

The involvement of capping agents on the surface of nanomaterials was further confirmed using FTIR technique (Fig. 7). The results revealed the presence of hydroxyl groups in high concentration on the surface of Ag NPs at 3418 cm^{-1} (Fig. 7A). Moreover, alkyl -CH_2- groups were found at 2922 cm^{-1} and 2853 cm^{-1} with P-C organophosphorus compounds at 1463 cm^{-1}. Attachment of amines was confirmed at 1625 cm^{-1} (NH group, probably belonging to

diethanolamine) and at 1041 cm^{-1} (C-N group of aliphatic amines) which also supports GCMS findings. Reducing action of amines was corroborated by the presence of NO group at 1374 cm^{-1}. Abundance of halides and carbon-metal bonds was confirmed at 550-400 cm^{-1}. Analogous FTIR pattern was obtained for other Ag NPs synthesized from *S. platensis* [49].

Similarly, for TiO_2 NPs hydroxy groups were detected at 3400 cm^{-1} with alkyl -CH_2- groups at 2930 cm^{-1} and 2850 cm^{-1} (Fig. 7B). Organophosphorus P-C group, belonging possibly to phospholipids or proteins, was confirmed at 1460 cm^{-1} and C-O groups were identified at 1120 cm^{-1}. Functional groups of amines were detected at 1630 cm^{-1} and 1040 cm^{-1} belonging to NH and CN groups respectably. Nitro compounds with NO groups were noted at 1380 cm^{-1}. Low transmittance signal for 550-400 cm^{-1} suggests the presence of halides and carbon-metal bonds in high concentration.

The functional groups present on the surface of $Co(OH)_2$ NMs and Co_3O_4 NMs were comparable with the ones found in the nanomaterials discussed so far (Fig. 7C). In particular, hydroxyl groups in abundance were detected at 3401 cm^{-1} with carbonyl groups at 2924 cm^{-1} and 2854 cm^{-1}. Organophosphorus P-C groups were found at 1462 cm^{-1}. Attachment of amines was confirmed at 1611 cm^{-1} and 1045 cm^{-1} belonging to NH and CN groups, respectively. Nitro compounds were identified at 1377 cm^{-1}. Only in the case of $Co(OH)_2$ NMs, the peak at 3632 cm^{-1} was caused by stretching vibration of OH group in its structure. Like the other synthesized nanomaterials, there is a visible abundance of halides and metal-carbon bonds at 550-400 cm^{-1}.

FTIR results show similar pattern of functional groups acting as capping agents during the reaction. The findings further confirm involvement of secondary metabolites, especially amines, as active compounds for the synthesis of various nanomaterials.

The XRD patterns are presented in Fig 4. Both Ag NPs before and after calcination show AgCl and Ag phases in their structure with possibly attached organic metabolites (Fig. 8A). The product after calcination shows increased intensity of peaks corresponding to Ag phase. The findings were matched with three phases in Crystallography Open Database (COD) with database ID codes: 9011666, 9011673, and 1100136 corresponding to cubic AgCl, monoclinic AgCl, and cubic Ag, respectively. The average crystallite size estimated using the Debye-Scherrer's equation was

15.22 nm for AgCl phase and 9.72 nm for Ag before calcination with increase after calcination to 26.01 nm for AgCl and 24.86 nm for Ag.

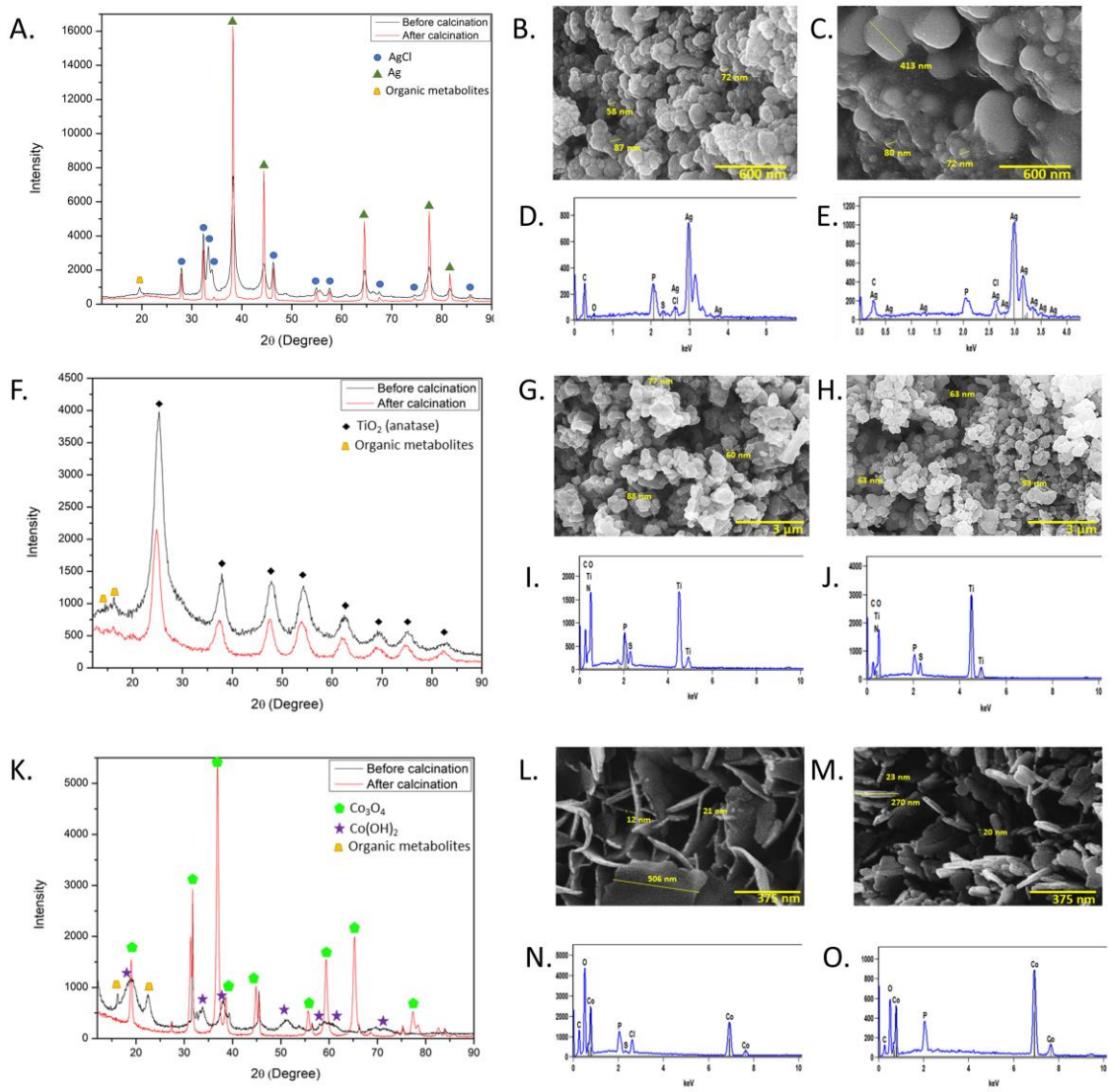

Figure 8 Crystallographic and microscopic studies of prepared nanomaterials (A) XRD spectrum of Ag NPs, (B) SEM image of Ag NPs before calcination, (C) SEM image of Ag NPs after calcination, (D) EDX of Ag NPs before calcination, (E) EDX of Ag NPs after calcination, (F) XRD spectrum of TiO_2 NPs, (G) SEM image of TiO_2 NPs before calcination, (H) SEM image of TiO_2 NPs after calcination, (I) EDX of TiO_2 NPs before calcination, (J) EDX of TiO_2 NPs after calcination, (K) XRD spectrum of $Co(OH)_2$ NM and Co_3O_4 NM, (L) SEM image of $Co(OH)_2$ NM (before calcination), (M) SEM image of Co_3O_4 NM (after calcination), (N) EDX of $Co(OH)_2$ NM (before calcination), (O) EDX of Co_3O_4 NM (after calcination).

It should be noted that presence of both Ag and AgCl phases was confirmed by using *Scenedesmus sp* green microalgae culture for intracellular production of NPs while their

crystallite size was not evaluated [50]. Current research on Ag NPs utilizing *S. platensis* confirmed the presence of Ag phase [20,21]. The additional occurrence of AgCl in the present study indicates the key role of secondary metabolites from extract in the reaction mechanism leading to the synthesis of NPs.

In case of TiO_2 NPs (Fig. 8F), the observed XRD pattern matches tetragonal TiO_2 anatase (COD ID code 9008215) with probably secondary metabolites attached. After calcination the anatase phase remains stable and peaks intensity decrease. The crystallite size was estimated to be 4.81 nm for TiO_2 before calcination and a slight decrease to 4.62 nm was obtained after calcination.

Similar crystallite size (4.19 nm) of anatase TiO_2 NPs was previously obtained by other authors [51] using chemical synthesis involving acetylacetone, n-butanol, and 4-dodecylbenzene sulfonic acid in a complex and time-consuming procedure. More eco-friendly method involving the use *S. platensis* living culture managed to obtain crystallite size of 17.3 nm [23]. The present study managed to produce small crystallite size of anatase TiO_2 NPs while using facile and environmentally friendly method.

The obtained XRD spectrum of $Co(OH)_2$ NMs (Fig. 8K) is in well-agreement with hexagonal $Co(OH)_2$ with COD ID code 1010267, even with secondary metabolites as in the other synthesized materials. The calcination resulted in phase transition to Co_3O_4 NMs which matches with cubic Co_3O_4 with COD ID code 9005897. The average crystallite sizes of NMs were estimated to be 3.52 and 13.28 nm for $Co(OH)_2$ and Co_3O_4, respectively.

Previous studies reported the formation of $Co(OH)_2$ NMs by means of a chemical method utilizing mainly hydrazine or hydrazine hydrate which resulted in crystallite sizes of 2.1 nm and 12.4 nm, respectively [52,53]. Green synthesized $Co(OH)_2$ NMs were obtained by using *Litchi cinensis* fruit extract with crystallite size of 24.25 nm and 30.28 nm when following the boiling or the microwave route, respectively [54]. While red algae extract was used to obtain Co_3O_4 NMs with crystallite size 26.5 nm, only hydrothermal method managed to produce crystallite size of 13.8 nm like the current study [55,56]. It should be noted that, to best of our knowledge, this work represents the first contribution in the literature where Co NPs were synthesized using a cyanobacterial extract to promote reduction, nucleation and capping.

Morphology of the obtained NMs was studied using SEM and EDX techniques (Fig. 8). The findings revealed oval shape of Ag NPs before calcination with size range 58-72 nm (Fig. 8B) with confirmed presence of silver as well as carbon, oxygen, phosphorus, sulphur and chloride from the *S. platensis* extract (Fig. 8D). After calcination the agglomerates of Ag NPs having size in the range 72-413 nm can be observed in Fig 4C. The EDX analysis showed the presence of similar elements as before calcination except sulphur (Fig. 8E).

Similar spherical shape was observed for TiO_2 NPs having size 60-88 nm (Fig. 8G). In addition, the sample show high tendency of NPs to form agglomerates of various sizes. The EDX analysis confirmed the presence of titanium, carbon, oxygen, nitrogen, phosphorus, and sulphur in their structure (Fig 4I). Calcination slightly increased the size of TiO_2 NPs to 63-93 nm (Fig. 8H). Moreover, the same agglomeration tendency earlier discussed was observed for calcined samples. The same elements were detected with EDX technique as before calcination (Fig. 8J).

Interestingly, nanoflake shape was observed for $Co(OH)_2$ NMs with 12-21 nm width and around 500 nm length (Fig. 8L). The EDX analysis showed the presence of cobalt, carbon, oxygen, phosphorus, sulphur, and chloride in their structure (Fig 8N). After phase transition to Co_3O_4 NMs during calcination, the nanoflake shape is maintained with around 20 nm width (Fig. 8M). The EDX analysis confirmed cobalt, carbon, oxygen, and phosphorus in their structure (Fig. 8O). To the best of our knowledge, it is the first time nanoflake shape of $Co(OH)_2$ NMs and Co_3O_4 NMs was obtained using green chemistry method.

The results further corroborate the involvement of *S. platensis* extract in the synthesis of various nanomaterials. Moreover, the products have various shapes and size ranges which show a great potential of secondary metabolites to fabricate different morphologies of nanomaterials.

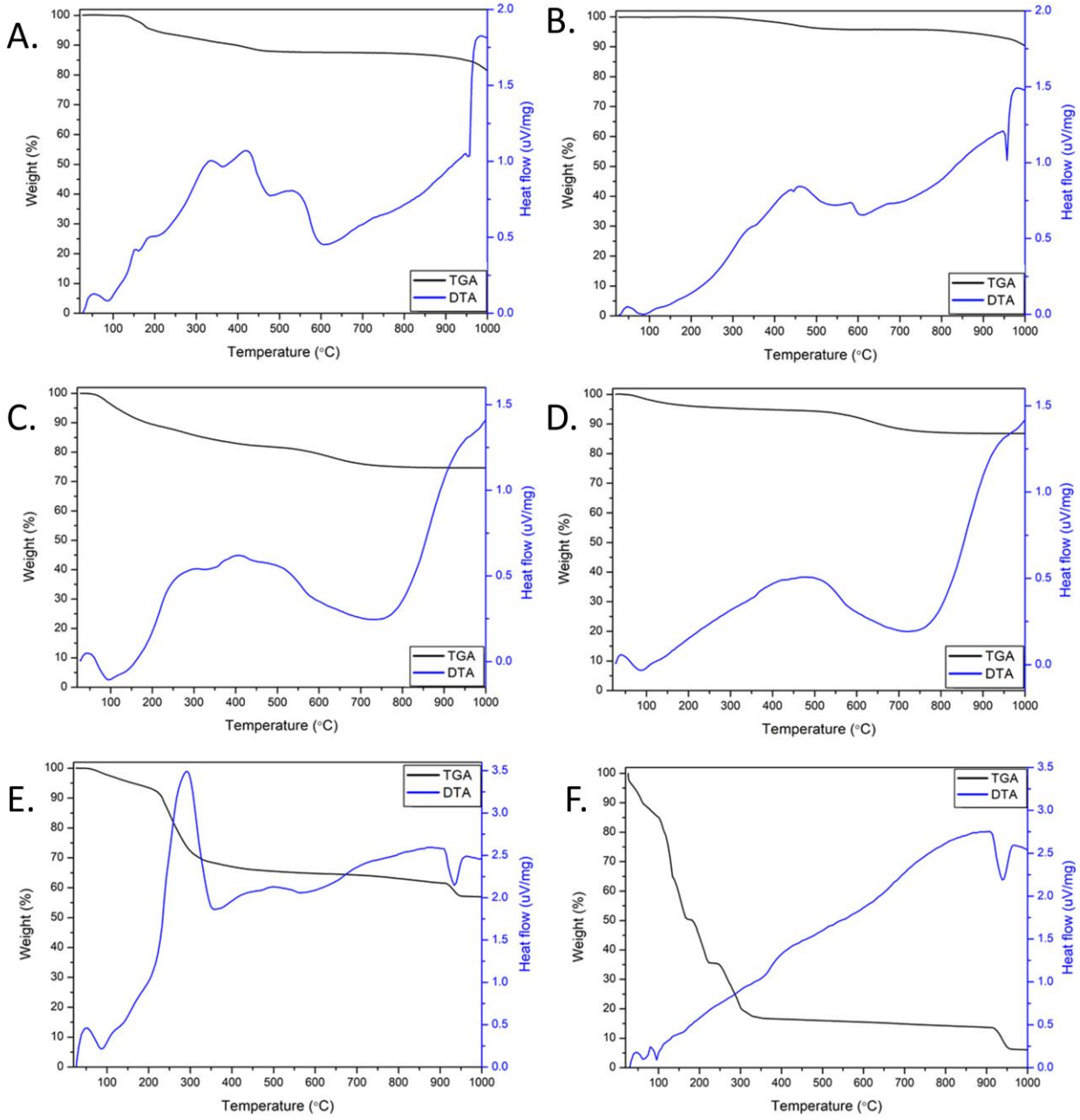

Figure 9 Thermogravimetric analysis of the prepared nanomaterials (A) Ag NPs before calcination, (B) Ag NPs after calcination, (C) TiO_2 NPs before calcination, (D) TiO_2 NPs after calcination, (E) $Co(OH)_2$ NMs (before calcination), (F) Co_3O_4 NMs (after calcination).

Thermal properties of the materials were measured in air by both thermal gravimetric analysis (TGA) and differential thermal analysis (DTA) curves (Fig. 9). In addition, decomposition temperatures at which the materials lose 5% of their mass were defined as Td. In case of Ag NPs before (Fig. 9A) and after calcination (Fig. 9B) three main stages can be observed, i.e. 25-100°C,

100-600°C and 600-1000°C. The slight weight decreases at 952°C when lowering the heat flow corresponds to the melting point of silver. At the first stage, DTA curve indicates exothermal reactions possibly due to the activity of temperature-sensitive compounds at the surface, however with only slight mass difference (weight around 99.9%) in both materials. The progressive temperature increased results in decomposition of secondary metabolites present on Ag NPs surface with heat release and weight observed at 87.58% and 95.76% for Ag NPs before and after calcination, respectively. Above 600°C, loss of molecular oxygen is shown and at the end of the analysis the weight of the samples was 81.41% and for Ag NPs before and after calcination, respectively. In addition, Td values were measured at 197°C for Ag NPs before calcination and increased up to 842°C after calcination. Such difference in Td and the percentage of weight loss can be ascribed to the partial loss or structure changes of secondary metabolites present on the surface due to calcination procedure.

Thermal stability of Ag NPs has been researched and showed final weight at around 70% at 800°C with around 60% weight at 600°C in two separate studies [42,57]. The research on green synthesized Ag/AgCl nanoparticles from *Oedera genistifolia* plant showed similar 70% weight at 900°C [58]. The improved thermal stability of Ag NPs before and after calcination synthesized from S. platensis in the current study further confirms the importance of secondary metabolites on the surface in the achievement of thermally stable nanomaterials.

Similar stages of thermal sensitivity can be observed in TiO_2 NPs before (Fig. 9C) and after calcination (Fig. 9D). Interestingly, until 100°C endothermic loss of water occurs which changed the weight of TiO2 NPs to 96.18% and to 98.33% before and after calcination, respectively. Next, in the 100-750°C interval, the exothermic decomposition of secondary metabolites is observed for TiO2 NPs with weight at 75.31% and 87.54% before and after calcination, respectively. Further temperature increase resulted in loss of molecular oxygen and the final weight at 1000°C was recorded at 74.65% and 86.81% for TiO_2 NPs before calcination and after calcination, respectively. Moreover, Td values for TiO_2 NPs were observed at 112°C and 359°C before and after calcination, respectively.

The TGA studies on TiO_2 NPs synthesized via green routes involving plants, report final weights of about 85% at 950°C and 76.74% at 800°C after calcination at 500°C [59,60]. The current findings show good thermal stability as well as difference in weight loss between samples before and after calcination similar to Ag NPs 10 %. Moreover, a broader DTA peak at 150-750°C in TiO_2 NPs reveals a difference in the exothermal reactions taking place likely due to possible distinct bonding of secondary metabolites with metals.

Thermal behaviour was also measured for $Co(OH)_2$ NMs (Fig. 9E) and Co_3O_4 NMs (Fig. 9F). Both materials show mass loss at 25-100°C corresponding to exothermal reactions of temperature-sensitive metabolites, resulting in weights at 97.73% for $Co(OH)_2$ NMs and 85.06% for Co_3O_4 NMs. Then, at around 300°C, $Co(OH)_2$ NMs exhibit partial oxidation to Co_3O_4 NMs which may be also accompanied by the loss or structural changes of secondary metabolites on the surface after which the weight was recorded at 68.23%. Subsequently, at around 600°C loss of molecular oxygen is shown and the final weight for $Co(OH)_2$ NMs at 1000°C was recorded at 56.98%. Prepared Co_3O_4 NMs display exothermal degradation of secondary metabolites at 100-300°C with a weight at 20.20% which remained relatively stable when further increasing the temperature even though possible structural changes resulted in heat release. The Co_3O_4 NMs weight at the end of the analysis was equal to 6.08%. Both $Co(OH)_2$ NMs and Co_3O_4 NMs DTA curves show endothermal peak at around 950°C followed by a mass loss which is probably due to reaction with Al_2O_3, component of crucible used during the analysis, resulting in appearance of blue colour as it was reported in the literature [61]. In case of $Co(OH)_2$ NMs and Co_3O_4 NMs Td values were recorded at 161°C and 39°C, respectively. The decrease in Td values is probably due to change in thermal behaviour of the materials possibly related to the phase transition as it was observed in the XRD analysis.

So far, green synthesized from plants, quasi-spherical Co_3O_4 NMs were reported to have around 83% weight at 980°C [62]. The significant weight loss observed during current TGA analysis of $Co(OH)_2$ NMs and Co_3O_4 NMs in comparison with other NMs can be attributed to their distinct high content of organic metabolites and unique shape.

Zeta potential measurement was performed to analyse the stability of prepared nanomaterials in water suspension and compare their electrostatic repulsion or attraction behaviour (Fig. 10 and Tab. 4). The findings revealed average zeta potential values reported in Tab. 4 along with the corresponding standard deviation.

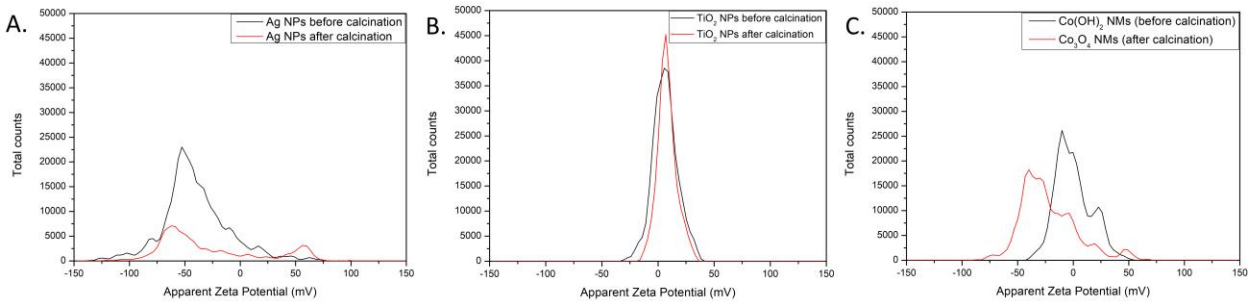

Figure 10 Zeta potential measurements of the prepared nanomaterials. A) Ag NPs before and after calcination, (B) TiO_2 NPs before and after calcination, (C) $Co(OH)_2$ NMs and Co_3O_4 NMs.

Table 4 Average zeta potential measurements and their standard deviation.

	Ag NPs before calcination	Ag NPs after calcination	TiO_2 NPs before calcination	TiO_2 NPs after calcination	$Co(OH)_2$NMs before calcination	Co_3O_4NMs after calcination
Zeta potential (mV)	-40.2 ± 0.89	-29.1 ± 2.62	6.25 ± 0.32	8.05 ± 0.05	-0.82 ± 1.53	-22.3 ± 0.51

Good stability in water suspension was noted for Ag NPs before calcination which decreased to moderate after calcination procedure. In the literature, zeta potential was measured for Ag NPs before calcination synthesized using water and methanolic *S. platensis* extract revealing the values of -15.90 mV and -43.60 mV, respectively [63,64]. Most probably the composition of extracted secondary metabolites from *S. platensis* can also play a role in stabilizing NMs in water suspension.

The opposite charge on the surface with poor stability was noted for TiO_2 NPs before and after calcination. The rapid ability to coagulate, possibly due to the metabolites on the surface, might be a limitation in efficient action of the nanoparticles. The quick agglomeration was also measured for $Co(OH)_2$ NMs (before calcination) which improved after calcination to Co_3O_4 NMs to a relatively poor stability.

Six types of NMs: Ag NPs (before and after calcination), TiO_2 NPs (before and after calcination), $Co(OH)_2$ NMs, and Co_3O_4 NMs and relative extracts before synthesis were tested against three Candida species to evaluate their inhibitory effect, through broth microdilution technique. The inhibitory concentrations of nanomaterials having effects on fungal growth ranged from 12 µg/ml to 100 µg/ml. In Table 5, the MIC values of nanomaterials were listed for *C. albicans, C. glabrata* and *C. krusei* detected with and without light exposition. Co_3O_4 NMs after calcination, TiO_2 NPs both before and after calcination and all extracts before synthesis, have no inhibitory activity against *Candida* species under all experimental conditions tested. The MIC wells presenting lowest growth after 48 hours of incubation were chosen to determine the minimum fungicidal concentration (MFC) against the *Candida* species that was assessed between 25 µg/ml to 100 µg/ml.

Table 5 MIC and MFC determination.

	C. albicans		*C. glabrata*		*C. krusei*	
	MIC (mg/mL)	MFC (mg /mL)	MIC (mg /mL)	MFC (mg /mL)	MIC (mg /mL)	MFC (mg /mL)
Ag NPs 1 dark	50	50	25	50	50	50
Ag NPs 1 light	50	50	50	50	12	25
Ag NPs 2 dark	NE	NE	NE	NE	50	50
Ag NPs 2 light	NE	NE	100	100	25	25

$Co(OH)_2$ NMs dark	50	100	25	50	25	5
$Co(OH)_2$ NMs light	100	100	25	50	12	25

Ag NPs 1 = before calcination; Ag NPs 2 = after calcination; $Co(OH)_2$ NMs = before calcination; NE = No inhibitory effects on fungal growth.

Both Ag NPs before calcination and $Co(OH)_2$ NMs (before calcination) showed antifungal activity in all tested conditions and *Candida spp*. Calcination process seems to reduce the antifungal properties of Ag NPs, as the material only managed to inhibit the growth of *C. glabrata* in the presence of light and *C. krusei* in the dark and light. Calcination of $Co(OH)_2$ NMs and subsequent phase transition to Co_3O_4 NMs significantly changed the properties of the nanomaterial which did not exhibit antifungal properties in the tested concentrations. In addition, TiO_2 NPs did not inhibit *Candid*a growth before and after calcination in the tested concentrations as well as extract used for the synthesis of NMs. *Candida* species exposed to light, used as a control, showed no alterations in growth.

Considering tested fungal isolates, *C. albicans* was found to be the most resistant to the NMs activity with increased MIC value in the presence of light. Similar increase in the MIC value was detected in case of Ag NPs before calcination treated *C. glabrata*, however, Ag NPs after calcination were found to be antifungal only in the presence of light. The most susceptible fungal pathogen to NMs activity was *C. krusei* which showed decrease in both MIC and MFC values in the presence of light even up to 4 times (MIC of Ag NPs before calcination, $p<0.05$).

The influence of light on antimicrobial activity has been studied before mainly on the bacterial cells [65,66]. It has been proven that light generates more reactive oxygen species (ROS) which damages the bacterial cells [67]. The recent research on light-activated chemically synthesized NMs found that light can reduce *C. albicans* biofilms (Ag NPs) and inhibit Fusarium oxysporum growth (N and F co-doped TiO2 NPs) [68,69]. However, the light influences not only the performance of NMs, but also the growth of fungi triggering expression of different metabolic pathways [70]. In the current study, *C. albicans* exposed to $Co(OH)_2$ NMs (before calcination) and *C. glabrata* exposed to Ag NPs before calcination required increased concentrations of NMs to

inhibit fungal growth. The results suggest potential activation of fungal defence mechanisms in the presence of light which requires further studies.

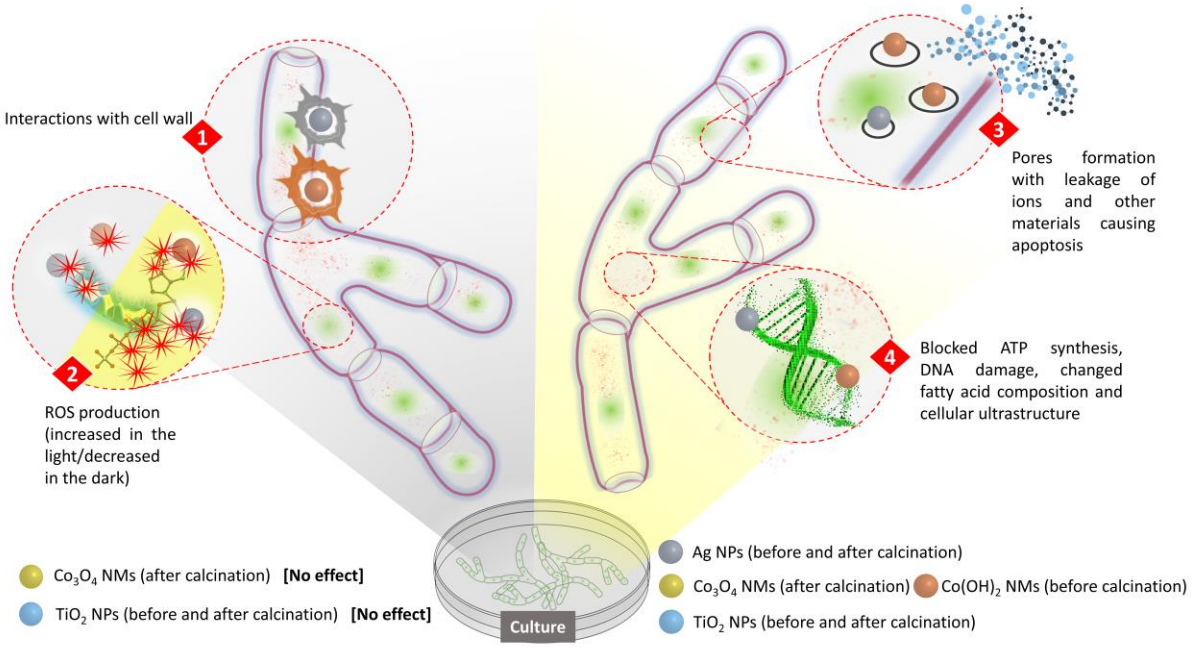

Figure 11 Hypothesized mechanism of NMs antifungal activity.

The proposed antifungal mechanism in depicted in Fig 11. The first interactions occur possibly between NMs and fungal cell wall which can cause disintegration and damages also to the cell membrane [48]. The process activates ROS production which is usually enhanced in the presence of light [71]. As a result, the fungal cell exhibits oxidative stress causing formation of pores, leakage of cell content and apoptosis [72]. At the same time, ATP synthesis is blocked, DNA is damaged, fatty acid composition is changed and overall ultrastructure of the cell is disturbed [73]. The exact molecular mechanism leading to above mentioned effects is a result of interactions between cell components and specific structure (size, shape) as well as composition (identified phases) of the synthesized NMs and may differ accordingly [74]. Additionally, Ag NPs can release Ag^+ ions which have high affinity and may bind to the thiol group (-SH) of the proteins affecting their original structure and activity (denaturation) [68]. The antifungal properties of $Co(OH)_2$ NMs were not studied before, however, it is probable that due to the presence of hydroxy group (-OH) in their structure they may affect hydrogen bonds formation in the proteins

causing structural changes and inhibiting proper protein functions in the cell. The exact mechanism of the antifungal activities of various NMs requires further research.

3.4 Conclusions

The study showed the potential of secondary metabolites from *S. platensis* to participate in the synthesis of various NMs. The involvement of amines among other compounds was revealed by GCMS and FTIR analyses. The phases identification in XRD analysis confirmed the presence of Ag and AgCl phases in Ag NPs, TiO_2 anatase in TiO_2 NPs, $Co(OH)_2$ in $Co(OH)_2$ NMs and Co_3O_4 in Co_3O_4 NMs. The SEM findings showed oval and spherical shapes for Ag NPs and TiO2 NPs, respectively with nanoflake shape of both $Co(OH)_2$ NMs and Co_3O_4 NMs. EDX further confirmed the presence of organic content on the surface of the prepared NMs. In addition, Ag NPs showed the best thermal stability of all the synthesized NMs which increased after calcination. It has been found that Ag NPs exhibited the best stability in water suspension, even though it decreased after calcination.

We have also evaluated, for the first time, the capability of six NMs to act against several *Candida* species and our data have supported our hypothesis: Ag NPs (before and after calcination) and $Co(OH)_2$ NMs have shown antifungal activity for all *Candida* tested. Interestingly, these nanostructures exhibited high antimicrobial activity on *C. glabrata* that was amphotericin resistant. It is apparent that the action mechanism of the NPs also depends on light conditions while the underlying molecular processes involved require further investigation.

Our results led us to speculate that both the composition of nanomaterials and the different experimental conditions (presence/absence of light) may have different mechanisms of cytolysis, inducing candidacidal effect through mechanisms already described, such as insertion of functional pores into target membranes, induction of apoptosis, alteration of macromolecules structure, or inhibition of ATP synthesis.

These findings, together with the increase of microbial resistance to antifungal drugs, encourage to carry out further studies to also determine the antibacterial activity against multi-drug resistance pathogens as well as the biocompatibility, cytotoxicity and safety of these nanostructures, with a view to their possible use in the medical field.

3.5 References

1. de Oliveira Santos GC, Vasconcelos CC, Lopes AJO, de Sousa Cartágenes M do S, Filho AKDB, do Nascimento FRF, et al. Candida Infections and Therapeutic Strategies: Mechanisms of Action for Traditional and Alternative Agents. Front Microbiol. 2018;9. https://www.frontiersin.org/article/10.3389/fmicb.2018.01351

2. Chow EWL, Pang LM, Wang Y. From Jekyll to Hyde: The Yeast–Hyphal Transition of Candida albicans. Pathogens. 2021;10(7). https://www.mdpi.com/2076-0817/10/7/859

3. Becerra MR, Tantaleán JA, Suárez VJ, Alvarado MC, Candela JL, Urcia FC. Epidemiologic surveillance of nosocomial infections in a Pediatric Intensive Care Unit of a developing country. BMC Pediatr. 2010;10(1):66. https://doi.org/10.1186/1471-2431-10-66

4. Jencson AL, Cadnum JL, Piedrahita C, Donskey CJ. Hospital Sinks Are a Potential Nosocomial Source of Candida Infections. Clin Infect Dis. 2017 Nov 13;65(11):1954-5. https://doi.org/10.1093/cid/cix629

5. De Rose DU, Santisi A, Ronchetti MP, Martini L, Serafini L, Betta P, et al. Invasive Candida Infections in Neonates after Major Surgery: Current Evidence and New Directions. Pathogens. 2021 Mar; 10(3):319. doi: 3390/pathogens10030319

6. von Lilienfeld-Toal M, Wagener J, Einsele H, Cornely OA, Kurzai O. Invasive Fungal Infection. Dtsch Arztebl Int. 2019 Apr;116(16):271–8. doi: 10.3238/arztebl.2019.0271.

7. Faria DR, Melo RC, Arita GS, Sakita KM, Rodrigues-Vendramini FAV, Capoci IRG, et al. Fungicidal Activity of a Safe 1,3,4-Oxadiazole Derivative Against Candida albicans. Pathogens. 2021;10(3). https://www.mdpi.com/2076-0817/10/3/314

8. Berkow EL, Lockhart SR. Fluconazole resistance in Candida species: a current perspective. Infect Drug Resist. 2017;10:237–45.

9. Pristov KE, Ghannoum MA. Resistance of Candida to azoles and echinocandins worldwide. Clin Microbiol Infect Off Publ Eur Soc Clin Microbiol Infect Dis. 2019 Jul;25(7):792–8.

10. Jalal M, Ansari MA, Alzohairy MA, Ali SG, Khan HM, Almatroudi A, et al. Anticandidal activity of biosynthesized silver nanoparticles: effect on growth, cell morphology, and key virulence attributes of Candida species. Int J Nanomedicine. 2019;14:4667–79.

11. Hosseini SS, Ghaemi E, Noroozi A, Niknejad F. Zinc Oxide Nanoparticles Inhibition of Initial Adhesion and ALS1 and ALS3 Gene Expression in Candida albicans Strains from Urinary Tract Infections. Mycopathologia. 2019 Apr;184(2):261–71.

12. Muñoz-Escobar A, Reyes-López SY. Antifungal susceptibility of Candida species to copper oxide nanoparticles on polycaprolactone fibers (PCL-CuONPs). PLOS One. 2020;15(2):e0228864.

13. Ahmadpour Kermani S, Salari S, Ghasemi Nejad Almani P. Comparison of antifungal and cytotoxicity activities of titanium dioxide and zinc oxide nanoparticles with amphotericin B against different Candida species: In vitro evaluation. J Clin Lab Anal. 2021 Jan;35(1):e23577.

14. de Alteriis E, Maselli V, Falanga A, Galdiero S, Di Lella FM, Gesuele R, et al. Efficiency of gold nanoparticles coated with the antimicrobial peptide indolicidin against biofilm formation and development of Candida spp. clinical isolates. Infect Drug Resist. 2018;11:915–25.

15. Li X, Wang L, Fan Y, Feng Q, Cui F. Biocompatibility and toxicity of nanoparticles and nanotubes. J Nanomater. 2012;2012:548389. https://doi.org/10.1155/2012/548389

16. Ahmed B, Hashmi A, Khan MS, Musarrat J. ROS mediated destruction of cell membrane, growth and biofilms of human bacterial pathogens by stable metallic AgNPs functionalized from bell pepper extract and quercetin. Adv Powder Technol. 2018;29: 1601–1616. doi:10.1016/J.APT.2018.03.025

17. Ali K, Saquib Q, Ahmed B, Siddiqui MA, Ahmad J, Al-Shaeri M, et al. Bio-functionalized CuO nanoparticles induced apoptotic activities in human breast carcinoma cells and toxicity against Aspergillus flavus: An in vitro approach. Process Biochem. 2020;91: 387–397. doi:10.1016/j.procbio.2020.01.008

18. Maqbool Q, Barucca G, Sabbatini S, Parlapiano M, Ruello ML, Tittarelli F. Transformation of industrial and organic waste into titanium doped activated carbon – cellulose nanocomposite for

rapid removal of organic pollutants. J Hazard Mater. 2022;423: 126958. doi:10.1016/j.jhazmat.2021.126958

19. Pathak J, Rajneesh, Maurya PK, Singh SP, Häder D-P, Sinha RP. Cyanobacterial farming for environment friendly sustainable agriculture practices: innovations and perspectives. Front Environ Sci. 2018;6. https://www.frontiersin.org/article/10.3389/fenvs.2018.00007

20. Lea MC. Allotropic forms of silver. Am J Sci. 1889;s3-37(222):476–91. https://www.ajsonline.org/content/s3-37/222/476

21. Ismail GA, Allam NG, El-Gemizy WM, Salem MA. The role of silver nanoparticles biosynthesized by Anabaena variabilis and Spirulina platensis cyanobacteria for malachite green removal from wastewater. Environ Technol. 2021 Dec;42(28):4475–89.

22. Al-Zahrani FAM, El-Shishtawy RM, Ahmed NSE, Awwad NS, Hamdy MS, Asiri AM. Photocatalytic decolourization of a new water-insoluble organic dye based on phenothiazine by ZnO and TiO2 nanoparticles. Arab J Chem. 2020;13(2):3633–8. https://www.sciencedirect.com/science/article/pii/S1878535219301819

23. Sathiyan K, Bar-Ziv R, Mendelson O, Zidki T. Controllable synthesis of TiO2 nanoparticles and their photocatalytic activity in dye degradation. Mater Res Bull. 2020;126:110842. https://www.sciencedirect.com/science/article/pii/S0025540819327485

24. Jafari S, Mahyad B, Hashemzadeh H, Janfaza S, Gholikhani T, Tayebi L. Biomedical applications of TiO(2) nanostructures: recent advances. Int J Nanomedicine. 2020;15:3447–70.

25. Mehrabani MG, Karimian R, Rakhshaei R, Pakdel F, Eslami H, Fakhrzadeh V, et al. Chitin/silk fibroin/TiO2 bio-nanocomposite as a biocompatible wound dressing bandage with strong antimicrobial activity. Int J Biol Macromol. 2018;116:966–76. https://www.sciencedirect.com/science/article/pii/S0141813018307062

26. Fatima S, Ali K, Ahmed B, Al Kheraif AA, Syed A, Elgorban AM, et al. Titanium dioxide nanoparticles induce inhibitory effects against planktonic cells and biofilms of human oral cavity

isolates of Rothia mucilaginosa, Georgenia sp. and Staphylococcus saprophyticus. Pharmaceutics. 2021;13: 1564. doi:10.3390/pharmaceutics13101564/S1

27. Ansari SM, Bhor RD, Pai KR, Sen D, Mazumder S, Ghosh K, et al. Cobalt nanoparticles for biomedical applications: Facile synthesis, physiochemical characterization, cytotoxicity behavior and biocompatibility. Appl Surf Sci. 2017;414:171–87. https://www.sciencedirect.com/science/article/pii/S0169433217306530

28. Anwar A, Numan A, Siddiqui R, Khalid M, Khan NA. Cobalt nanoparticles as novel nanotherapeutics against Acanthamoeba castellanii. Parasites and Vectors. 2019;12: 1–10. doi:10.1186/S13071-019-3528-2.

29. Ahmad N, Anae J, Khan MZ, Sabir S, Yang XJ, Thakur VK, et al. Visible light-conducting polymer nanocomposites as efficient photocatalysts for the treatment of organic pollutants in wastewater. J Environ Manage. 2021 Jul;295:113362.

30. Zarrouk C. Contribution à l'étude d'une cyanophycée: influence de divers facteurs physiques et chimiques sur la croissance et la photosynthèse de Spirulina maxima (Setch et Gardner) Geitler. M Sc Thesis, Universitè de Paris. 1966. http://www.worldcat.org/oclc/491818851

31. Cantón E, Pemán J, Gobernado M, Viudes A, Espinel-Ingroff A. Patterns of amphotericin B killing kinetics against seven Candida species. Antimicrob Agents Chemother. 2004 Jul;48(7):2477-82.

32. Andrews JM. Determination of minimum inhibitory concentrations. J. Antimicrob. Chemother, 2001. 48 Suppl 1, 5–16. https://doi.org/10.1093/jac/48.suppl_1.5

33. Newman JDS, Blanchard GJ. Formation of gold nanoparticles using amine reducing agents. Langmuir. 2006 Jun 1;22(13):5882–7. https://doi.org/10.1021/la060045z

34. Hamzah MO, Khenfouch M, Rjeb A, Sayouri S, Houssaini DS, Darhouri M, et al. Surface chemistry changes and microstructure evaluation of low density nanocluster polyethylene under natural weathering: A spectroscopic investigation. J. Phys.: Conf. Ser. 2018. 984 (1):012010. doi: 10.1088/1742-6596/984/1/012010

35. Xu C, Lin J, Yan D, Guo Z, Austin DJ, Zhan H, et al. Pd nanoclusters supported by amine-functionalized covalent organic frameworks for benzyl alcohol oxidation. ACS Appl Nano Mater. 2020 Jul 24;3(7):6416–22. https://doi.org/10.1021/acsanm.0c00884

36. Labanni A, Zulhadjri, Handayani D, Ohya Y, Arief S. Size controlled synthesis of well-distributed nano-silver on hydroxyapatite using alkanolamine compounds. Ceram Int. 2020;46(5):5850–5. https://www.sciencedirect.com/science/article/pii/S0272884219332134

37. Tarutani N, Kato R, Uchikoshi T, Ishigaki T. Spontaneously formed gradient chemical compositional structures of niobium doped titanium dioxide nanoparticles enhance ultraviolet- and visible-light photocatalytic performance. Sci Rep. 2021;11(1):15236. https://doi.org/10.1038/s41598-021-94512-x

38. Yang J, Zeng Z, Kang J, Betzler S, Czarnik C, Zhang X, et al. Formation of two-dimensional transition metal oxide nanosheets with nanoparticles as intermediates. Nat Mater. 2019;18(9):970–6. https://doi.org/10.1038/s41563-019-0415-3

39. Ontong JC, Singh S, Nwabor OF, Chusri S, Voravuthikunchai SP. Potential of antimicrobial topical gel with synthesized biogenic silver nanoparticle using Rhodomyrtus tomentosa leaf extract and silk sericin. Biotechnol Lett. 2020;42(12):2653–64. https://doi.org/10.1007/s10529-020-02971-5

40. Rajar K, Sirajuddin, Balouch A, Bhanger M ~I., Shah MT, Shaikh T, et al. Succinic acid functionalized silver nanoparticles (Suc-Ag NPs) for colorimetric sensing of melamine. Appl Surf Sci. 2018 Mar;435:1080–6.

41. Chakraborty S, Chelli VR, Das RK, Giri AS, Golder AK. Bio-mediated silver nanoparticle synthesis: mechanism and microbial inactivation. Toxicol Environ Chem. 2017 Mar 16;99(3):434–47. https://doi.org/10.1080/02772248.2016.1214271

42. Ameen F, Abdullah MMS, Al-Homaidan AA, Al-Lohedan HA, Al-Ghanayem AA, Almansob A. Fabrication of silver nanoparticles employing the cyanobacterium Spirulina platensis and its bactericidal effect against opportunistic nosocomial pathogens of the respiratory tract. J Mol

Struct. 2020;1217:128392. https://www.sciencedirect.com/science/article/pii/S0022286020307171

43. Attia MS, El-Sayyad GS, Saleh SS, Balabel NM, El-Batal AI. Spirulina platensis-polysaccharides promoted green silver nanoparticles production using gamma radiation to suppress the expansion of pear fire blight-producing Erwinia amylovora. J Clust Sci. 2019;30(4):919–35. https://doi.org/10.1007/s10876-019-01550-7

44. Cihlar J, Tinoco Navarro LK, Kasparek V, Michalicka J, Cihlar J, Kastyl J, et al. Influence of LA/Ti molar ratio on the complex synthesis of anatase/brookite nanoparticles and their hydrogen production. Int J Hydrogen Energy. 2021;46(12):8578–93. https://www.sciencedirect.com/science/article/pii/S0360319920346450

45. Hifney AF, Abdel-Wahab DA. Phyco-based synthesis of TiO2 nanoparticles and their influence on morphology, cyto-ultrastructure and metabolism of Spirulina platensis. Rend Lincei Sci Fis e Nat. 2019;30(1):185–95. https://doi.org/10.1007/s12210-019-00770-3

46. Iravani S, Varma RS. Sustainable synthesis of cobalt and cobalt oxide nanoparticles and their catalytic and biomedical applications. Green Chem. 2020;22(9):2643–61. http://dx.doi.org/10.1039/D0GC00885K

47. Hafeez M, Shaheen R, Akram B, Zain-ul-Abdin, Haq S, Mahsud S, et al. Green synthesis of cobalt oxide nanoparticles for potential biological applications. Mater Res Express. 2020 Feb;7(2):25019.

48. Iqbal Javed, Abbasi BA, Batool R, Khalil AT, Hameed S, Kanwal S, et al. Biogenic synthesis of green and cost effective cobalt oxide nanoparticles using Geranium wallichianum leaves extract and evaluation of in vitro antioxidant, antimicrobial, cytotoxic and enzyme inhibition properties. Mater Res Express. 2019;6(11):115407

49. Ameen F, Alsamhary K, Alabdullatif JA, ALNadhari S. A review on metal-based nanoparticles and their toxicity to beneficial soil bacteria and fungi. Ecotoxicol Environ Saf. 2021 Apr;213:112027.

50. Kashyap M, Samadhiya K, Ghosh A, Anand V, Lee H, Sawamoto N, et al. Synthesis, characterization and application of intracellular Ag/AgCl nanohybrids biosynthesized in Scenedesmus sp. as neutral lipid inducer and antibacterial agent. Environ Res. 2021 Oct;201:111499.

51. Šutka A, Eglitis R, Kuzma A, Smits K, Zukuls A, Prades JD, et al. Photodoping-Inspired Room-Temperature Gas Sensing by Anatase TiO2 Quantum Dots. ACS Appl Nano Mater. 2021 Mar 26;4(3):2522–7. https://doi.org/10.1021/acsanm.0c03089

52. Shakir I, Almutairi Z, Shar SS, Nafady A. Synthesis of Co(OH)2/CNTs nanocomposite with superior rate capability and cyclic stability for energy storage applications. Mater Res Express. 2020 Dec;7(12):125501.

53. Wang Y, Yang C, Li Z, Liang Z, Cao G. The -NH(x) Group Induced Formation of 3D α-Co(OH)(2) Curly Nanosheet Aggregates as Efficient Oxygen Evolution Electrocatalysts. Small. 2020 Jun;16(25):e2001973.

54. Onwudiwe DC, Ravele MP, Elemike EE. Eco-friendly synthesis, structural properties and morphology of cobalt hydroxide and cobalt oxide nanoparticles using extract of Litchi chinensis. Nano-Structures & Nano-Objects. 2020;23:100470. https://www.sciencedirect.com/science/article/pii/S2352507X20300317

55. Ajarem JS, Maodaa SN, Allam AA, Taher MM, Khalaf M. Benign synthesis of cobalt oxide nanoparticles containing red algae extract: antioxidant, antimicrobial, anticancer, and anticoagulant activity. J Clust Sci. 2022;33(2):717–28. https://doi.org/10.1007/s10876-021-02004-9

56. Nakate UT, Bhuyan P, Yu YT, Park S. Synthesis and characterizations of highly responsive H2S sensor using p-type Co3O4 nanoparticles/nanorods mixed nanostructures. Int J Hydrogen Energy. 2022;47(12):8145–54. https://www.sciencedirect.com/science/article/pii/S0360319921048151

57. Kaliamurthi S, Selvaraj G, Çakmak ZE, Çakmak T. Production and characterization of spherical thermostable silver nanoparticles from Spirulina platensis (Cyanophyceae). Phycologia. 2016;55(5):568–76. https://doi.org/10.2216/15-98.1

58. Okaiyeto K, Ojemaye MO, Hoppe H, Mabinya L V, Okoh AI. Phytofabrication of silver/silver chloride nanoparticles using aqueous leaf extract of Oedera genistifolia: characterization and antibacterial potential. Molecules. 2019;24(23). https://www.mdpi.com/1420-3049/24/23/4382

59. Balaji S, Guda R, Mandal BK, Kasula M, Ubba E, Khan F-RN. Green synthesis of nano-titania (TiO2 NPs) utilizing aqueous Eucalyptus globulus leaf extract: applications in the synthesis of 4H-pyran derivatives. Res Chem Intermed. 2021;47(9):3919–31. https://doi.org/10.1007/s11164-018-03720-0

60. Saranya KS, Vellora Thekkae Padil V, Senan C, Pilankatta R, Saranya K, George B, et al. Green synthesis of high temperature stable anatase titanium dioxide nanoparticles using gum kondagogu: characterization and solar driven photocatalytic degradation of organic dye. Nanomaterials. 2018;8(12). https://www.mdpi.com/2079-4991/8/12/1002

61. da Silva Cava S, Tebcherani SM, Pianaro SA, Paskocimas CA, Longo E, Varela JA. Structural and spectroscopic analysis of gamma-Al2O3 to alpha-Al2O3-CoAl2O4 phase transition. Mater Chem Phys. 2006;102–8.

62. Akhlaghi N, Najafpour-Darzi G, Younesi H. Facile and green synthesis of cobalt oxide nanoparticles using ethanolic extract of Trigonella foenumgraceum (Fenugreek) leaves. Adv Powder Technol. 2020;31(8):3562–9. https://www.sciencedirect.com/science/article/pii/S092188312030337X

63. Ismail GA, El-Sheekh MM, Samy RM, Gheda SF. Antimicrobial, antioxidant, and antiviral activities of biosynthesized silver nanoparticles by phycobiliprotein crude extract of the cyanobacteria Spirulina platensis and Nostoc linckia. Bionanoscience. 2021;11(2):355–70. https://doi.org/10.1007/s12668-021-00828-3

64. LewisOscar F, Nithya C, Vismaya S, Arunkumar M, Pugazhendhi A, Nguyen-Tri P, et al. In vitro analysis of green fabricated silver nanoparticles (AgNPs) against Pseudomonas aeruginosa PA14 biofilm formation, their application on urinary catheter. Prog Org Coatings. 2021;151:106058. https://www.sciencedirect.com/science/article/pii/S0300944020312698

65. Leng B, Zhang X, Chen S, Li J, Sun Z, Ma Z, et al. Highly efficient visible-light photocatalytic degradation and antibacterial activity by GaN:ZnO solid solution nanoparticles. J Mater Sci Technol. 2021;94:67–76. https://www.sciencedirect.com/science/article/pii/S100503022100400X

66. Zahid M, Papadopoulou EL, Suarato G, Binas VD, Kiriakidis G, Gounaki I, et al. Fabrication of visible light-induced antibacterial and self-cleaning cotton fabrics using manganese doped TiO2 nanoparticles. ACS Appl Bio Mater. 2018 Oct 15;1(4):1154–64. https://doi.org/10.1021/acsabm.8b00357

67. Mutalik C, Krisnawati DI, Patil SB, Khafid M, Atmojo DS, Santoso P, et al. Phase-Dependent MoS2 nanoflowers for light-driven antibacterial application. ACS Sustain Chem Eng. 2021 Jun 14;9(23):7904–12. https://doi.org/10.1021/acssuschemeng.1c01868

68. Astuti SD, Puspita PS, Putra AP, Zaidan AH, Fahmi MZ, Syahrom A, et al. The antifungal agent of silver nanoparticles activated by diode laser as light source to reduce C. albicans biofilms: an in vitro study. Lasers Med Sci. 2019;34(5):929–37. https://doi.org/10.1007/s10103-018-2677-4

69. Mukherjee K, Acharya K, Biswas A, Jana NR. TiO2 Nanoparticles Co-doped with nitrogen and fluorine as visible-light-activated antifungal agents. ACS Appl Nano Mater. 2020 Feb 28;3(2):2016–25. https://doi.org/10.1021/acsanm.0c00108

70. Yu Z, Fischer R. Light sensing and responses in fungi. Nat Rev Microbiol. 2019;17(1):25–36. https://doi.org/10.1038/s41579-018-0109-x

71. Tian Q, Yang Y, Li A, Chen Y, Li Y, Sun L, et al. Ferrihydrite nanoparticles as the photosensitizer augment microbial infected wound healing with blue light. Nanoscale. 2021;13(45):19123–32. http://dx.doi.org/10.1039/D1NR05364G

72. Elbahnasawy MA, Shehabeldine AM, Khattab AM, Amin BH, Hashem AH. Green biosynthesis of silver nanoparticles using novel endophytic Rothia endophytica: characterization and anticandidal activity. J Drug Deliv Sci Technol. 2021;62:102401. https://www.sciencedirect.com/science/article/pii/S1773224721000812

73. Nisar P, Ali N, Rahman L, Ali M, Shinwari ZK. Antimicrobial activities of biologically synthesized metal nanoparticles: an insight into the mechanism of action. J Biol Inorg Chem. 2019 Oct;24(7):929–41. doi: 10.1007/s00775-019-01717-7.

74. Pillai AM, Sivasankarapillai VS, Rahdar A, Joseph J, Sadeghfar F, Anuf A R, et al. Green synthesis and characterization of zinc oxide nanoparticles with antibacterial and antifungal activity. J Mol Struct. 2020;1211:128107. https://www.sciencedirect.com/science/article/pii/S0022286020304324

Chapter 4

Co_3O_4 nanomaterials synthesized from microalgae: structural properties and catalytic activity for CO oxidation

4.1 Introduction

Carbon monoxide is a by-product of incomplete fossil fuel combustion that can give rise to serious health issues such as hypoxia, apart from environmental problems such as photochemical smog [1]. Rapid urban development and industrialization resulted in a sharp increase in CO emissions generated by metallurgy, thermal power plants, petrochemical industries, coal mines, and other fields [2,3]. Moreover, during the cold start of an engine, when the automotive three-way-catalyst does not yet function, mainly CO is discharged into the atmosphere [4]. Hence, many past studies focused on CO elimination, out of which the most economical and effective method is catalytic CO oxidation to less toxic CO_2. Furthermore, carbon monoxide oxidation in recirculated flue gas of an internal combustion engine is also a means to increase combustion efficiency, thus leading to the reduction of fossil fuel consumption [5,6]. Apart from the well-established nobel metal catalysts, cobalt (II, III) oxide nanomaterials (Co_3O_4 NMs) have received considerable attention due to their abundance, low production costs, and excellent low-temperature catalytic performance [7–9].

Despite the progress and improvements in Co_3O_4 catalyst design, the synthesis methods are usually chemical or physical, while a biological approach has not yet been extensively studied. Recently, pollen has been used as a bio-template in catalyst preparation, providing a porous structure to deposit Co_3O_4 [10]; however, the effect of the extract on Co_3O_4 synthesis was not studied. Organisms possess a variety of metabolites that can be used as reducing agents while maintaining economic and environmentally-friendly aspects [11,12]. Among various organisms,

microalgae are gaining more attention due to the quick production of nutrient-rich biomass, as a result of a higher CO_2 fixation rate during photosynthesis than terrestrial plants [13]. Jahdaly et al. demonstrated the potential of marine red algae extract (*Grateloupia sparsa*) for Co_3O_4 NMs preparation, which were then used as an accessible electrode for energy storage applications [14]. The obtained remarkable performance and stability showed the potential of algal extract to fabricate high-value Co_3O_4 NMs by a sustainable strategy. However, the Co_3O_4 NMs synthesized using biological extract have not been tested for CO oxidation activity so far.

Current research typically focuses on Co_3O_4 NMs synthesized via chemical or physical approaches, i.e. their characterization and description of catalytic activity. Several spectroscopic and theoretical studies aimed at understanding the catalytic mechanism of Co_3O_4 NMs were reported [15–21]. Although Pollard et al. suggested CO adsorption on Co^{2+}, other theoretical studies have claimed CO adsorption on Co^{3+} ions and considered them as active sites [15]. The abundance of Co^{3+} ions on the surface was also suggested to be responsible for cryogenic (-77°C) CO oxidation activity by Co_3O_4 nanorods with exposed (110) planes [16]. The morphology-dependent activity of Co_3O_4 NMs surfaces was determined as (110) > (100) > (111) by a theoretical study [17]. However, Teng et al. proved that plate-like Co_3O_4 with exposed (111) planes were more active than cubic- and rod-shaped Co_3O_4 which exhibited (100) and (110) planes, respectively [18]. Thus, other properties were investigated to establish the relation between structure and exhibited activity. Recently, the involvement of other crystal planes has been studied by synthesizing various morphologies such as straw-like nanorods, flower-like nanosheets, or honeycomb- and raspberry-shaped nanoparticles [19,20]. The results revealed complex surface chemistry with reactivity depending on the exposed crystal facets, morphologies, and crystal sizes.

Another method to study the relationship between structure and activity is the introduction of heteroatoms to induce structural defects. Lou et al. reported that doping heteroatoms with larger ionic radii changed the lattice parameter and promoted reducibility as well as oxygen mobility [22]. The doping effect was investigated for potassium, phosphorous, chlorine, and alkali

metals (Na, K, and Li) [23–26], revealing structural defects with either enhancing or inhibiting effects. However, the combined effect of multiple elements has not been studied so far.

In the study presented herein, methanolic extracts of three different microalgae were used to synthesize Co_3O_4 NMs: *Spirulina platensis* (blue-green algae), *Chlorella vulgaris* (green algae), and *Haematococcus pluvialis* (green algae). To the best of our knowledge, this is the first work dealing with Co_3O_4 NMs synthesized from extracts of *C. vulgaris* and *H. pluvialis*. The involvement of metabolites was examined by Ultraviolet-visible (UV-Vis) and attenuated total reflection Fourier transform infrared spectroscopy (ATR-FTIR) techniques of the extract used for the synthesis, as well as the extract after the synthesis. The obtained Co_3O_4 NMs were characterized using X-ray diffraction (XRD), Brunauer-Emmett-Teller (BET), UV-Vis, scanning electron microscopy (SEM), transmission electron microscopy (TEM), electron energy loss spectroscopy (EELS), X-ray photoelectron spectroscopy (XPS), and ATR-FTIR. In addition, the catalysts were tested for CO oxidation to establish a connection between structure (for calcination 450-800°C) and the catalytic activity. The catalytic performance was measured in a continuous-flow reactor at room temperature, and the mechanism was studied directly using in situ DRIFTS and DSC, and indirectly by H_2-TPR and O_2-TPD. Altogether, the results revealed the prospects of Co_3O_4 NMs structural modifications via extract components, which may stimulate further studies of CO oxidation and related reactions.

4.2 Materials and methods

4.2.1 Catalyst preparation

S. platensis (courtesy of TOLO Green, Arborea, Italy) and *C. vulgaris* (CCALA 902) cultures were cultivated in Modified Zarrouk Medium and BBM medium, respectively, at 25°C with stirring (250 RPM) and 30 µmol m^{-2} s^{-1} photosynthetic photon flux density (PPFD). *H. pluvialis* (CCALA 840) culture was grown in Modified OHM medium at 31°C with shaking (Zetalab®, Italy) and 50 µmol m-2 s-1 PPFD. The culture was supplemented with 10 mM CH_3COONa twice a week to improve the growth and then daily for two weeks to increase the astaxanthin content. Modified Zarrouk medium was prepared with pH adjustment to 9.0, thereafter autoclaved, and, after the solution cooled down, K_2SO_4 and $MgSO_4$ were added to the medium as axenic. Similarly, BBM and

Modified OHM media were prepared, pH was set to 6.2 and 8.0 for BBM and Modified OHM media, respectively, and the media were autoclaved.

The cultures were cultivated until reaching OD_{750} around 0.6, 0.4, and 0.3 for *S. platensis*, *C. vulgaris*, and *H. pluvialis*, respectively. Then, the biomass was separated from the media by centrifugation at 4°C (1500 RPM for *S. platensis*, 2000 RPM for *C. vulgaris*, and 1200 RPM *for H. pluvialis*) and dried at room temperature for 7 days. The obtained biomass was weighted, yielding 9 g of *S. platensis*, 2.75 g of *C. vulgaris*, and 2.5 g of *H. pluvialis* used for extract preparation.

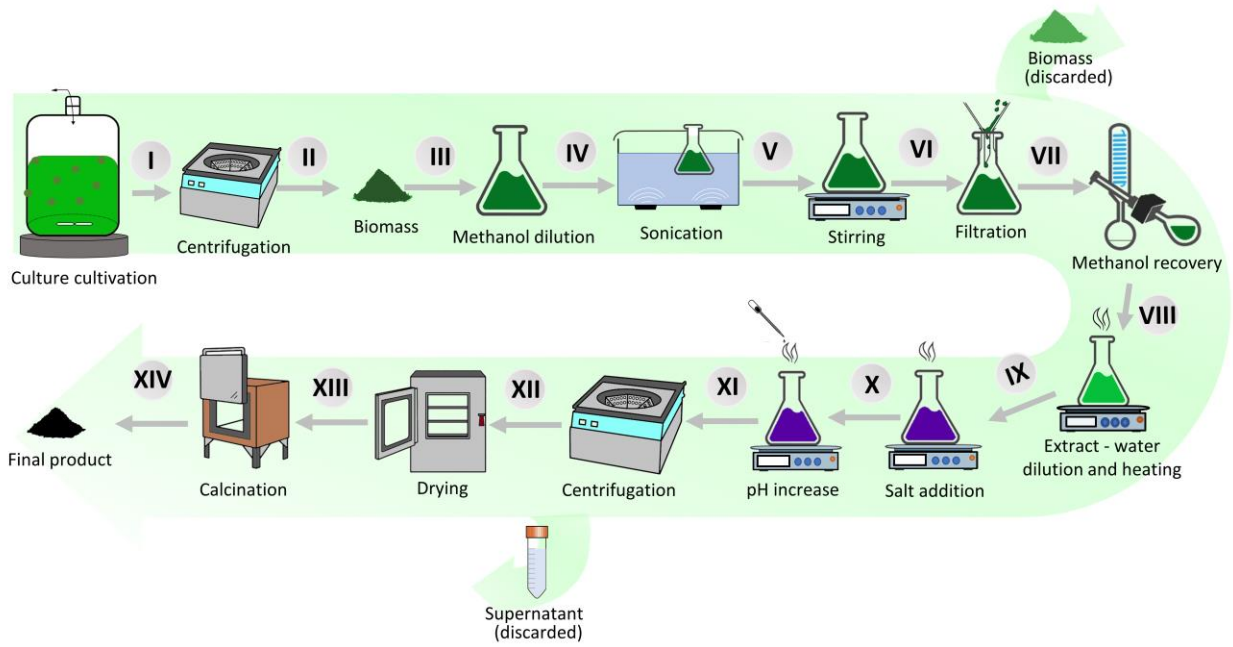

Figure 12 Methodology of Co_3O_4 NMs synthesis from microalgae.

The Co_3O_4 NMs synthesis procedure from microalgae is depicted in Fig. 12. First, the obtained algal biomass was suspended in methanol (Merck® LiChrosolv® hypergrade) according to the weight (540 ml for *S. platensis*, 165 ml for *C. vulgaris*, 150 ml for *H. pluvialis*). The flasks were sonicated for 30 min (Soltec® Sonica® 2400 ETH S3) and then stirred at 250 RPM (IKA® RH Digital Magnetic Stirrer) for 30 min. Next, the biomass was removed using standard filtration paper (Whatman®), and the solutions were evaporated using a rotary evaporator (Buchi Rotavapor™ R-210 Rotary Evaporator System) to remove about 70% of methanol. Finally, the concentrated

extracts were diluted using MiliQ H_2O (Millipore®, Milan, Italy) to 1080 ml, 330 ml, and 300 ml for *S. platensis*, *C. vulgaris*, and *H. pluvialis*, respectively.

The prepared extracts were heated to 85°C by stirring at 250 RPM (IKA® RH Digital Magnetic Stirrer) while the extract sample was taken and labeled as extract before the synthesis (Fig. 12IX). In the next step, 13.52 g, 4.29 g, or 3.90 g of cobalt (II) chloride hexahydrate (Carlo Erba®, Italy) was added to *S. platensis, C. vulgaris*, and *H. pluvialis* extract, respectively. After 15 min, the pH was raised up to 8 (*S. platensis* and *C. vulgaris*) and 10 (*H. pluvialis*) using 1.25 M NaOH. After salt addition, the flasks were continuously heated and stirred for 1.5 h. Then, the solutions were removed from the heat source and left to cool down to room temperature. The obtained nanomaterials were separated from the supernatant by centrifugation at 4°C with 4000 RPM (Heraeus® Megafuge® 1.0R) and dried at 80°C for 24 h. The supernatant was labeled as an extract after the synthesis (Fig. 12XII). Next, the products were calcined in a muffle furnace (Gelman Instrument®) for 3 h at 450, 650 or 800°C. Finally, the nanomaterials were stored at room temperature in the dark. The samples were labeled according to the species used for the synthesis (*S. platensis* – SP, *C. vulgaris* – CH, *H. pluvialis* - HA) and their calcination temperature. A commercially available Co_3O_4 NM (Sigma-Aldrich®, Italy) was labeled as SA400 and used after 400°C calcination following the procedure described previously 8.

4.2.2 Characterization

UV-Vis measurements were performed on a UV-1600PC spectrophotometer at room temperature. The extract samples before and after synthesis were used as obtained and measured in the 200-1000 nm wavelength range. The nanomaterials were suspended in deionized water (10 mg/ml) and sonicated for 15 min, followed by measurement in the wavelength range from 300 to 1000 nm. The direct bandgap energy was calculated from the Tauc relation (Equation 1):

$$(\alpha h\nu)^2 = (h\nu - E_g) \quad (1)$$

where α is the molar extinction coefficient, h is Plank's constant, v is the light frequency, and E_g is the band gap energy. The bandgap energy was calculated by linear fit extrapolation of the plot of $(\alpha hv)^2$ against energy (hv).

For attenuated total reflection Fourier transform infrared spectroscopy (ATR-FTIR), an FT-IR spectrophotometer (Vertex-70, Bruker Optics®) was used, equipped with an ATR unit (ZnSe crystal) and a liquid N_2-cooled mercury cadmium telluride (MCT) detector. The extract samples (before and after synthesis) were diluted in ethanol in a 1:4 ratio, and the flow rate was adjusted to 5 ml/min. The spectra were recorded using OPUS 6.5 software by performing 128 scans from 4000 to 900 cm^{-1} range in absorbance mode with 4 cm^{-1} resolution.

Crystallographic parameters were examined by X-ray diffraction (XRD) at angles of diffraction (2θ) between 15° and 90° using a Cu-Kα radiation source (wavelength λ = 1.5406 Å). The measurement was carried out at 40 kV operating voltage and 30 mA current. The results were analyzed by Rietveld refinement using HighScore Plus® (v5.1) connected with ICDD® database. The d-spacing (d) was calculated based on the following equation (Equation 2):

$$d = \frac{\lambda}{2 \sin \theta} \quad (2)$$

where λ is the wavelength of the incident X-ray beam (1.5406 Å), and θ is the angle of detector position from the incident X-ray beam. Based on the d-spacing values, the average lattice parameter (a) was calculated based on the following equation (Equation 3):

$$a = d \times \sqrt{h^2 + k^2 + l^2} \quad (3)$$

with h, k, and l corresponding to the Miller indices.

N_2 adsorption-desorption isotherms were recorded at 77K using an ASAP 2020 instrument (Micromeritics Inc., USA). Before each run, a known mass sample (ca. 0.18 g) was heated to 120°C under vacuum for 2 h. Brunauer-Emmett-Teller (BET) and Barrett-Joyner-Halenda (BJH) models were used to calculate specific surface area and pore size/volume, respectively.

Prior to scanning electron microscopy (SEM), specimens were sputter-coated with an 8 nm layer of platinum and gold. The surface morphology was observed using a FEG-250, Quanta instrument with an accelerating voltage of 5 kV. Transmission electron microscopy (TEM) was performed on a FEI TECNAI F20 field emission microscope equipped with a GATAN GIF Tridiem energy filter and a GATAN Rio16 CMOS camera. The microscopy images were analyzed using ImageJ software (1.52a). Selected area electron diffraction (SAED) and electron energy loss spectroscopy (EELS) were employed to determine the structure and elemental composition in Co_3O_4 NMs, respectively.

X-ray photoelectron spectroscopy (XPS) spectra were acquired at room temperature in a UHV chamber (base pressure $< 3 \times 10^{-10}$ mbar) equipped with a Specs XR50© high-intensity non-monochromatic Al/Mg dual anode and a Phoibos 100© hemispherical electron energy analyzer with multichannel plate detector. All measurements were performed using the Al anode at 1486.6 eV, at normal emission geometry, and in fixed analyzer transmission with a pass energy of 20 eV. The spectra were calibrated to the C1s peak at 284.8 eV and analyzed using CasaXPS.

For universal attenuated total reflection Fourier transform infrared spectroscopy (UATR-FTIR), measurements were done by another Fourier-transform infrared spectrometer (FTIR) (PerkinElmer Universal ATR, PerkinElmer, Waltham, MA, USA) coupled to Frontier Universal Diamond/ZnSe ATR crystal with a pressure arm. Each specimen was suitably pressed against the ATR crystal with the aid of the pressure arm to maintain proper contact between the sample and the ATR crystal. The FTIR spectrometer was operated in the 4000–400 cm^{-1} wavenumber range with 4 cm^{-1} resolution. Absorption intensity versus wavenumber plots were digitally recorded by averaging 64 scans using Spectrum software (PerkinElmer Spectrum 10; PerkinElmer).

H_2-Temperature Programmed Reduction (H_2-TPR) experiments were performed in a continuous-flow fixed-bed quartz reactor under atmospheric pressure. For H_2-TPR, 20 mg of the sample were placed between quartz plugs. After pre-treatment (20 vol% O_2 in Ar, total flow: 50ml/min) at 400°C for 30 min (heating rate 10°C/min) and cooling to 30°C in 100 vol% Ar (total flow 50ml/min), each sample was heated from RT to 800°C (heating rate of 5°C min^{-1}) in a mixture of 5 vol.% H_2 in Ar (total flow: 50 ml/min). Hydrogen consumption was measured by a mass

spectrometer (Pfeiffer Hicube RGA, Pfeiffer Vacuum) with a MS signal of H_2 (m/z = 2) detected online using Quadera software (v.4.40.019).

For O_2-Temperature Programmed Desorption (O_2-TPD), 50 mg of a sample was placed between quartz plugs in a continuous-flow reaction system and pre-treated (20 vol% O_2 in N_2, total flow: 50ml/min) at 400°C for 30 min (heating rate 10°C/min), followed by cooling down to RT. Then, each sample was heated from RT to 500°C under vacuum with a heating ramp rate of 10°C/min. The gas stream was analyzed by a mass spectrometer (Balzers Quadstar 422), monitoring the MS signal of O (m/z=16).

4.2.3 Catalytic CO oxidation

Differential scanning calorimetry (DSC) analysis during CO oxidation was performed on Netzsch STA 409 PC Luxx® in an alumina crucible. Before each cycle, samples (10 mg) were pre-treated in 20 vol% O_2 in He (total flow: 50ml/min) at 400°C for 30 min (heating rate 10°C/min). After cooling down to 25°C under He, different vol.% of CO and O_2 were introduced under He flow (total flow 20 mL/min) in 10 min intervals: at 10 min CO, 20 min CO + O_2, 30 min O_2, 40 min CO + O_2, and 50 min CO.

CO oxidation was conducted in a continuous-flow fixed-bed quartz reactor under atmospheric pressure. Typically, 20 mg of catalyst placed between quartz plugs was loaded into the reactor and pre-treated (20 vol% O_2 in Ar, total flow: 50 ml/min) at 400°C for 30 min (heating rate 10°C/min). The catalyst bed temperature was controlled by a thermocouple. Subsequently, the sample was cooled to 30°C, and a mixture of 5 vol% CO, 10 vol% O_2, and 85 vol% Ar (total flow 50 mL/min) was introduced. A mass spectrometer (Pfeiffer Hicube RGA, Pfeiffer Vacuum) was used to monitor the effluent gas, and the MS signals of CO (m/z = 28), O_2 (m/z = 32), CO_2 (m/z = 44) and H_2O (m/z = 18) were recorded online using Quadera software (v.4.40.019).

Diffuse reflectance infrared Fourier transform spectroscopy (DRIFTS) studies were carried out on a Bruker Vertex 70 spectrometer with a liquid N_2-cooled MCT detector. A stainless-steel flow cell (Pike) features a CaF_2 window and an oven. The inlet of the cell was connected to a gas manifold system with calibrated mass flow controllers to adjust the gas mixtures (pre-treatment: 20 vol% O_2 in Ar, total flow: 50 ml/min, reaction: 5 vol% CO, 10 vol% O_2 in Ar, total flow: 50 ml/min) and

a mass spectrometer (Pfeiffer Hicube RGA, Pfeiffer Vacuum). Each sample was pre-treated at 400°C with a temperature ramp of 10°C/min and kept at the maximum temperature for 30 min (20 vol% O_2 in Ar). Next, the sample was cooled to room temperature (100 vol% Ar), and the gases were switched to reaction conditions. The reaction temperature was increased by 5°C/min and kept at the maximum temperature of 300°C. DRIFTS spectra were recorded with 4 cm^{-1} resolution using OPUS 6.5 software by averaging 128 scans to achieve a good signal-to-noise ratio.

4.3 Results and discussion

4.3.1 Analysis of extracts

S. platensis, C. vulgaris, and *H. pluvialis* were investigated to determine differences in their morphology and metabolomic profile [27,28]. *S. platensis* is a well-known source of proteins with less abundant lipid and carbohydrate content. On the contrary, *C. vulgaris* has a decreased protein content and has been used mainly for its high lipid accumulation, while *H. pluvialis* is a source of astaxanthin belonging to carotenoids. Therefore, the effect of the metabolite composition on the synthesis process was evaluated by comparing the extract before and after synthesis by UV-Vis and ATR-FTIR (Fig. 13).

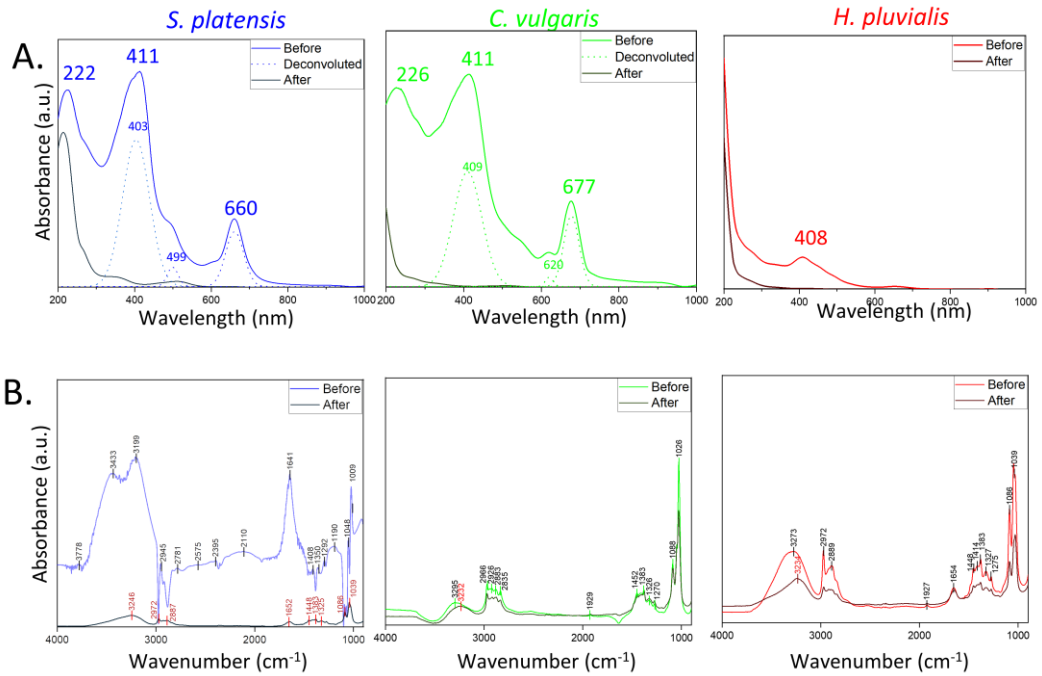

Figure 13 Analysis of the extract before and after synthesis: (A) UV-Vis, (B) ATR-FTIR.

UV-Vis spectra of the extract before and after synthesis are presented in Fig. 13A. Before synthesis, three major peaks were identified in the *S. platensis* extract: at 222 nm, 411 nm, and 660 nm. The first peak can be assigned to proteins owing to the presence of the carbonyl group in the peptide bond. The same peak was used to determine the presence and isolate various peptides from *S. platensis* by Lu et al. [29]. The peaks at 411 nm and 660 nm can be attributed to abundant compounds in the extract, such as carotenoids, chlorophylls, and phycocyanin with overlapping absorbance maxima [30]. Similar values were observed for *C. vulgaris* extract before synthesis, with peaks at 226 nm, 411 nm, and 677 nm, the redshift probably due to structural differences between molecules belonging to the same group of metabolites [31]. The *H. pluvialis* extract before synthesis exhibited one major peak at 408 nm characteristic of astaxanthin, usually observed at 450-500 nm; however, the absorbance peak shifted towards 400 nm after water dilution [32]. After synthesis, all extracts show decreased absorbance, suggesting that the molecules from microalgae were indeed involved in the synthesis of Co_3O_4 NMs.

The presence of functional groups in the extract before and after synthesis was further investigated by ATR-FTIR. The *S. platensis* extract exhibits a variety of identified functional groups belonging to proteins, lipids, and carbohydrates (Fig. 13B). Comparably, *C. vulgaris* and *H.*

pluvialis extracts show a lower peak intensity for functional groups of proteins and increased intensity of carbonyl groups belonging to carbohydrates (Fig 2B). After synthesis, *S. platensis* extract showed an intensity decrease in all previously identified peaks with visible redshift. In cases of *C. vulgaris* and *H. pluvialis*, the decrease was less significant, and redshift was observed around 3000 cm^{-1}, attributed to the NH group of proteins. Altogether, the results confirm a significant involvement of metabolites from the extract, mainly proteins and carbohydrates, in the Co_3O_4 NMs synthesis.

Recent studies showed the potential of extracts to synthesize highly active Co_3O_4 NMs. Poonguzhali et al. utilized a fresh lemon juice-assisted auto-combustion method to synthesize Co_3O_4 NMs as gas sensors [33]. The response was measured as a change in resistance due to chemical reactivity between the produced oxygen ions and tested gases such as H_2, CO_2, LPG, and $(CH_3)_2CO$. The material exhibited a short recovery-response time showing promising gas sensor applications. In a separate study, Khalid et al., tested Co_3O_4 NMs prepared by employing green chili or sunflower seed extracts and compared them with synthesis without extract [34]. The utilization of sunflower seed extract resulted in the synthesis of Co_3O_4 NMs with the best photocatalytic and capacitive behaviour among prepared materials. Although both studies proved the high catalytic activity of Co_3O_4 NMs, the extracts used for the synthesis were not analyzed, and therefore the role of the metabolites remained unclear. In the present study, the utilization of microalgal metabolites has been evaluated to provide insights into the synthesis mechanism. In the next steps, the obtained catalysts were characterized to establish a connection between synthesis, properties, and catalytic activity.

4.3.2 Characterization of Co_3O_4 NMs

The crystal structure of synthesized algae-derived catalysts and the commercial reference cobalt oxide were characterized by XRD. All samples show a diffraction pattern of Fd-3m cubic spinel Co_3O_4 (JCPDS 01-078-5622) with (111), (220), (311), (400), (511), and (440) reflections (Fig. 14A). Moreover, Co_3O_4 NMs synthesized from *C. vulgaris* and *H. pluvialis* extracts exhibited additional peaks next to (220) and (400), belonging to NaCl (JCPDS 01-079-9877) formed probably due to the use of NaOH and $CoCl_2 \cdot 6\ H_2O$ during synthesis. Another factor that causes changes in the

pattern is the calcination temperature which, consistently with literature, shifted all peak positions to higher values probably due to the lattice contraction [35].

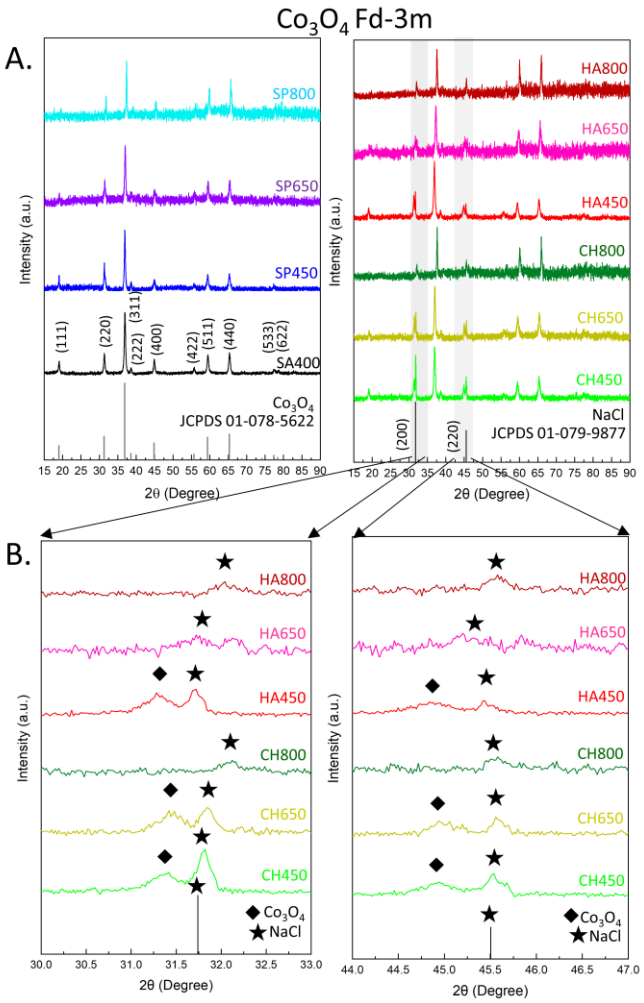

Figure 14 XRD analysis of Co3O4 NMs: (A) wide angle, (B) selected magnified regions.

Moreover, structural changes were observed for HA650, for which (111) was absent, as well as CH800 and HA800, for which (111), (220), and (400) were not present in the pattern (Fig. 14B). In addition, crystallite sizes increased with calcination temperature, with slight changes for Co_3O_4 NMs from *S. platensis*, but more pronounced growth for Co_3O_4 NMs from *C. vulgaris* and *H. pluvialis* (Tab. 1). The crystallite size increase indicates sintering of Co_3O_4 NMs. Increased calcination temperature also caused a reduction of interplanar distances, indicating a more strained crystal lattice formation. The lattice parameter and volume decreased with temperature for Co_3O_4 NMs. In particular, a small decrease was observed for *S. platensis* and *C. vulgaris*

between 450 to 650°C, while a more prominent decrease occurred for other Co_3O_4 NMs (Tab. 1, Fig. S4B). A similar tendency was observed for Co_3O_4 NMs synthesized via a chemical method and calcined at 400, 600, and 800°C [36]. The applied thermal energy is contributing to a more orderly ion arrangement, decreasing the unit cell size (lattice contraction).

N_2 physisorption isotherms were acquired to determine the textural properties of Co_3O_4 NMs. The adsorption-desorption isotherms belong to type IV isotherms according to the IUPAC classification with an H1 hysteresis loop suggesting the presence of meso- and macro-pores in the catalysts [37]. The pore distribution graphs, reveal a narrow spread at 2.5-4 nm width for all samples. In addition, SA400 Co_3O_4 NMs show a bell-shaped pore distribution at around 5-80 nm. The high porosity correlates with a large surface area of SA400 Co_3O_4 NMs (43.7 m^2/g) and huge pores volume (Tab. 6). However, even though SA400 Co_3O_4 NMs, CH450 Co_3O_4 NMs, and HA450 Co_3O_4 NMs show similar average pore width, their pore volume varies, suggesting pore blocking in the catalysts synthesized using microalgae. The porosity change with increasing temperature has been studied before [38]. The calcination temperature was found to increase Co atom migration that leads to bigger Co_3O_4 crystallites which, in turn, cause structural strain in the material. This results in a shrinkage of the formed porous structures which finally collapse into quasi-spherical particles. Moreover, the gases formed during organic residue decomposition can further destroy structural integrity, or it may lead to carbon deposition decreasing the catalytic activity. These findings have been confirmed in the current study. Increasing the calcination temperature decreased porosity, pore volume, and surface area, with the most significant surface area decrease for Co_3O_4 NMs obtained when using *H. pluvialis* extract (from 29.2 to 5 m2/g). A similar effect has been observed for Co_3O_4 NMs synthesized using a metal-organic framework, with the surface area decreasing from 120.9 m^2/g to 22.6 m^2/g upon calcination temperature increase from 300°C to 400°C, likely due to increasing crystallite size [38].

Table 6 Structural properties of the different Co_3O_4 NMs.

Sample	Crystallite size (nm)	Lattice parameter a=b=c (Å)	Volume (Å^3)	BJH adsorption cumulative pores volume (cm^3/g)	BJH average pore width (nm)	BET surface area (m^2/g)
SA400	21.9	8.067	524.878	0.2657	26.8	43.7
SP450	26.1	8.068	525.155	0.0285	16.1	6.9
SP650	24.1	8.057	522.661	0.0240	18.5	6.1
SP800	28.6	7.980	508.216	0.0120	38.1	3.4
CH450	16.4	8.058	523.141	0.0680	25.6	13.3
CH650	24.0	8.054	522.401	0.0743	37.3	11.3
CH800	40.3	7.951	502.690	0.0188	28.6	4.6
HA450	18.4	8.078	527.215	0.1706	24.4	29.2
HA650	23.1	8.014	514.735	0.1408	39.2	19.5
HA800	42.2	7.958	504.059	0.0152	14.7	5.0

The morphologies of the commercial and synthesized Co_3O_4 NMs were examined by SEM. As presented in Fig. 15, SA400 Co_3O_4 NMs are spherical or quasi-spherical agglomerates with high porosity confirming the BET findings. Octahedral shape was observed for SP450 Co_3O_4 NMs with more abundant hollow spherical agglomerates upon increasing calcination temperature. Nanosheet morphologies were observed for CH450 and HA450 Co_3O_4 NMs with similar tendency regarding spherical form with rising calcination temperature, as described previously [38]. High resolution TEM images show lattice fringes corresponding to the (111) crystalline plane. The

obtained SAED patterns of the powder materials show characteristic diffraction rings, which can be attributed to (111), (220), (311), (400), (511), and (440), in line with the XRD findings.

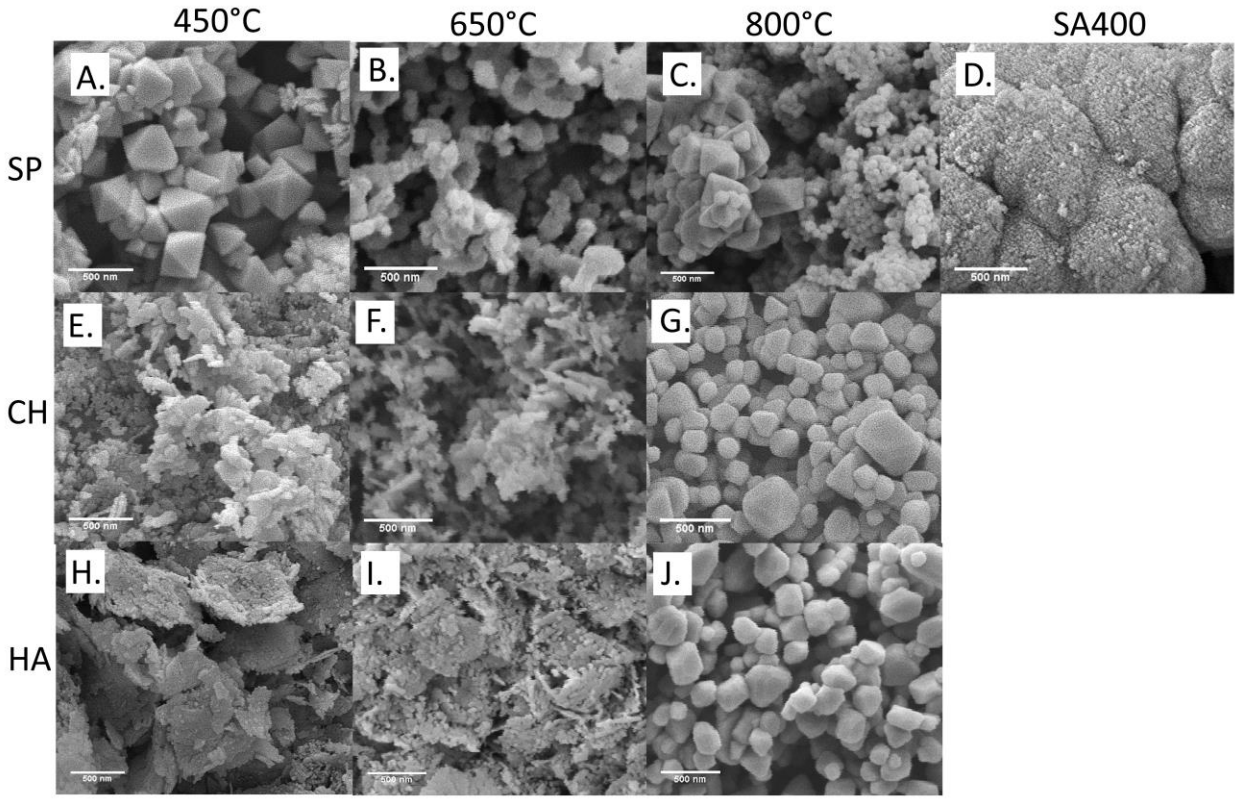

Figure 15 SEM analysis of Co_3O_4 NMs: (A) SP450, (B) SP650, (C) SP800, (D) SA400, (E) CH450, (F) CH650, (G) CH800, (H) HA450, (I) HA650, (J) HA800.

The local valence state of Co_3O_4 NMs was studied in the TEM using the EELS technique. The O K-edge displays peaks a, b, and c in the 533-553 eV range. Peak a, referred to as the pre-edge peak, is ascribed to O 2p unoccupied states hybridization with the Co 3d orbital, while peaks b and c originate from O 2p state hybridization with Co 4sp band [39]. The increased pre-edge peak intensity compared with peak b is considered as a fingerprint for Co_3O_4 due to the high number of unoccupied Co 3d states [40]. Moreover, the decreased electron counts of peaks a and b are correlated with oxygen vacancies in Co_3O_4 NMs [41,42], with rich oxygen vacancy indicated for SA400 Co_3O_4 NMs, followed by CH450, HA450, and SP450 Co_3O_4 NMs. The EELS spectra also display Co L3 and L2 edges at 780-800 eV, stemming from 2p3/2 and 2p1/2 core-shell electrons transition into 3d orbitals in a pattern typical for Co_3O_4 [39].

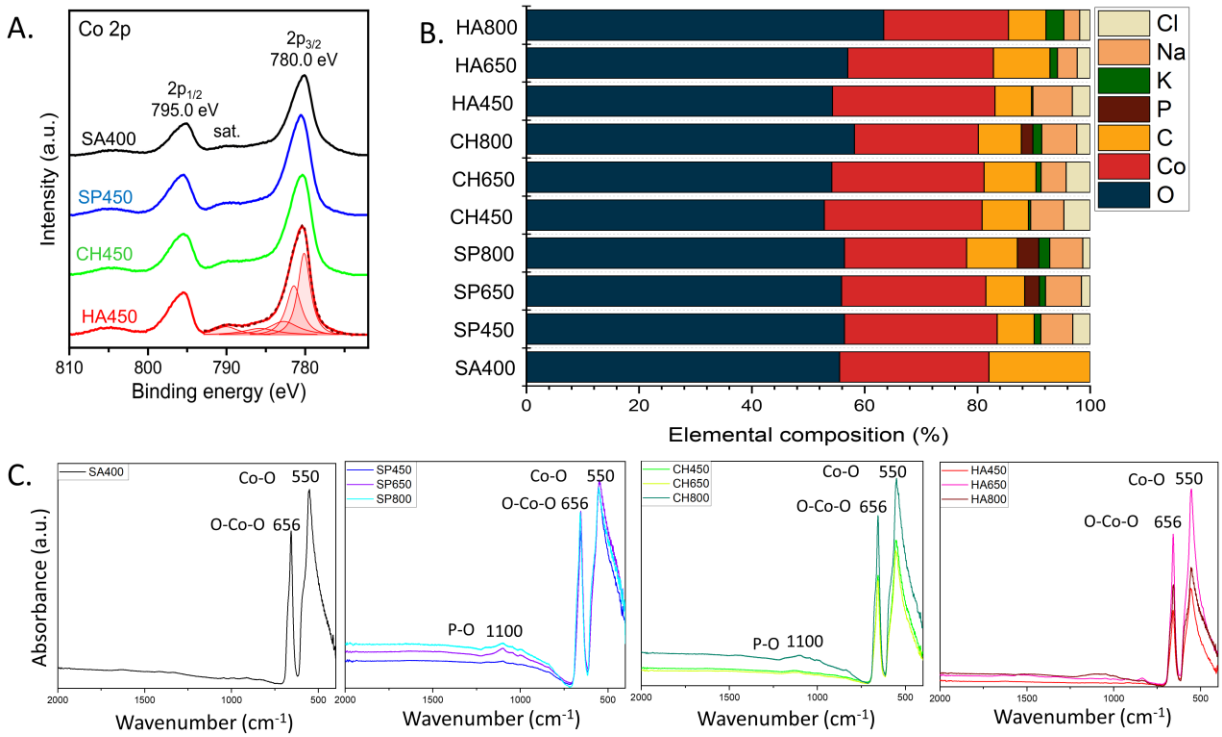

Figure 16 Composition of Co_3O_4 NMs: (A) XPS Co 2p spectra, (B) elemental composition based on XPS analysis, (C) UATR-FTIR spectra.

Catalyst composition was examined by XPS. The results confirmed the Co3O4 phase in the samples (Fig. 16A), as previously indicated by XRD and EELS analyses. The Co 2p3/2 peak was deconvoluted into three primary and two satellite signals, as shown for HA450 (the same deconvolution holds true for the analogous peak of SP450, CH450 and SA400). The main signals at 780, 782, and 783 eV were attributed to Co^{3+} in Co_3O_4 lattice, with Co^{2+} in the Co_3O_4 lattice, and Co^{2+} in octahedral positions in a CoO lattice, respectively [43]. The presence of CoO on the surface might be a result of vacuum reduction during XPS measurements [43,44]. The relative composition, derived from the XPS spectra, is displayed in Fig. 16B. The samples have similar oxygen content with a slight increase upon rising calcination temperature. The Co_3O_4 NMs synthesized using microalgae extract also showed the presence of sodium (from sodium hydroxide) and chlorine (from cobalt salt) added during the synthesis process, as also observed by XRD. In addition, Co_3O_4 NMs synthesized using microalgal extract contained potassium, whose percentage increases with calcination temperature, and phosphorus that was observed only in SP650, SP800, and CH800 Co_3O_4 NMs. Both potassium and phosphorus originated from the

microalgae extract, which once more indicates the involvement of metabolites during synthesis. The variable potassium, phosphorus, carbon, and oxygen contents suggest surface segregation, which may also cause the differences in the Co_3O_4 NMs crystallographic parameters (Tab. 6). The XPS results were confirmed by UATR-IR analysis of Co_3O_4 NMs, which also revealed the presence of phosphorous via a phosphorous-oxygen stretching vibration at 1100 cm^{-1} [45] in SP650, SP800, and CH800 Co_3O_4 NMs (Fig. 16C). All UATR-IR spectra showed peaks at 550 cm^{-1} belonging to Co-O stretching and 656 cm^{-1} corresponding to O-Co-O bridging vibration due to Co-O linkage [46]. Moreover, no organic ligands were detected on the surface.

4.3.3 Reducibility and oxygen availability of Co_3O_4 NMs

The redox behavior of active cobalt species was further investigated by H_2-TPR, as presented in Fig. 17A. Typically, Co_3O_4 NMs exhibit two peaks corresponding to reduction of Co^{3+} to Co^{2+} and Co^{2+} to Co^0, which may partly overlap. A lower temperature of H_2 consumption indicates weaker Co-O bond strength, which should lead to higher oxidation activity [47]. The lowest TPR temperatures of both peaks was observed for SA400 Co_3O_4 NMs, followed by HA450, CH450, and SP450 Co_3O_4 NMs. The lower temperature for HA450 than CH450 Co_3O_4 NMs shows their potential for oxidation performance, which could be hindered by other factors, such as the presence of sodium and chlorine. Increasing the calcination temperature shifted the peak positions to higher TPR temperature, which should be a descriptor of lower CO_2 production. For HA650 and HA800 Co_3O_4 NMs, only one TPR peak was observed, likely due to calcination-induced changes in the structure.

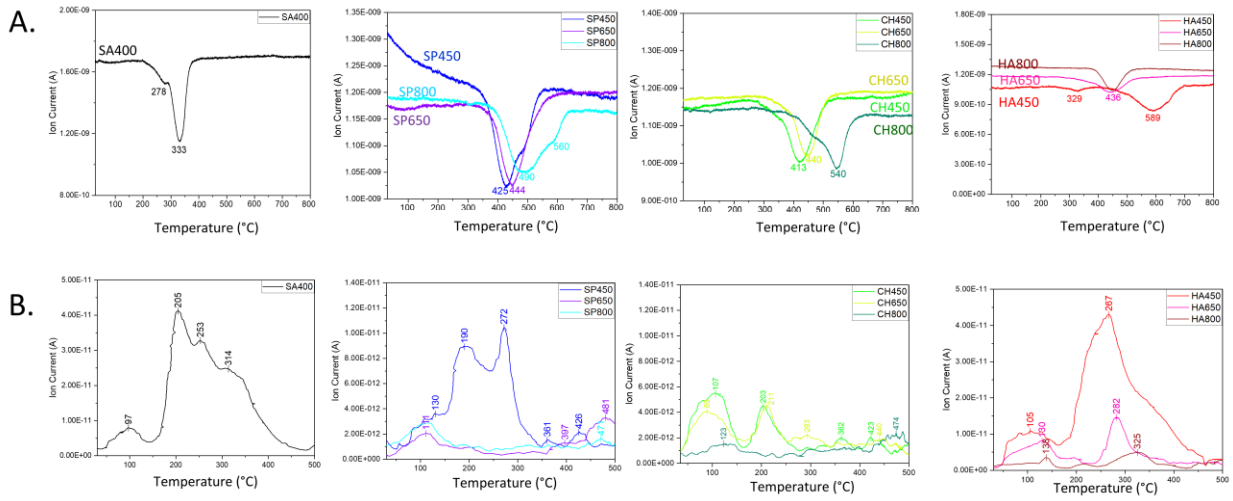

Figure 17 (A) H_2-TPR, (B) O_2-TPD of Co_3O_4 NMs.

The desorption of oxygen from the catalysts' surface, revealing the availability of oxygen species, was then investigated by O_2-TPD (Fig. 17B). Three types of oxygen species were detected in the spectra, depending on the temperature range: oxygen species adsorbed on the oxygen vacancies at 50-150°C, surface active lattice oxygen ions at 150-450°C, and lattice oxygen at 450-500°C [48]. The largest oxygen desorption area was observed for SA400 Co_3O_4 NMs, mostly as surface active lattice oxygen ions, which results in efficient oxidation performance according to the Mars-van-Krevelen (MvK) mechanism. High surface-active oxygen content was also observed for HA450 and SP450 Co_3O_4 NMs. On the contrary, CH450 Co_3O_4 NMs showed an increased amount of molecular oxygen adsorbed on the oxygen vacancies, which may predict their improved catalytic action compared with other Co_3O_4 NMs synthesized from the microalgal extract. Moreover, increasing the calcination temperature decreased the amount of desorbed oxygen, thus decreasing the Co_3O_4 NMs oxidation ability.

4.3.4 CO oxidation on Co_3O_4 NMs

To better understand CO oxidation on the Co_3O_4 NMs, a DSC technique was applied (Fig. 18). The energy released was calculated based on the measured peak areas. The strongest exothermicity with -14.4 J/g was observed for SA400 Co_3O_4 NMs, with significantly reduced energy of -0.4, -2.4, and -6.5 J/g for SP450, CH450, and HA450 Co_3O_4 NMs, respectively. When exposed to CO several processes can take place including CO_2 or carbonate formation 8. During initial adsorption, CO

interacts with Co active sites and neighboring oxygen, resulting in CO2 formation. Filling of the generated oxygen vacancy with the oxygen atom of CO may lead to dissociation and carbon deposition (which may be re-oxidized upon oxygen exposure) [21]. Both CO and carbon oxidation are exothermic and can occur in parallel [49]. The strongest exothermicity for SA400 Co_3O_4 NMs is connected with its high activity. However, the differences to other samples might originate from the formation of different carbonate species on the surface. Subsequent molecular oxygen dosing led to smaller heat release. This difference may be due to active oxygen species only present after pretreatment or to adsorbed CO attached to the surface [8]. After a 10 min treatment with (pure) oxygen, the heat release remained reduced. A decrease in exothermicity was also observed for SA400 Co_3O_4 NMs in a second cycle with different percentages of gases. The results suggest a complex network of different interactions due to CO and O_2 competing for active sites, as discussed previously [8,21].

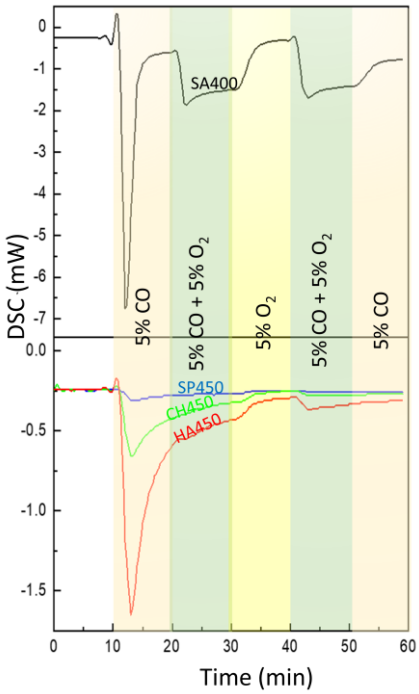

Figure 18 DSC analysis of Co_3O_4 NMs: SA400, SP450, CH450, and HA450.

The various catalysts were then tested for CO oxidation in a flow reactor, with the results shown in Fig. 19. The CO oxidation activity of Co_3O_4 NMs synthesized from the extract is described for the first time along with a comparison to commercial Co_3O_4 NMs. The most intense CO_2 signal corresponding to the highest catalytic activity was observed for SA400 Co_3O_4 NMs, followed by

CH450, HA450, and SP450 Co_3O_4 NMs. Such sequence correlates well with the one related to oxygen vacancies content revealed by EELS. Among the tested microalgae, for Co_3O_4 NMs calcined at the same temperature, the highest activity was observed for the Co_3O_4 NMs synthesized using *C. vulgaris* extract, while after calcination at 800°C Co_3O_4 NMs synthesized using *S. platensis* extract were the most active. Increasing calcination temperature decreased the catalytic activity of Co_3O_4 NMs synthesized from microalgae, which might be related to a decrease in surface area (Tab. 6) However, it increased signal stability with only an activity

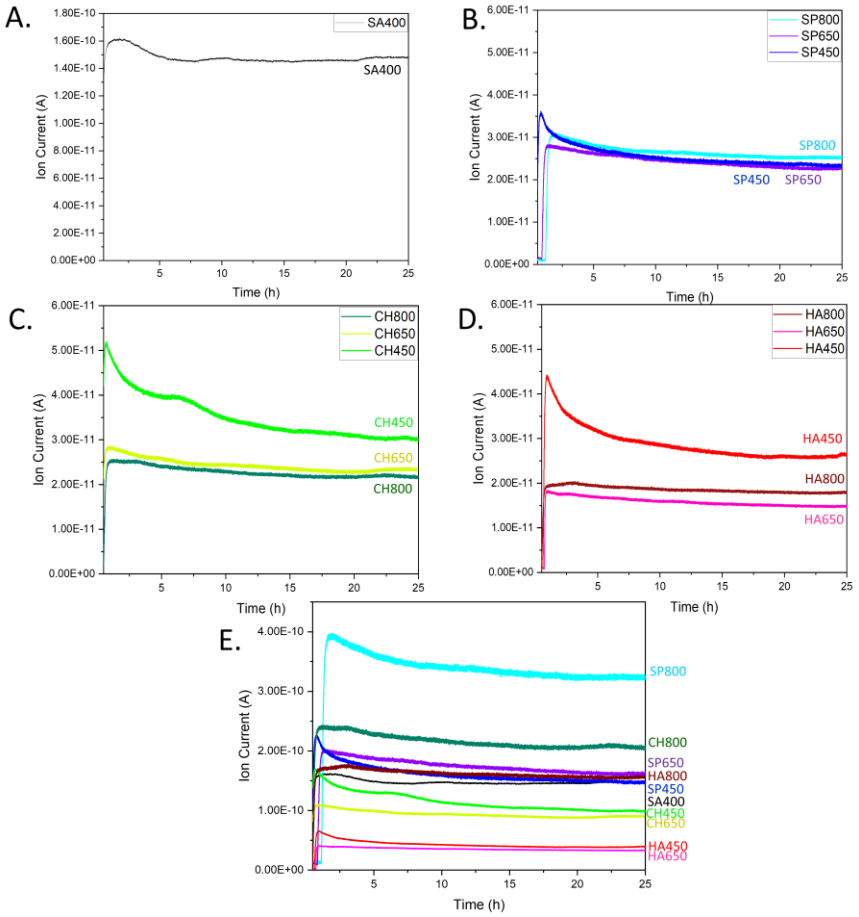

decrease by ca. 11-19% for Co_3O_4 NMs calcined at 800°C and 35-41% decline for Co_3O_4 NMs calcined at 450°C.

Figure 19 CO oxidation over Co_3O_4 NMs: MS spectra of CO_2 for (A) SA400, (B) SP, (C) CH, (D) HA, (E) CO_2 signal normalized per surface area of SA400.

The variable catalytic activity was also normalized relative to the per surface area of SA400 (Fig. 19E), revealing high catalytic surface activity of SP800, CH800, and SP650 Co_3O_4 NMs containing phosphorous, as indicated by XPS. The effect of phosphorus has been studied before, mainly as a dopant in Co_3O_4 NMs. During peroxymonosulfate (PMS) activation, due to the presence of phosphorus, more active cobalt sites were exposed, thereby exhibiting higher affinity and easier electron transfer for PMS, while weakening O–O bond for the rapid generation of radicals [50]. Accelerated charge transfer was also observed for Co_3O_4 anchored on nitrogen-doped carbon nanotubes, with observed oxygen vacancies mobility to the Co3O4 lattice, inducing active species Co–O–P. Moreover, the resulting lattice dislocations were examined for their enhanced adsorption and catalytic sites interaction with polysulfides [18].

On the materials of the current study, CO oxidation is believed to follow a Mars-Van-Krevelen (MvK) mechanism which involves reactant adsorption, lattice oxygen activation, reaction with active lattice oxygen, and product desorption, followed by replenishment of oxygen vacancies by gas-phase oxygen [8,51]. In addition, the possibility of reaction between CO and chemisorbed oxygen cannot be excluded (Langmuir–Hinshelwood mechanism) [46]. Thus, increased oxygen mobility induced by phosphorous should improve the catalytic process. The enhancing effect of phosphorous is persistent despite the presence of sodium and chlorine, which were previously reported for their reducing effect on oxygen mobility, poisoning catalytic oxidation [19,20]. However, a decrease in sodium and chlorine content in HA650 Co_3O_4 NMs compared to HA450 Co_3O_4 NMs did not increase their activity. Nevertheless, HA800 Co_3O_4 NMs show much better performance, probably due to higher potassium content. Potassium in the Co_3O_4 NMs lattice was previously described for promoting oxygen activation by stimulating CO_2 desorption, resulting in a more facile CO oxidation process [17]. So far, the influence of phosphorous, potassium, chlorine, and sodium has been described, when the elements were introduced separately to Co_3O_4 NMs, whereas their simultaneous effect on CO oxidation had not been tested. The catalytic activity was also studied by calculating bandgap energy, representing the minimum energy required to excite an electron up to the conduction band from the valence band. The lowest values were noted for SP800, CH800, and SP650 Co_3O_4 NMs following the order of surface activity

as depicted in Fig. 8E. The values belong to the charge transfer range between heterovalent cobalt ions, which may explain their electron mobility and lattice oxygen activity [52].

The catalytic reaction was further studied by in situ DRIFTS, monitoring species absorbed on the catalysts (Fig. 9). During CO oxidation, the IR results revealed (gas phase) bands of the product CO_2 at 2360 cm^{-1}, as well as peaks of (gas phase) CO at 2170 and 2120 cm^{-1} [53]. The bands in the 1000-1700 cm^{-1} region correspond to various vibrations of adsorbed carbonates, which likely just act as spectators [46]. The SA400 Co_3O_4 NMs showed formation of bridged carbonates at 1629 cm^{-1}, bidentate at 1513 cm^{-1}, and monodentate at 1425, 1317, and 1043 cm^{-1}, while Co_3O_4 NMs synthesized using microalgae extract showed mostly monodentate (1541, 1540, 1450, 1340, 1294, 1290, 1051, 1054, 1050, 1047, 1045, 1043) and bridged carbonates (1153, 1143, 1138, 1136, 11341130, 1111, 1107) [46]. The higher intensity of carbonate formation in SA400 Co_3O_4 NMs is correlated with its high CO_2 production activity, while other Co_3O_4 NMs show less prominent performance with a tendency towards monodentate formation upon higher calcination temperature. When the temperature was increased up to 110°C on SA400 Co_3O_4 NMs (Fig. 9B), carbonate species decreased, whereas more gaseous CO_2 was visible at 2360 cm^{-1}. In

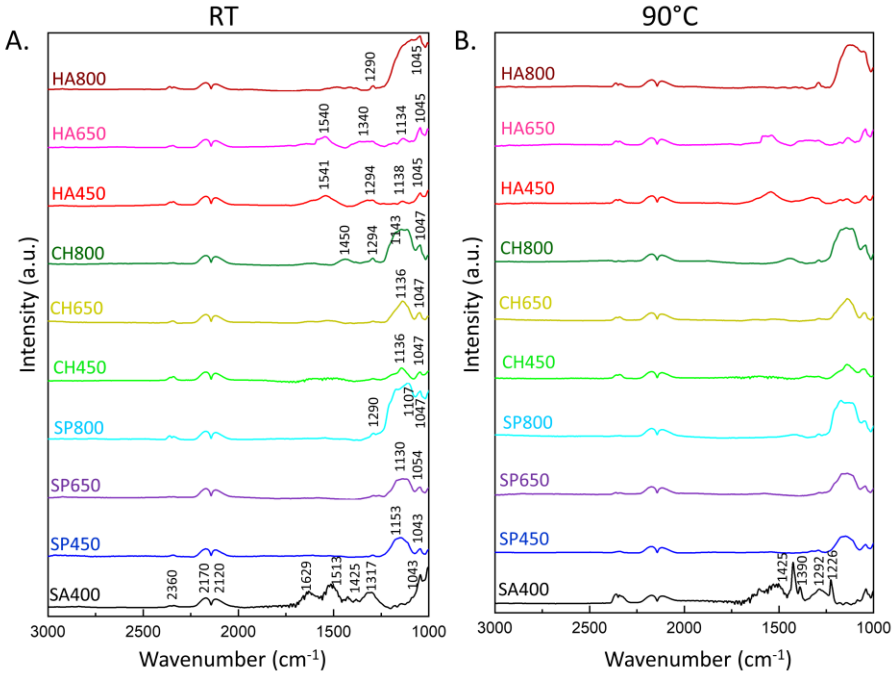

the case of Co_3O_4 NMs synthesized from microalgae, the carbonate species rather remained on the surface, suggesting higher thermal stability.

Figure 20 In-situ DRIFTS spectra of CO oxidation on Co_3O_4 NMs: (A) at room temperature (RT) after 25 minutes of the reaction, (B) at 90°C.

Although the surface area of Co_3O_4 NMs obtained via a biological method was smaller than that of commercial Co_3O_4 NMs, their normalized catalytic activity showed the potential to improve CO oxidation due to microalgal components such as phosphorous or potassium.

4.4 Conclusions

The present study exploited microalgae extracts from three different species and different calcination temperatures for the synthesis of various Co_3O_4 NMs, using commercial spinel Co_3O_4 as reference. The focus was on the relationship between the structure, morphology, composition and CO oxidation activity of Co_3O_4 NMs. The catalyst structure/composition were characterized by XRD, SEM/TEM/EELS, XPS, their reducibility by H_2-TPR, and oxygen species O_2-TPD. Higher calcination temperature caused surface segregation of phosphorous and potassium (originating from the extract), which further modified the properties of Co_3O_4 NMs. The catalysts were tested for CO oxidation, revealing highest activity of commercial Co3O4 NMs. However, when normalized to surface area, the activity of Co_3O_4 NMs from microalgae calcined at high temperature was superior. The presence of phosphorous and potassium increased the catalytic activity despite the previously reported poisoning effect of sodium and chlorine (which were also present). During CO oxidation, in situ DSC and DRIFTS revealed the complexity of interactions between reactants and Co_3O_4 NMs. The low surface area of Co_3O_4 NMs synthesized using microalgae is currently a limiting factor, but future studies of a modified synthesis technique increasing the surface area would yield highly active Co_3O_4 NMs from biological extracts. Overall, the present study demonstrates the potential of microalgae to synthesize nanomaterials with environmentally-friendly properties which can be used for a broad range of applications.

4.5 References

1. Westberg, K.; Cohen, N.; Wilson, K. W. Carbon Monoxide: Its Role in Photochemical Smog Formation. Science (80. 1971, 171 (3975), 1013–1015. https://doi.org/10.1126/SCIENCE.171.3975.1013.

2. Crippa, M.; Solazzo, E.; Guizzardi, D.; Van Dingenen, R.; Leip, A. Air Pollutant Emissions from Global Food Systems Are Responsible for Environmental Impacts, Crop Losses and Mortality. Nat. Food 2022 311 2022, 3 (11), 942–956. https://doi.org/10.1038/s43016-022-00615-7.

3. Wang, L.; Liu, Z.; Yang, H.; Li, H.; Yu, M.; He, T.; Luo, Z.; Liu, F. A Novel Biomass Thermoresponsive Konjac Glucomannan Composite Gel Developed to Control the Coal Spontaneous Combustion: Fire Prevention and Extinguishing Properties. Fuel 2021, 306, 121757. https://doi.org/10.1016/J.FUEL.2021.121757.

4. Yusuf, A. A.; Inambao, F. L. Effect of Cold Start Emissions from Gasoline-Fueled Engines of Light-Duty Vehicles at Low and High Ambient Temperatures: Recent Trends. Case Stud. Therm. Eng. 2019, 14, 100417. https://doi.org/10.1016/J.CSITE.2019.100417.

5. Shere, A.; Subramanian, K. A. Emissions Reduction in an Automotive Compression Ignition Engine Using Hydrogen and Exhaust Gas Recirculation. https://doi.org/10.1080/01430750.2022.2091032 2022, 43 (1), 8220–8238. https://doi.org/10.1080/01430750.2022.2091032.

6. Han, L.; Duan, J.; Qian, D.; Gong, Y.; Wang, Y.; Xie, F.; Su, Y. Research on Homogeneous Charge Compression Ignition Combustion of Intake Port Exhaust Gas Recirculation Based on Cam Drive Hydraulic Variable Valve Actuation Mechanism. Energies 2022, Vol. 15, Page 438 2022, 15 (2), 438. https://doi.org/10.3390/EN15020438.

7. Dien, L. X.; Chinh, H. D.; Nga, N. K.; Luque, R.; Osman, S. M.; Voskressensky, L. G.; Lam, T. D.; Ishida, T.; Murayama, T. Facile Synthesis of Co3O4@SiO2/Carbon Nanocomposite Catalysts from Rice Husk for Low-Temperature CO Oxidation. Mol. Catal. 2022, 518, 112053. https://doi.org/10.1016/J.MCAT.2021.112053.

8. Yigit, N.; Genest, A.; Terloev, S.; Rupprechter, G. Active Sites and Deactivation of Room Temperature CO Oxidation on Co 3 O 4 Catalysts: Combined Experimental and Computational Investigations. J. Phys. Condens. Matter J. Phys. Condens. Matter 2022, 34, 10. https://doi.org/10.1088/1361-648X/ac718b.

9. Rupprechter, G. Operando Surface Spectroscopy and Microscopy during Catalytic Reactions: From Clusters via Nanoparticles to Meso-Scale Aggregates. Small 2021, 17 (27), 2004289. https://doi.org/10.1002/SMLL.202004289.

10. Jiang, B.; Huang, M.; Cai, D.; Tan, K. B.; Zhan, G. Fabrication of Pt/Co3O4 Nanocatalysts Based on Pollen Template for Low-Temperature CO Oxidation. Catal. Commun. 2023, 174, 106597. https://doi.org/10.1016/J.CATCOM.2022.106597.

11. Jamkhande, P. G.; Ghule, N. W.; Bamer, A. H.; Kalaskar, M. G. Metal Nanoparticles Synthesis: An Overview on Methods of Preparation, Advantages and Disadvantages, and Applications. J. Drug Deliv. Sci. Technol. 2019, 53, 101174. https://doi.org/10.1016/J.JDDST.2019.101174.

12. Maqbool, Q.; Yigit, N.; Stöger-Pollach, M.; Ruello, M. L.; Tittarelli, F.; Rupprechter, G. Operando Monitoring of a Room Temperature Nanocomposite Methanol Sensor. Catal. Sci. Technol. 2022. https://doi.org/10.1039/D2CY01395A.

13. Jacob, J. M.; Ravindran, R.; Narayanan, M.; Samuel, S. M.; Pugazhendhi, A.; Kumar, G. Microalgae: A Prospective Low Cost Green Alternative for Nanoparticle Synthesis. Curr. Opin. Environ. Sci. Heal. 2021, 20, 100163. https://doi.org/10.1016/J.COESH.2019.12.005.

14. Al Jahdaly, B. A.; Abu-Rayyan, A.; Taher, M. M.; Shoueir, K. Phytosynthesis of Co3O4Nanoparticles as the High Energy Storage Material of an Activated Carbon/Co3O4Symmetric Supercapacitor Device with Excellent Cyclic Stability Based on a Na2SO4Aqueous Electrolyte. ACS Omega 2022, 7 (27), 23673–23684. https://doi.org/10.1021/acsomega.2c02305.

15. Pollard, M. J.; Weinstock, B. A.; Bitterwolf, T. E.; Griffiths, P. R.; Piers Newbery, A.; Paine, J. B. A Mechanistic Study of the Low-Temperature Conversion of Carbon Monoxide to Carbon Dioxide

over a Cobalt Oxide Catalyst. J. Catal. 2008, 254 (2), 218–225. https://doi.org/10.1016/J.JCAT.2008.01.001.

16. Xie, X.; Li, Y.; Liu, Z. Q.; Haruta, M.; Shen, W. Low-Temperature Oxidation of CO Catalysed by Co3O4 Nanorods. Nat. 2009 4587239 2009, 458 (7239), 746–749. https://doi.org/10.1038/nature07877.

17. Wang, H. F.; Kavanagh, R.; Guo, Y. L.; Guo, Y.; Lu, G.; Hu, P. Origin of Extraordinarily High Catalytic Activity of Co3O4 and Its Morphological Chemistry for CO Oxidation at Low Temperature. J. Catal. 2012, 296, 110–119. https://doi.org/10.1016/J.JCAT.2012.09.005.

18. Teng, Y.; Kusano, Y.; Azuma, M.; Haruta, M.; Shimakawa, Y. Morphology Effects of Co3O4 Nanocrystals Catalyzing CO Oxidation in a Dry Reactant Gas Stream. Catal. Sci. Technol. 2011, 1 (6), 920–922. https://doi.org/10.1039/C1CY00113B.

19. Wu, R. C.; Tang, C. W.; Chang, M. B.; Chang, C. C.; Wang, C. C.; Wang, C. Bin. Morphology-Controlled Fabrication of Co3O4 Catalysts and Performance Towards Low Temperature CO Oxidation. Catal. Letters 2020, 150 (12), 3523–3532. https://doi.org/10.1007/s10562-020-03249-1.

20. Fuchigami, T.; Kimata, R.; Haneda, M.; Kakimoto, K. I. Complex Three-Dimensional Co3O4 Nano-Raspberry: Highly Stable and Active Low-Temperature CO Oxidation Catalyst. Nanomater. 2018, Vol. 8, Page 662 2018, 8 (9), 662. https://doi.org/10.3390/NANO8090662.

21. Lukashuk, L.; Yigit, N.; Rameshan, R.; Kolar, E.; Teschner, D.; Hävecker, M.; Knop-Gericke, A.; Schlögl, R.; Föttinger, K.; Rupprechter, G. Operando Insights into CO Oxidation on Cobalt Oxide Catalysts by NAP-XPS, FTIR, and XRD. ACS Catal. 2018, 8 (9), 8630–8641. https://doi.org/10.1021/acscatal.8b01237.

22. Lou, Y.; Wang, L.; Zhao, Z.; Zhang, Y.; Zhang, Z.; Lu, G.; Guo, Y.; Guo, Y. Low-Temperature CO Oxidation over Co3O4-Based Catalysts: Significant Promoting Effect of Bi2O3 on Co3O4 Catalyst. Appl. Catal. B Environ. 2014, 146, 43–49. https://doi.org/10.1016/J.APCATB.2013.06.007.

23. Wang, L.; Hu, W.; Shang, Z.; Cao, X.; Guo, Y.; Li, J.; Gu, Q.; Li, K.; Li, X. Regulating Potassium State to Enable the High Performance of Co3O4 for Catalytic Oxidation. Fuel 2023, 335, 126968. https://doi.org/10.1016/J.FUEL.2022.126968.

24. Huang, Y.; Lv, D.; Zhang, G.; Cai, Y.; Li, Q.; Wang, H.; Ma, Z. Phosphorization-Introduced Defect-Rich Phosphorus-Doped Co3O4with Propelling Adsorption-Catalysis Transformation of Polysulfide. Energy and Fuels 2022, 36 (6), 3339–3346. https://doi.org/10.1021/acs.energyfuels.1c04427.

25. Li, M.; Bi, F.; Xu, Y.; Hao, P.; Xiang, K.; Zhang, Y.; Chen, S.; Guo, J.; Guo, X.; Ding, W. Effect of Residual Chlorine on the Catalytic Performance of Co3O4 for CO Oxidation. ACS Catal. 2019, 9 (12), 11676–11684. https://doi.org/10.1021/acscatal.9b03797.

26. Tang, W.; Weng, J.; Lu, X.; Wen, L.; Suburamanian, A.; Nam, C. Y.; Gao, P. X. Alkali-Metal Poisoning Effect of Total CO and Propane Oxidation over Co3O4 Nanocatalysts. Appl. Catal. B Environ. 2019, 256, 117859. https://doi.org/10.1016/J.APCATB.2019.117859.

27. Silva, S. C.; Ferreira, I. C. F. R.; Dias, M. M.; Filomena Barreiro, M. Microalgae-Derived Pigments: A 10-Year Bibliometric Review and Industry and Market Trend Analysis. Mol. 2020, Vol. 25, Page 3406 2020, 25 (15), 3406. https://doi.org/10.3390/MOLECULES25153406.

28. Sandgruber, F.; Gielsdorf, A.; Baur, A. C.; Schenz, B.; Müller, S. M.; Schwerdtle, T.; Stangl, G. I.; Griehl, C.; Lorkowski, S.; Dawczynski, C. Variability in Macro- and Micronutrients of 15 Commercially Available Microalgae Powders. Mar. Drugs 2021, Vol. 19, Page 310 2021, 19 (6), 310. https://doi.org/10.3390/MD19060310.

29. Lu, J.; Ren, D. F.; Xue, Y. L.; Sawano, Y.; Miyakawa, T.; Tanokura, M. Isolation of an Antihypertensive Peptide from Alcalase Digest of Spirulina Platensis. J. Agric. Food Chem. 2010, 58 (12), 7166–7171. https://doi.org/10.1021/JF100193F.

30. Marzorati, S.; Schievano, A.; Idà, A.; Verotta, L. Carotenoids, Chlorophylls and Phycocyanin from Spirulina: Supercritical CO2 and Water Extraction Methods for Added Value Products Cascade. Green Chem. 2020, 22 (1), 187–196. https://doi.org/10.1039/C9GC03292D.

31. Sukhikh, S.; Prosekov, A.; Ivanova, S.; Maslennikov, P.; Andreeva, A.; Budenkova, E.; Kashirskikh, E.; Tcibulnikova, A.; Zemliakova, E.; Samusev, I.; Babich, O. Identification of Metabolites with Antibacterial Activities by Analyzing the FTIR Spectra of Microalgae. Life 2022, 12 (9), 1395. https://doi.org/10.3390/life12091395.

32. Tokarz, D.; Cisek, R.; El-Ansari, O.; Espie, G. S.; Fekl, U.; Barzda, V. Organization of Astaxanthin within Oil Bodies of Haematococcus Pluvialis Studied with Polarization-Dependent Harmonic Generation Microscopy. PLoS One 2014, 9 (9), e107804. https://doi.org/10.1371/JOURNAL.PONE.0107804.

33. Poonguzhali, R. V.; Kumar, E. R.; Srinivas, C.; Alshareef, M.; Aljohani, M. M.; Keshk, A. A.; El-Metwaly, N. M.; Arunadevi, N. Natural Lemon Extract Assisted Green Synthesis of Spinel Co3O4 Nanoparticles for LPG Gas Sensor Application. Sensors Actuators B Chem. 2023, 377, 133036. https://doi.org/10.1016/J.SNB.2022.133036.

34. Khalid, N. R.; Gull, A.; Ali, F.; Tahir, M. B.; Iqbal, T.; Rafique, M.; Assiri, M. A.; Imran, M.; Alzaid, M. Bi-Functional Green-Synthesis of Co3O4 NPs for Photocatalytic and Electrochemical Applications. Ceram. Int. 2022, 48 (21), 32009–32021. https://doi.org/10.1016/J.CERAMINT.2022.07.138.

35. Makhlouf, S. A.; Bakr, Z. H.; Aly, K. I.; Moustafa, M. S. Structural, Electrical and Optical Properties of Co3O4 Nanoparticles. Superlattices Microstruct. 2013, 64, 107–117. https://doi.org/10.1016/J.SPMI.2013.09.023.

36. Tharasan, P.; Somprasong, M.; Kenyota, N.; Kanjana, N.; Maiaugree, W.; Jareonboon, W.; Laokul, P. Preparation and Electrochemical Performance of Nanostructured Co3O4 Particles. J. Nanoparticle Res. 2022, 24 (6), 1–14. https://doi.org/10.1007/s11051-022-05509-0.

37. Al-Ghouti, M. A.; Da'ana, D. A. Guidelines for the Use and Interpretation of Adsorption Isotherm Models: A Review. J. Hazard. Mater. 2020, 393, 122383. https://doi.org/10.1016/J.JHAZMAT.2020.122383.

38. Lü, Y.; Zhan, W.; He, Y.; Wang, Y.; Kong, X.; Kuang, Q.; Xie, Z.; Zheng, L. MOF-Templated Synthesis of Porous Co3O4 Concave Nanocubes with High Specific Surface Area and Their Gas Sensing Properties. ACS Appl. Mater. Interfaces 2014, 6 (6), 4186–4195. https://doi.org/10.1021/am405858v.

39. Zhao, Y.; Feltes, T. E.; Regalbuto, J. R.; Meyer, R. J.; Klie, R. F. In Situ Electron Energy Loss Spectroscopy Study of Metallic Co and Co Oxides. J. Appl. Phys. 2010, 108 (6), 063704. https://doi.org/10.1063/1.3482013.

40. Barreca, D.; Gasparotto, A.; Lebedev, O. I.; MacCato, C.; Pozza, A.; Tondello, E.; Turner, S.; Van Tendeloo, G. Controlled Vapor-Phase Synthesis of Cobalt Oxide Nanomaterials with Tuned Composition and Spatial Organization. CrystEngComm 2010, 12 (7), 2185–2197. https://doi.org/10.1039/B926368N.

41. Zhuang, L.; Jia, Y.; He, T.; Du, A.; Yan, X.; Ge, L.; Zhu, Z.; Yao, X. Tuning Oxygen Vacancies in Two-Dimensional Iron-Cobalt Oxide Nanosheets through Hydrogenation for Enhanced Oxygen Evolution Activity. Nano Res. 2018, 11 (6), 3509–3518. https://doi.org/10.1007/s12274-018-2050-8.

42. Zhu, H.; Song, X.; Han, X.; Zhang, X.; Bao, J.; Zhang, N.; He, G. Co3O4Nanosheets Preferentially Growing (220) Facet with a Large Amount of Surface Chemisorbed Oxygen for Efficient Oxidation of Elemental Mercury from Flue Gas. Environ. Sci. Technol. 2020, 54 (14), 8601–8611. https://doi.org/10.1021/acs.est.0c03427.

43. Choya, A.; De Rivas, B.; Gutiérrez-Ortiz, J. I.; López-Fonseca, R. On the Effect of the Synthesis Route of the Support in Co3O4/CeO2 Catalysts for the Complete Oxidation of Methane. Ind. Eng. Chem. Res. 2022, 2022, 17854–17865. https://doi.org/10.1021/acs.iecr.2c03245.

44. Lukashuk, L.; Yigit, N.; Li, H.; Bernardi, J.; Föttinger, K.; Rupprechter, G. Operando XAS and NAP-XPS Investigation of CO Oxidation on Meso- and Nanoscale CoO Catalysts. Catal. Today 2019, 336, 139–147. https://doi.org/10.1016/J.CATTOD.2018.12.052.

45. Bekiaris, G.; Peltre, C.; Jensen, L. S.; Bruun, S. Using FTIR-Photoacoustic Spectroscopy for Phosphorus Speciation Analysis of Biochars. Spectrochim. Acta Part A Mol. Biomol. Spectrosc. 2016, 168, 29–36. https://doi.org/10.1016/J.SAA.2016.05.049.

46. Ahmed, I.; Wageh, S.; Rehman, W.; Iqbal, J.; Mir, S.; Al-Ghamdi, A.; Khalid, M.; Numan, A. Evaluation of the Synergistic Effect of Graphene Oxide Sheets and Co3O4 Wrapped with Vertically Aligned Arrays of Poly (Aniline-Co-Melamine) Nanofibers for Energy Storage Applications. Polym. 2022, Vol. 14, Page 2685 2022, 14 (13), 2685. https://doi.org/10.3390/POLYM14132685.

47. Feng, B.; Shi, M.; Liu, J.; Han, X.; Lan, Z.; Gu, H.; Wang, X.; Sun, H.; Zhang, Q.; Li, H.; Wang, Y.; Li, H. An Efficient Defect Engineering Strategy to Enhance Catalytic Performances of Co3O4 Nanorods for CO Oxidation. J. Hazard. Mater. 2020, 394, 122540. https://doi.org/10.1016/J.JHAZMAT.2020.122540.

48. Wang, X.; Li, X.; Mu, J.; Fan, S.; Chen, X.; Wang, L.; Yin, Z.; Tadé, M.; Liu, S. Oxygen Vacancy-Rich Porous Co3O4 Nanosheets toward Boosted NO Reduction by CO and CO Oxidation: Insights into the Structure-Activity Relationship and Performance Enhancement Mechanism. ACS Appl. Mater. Interfaces 2019, 11 (45), 41988–41999. https://doi.org/10.1021/acsami.9b08664.

49. Kersell, H.; Hooshmand, Z.; Yan, G.; Le, D.; Nguyen, H.; Eren, B.; Wu, C. H.; Waluyo, I.; Hunt, A.; Nemšák, S.; Somorjai, G.; Rahman, T. S.; Sautet, P.; Salmeron, M. CO Oxidation Mechanisms on CoOx-Pt Thin Films. J. Am. Chem. Soc. 2020. https://doi.org/10.1021/jacs.0c01139.

50. Gao, Q.; Li, H.; Wang, X.; Han, B.; Xia, K.; Wu, J.; Zhou, C.; Dong, J. Doping Phosphorus into Co3O4: A New Promising Pathway to Boost the Catalytic Activity for Peroxymonosulfate Activation. Appl. Surf. Sci. 2022, 574, 151632. https://doi.org/10.1016/J.APSUSC.2021.151632.

51. Song, L.; Liu, Y.; Zhang, S.; Zhou, C.; Ma, K.; Yue, H. Tuning Oxygen Vacancies of the Co3O4Catalyst through an Ethanol-Assisted Hydrothermal Method for Low-Temperature CO Oxidation. Ind. Eng. Chem. Res. 2022, 61 (40), 14783–14792. https://doi.org/10.1021/acs.iecr.2c01183.

52. Qiao, L.; Xiao, H. Y.; Meyer, H. M.; Sun, J. N.; Rouleau, C. M.; Puretzky, A. A.; Geohegan, D. B.; Ivanov, I. N.; Yoon, M.; Weber, W. J.; Biegalski, M. D. Nature of the Band Gap and Origin of the Electro-/Photo-Activity of Co3O4. J. Mater. Chem. C 2013, 1 (31), 4628–4633. https://doi.org/10.1039/c3tc30861h.

53. Zhang, Q.; Mo, S.; Li, J.; Sun, Y.; Zhang, M.; Chen, P.; Fu, M.; Wu, J.; Chen, L.; Ye, D. In Situ DRIFT Spectroscopy Insights into the Reaction Mechanism of CO and Toluene Co-Oxidation over Pt-Based Catalysts. Catal. Sci. Technol. 2019, 9 (17), 4538–4551. https://doi.org/10.1039/C9CY00751B.

Chapter 5

Photocatalytic activity of silver nanoparticles synthesized from microalgae against Brilliant Blue R dye

5.1 Optimization of Brilliant Blue R photocatalytic degradation by silver nanoparticles synthesized using *C. vulgaris*

5.1.1 Introduction

The discharge of dyes from various industries into waterbodies is a major source of environmental pollution, which can affect aquatic biota as well as humans. It is estimated that more than 700000 tons of synthetic dyes are produced annually, with about 15% released to the environment after processing [1]. Once released into a water body, dyes can block solar light penetration, which reduces photosynthetic activity and inhibits the growth of aquatic biota [2]. In addition, due to their recalcitrant nature, they are resistant to degradation, resulting in prolonged exposure and accumulation in living organisms [3]. As a result, they can cause allergies, skin irritation, respiratory disorders, mutagenicity, and carcinogenicity [4]. Therefore, it is crucial to apply the proper wastewater treatment method before their discharge.

One of the dyes commonly used in the laboratory is Brilliant Blue R (BBR), known for its intense blue colour, often utilized for protein gel staining to visualize and analyze protein bands. It belongs to the class of triphenylmethane dyes, which contain three phenyl rings linked to a central carbon atom [5]. In its structure, conjugated double bonds in the aromatic rings enable electron delocalization with resonance stabilization, which allows electronic charge distribution and prevents the formation of reactive sites [6]. Combined with a lack of highly labile functional groups, the removal of BBR requires specialized techniques for its degradation [7].

In an attempt to discover economical and environmentally friendly treatment, several biological methods have been researched [8]. The mechanism behind it involves the use of enzymes found in the cell structures of microorganisms [9]. However, the treatment requires a longer time in a controlled, optimally favorable environment. Another common method is adsorption, which involves the adhesion of dye molecules into adsorbent through physical or chemical interactions [9]. While short reaction time is the advantage of using materials such as activated carbon or zeolites, the pollutants are collected and transferred, but not eliminated from the environment [9]. A different method, combining both high efficiency and short time, is the use of advanced oxidation processes (AOPs) based on the production of hydroxyl free radicals with high oxidizing ability.

Photocatalysis has emerged as a promising method utilizing light energy to generate reactive oxygen species (ROS) that can degrade the dye into less toxic substances [10]. Among various photocatalysts, silver nanoparticles (Ag NPs) have attracted attention due to their strong light absorption in the visible region and prominent activity [11]. Moreover, their synthesis process can be sustainable and environmentally friendly when the metabolites from organisms are used as reducing and stabilizing agents [12]. One of the organisms investigated for the synthesis of nanoparticles is microalgae, owing to their rapid biomass increase and abundance of valuable metabolites. The study by Rajkumar et al. showed the potential of Ag NPs from Chlorella vulgaris to photocatalyse methylene blue dye under sunlight irradiation [13], however, to the best of our knowledge, the activity of Ag NPs from *C. vulgaris* extract against BBR dye has not been assessed so far.

From the perspective of the significance of biological synthesis, the *C. vulgaris* methanolic extract was utilized to synthesize Ag NPs. The material was also calcined to determine the influence of its organic content on the structure and activity. The product was tested for the first time for photocatalytic degradation of BBR dye in visible light considering the influence of various parameters such as light intensity, dye concentration, catalyst concentration, pH, or presence of organic content on the photocatalytic action. Herein, the material characteristics-to-

photocatalytic performances are evaluated, and the degradation mechanisms are explored for the optimization of the removal of hazardous BBR dye from the environment.

5.1.2 Material and methods

5.1.2.1 Synthesis of nanoparticles

The *Chlorella vulgaris* (CCALA 902) culture was grown in BBM medium supplemented with 60 mM $NaHCO_3$ with stirring and irradiation of 58W fluorescent lamps (Osram®) with 60 µmol*m-2*s-1 photon flux. The culture was kept for 30 days to acquire an adequate quantity of biomass. Then, it was centrifuged at 1500 RPM at 4 °C (Heraeus® Megafuge® 1.0R) to remove the medium, and the algal biomass was dried at room temperature.

In the next step, 0.9 g of dried residue was mixed with 54 mL of methanol (Merck® LiChrosolv® hypergrade). The flask was sonicated for 30 min (Soltec® Sonica® 2400 ETH S3) followed by stirring at 250 RPM (IKA® RH Digital Magnetic Stirrer) for the next 30 min to break down the cell walls and release the metabolites into the solvent. The leftover biomass was removed by filtration using standard filtration paper (Whatman®) and then the liquid was evaporated using a rotary evaporator (BUCHI Rotavapor™ R-210 Rotary Evaporator System) to discard about 70% of methanol. The concentrated extract was diluted with MiliQ H_2O (Millipore®, Milan, Italy) to the final volume of 180 mL and it was used for the Ag NPs synthesis process.

For Ag NPs synthesis procedure, the prepared extract was heated to 85°C and stirred at 250 RPM (IKA® RH Digital Magnetic Stirrer). When the temperature of the extract reached 85°C, 0.1 M of silver nitrate (Carlo Erba®) was added, and after 15 min pH of the solution was increased up to 8 using 1.25 M NaOH. Starting from the moment of silver nitrate addition, the reaction continued for 1.5 h and then it was removed from the hot plate stirrer for maturation at room temperature. Then, the liquid was centrifuged at 4000 RPM at 8°C (Heraeus® Megafuge® 1.0R) followed by the repeated washing of the residue in the two washing cycles with MiliQ H2O (Millipore®, Milan, Italy). Next, Ag NPs were dried at 80°C for 24 h, ground using mortar and pestle, and divided into two parts. One part was stored in an Eppendorf tube in the absence of light (before calcination – Ag NPs BC) and the other was calcined in a muffle furnace (Gelman Instrument®) for 2 h at 600°C

(after calcination – Ag NPs AC). After the calcination procedure, all the samples were stored in the same conditions.

5.1.2.2 Characterization

The structure of Ag NPs was studied by X-Ray Diffraction (XRD) using X-Ray Diffractometer (D8 Advance, Bruker AXS®). The scanning was performed with a diffraction angle between 12° and 90° at 0.1° per 10 s, at 40 kV and 30 mA using CuKα (λ =1.54 Å) radiation. The existing phases in obtained Ag NPs were identified by using Diffrac.Eva software v.6.1.0.4 according to the COD database. The crystallite size was calculated from Debye-Scherrer's formula after baseline correction.

Functional groups and important bonds existing in the Ag NPs were determined by Fourier-Transform Infrared Spectroscopy (FTIR) using FT/IR-6700 (Jasco, Tokyo, Japan) in the range of 500-4000 cm^{-1}.

The surface morphology of prepared Ag NPs was studied by Scanning Electron Microscopy (SEM) using Hitachi S4000 FEG HRSEM (Hitachi Ltd., Tokyo, Japan) operated at 20 kV. The image acquisition was performed with Quartz PCI software (Quartz Imaging Corporation, Vancouver, Canada). Prior SEM analysis, the samples were coated with 2 nm of platinum to enhance the contrast. The composition assessment of Ag NPs was examined through EDX analysis using UltraDry EDX Detector (Thermo Fisher Scientific®, Madison, Wisconsin, USA), and NSS3 software (Thermo Fisher Scientific®, Madison, Wisconsin, USA).

Thermal properties of Ag NPs were studied with Thermogravimetric Analysis (TGA) using Differential Thermal Analyzer TG/DSC (NETZSCH® STA 409 PC) with airflow 100 mL/min and in a heating range 25– 1000°C at 10°C/min.

The optical properties were examined by UV-Vis absorption measurements using CARY 50 spectrophotometer (Varian Inc., Australia) with a cell path length of 10 mm in the wavelength range of 200–750 nm. The direct bandgap energy was calculated from the Tauc relation (Equation 1):

$$(\alpha h\nu)^2 = (h\nu - E_g) \quad (1)$$

Where α is the molar extinction coefficient, h is the Plank's constant, v is the light frequency, and Eg is the band gap energy. The bandgap energy was calculated by linear fit extrapolation of the plot of $(\alpha hv)^2$ against energy.

5.1.2.3 In-situ photocatalysis

The scheme of the in-situ photocatalytic setup is shown in Fig. 21. First, calibration line was obtained by assessing the correlation between absorbance and concentration of the dye. Before testing Ag NPs photocatalytic abilities, they were combined with 50 mL of ddH_2O and sonicated for 15 min in a sonication bath (Soltec® Sonica® 2400 ETH S3) to ensure even dispersion. First, the baseline of the dispersed Ag NPs solution was created. Next, the solution was mixed with different concentrations of BBR dye (Sigma-Aldrich®) in ethanol (500 mg/L). The flask was stirred constantly for 30 minutes without any exposure to light to achieve reaction equilibrium. Then, the light was switched on and the irradiation by a warm white 10.5 W LED bulb (Phillips) was measured with a luxmeter (HD2302.0 Delta-Ohm, Padua, Italy). The emission spectrum of the radiation source as supplied by the manufacturer is shown in Fig. 22. The liquid was flowing continuously between the flask and a 10 mm flow-through cuvette attached to the UV-Vis Spectrophotometer (Cary 50, Varian®). The measurements were conducted in the range of 400-750 nm every 10 minutes. The experiments with the highest degradation efficiency were performed in triplicate to accurately evaluate the photocatalytic potential of the material.

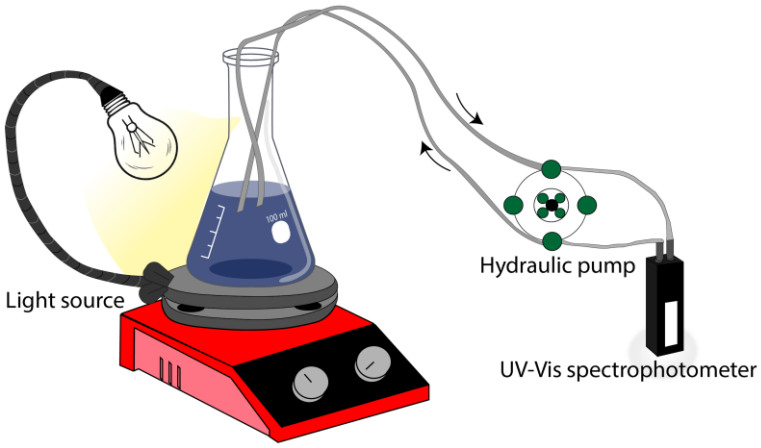

Figure 21 Photocatalytic setup

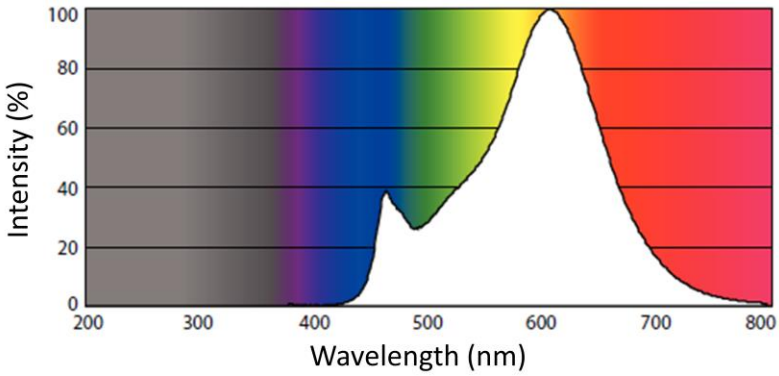

Figure 22 Emission spectrum of the light source provided by manufacturer.

The efficiency of the BBR dye degradation by Ag NPs was calculated as (Equation 2):

$$Degradation\ efficiency\ (\%) = 100 - \left({}^{C}/_{C_0} \cdot 100\right) \quad (2)$$

where C_0 is the initial BBR dye concentration, and C is the final concentration of the dye at the end of the degradation period.

The obtained data were fit using OriginPro 2021© 9.8 according to the pseudo-first order reaction model according to the Equation 3:

$$C = C_0 * e^{-{}^{k}/_{t}} \quad (3)$$

Where t is time and k (min^{-1}) is the reaction constant.

5.1.3 Results and discussion

5.1.3.1 Characterization

The XRD analysis was performed to determine the purity and crystallinity of the synthesized Ag NPs (Fig. 23A). The results of the analysis confirmed the presence of a highly pure and crystalline material, indicating a successful synthesis process. The identified phases in Ag NPs BC belong mostly to Ag_2O (COD 1010486) and Ag (COD 1100136) with low intensity peaks in 19-20° corresponding to Ag_2CO_3 (COD 4318190 and COD 4318187). After calcination, Ag NPs AC show the presence of only Ag phase (COD 9012961), which suggests the important role of organic content in stabilizing Ag NPs structure. Based on the XRD results, full width at half maximum

(FWHM) values were calculated and used for Debye-Scherrer's formula. The crystalline size for Ag NPs BC was determined as 16.44 nm for Ag_2O and 15.70 nm for Ag with the average size of 16.07 nm. Calcination increased the crystalline size of Ag NPs AC to 24.61 nm.

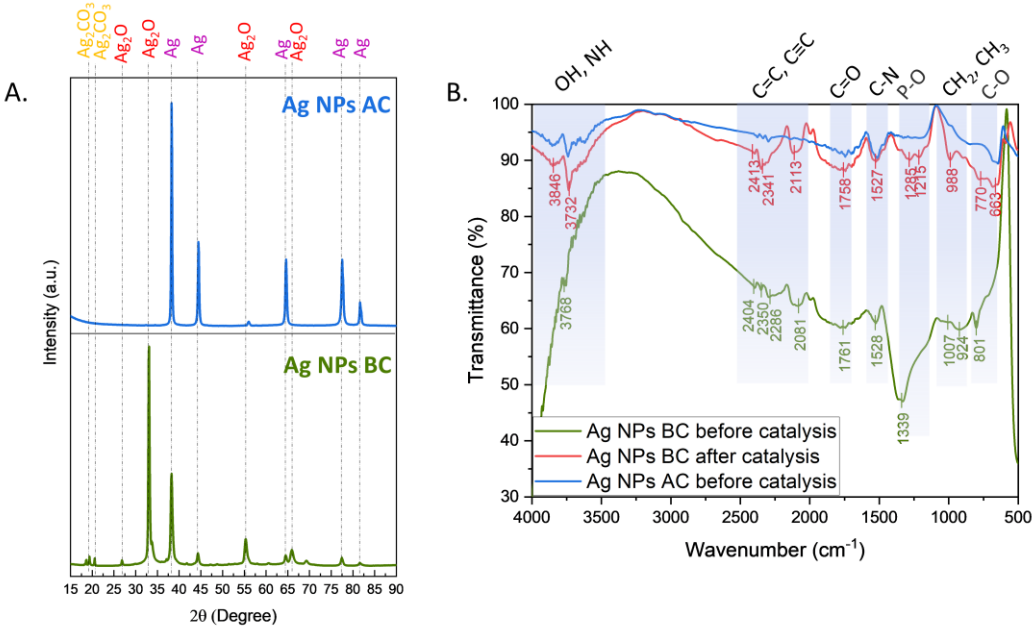

Figure 23 Crystallographic and spectroscopic analyses (A) XRD, (B) FTIR, BC – before calcination, AC – after calcination.

The reported Ag NPs synthesized using *C. vulgaris* utilized water as a solvent to extract metabolites and resulted in the formation of only Ag phase in their structure [13–15]. The methanolic extract of *C. vulgaris* was studied previously for its high antioxidant activity owing to the presence of phenolic and flavonoids constituents as compared to the standard ascorbic acid [16]. The current results show the potential of *C. vulgaris* to obtain a variety of materials depending on composition of the solution to which the metal precursor is added. The organic content was further examined by FTIR analysis.

The FTIR technique was applied to study the behavior of the capping agents on Ag NPs before and after synthesis as well as before and after calcination (Fig. 23B). The results revealed an abundance of functional groups originating from the *C. vulgaris* extract such as OH, NH, C=C, C≡C, C=O, C-N, P-O, CH_2, CH_3, and C-O with the highest intensity before calcination [17–19]. After catalysis, the wavenumber values of the peaks shifted, which might be correlated with changes

in the structure or organic molecules due to the interactions with radicals generated upon light irradiation. Moreover, the intensity of the peaks increased which further proves the active participation of the capping compounds in the photocatalytic process. The calcination process significantly increased the intensity of the peaks to around 95% which proves the efficient removal of organic content from the Ag NPs surface.

The morphology of the obtained Ag NPs was observed using SEM-EDX analyses (Fig. 24). The Ag NPs BC exhibit irregular shapes with oval and ellipsoidal shapes. The elemental analysis revealed the presence of silver, oxygen, carbon, phosphorous, and sulfur in the structure with homogenic distribution. The Ag NPs AC show the tendency to agglomeration or coalescence with more oval shape. The calcination resulted in the removal of sulfur from the Ag NPs while phosphorus remained as a part of their structure. Similarly, all detected elements show homogeneous distribution. Partial removal of organic content from Ag NPs changed the morphology of the material which further proves the important role of organic content in stabilizing the structure and preventing agglomeration.

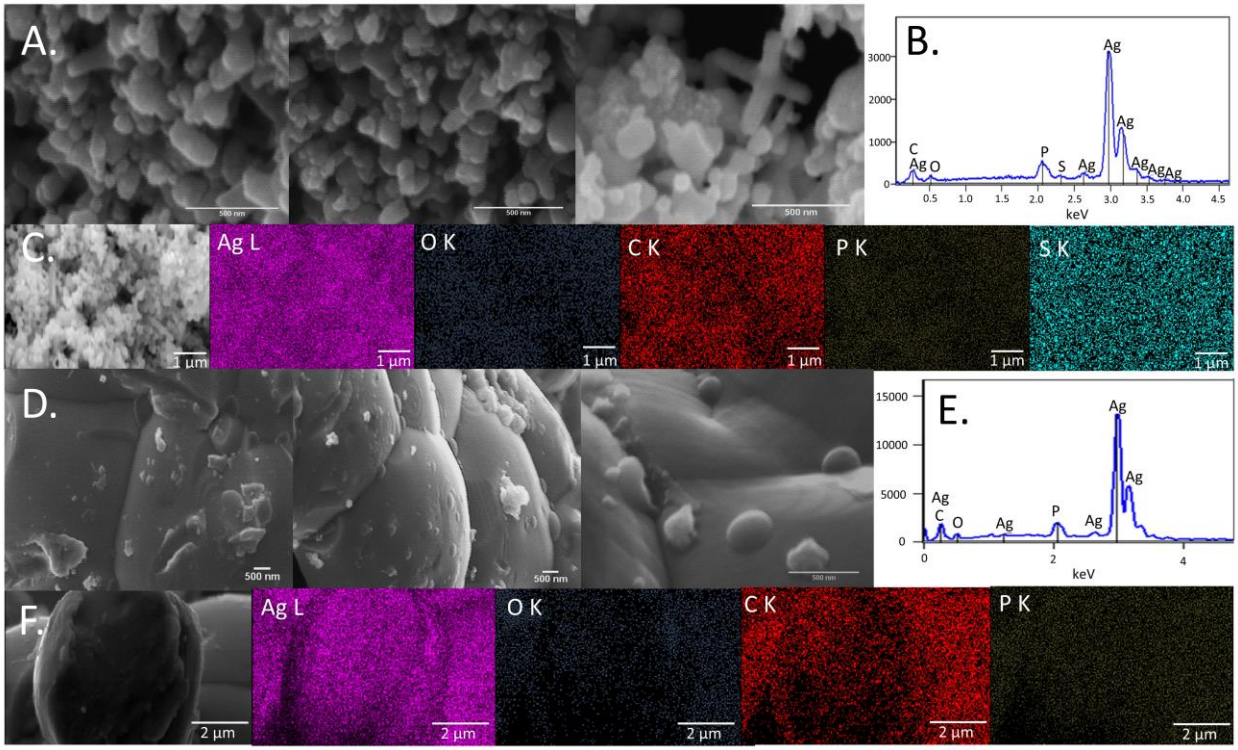

Figure 24 Microscopy analysis, (A) SEM of Ag NPs BC, (B) EDX spectrum of Ag NPs BC, (C) EDX mappings of Ag NPs BC, (D) SEM of Ag NPs AC, (E) EDX spectrum of Ag NPs AC, (F) EDX mappings of Ag NPs AC.

Thermal properties of the Ag NPs were assessed by TGA analysis (Fig. 25A-C). For Ag NPs BC two major weight losses can be observed: in the 25 - 300°C and 300 - 600°C. The first weight loss with DTG peak at 161°C resulting in the loss of 28.5% weight can be attributed to the water loss and decomposition of the temperature-sensitive organic compounds. The second weight loss with DTG peak at 403°C led to decrease of 7.3% of the weight which is probably due to the decomposition of the phenolic compounds present on Ag NPs BC surface [20]. Further increase in temperature did not change the weight significantly with final weight at around 65%. In addition, DTA analysis proved the exothermic nature of the decomposition of the organic compounds described previously with an endothermic peak at 960°C indicating the melting point of silver [21].

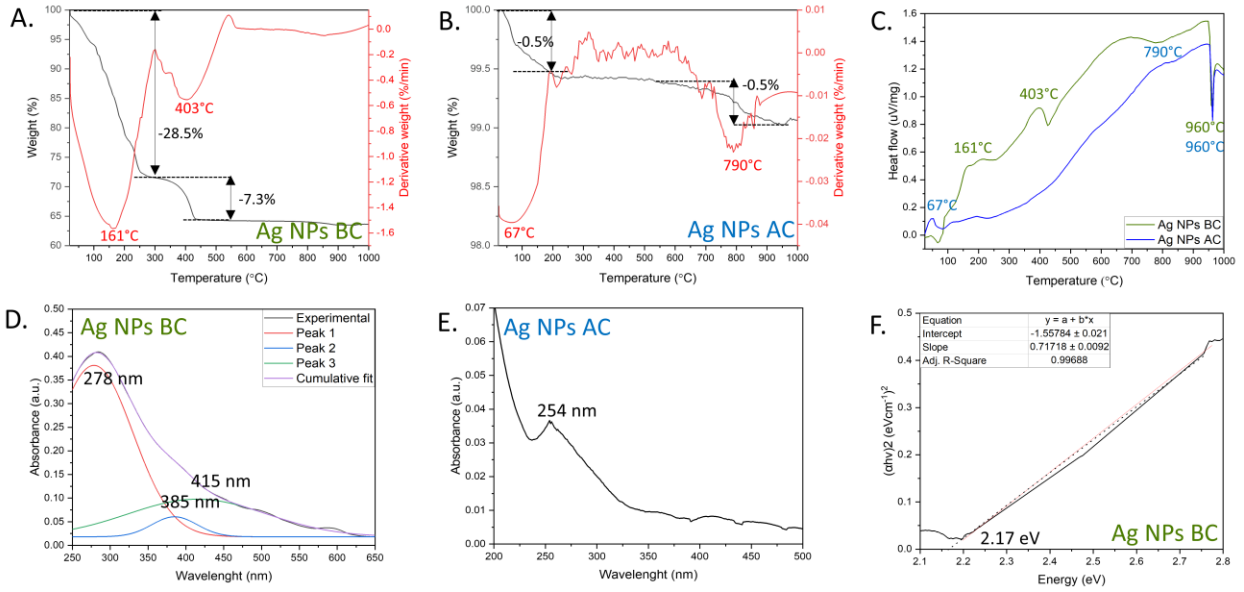

Figure 25 Thermal and optical properties of Ag NPs, (A) TG and DTG of Ag NPs BC, (B) TG and DTG of Ag NPs AC, (C) DTA of Ag NPs BC and Ag NPs AC, (D) UV-Vis spectrum of Ag NPs BC, (E) UV-Vis spectrum of Ag NPs AC, (F) Tauc plot of Ag NPs BC.

The Ag NPs AC subjected to the same analysis show much smaller weight loss. In the 25 - 200°C the weight decreased by 0.5% with DTG peak at 67°C which can be attributed to the physically adsorbed water molecules or oxidation of the remaining organic content on the Ag NPs AC surface [20]. The next weight loss occurred at around 700 - 900°C with the decrease of 0.5% and DTG peak at 790°C which is probably due to the decarbonization [22]. At the end of the measurements, the final weight was recorded at around 99%. Similarly to Ag NPs BC, the reactions were exothermic with endothermic melting silver point at 960°C. Overall, the results show the high organic content of Ag NPs BC in comparison with Ag NPs AC which supports the FTIR and EDX findings.

The optical properties of Ag NPs were studied by applying UV-Vis spectroscopy (Fig. 25D-E). Upon light excitation at specific wavelength, electrons in the conduction band undergo a collective oscillation known as a surface plasmon resonance. The effect results in the strong scattering and absorption of light and can be an indicator of the potential photocatalytic activity. The UV-Vis spectrum of Ag NPs BC shows a broad absorbance band which after deconvolution reveals the presence of three separate peaks. The peaks at 278 nm and 385 nm probably belong to the

metabolites present on the surface. The presence of additional peaks in the UV-Vis spectrum due to the activity of organic molecules has been observed before [23]. The characteristic surface plasmon resonance of Ag NPs was detected at 415 nm and it is consistent with the literature with values recorded in the 400 – 500 nm range [24]. Furthermore, the Ag NPs BC can be photoactivated in the visible light spectrum.

After calcination, the absorbance values significantly decreased which might be the effect of the structural defects and change in the electronic structure induced by high temperature. The peak at 254 nm of Ag NPs AC is attributed to the electronic transition to metallic Ag [25] which is consistent with the phase transition observed in XRD analysis. Thus, high temperature treatment impaired the photocatalytic activity of Ag NPs.

Based on the UV-Vis spectrum, the band gap energy of Ag NPs BC was calculated (Fig. 25F). The parameter is defined as an energy difference between the highest occupied energy state of electrons in the valence band and the lowest unoccupied state of the conduction band. It determines the ability of the material to absorb light, generate electron-hole pairs, and initiate a photocatalytic reaction. The band gap energy of Ag NPs BC was calculated at 2.17 eV and similar band gap values were reported previously [26].

5.1.3.2 Photocatalytic activity

5.1.3.2.1 Influence of light

The dye degradation activity of Ag NPs BC was first assessed in the dark conditions (Fig. 26). The results show a slight decrease in the dye concentration, however, after an initial 30 minutes the concentration stabilizes and starts to reach equilibrium. The interactions between dye and Ag NPs BC are due to physisorption mainly due to the weak van der Waals forces [27]. At the end of the experiment, around 10% of the dye was degraded and k value was measured at k = 0.00118 min^{-1}. Based on the obtained results, the next experiments were performed after 30 min in dark conditions to allow the reaction to reach equilibrium and more precisely access the effect of various factors on the photocatalytic performance of Ag NPs.

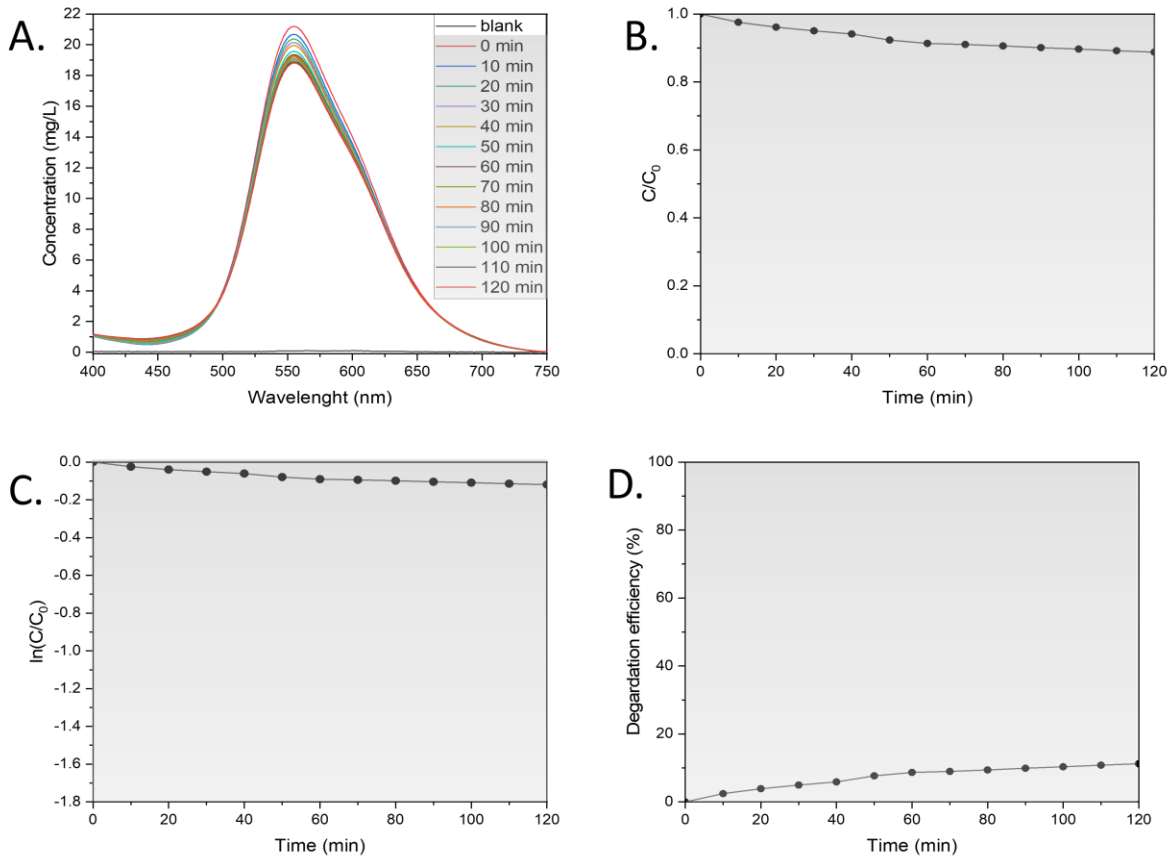

Figure 26 Degradation of BBR dye in the dark (A) UV–Vis spectral changes for the degradation of dye, (B) changes in dye concentration, (C) pseudo-first-order kinetic plot, (D) percentage degradation efficiency.

The first factor tested for photocatalytic activity was light intensity. In photocatalyst, the generation of electron and hole pairs is dependent upon the intensity or strength of the light that is directed onto it. When the intensity of light increases, there is a corresponding increase in the transfer of electrons from the valence band to the conduction band [28]. This leads to an amplified generation of hydroxyl or oxygen radicals playing a crucial role in the degradation of organic molecules [28]. The concentration of BBR dye was measured in three different light intensities 75, 150, and 300 µmol/m^2/s (Fig. 27).

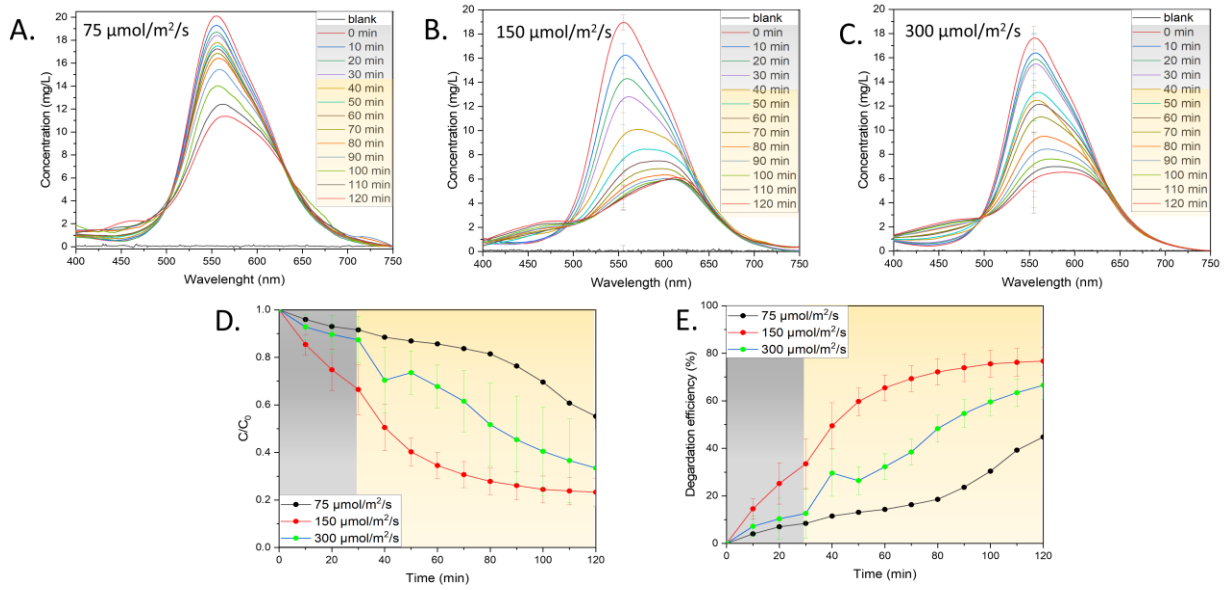

Figure 27 Influence of light on the photocatalytic activity (A-C) UV–Vis spectral changes in the varying light irradiation, (D) changes in dye concentration, (E) percentage degradation efficiency.

The lowest tested light intensity (75 µmol/m^2/s) resulted in the lowest decrease in the concentration of the dye with final degradation efficiency of around 40% and k value 0.00402 min^{-1}. A significant increase was recorded with increasing twice the light intensity which resulted in the remarkable degradation efficiency of around 76.7% with k equal to 0.01642 min^{-1}. Further increase in light intensity showed a rapid change during the first 10 min of illumination which could relate to the production of intermediates of BBR degradation products. At the end of the experiment, the degradation efficiency was recorded at around 66.5% with k value of 0.01041 min^{-1}. The decrease in the degradation intensity in the highest light intensity might be due to the influence of heat provided to the system. The results proved the important role of light intensity for BBR dye degradation using Ag NPs BC with higher number of absorbed light photons leading to the high likelihood of the BBR dye degradation taking place.

5.1.3.2.2 Influence of dye concentration

The light availability can also be influenced by changing the concentration of the BBR dye in the solution. The dye molecules can absorb light which results in fewer photons reaching the catalyst surface leading to the decreased production of radicals. The effect of changing BBR dye concentration within the range 4-34 mg/L is shown in Fig. 28. As expected, the highest decrease

in the BBR concentration was observed for the lowest tested BBR dye concentration of 4 mg/L with degradation efficiency around 80% and k value of 0.01983 min^{-1}. Increase of the BBR dye concentration decreases the degradation efficiency to around 76.7% and k value 0.01642 min^{-1}. The highest tested BBR dye concentration showed a degradation efficiency around 31.6% with k value 0.00314 min^{-1}. Other than the easier light availability, the low degradation of the dye allows easier access of the molecules to the active sites on the catalyst surface and prevents agglomeration [28]. Considering that the BBR dye is present in the wastewater due to many washing cycles [29], it shows the potential of Ag NPs BC for its efficient removal.

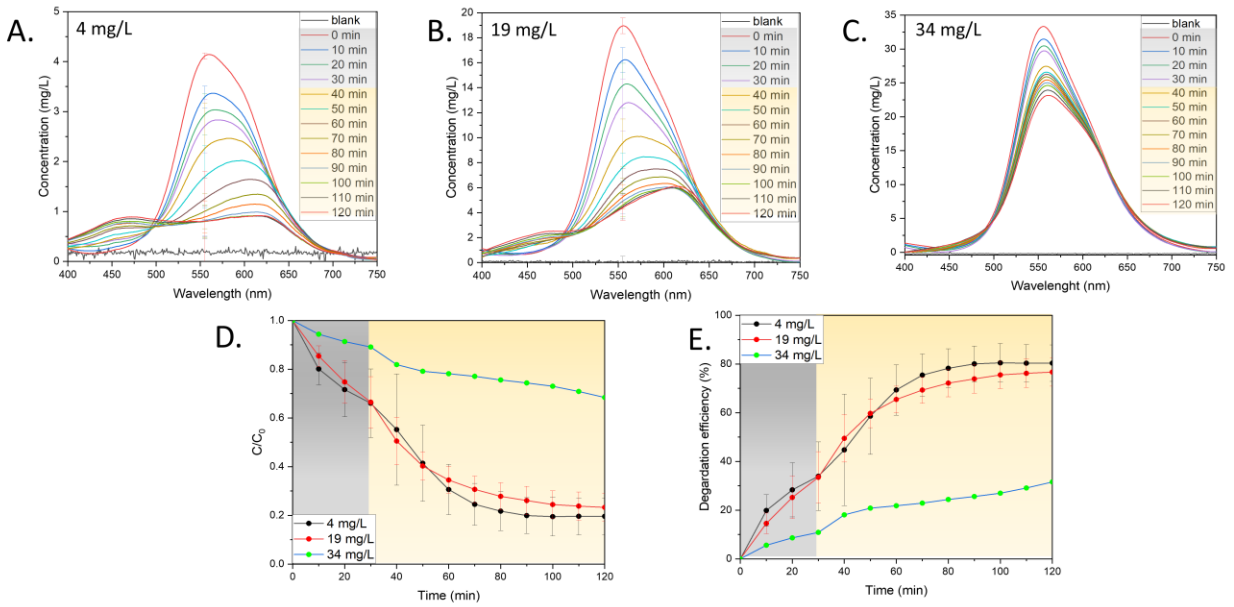

Figure 28 Influence of dye concentration on the photocatalytic activity (A-C) UV–Vis spectral changes in the varying dye concentration, (D) changes in dye concentration, (E) percentage degradation efficiency.

5.1.3.2.3 Influence of catalyst dosage

The influence of the availability of the active sites on the catalyst surface has been tested by varying the catalyst dosage in the range 62.5-250 mg/L (Fig. 29). The lowest tested concentration of Ag NPs BC resulted in only a slight decrease in BBR dye concentration with degradation efficiency of 18.8% and k value of 0.00144 min^{-1}. Increasing twice the catalyst dosage significantly improved the photocatalytic performance with recorded degradation efficiency of around 76.7% and k value of 0.01642 min^{-1}. The highest tested catalyst dosage of 250 mg/L revealed a rapid

decrease in the BBR concentration after switching on the light with peak shift which can be attributed to the formation of intermediates. The degradation efficiency of the reaction was observed at around 90.6% with k value of 0.04402 min^{-1}. Based on the obtained results, the availability of the active sites on the Ag NPs BC surface plays a crucial role in the photocatalytic degradation of the BBR dye. However, it has been reported that the increase can be observed up to a certain limit as the excess of the catalyst might turn the solution more turbid thus hindering the light penetration [30].

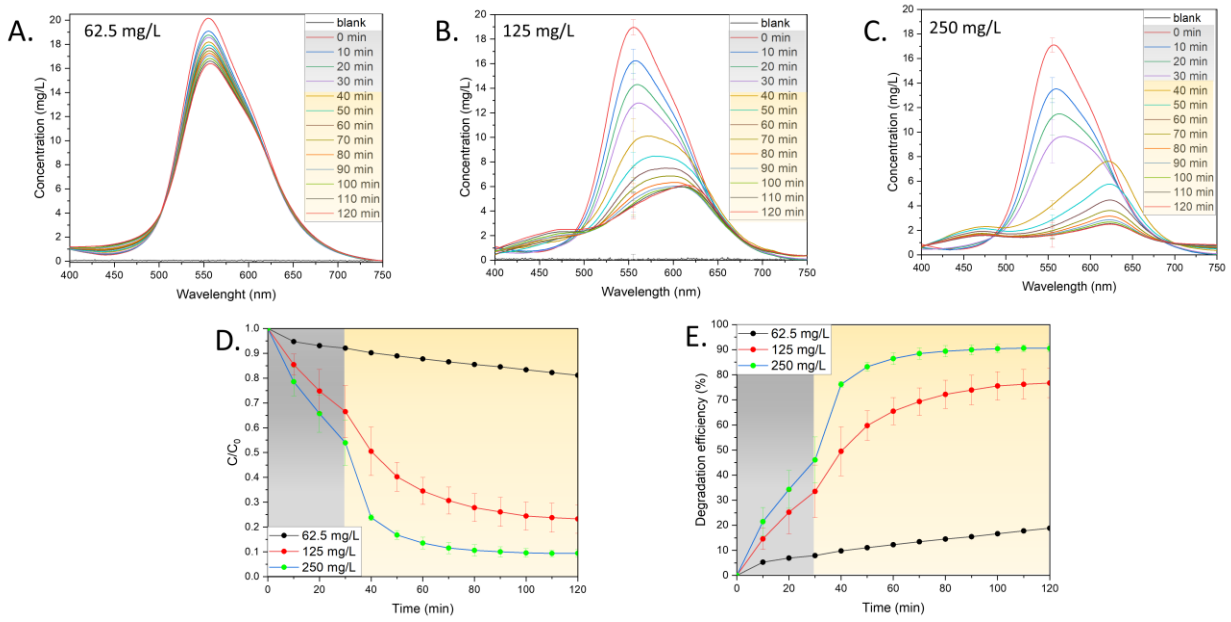

Figure 29 Influence of catalyst concentration on the photocatalytic activity (A-C) UV–Vis spectral changes in the varying catalyst concentration, (D) changes in dye concentration, (E) percentage degradation efficiency.

5.1.3.2.4 Influence of pH

Another tested factor for the photocatalytic performance of Ag NPs BC was pH of the solution in the range 3-11 (Fig. 30). In pH 3, the photocatalytic degradation efficiency was recorded at 21.3% with k value of 0.00142 min^{-1} while pH 7 and 11 showed a degradation efficiency of around 76.7% and 71.4% with k values of 0.01642 min^{-1} and 0.01311 min^{-1}, respectively. The interpretation of pH effect is challenging due to its multiple roles such as changing electrostatic interactions between the catalyst surface, solvent molecules, substrate, and formed radicals [31]. The alkaline medium might have facilitated the formation of hydroxyl radicals which improved the BBR dye

removal process [32]. The effect can continue up to a specific pH value when the negatively charged catalyst demonstrates Coulomb repulsion between the catalyst surface and present hydroxyl anions, diminishing formation of radicals [33].

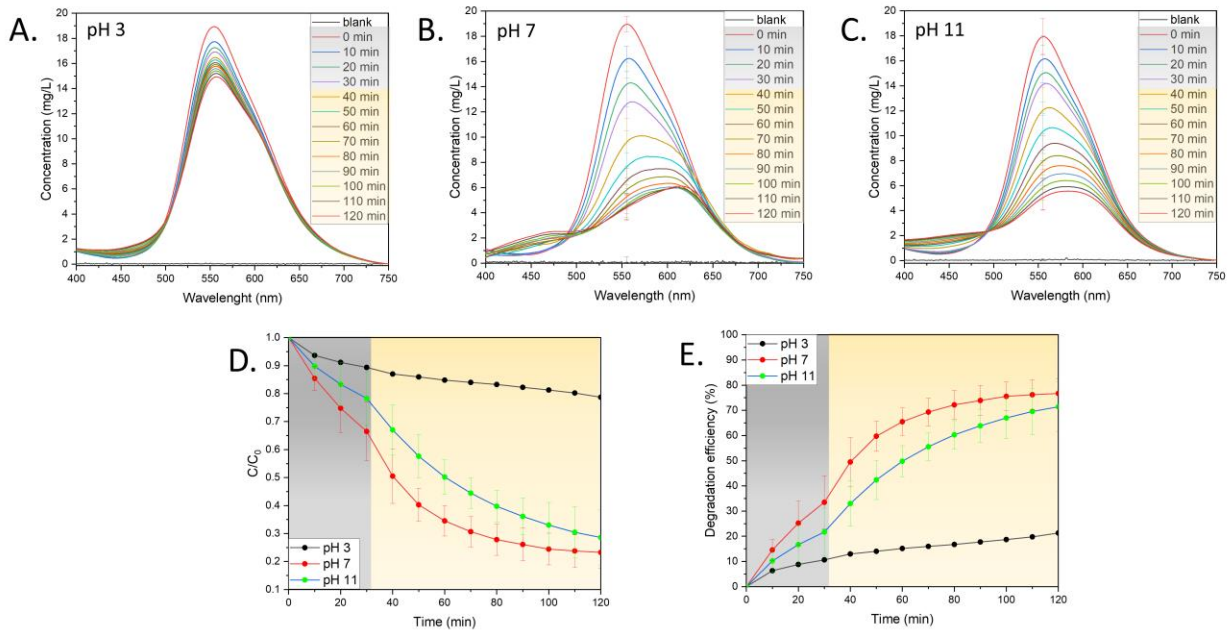

Figure 30 Influence of pH on the photocatalytic activity (A-C) UV–Vis spectral changes in the varying pH, (D) changes in dye concentration, (E) percentage degradation efficiency.

5.1.3.2.5 Influence of calcination

In the final set of experiments, the influence of the removal of the organic content by calcination was tested on photocatalytic activity (Fig. 31). The Ag NPs AC exhibited only a slight change in the BBR dye concentration with degradation efficiency around 10.7% and k value of 0.00245 min^{-1}. In comparison, Ag NPs BC in the same conditions showed the degradation efficiency of 76.7% and k value of 0.01642 min^{-1}. Without any catalyst around 6.5% of the dye was degraded and k value was calculated at 0.00049 min^{-1}. The effect of calcination was usually tested before on TiO_2-Ag catalysts when the temperature affected the morphology of the TiO_2 to improve its photocatalytic activity [34,35]. However, Nasab et al. reported the activity of Ag/Ag_2O NPs in the UVA spectrum which might suggest that after the calcination the material requires higher energy wavelengths for photoactivation increasing the cost of the degradation process [36].

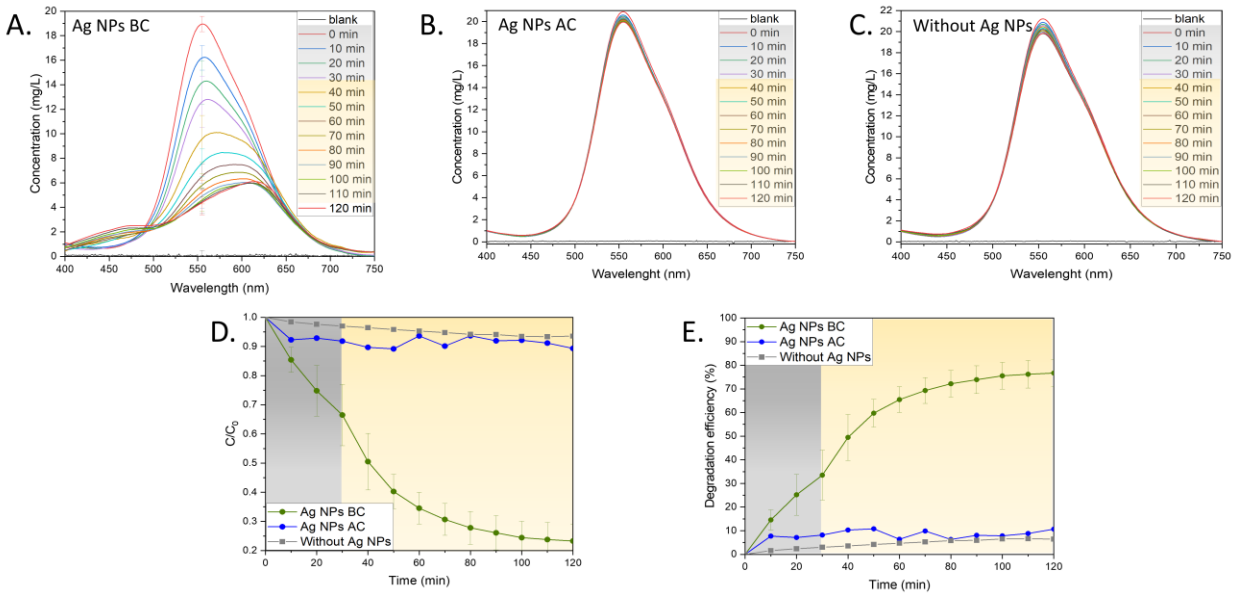

Figure 31 Influence of calcination on the photocatalytic activity (A) UV–Vis spectral changes before calcination, (B) UV–Vis spectral changes after calcination, (C) UV–Vis spectral changes without catalyst, (D) changes in dye concentration, (E) percentage degradation efficiency.

5.1.3.2.6 Mechanism of dye degradation

Based on the obtained results, the mechanism of BBR dye degradation is proposed as shown in the equations below (4-10) [32,37,38]. The mechanism of the dye degradation process is associated with the excitation of electrons (e^-) from the valence band to conduction band upon light irradiation (Eq. 4). After their transfer, positively charged holes (h^+) react with water molecules producing H^+ and •OH radical (5). The free electrons convert molecular oxygen into $•O_2^-$ (6) which reacts with water molecules generating •OOH (7) rearranged into H_2O_2 (8). After the reaction with $•O_2^-$, •OH is produced (9) which can also be generated as a result of interactions between hydroxyl ions and holes (10). The process generates •OH which plays an important role in the degradation of BBR dye.

Photocatalyst surface + hv → electron (e^-) + hole (h^+) (4)

$h^+ + H_2O \rightarrow H^+ + •OH$ (5)

$e^- + O_2 \rightarrow •O_2^-$ (6)

$•O_2^- + H_2O \rightarrow •OOH + OH^-$ (7)

$2\bullet OOH \rightarrow H_2O_2 + O_2$ (8)

$H_2O_2 + \bullet O_2^- \rightarrow \bullet OH + O_2 + OH^-$ (9)

$OH^- + h^+ \rightarrow \bullet OH$ (10)

The degradation of BBR dye was previously studied based on sonochemical process which also involves generation of hydroxyl radicals [39]. There are two major pathways that were identified, using LC-Q-TOF-MS analysis, as a result of either OH addition or hydrogen abstraction and disproportionation/hydroxylation reaction. Then, the intermediates undergo many reactions including oxidative cleavage, de-ethylation, or demethylation. There were 13 identified intermediates which can be subjected to further ring opening and other oxidative cleavages resulting in the mineralization reaction [39]. Moreover, the degradation pathway was also studied in the river water and yielded similar intermediate profile which shows that the process is independent from presence of other ions or substances in river water [40].

5.1.4 Conclusions

The development of efficient and stable photocatalysts is of paramount importance in the pursuit of high-efficiency reaction systems for addressing polluted water environments. Indeed, the search for effective photoactive materials capable of promoting photocatalytic reactions has been the focus of extensive research efforts. In the present study, C. vulgaris methanolic extract has been used to successfully synthesize Ag NPs BC which were also subjected to calcination (Ag NPs AC). The XRD findings showed the presence of Ag and Ag_2O phase in Ag NPs BC while Ag NPs AC contained only Ag phase. The calculated crystalline size was 16.07 nm and 24.61 nm for Ag NPs BC and Ag NPs AC respectively. The involvement of extract in the synthesis was confirmed by FTIR analysis revealing the abundance of chemical groups on the Ag NPs BC surface. The SEM analysis showed the irregular morphology and the presence of elements from the extract was examined by EDX. The TGA findings showed the difference in the organic content of the prepared Ag NPs and their optical properties were studied by UV-Vis analysis revealing visible light activation of Ag NPs BC with band gap energy of 2.17 eV.

The photocatalytic activity of Ag NPs BC against BBR dye was analyzed in the visible light testing various factors such as light intensity, dye concentration, catalyst dosage, pH, or calcination of the catalyst. The highest degradation efficiency of 90.6% with k value of 0.04402 min^{-1} was archived by increasing the catalyst dosage. Finally, the BBR dye degradation mechanism was proposed. Thus, the Ag NPs showed great potential as a photocatalyst against BBR dye which could also be explored for the degradation of various compounds.

5.1.5 References

1. J. Fito, M. Abewaa, A. Mengistu, K. Angassa, A.D. Ambaye, W. Moyo, T. Nkambule, Adsorption of methylene blue from textile industrial wastewater using activated carbon developed from Rumex abyssinicus plant, Sci. Reports 2023 131. 13 (2023) 1–17. https://doi.org/10.1038/s41598-023-32341-w.

2. A.N.M. Faizal, N.R. Putra, M.A.A. Zaini, Insight into the adsorptive mechanisms of methyl violet and reactive orange from water—a short review, Part. Sci. Technol. 41 (2023) 730–739. https://doi.org/10.1080/02726351.2022.2140462.

3. S.S. Emmanuel, C.O. Olawoyin, A.A. Adesibikan, E.A. Opatola, A Pragmatic Review on Bio-polymerized Metallic Nano-Architecture for Photocatalytic Degradation of Recalcitrant Dye Pollutants, J. Polym. Environ. 2023. (2023) 1–30. https://doi.org/10.1007/S10924-023-02986-9.

4. L. He, F. Michailidou, H.L. Gahlon, W. Zeng, Hair Dye Ingredients and Potential Health Risks from Exposure to Hair Dyeing, Chem. Res. Toxicol. 35 (2022) 901–915. https://doi.org/10.1021/acs.chemrestox.1c00427.

5. J. Zhao, Q.X. Wu, X. Du Cheng, T. Su, X.H. Wang, W.N. Zhang, Y.M. Lu, Y. Chen, Biodegradation and detoxification of the triphenylmethane dye coomassie brilliant blue by the extracellular enzymes from mycelia of Lactarius deliciosus, Front. Chem. Sci. Eng. 15 (2021) 421–436. https://doi.org/10.1007/s11705-020-1952-7.

6. D.F. Duxbury, The Photochemistry and Photophysics of Triphenylmethane Dyes in Solid and Liquid Media, Chem. Rev. 93 (1993) 381–433. https://doi.org/10.1021/cr00017a018.

7. A.R. Khataee, M.B. Kasiri, Photocatalytic degradation of organic dyes in the presence of nanostructured titanium dioxide: Influence of the chemical structure of dyes, J. Mol. Catal. A Chem. 328 (2010) 8–26. https://doi.org/10.1016/j.molcata.2010.05.023.

8. S. Dutta, J. Bhattacharjee, A comparative study between physicochemical and biological methods for effective removal of textile dye from wastewater, Dev. Wastewater Treat. Res. Process. (2022) 1–21. https://doi.org/10.1016/B978-0-323-85657-7.00003-1.

9. M. Shabir, M. Yasin, M. Hussain, I. Shafiq, P. Akhter, A.S. Nizami, B.H. Jeon, Y.K. Park, A review on recent advances in the treatment of dye-polluted wastewater, J. Ind. Eng. Chem. 112 (2022) 1–19. https://doi.org/10.1016/J.JIEC.2022.05.013.

10. D. Peramune, D.C. Manatunga, R.S. Dassanayake, V. Premalal, R.N. Liyanage, C. Gunathilake, N. Abidi, Recent advances in biopolymer-based advanced oxidation processes for dye removal applications: A review, Environ. Res. 215 (2022) 114242. https://doi.org/10.1016/J.ENVRES.2022.114242.

11. Y. Liu, C.H. Liu, T. Debnath, Y. Wang, D. Pohl, L. V. Besteiro, D.M. Meira, S. Huang, F. Yang, B. Rellinghaus, M. Chaker, D.F. Perepichka, D. Ma, Silver nanoparticle enhanced metal-organic matrix with interface-engineering for efficient photocatalytic hydrogen evolution, Nat. Commun. 2023 141. 14 (2023) 1–12. https://doi.org/10.1038/s41467-023-35981-8.

12. A. Sidorowicz, G. Fais, M. Casula, M. Borselli, G. Giannaccare, A.M. Locci, N. Lai, R. Orrù, G. Cao, A. Concas, Nanoparticles from Microalgae and Their Biomedical Applications, Mar. Drugs. 21 (2023) 352. https://doi.org/10.3390/md21060352.

13. R. Rajkumar, G. Ezhumalai, M. Gnanadesigan, A green approach for the synthesis of silver nanoparticles by Chlorella vulgaris and its application in photocatalytic dye degradation activity, Environ. Technol. Innov. 21 (2021) 101282. https://doi.org/10.1016/J.ETI.2020.101282.

14. M. Soleimani, M. Habibi-Pirkoohi, Biosynthesis of silver nanoparticles using Chlorella vulgaris and evaluation of the antibacterial efficacy against Staphylococcus aureus, Avicenna J. Med. Biotechnol. 9 (2017) 120–125. /pmc/articles/PMC5501138/ (accessed August 6, 2023).

15. A. Mahajan, A. Arya, T.S. Chundawat, Green synthesis of silver nanoparticles using green alga (Chlorella vulgaris) and its application for synthesis of quinolines derivatives, Synth. Commun. 49 (2019) 1926–1937. https://doi.org/10.1080/00397911.2019.1610776.

16. B. Pradhan, S. Patra, S.R. Dash, R. Nayak, C. Behera, M. Jena, Evaluation of the anti-bacterial activity of methanolic extract of Chlorella vulgaris Beyerinck [Beijerinck] with special reference

to antioxidant modulation, Futur. J. Pharm. Sci. 2021 71. 7 (2021) 1–11. https://doi.org/10.1186/S43094-020-00172-5.

17. Dilek (Yalcin) Duygu, Fourier transform infrared (FTIR) spectroscopy for identification of Chlorella vulgaris Beijerinck 1890 and Scenedesmus obliquus (Turpin) Kützing 1833, AFRICAN J. Biotechnol. 11 (2012). https://doi.org/10.5897/ajb11.1863.

18. M. Mecozzi, M. Pietroletti, M. Scarpiniti, R. Acquistucci, M.E. Conti, Monitoring of marine mucilage formation in Italian seas investigated by infrared spectroscopy and independent component analysis, Environ. Monit. Assess. 184 (2012) 6025–6036. https://doi.org/10.1007/s10661-011-2400-4.

19. M.L. Agazzi, S.E. Herrera, M.L. Cortez, W.A. Marmisollé, O. Azzaroni, Self-assembled peptide dendrigraft supraparticles with potential application in pH/enzyme-triggered multistage drug release, Colloids Surfaces B Biointerfaces. 190 (2020) 110895. https://doi.org/10.1016/J.COLSURFB.2020.110895.

20. L. David, B. Moldovan, Green Synthesis of Biogenic Silver Nanoparticles for Efficient Catalytic Removal of Harmful Organic Dyes, Nanomater. 2020, Vol. 10, Page 202. 10 (2020) 202. https://doi.org/10.3390/NANO10020202.

21. B. Kis, E.A. Moacă, L.B. Tudoran, D. Muntean, I.Z. Magyari-Pavel, D.I. Minda, A. Lombrea, Z. Diaconeasa, C.A. Dehelean, Ștefania Dinu, C. Danciu, Green Synthesis of Silver Nanoparticles Using Populi gemmae Extract: Preparation, Physicochemical Characterization, Antimicrobial Potential and In Vitro Antiproliferative Assessment, Materials (Basel). 15 (2022) 5006. https://doi.org/10.3390/ma15145006.

22. M.E.E. Zin, P. Moolkaew, T. Junyusen, W. Sutapun, Preparation of hybrid particles of Ag nanoparticles and eggshell calcium carbonate and their antimicrobial efficiency against beef-extracted bacteria, R. Soc. Open Sci. 10 (2023). https://doi.org/10.1098/RSOS.221197.

23. T. Shankar, P. Karthiga, K. Swarnalatha, K. Rajkumar, Green synthesis of silver nanoparticles using Capsicum frutescence and its intensified activity against E. coli, Resour. Technol. 3 (2017) 303–308. https://doi.org/10.1016/J.REFFIT.2017.01.004.

24. Z. Ma, J. Liu, Y. Liu, X. Zheng, K. Tang, Green synthesis of silver nanoparticles using soluble soybean polysaccharide and their application in antibacterial coatings, Int. J. Biol. Macromol. 166 (2021) 567–577. https://doi.org/10.1016/j.ijbiomac.2020.10.214.

25. L. Baia, S. Simon, UV-VIS and TEM assessment of morphological features of silver nanoparticles from phosphate glass matrices, Mod. Res. Educ. Top. …. (2007) 576–583. http://www.formatex.org/microscopy3/pdf/pp576-583.pdf (accessed August 11, 2023).

26. H. Mistry, R. Thakor, H. Bariya, Biogenesis and characterization of proficient silver nanoparticles employing marine procured fungi Hamigera pallida and assessment of their antioxidative, antimicrobial and anticancer potency, Biotechnol. Lett. 44 (2022) 1097–1107. https://doi.org/10.1007/s10529-022-03287-2.

27. V.S. Munagapati, H.Y. Wen, A.R.K. Gollakota, J.C. Wen, K.Y.A. Lin, C.M. Shu, V. Yarramuthi, P.K. Basivi, G.M. Reddy, G. V. Zyryanov, Magnetic Fe3O4 nanoparticles loaded guava leaves powder impregnated into calcium alginate hydrogel beads (Fe3O4-GLP@CAB) for efficient removal of methylene blue dye from aqueous environment: Synthesis, characterization, and its adsorption performance, Int. J. Biol. Macromol. 246 (2023) 125675. https://doi.org/10.1016/J.IJBIOMAC.2023.125675.

28. H. Roy, T.U. Rahman, M.A.J.R. Khan, M.R. Al-Mamun, S.Z. Islam, M.A. Khaleque, M.I. Hossain, M.Z.H. Khan, M.S. Islam, H.M. Marwani, A. Islam, M.M. Hasan, M.R. Awual, Toxic dye removal, remediation, and mechanism with doped SnO2-based nanocomposite photocatalysts: A critical review, J. Water Process Eng. 54 (2023) 104069. https://doi.org/10.1016/J.JWPE.2023.104069.

29. L.M. Chiarello, M. Mittersteiner, P.C. de Jesus, J. Andreaus, I.O. Barcellos, Reuse of enzymatically treated reactive dyeing baths: Evaluation of the number of reuse cycles, J. Clean. Prod. 267 (2020) 122033. https://doi.org/10.1016/J.JCLEPRO.2020.122033.

30. A. Nawaz, M. Atif, A. Khan, M. Siddique, N. Ali, F. Naz, M. Bilal, T.H. Kim, M. Momotko, H.U. Haq, G. Boczkaj, Solar light driven degradation of textile dye contaminants for wastewater treatment – studies of novel polycationic selenide photocatalyst and process optimization by response surface methodology desirability factor, Chemosphere. 328 (2023) 138476. https://doi.org/10.1016/J.CHEMOSPHERE.2023.138476.

31. V. Javanbakht, M. Mohammadian, Photo-assisted advanced oxidation processes for efficient removal of anionic and cationic dyes using Bentonite/TiO2 nano-photocatalyst immobilized with silver nanoparticles, J. Mol. Struct. 1239 (2021) 130496. https://doi.org/10.1016/J.MOLSTRUC.2021.130496.

32. Q. Lin, X. Huang, L. Lu, D. Tang, Snowflake-like CdS@ZnIn2S4 heterojunction-based photocatalyst-electrolyte effect: An innovative mode for photoelectrochemical immunoassay, Biosens. Bioelectron. 216 (2022) 114679. https://doi.org/10.1016/J.BIOS.2022.114679.

33. H.B. Uma, S. Ananda, M.B. Nandaprakash, High efficient photocatalytic treatment of textile dye and antibacterial activity via electrochemically synthesized Ni-doped ZnO nano photocatalysts, Chem. Data Collect. 24 (2019) 100301. https://doi.org/10.1016/J.CDC.2019.100301.

34. R.D. Desiati, M. Taspika, E. Sugiarti, Effect of calcination temperature on the antibacterial activity of TiO2/Ag nanocomposite, Mater. Res. Express. 6 (2019) 095059. https://doi.org/10.1088/2053-1591/AB155C.

35. C. Nutescu Duduman, C. Gómez de Castro, G.A. Apostolescu, G. Ciobanu, D. Lutic, L. Favier, M. Harja, Enhancing the TiO2-Ag Photocatalytic Efficiency by Acetone in the Dye Removal from Wastewater, Water (Switzerland). 14 (2022) 2711. https://doi.org/10.3390/w14172711.

36. N. Khandan Nasab, Z. Sabouri, S. Ghazal, M. Darroudi, Green-based synthesis of mixed-phase silver nanoparticles as an effective photocatalyst and investigation of their antibacterial properties, J. Mol. Struct. 1203 (2020) 127411. https://doi.org/10.1016/J.MOLSTRUC.2019.127411.

37. I. Groeneveld, M. Kanelli, F. Ariese, M.R. van Bommel, Parameters that affect the photodegradation of dyes and pigments in solution and on substrate – An overview, Dye. Pigment. 210 (2023) 110999. https://doi.org/10.1016/J.DYEPIG.2022.110999.

38. A. Ahmed, M. Usman, B. Yu, X. Ding, Q. Peng, Y. Shen, H. Cong, Efficient photocatalytic degradation of toxic Alizarin yellow R dye from industrial wastewater using biosynthesized Fe nanoparticle and study of factors affecting the degradation rate, J. Photochem. Photobiol. B Biol. 202 (2020) 111682. https://doi.org/10.1016/J.JPHOTOBIOL.2019.111682.

39. M.P. Rayaroth, U.K. Aravind, C.T. Aravindakumar, Sonochemical degradation of Coomassie Brilliant Blue: Effect of frequency, power density, pH and various additives, Chemosphere. 119 (2015) 848–855. https://doi.org/10.1016/J.CHEMOSPHERE.2014.08.037.

40. M.P. Rayaroth, U.K. Aravind, C.T. Aravindakumar, Ultrasound based AOP for emerging pollutants: from degradation to mechanism, Environ. Sci. Pollut. Res. 24 (2017) 6261–6269. https://doi.org/10.1007/s11356-016-6606-4

5.2 Biogenic silver nanoparticles from *H. pluvialis* extract for efficient photocatalytic removal of Brilliant Blue R

5.2.1 Introduction

In recent years, the growth of industries and the increase in urbanization have caused the widespread pollution of water sources. Among the pollutants discharged in wastewaters, one the most dangerous categories are the one represented by dyes, which are released into the environment as a result of various industrial activities, such as tanning, paper making, or textile colouring [1]. Those dyes in water inevitably increase the biochemical and chemical oxygen demand levels while also reducing sunlight penetration through water, causing an imbalance in the marine ecosystem [2]. In addition, the discharge of coloured wastewater into the environment is one of the main concerns because most dyes are harmful, carcinogenic, and teratogenic [2]. The conventional wastewater treatment processes might not be efficient in removing dyes to suitable concentration due to the complex molecular structure of the synthetic products; thus, new technologies to understand the degradation mechanism are vastly researched.

Brilliant Blue R (BBR) is one of the most common dyes used in the laboratory due to its ability to bind with proteins in a non-covalent interaction, forming a colored complex visible during protein gel electrophoresis. According to the molecular structure, BBR belongs to triphenylmethane dyes consisting of a central carbon atom connected to three phenyl rings [3]. The presence of aromatic rings and the absence of easily cleavable bonds reduces the susceptibility of the dye to chemical breakdown [4,5]. Therefore, the research aims for the development of efficient and sustainable solutions to minimize the impact of BBR on the environment.

One of the most promising emerging techniques is the advanced oxidation process (AOP) which uses strong oxidizing agents to break down organic compounds into less harmful substances [6]. One of the ways to produce highly reactive hydroxyl radicals participating in the degradation and mineralization of organic pollutants is photocatalysis. The mechanism behind it involves the absorption of light energy higher than the band gap energy of the catalyst resulting in the

excitation of the electron from the valence band to the conduction band [7]. The created holes and free electrons generate reactive oxygen species (ROS) after reacting with dissolved molecular oxygen and water [7]. ROS can in turn transform toxic organic molecules into less harmful low molecular weight products.

Among various photocatalysts, silver nanoparticles (Ag NPs) receive significant attention due to excellent photocatalytic activity under visible light irradiation. To date, different physical and chemical methods have been adopted for their synthesis, however, they are considered toxic and expensive due to the involvement of hazardous chemicals [8]. As an alternative, the metabolites derived from organisms can be used as reducing and stabilizing agents during the synthesis of nanoparticles [8]. In the literature, Ag NPs synthesized from plants were studied for photocatalytic degradation of BBR dye [9–11], however, the Ag NPs derived from microalgae Haematococcus pluvialis have not been yet tested for dye degradation activity.

The main objective of this study is to describe the Ag NPs obtained from methanolic *H. pluvialis* extract for the first time. The product was also calcined to determine the influence of organic content from *H. pluvialis* on the structure and activity. The obtained Ag NPs were characterized and applied for photocatalytic degradation of BBR dye under visible light in various conditions such as varying light intensity, dye concentration, catalyst concentration, pH, or presence of organic content. Altogether, the results provide an understanding between the properties and activity of Ag NPs which can be used for the efficient removal of hazardous BBR dye from the environment.

5.2.2 Materials and methods

5.2.2.1 Synthesis procedure

The *Haematococcus pluvialis* (CCALA 840) culture was grown in Modified OHM medium supplemented with 30 mM CH_3COONa with stirring and irradiation of 58W fluorescent lamps (Osram®) with 40 µmol/m^{-2}/s^{-1} photon flux. The culture was maintained for 30 days to obtain a suitable amount of biomass. Subsequently, it was centrifuged at 1500 RPM at 4°C (Heraeus® Megafuge® 1.0R) and the algal biomass was dried at room temperature.

In the next step, 0.9 g of dried residue was mixed with 54 mL of methanol (Merck® LiChrosolv® hypergrade). The flask was sonicated for 30 min (Soltec® Sonica® 2400 ETH S3) followed by stirring at 250 RPM (IKA® RH Digital Magnetic Stirrer) for the next 30 min to break down the cell walls and release the metabolites into the solvent. The leftover biomass was removed by filtration using standard filtration paper (Whatman®) and then the liquid was evaporated using a rotary evaporator (BUCHI Rotavapor™ R-210 Rotary Evaporator System) to discard about 70% of methanol. The concentrated extract was diluted with MiliQ H_2O (Millipore®, Milan, Italy) to the final volume of 180 mL and it was used for the Ag NPs synthesis process.

At the beginning of the synthesis procedure, the prepared extract was heated to 85°C and stirred at 250 RPM (IKA® RH Digital Magnetic Stirrer). Next, 0.1 M of silver nitrate (Carlo Erba®) was added to the extract, and after 15 min 1.25 M NaOH was used to increase the pH to 8. Starting from the moment of adding the precursor salt, the reaction continued for 1.5 h and then it was left for maturation in room temperature. Then, the liquid was centrifuged at 4000 RPM at 8°C (Heraeus® Megafuge® 1.0R) and collected Ag NPs were repeatedly washed in the two washing cycles with MiliQ H2O (Millipore®, Milan, Italy). Subsequently, the residue was dried at 80°C for 24 h, ground using mortar and pestle and divided into two parts. One part was stored in an Eppendorf tube in absence of light (before calcination – Ag NPs BC) and the other was calcined in muffle furnace (Gelman Instrument®) for 2 h at 600°C (after calcination – Ag NPs AC). After calcination, all the samples were stored in the same conditions.

5.2.2.2 Characterization

Obtained Ag NPs were studied by using X-Ray Diffractometer (D8 Advance, Bruker AXS®). The scanning was conducted with a diffraction angle between 12° and 90° at 0.1° per 10 s, at 40 kV and 30 mA using CuKα (λ =1.54 Å) radiation. The present phases were identified by using Diffrac.Eva software v.6.1.0.4 connected with the COD database. The crystallite size was calculated by applying Debye-Scherrer's formula after baseline correction.

The Fourier Transform Infrared Spectroscopy (FTIR) analysis was performed using FT/IR-6700 (Jasco, Tokyo, Japan) in the range of 500-4000 cm^{-1}.

The morphology of Ag NPs was analyzed by Scanning Electron Microscopy (SEM) using Hitachi S4000 FEG HRSEM (Hitachi Ltd., Tokyo, Japan) operated at 20 kV. The image acquisition was obtained using software Quartz PCI (Quartz Imaging Corporation, Vancouver, Canada). Before SEM analysis, the samples were coated with 2 nm of platinum to enhance the contrast. EDX analysis was performed using UltraDry EDX Detector (Thermo Fisher Scientific®, Madison, Wisconsin, USA), and NSS3 software (Thermo Fisher Scientific®, Madison, Wisconsin, USA).

Thermogravimetric Analysis (TGA) used to study thermal properties of Ag NPs using Differential Thermal Analyzer TG/DSC (NETZSCH® STA 409 PC) with airflow 100 mL/min and in a heating range 25 – 1000°C at 10°C/min.

UV-Vis absorption measurements were performed using CARY 50 spectrophotometer (Varian Inc., Australia) with a cell path length of 10 mm in the wavelength range of 200–750 nm. The direct bandgap energy was calculated from the Tauc relation (Equation 1):

$$(\alpha h\nu)^2 = (h\nu - E_g) \quad (1)$$

Where α is the molar extinction coefficient, h is the Plank's constant, ν is the light frequency, and E_g is the band gap energy. The bandgap energy was calculated by linear fit extrapolation of the plot of $(\alpha h\nu)^2$ against energy.

5.2.2.3 In-situ photocatalysis

First, calibration line was obtained by assessing the correlation between absorbance and previously determined concentrations of the dye. Before each photocatalytic experiment, to ensure even dispersion 50 mL of ddH2O was combined with Ag NPs and sonicated for 15 min in a sonication bath (Soltec® Sonica® 2400 ETH S3). At the beginning, the baseline of the dispersed Ag NPs solution was generated. Then, the reaction sample was mixed with different concentrations of BBR dye (Sigma-Aldrich®) in ethanol (500 mg/L). The flask was continuously stirred for 30 min in the absence of light to reach the reaction equilibrium. Next, the irradiation by a warm white 10.5 W LED bulb (Phillips) was provided. The irradiation power was measured through a luxmeter (HD2302.0 Delta-Ohm, Padua, Italy). The emission spectrum of the used light source is shown in Fig. 32. The liquid was circulated between the flask and a 10 mm flow-through

cuvette attached to the UV-Vis Spectrophotometer (Cary 50, Varian®). The measurements were conducted in the range of 400-750 nm every 10 minutes. The experiments with the highest degradation efficiency were performed in triplicate.

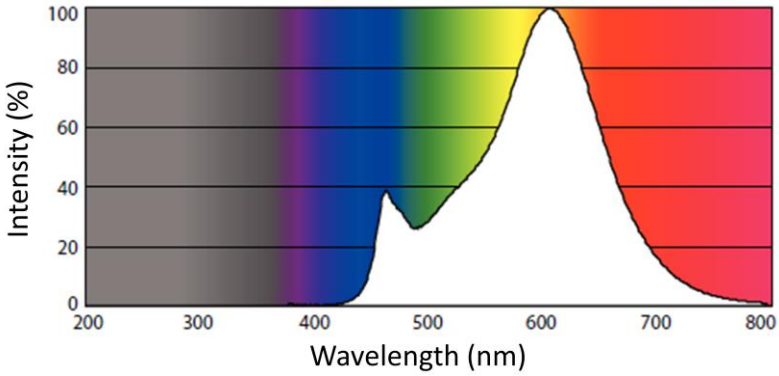

Figure 32 Emission spectrum of the light source provided by manufacturer.

The efficiency of the dye degradation by the synthesized Ag NPs was calculated as (Equation 2):

$$Degradation\ efficiency\ (\%) = 100 - \left({}^{C}/_{C_0} \cdot 100\right) \quad (2)$$

where C_0 is the initial BBR dye concentration, and C is the final concentration of the dye at the end of the degradation period.

The obtained data were fit using OriginPro 2021© 9.8 according to the pseudo-first order reaction model according to the Equation 3:

$$C = C_0 * e^{-{}^{k}/_{t}} \quad (3)$$

Where t is time and k is the reaction constant.

5.2.3 Results and discussion

5.2.3.1 Characterization

The crystal structure of the synthesized Ag NPs has been determined by XRD analysis (Fig. 33). The method provides valuable insights into the properties and behavior of the photocatalysts, which could be leveraged to enhance their performance in diverse applications. The Ag NPs BC exhibited the peaks belonging to the Ag_2O phase (COD 1010486), metallic Ag (COD 9008459) and

Ag_2CO_3 (COD 4318190). The calcination changed the XRD spectrum with only metallic Ag (COD 1509146) present in Ag NPs AC structure. The values from XRD spectra were used to calculate full width at half maximum (FWHM) which was applied to Debye-Scherrer's formula. The evaluated crystalline size for Ag NPs BC was 14.87 nm and 13.67 nm for Ag_2O and Ag phases respectively with an average size of 14.27 nm. After calcination the crystalline size increased to 34.78 nm for Ag NPs AC which shows the important role of metabolites in the stability of obtained Ag NPs.

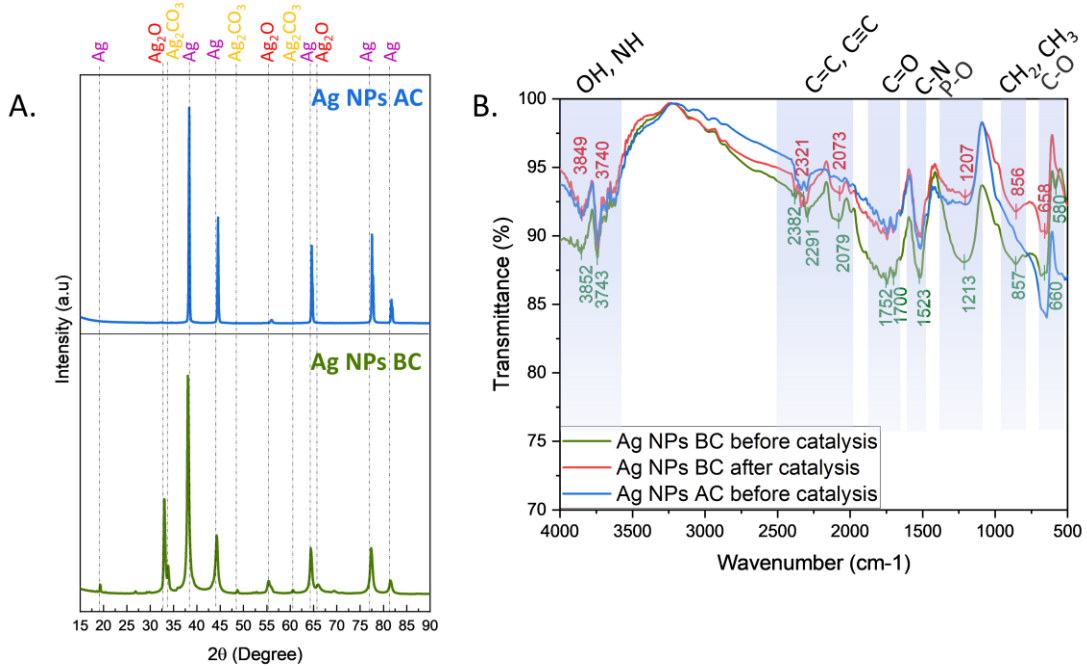

Figure 33 Crystallographic and spectroscopic analyses (A) XRD, (B) FTIR, BC – before calcination, AC – after calcination.

The metabolites from *H. pluvialis* have never been used for the synthesis of Ag NPs before. Industrially, *H. pluvialis* is mainly cultivated due to its high astaxanthin content in two stage approach, to first ensure high growth rates the green stage before inducing astaxanthin production in the red stage [12]. During favorable growth conditions in its green growth stage *H. pluvialis* is rich in proteins, which might act as reducing and stabilizing agents during the synthesis of Ag NPs [13]. Accordingly, the presence of metabolites from *H. pluvialis* on Ag NPs was further investigated by FTIR analysis.

The FTIR technique was used to determine the effect of photocatalytic action and calcination procedure on the organic content of Ag NPs. The FTIR spectrum of Ag NPs BC before calcination showed an affluence of functional groups such as OH, NH, C=C, C≡C, C=O, C-N, P-O, CH_2, CH_3, and C-O belonging to the various metabolites from *H. pluvialis* extract [14,15]. The Ag NPs BC collected after the photocatalysis process showed the shift in the wavenumber values and transmittance intensity which prove the involvement of organic capping content in the generation of radicals during photocatalysis. In addition, although the calcination managed to increase the intensity of the peaks, the spectrum of Ag NPs AC before catalysis is similar to Ag NPs BC after catalysis which shows the importance of functional groups in stabilizing the structure of Ag NPs.

The morphology of Ag NPs BC and Ag NPs AC was studied using SEM and EDX analyses (Fig. 34). The Ag NPs BC exhibit ellipsoidal or elongated shapes. The elemental analysis revealed the presence of silver, oxygen, carbon, phosphorus, and sulfur with homogeneous distribution. The material subjected to calcination was found to be agglomerated or coalescent with many Ag NPs fused together, however the tendency towards oval shapes can be observed. The composition of Ag NPs changed with the removal of sulfur due to calcination while the elemental distribution remained homogeneous. The results further prove the role of metabolites in Ag NPs with the change in material morphology and stability after partial removal of organic content.

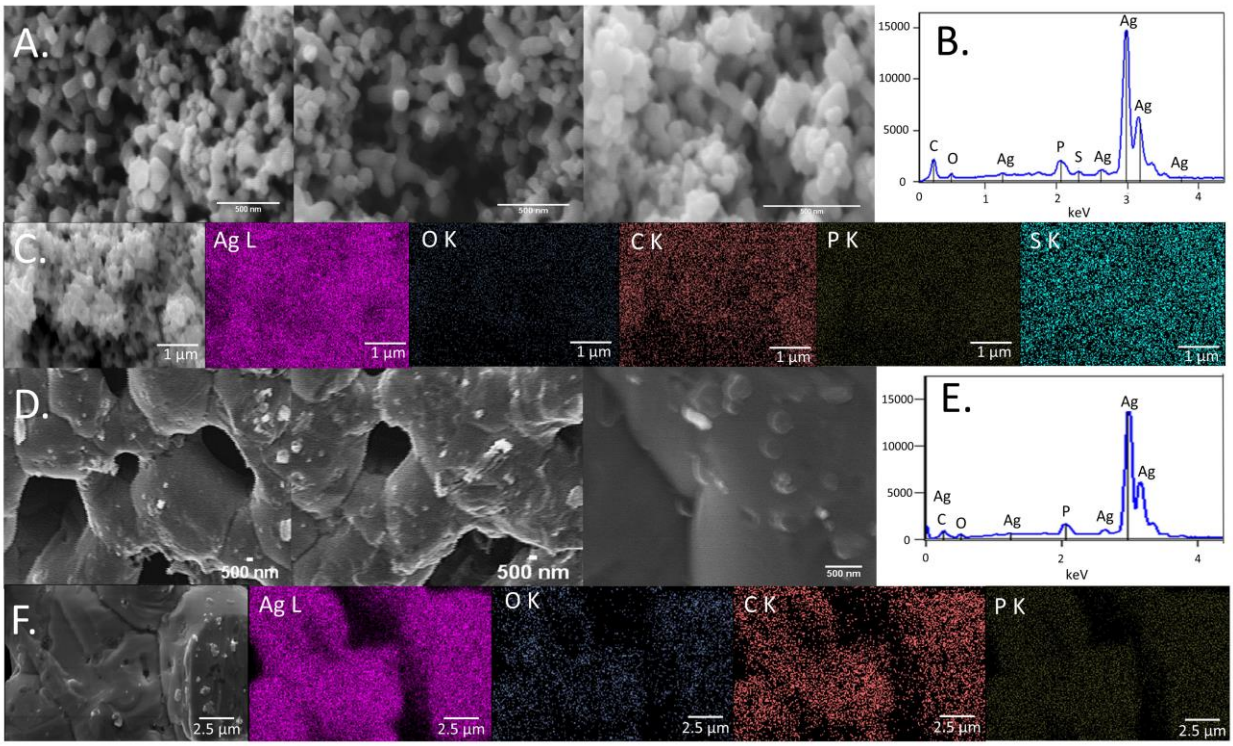

Figure 34 Microscopy analysis, (A) SEM of Ag NPs BC, (B) EDX spectrum of Ag NPs BC, (C) EDX mappings of Ag NPs BC, (D) SEM of Ag NPs AC, (E) EDX spectrum of Ag NPs AC, (F) EDX mappings of Ag NPs AC.

Thermal properties of the obtained materials were studied using TGA analysis (Fig. 35 A-C). The Ag NPs BC show the first major loss at the range of 25 – 200°C with DTG value at 26°C resulting in 14.5% weight loss. The decrease in that range is mostly attributed to water loss or decomposition of temperature-sensitive compounds acting as capping agents on Ag NPs BC surface [16]. The next decrease at 200 - 300°C range caused a 0.5% weight loss with DTG peak at 217°C probably due to decomposition of the phenolic compounds [17]. The further temperature increase did not result in significant changes in the weight with the final value at around 84%. The DTA peaks at 44°C and 140°C showed the exothermic nature of the decomposition with endothermic melting point of silver recorded at 960°C [18].

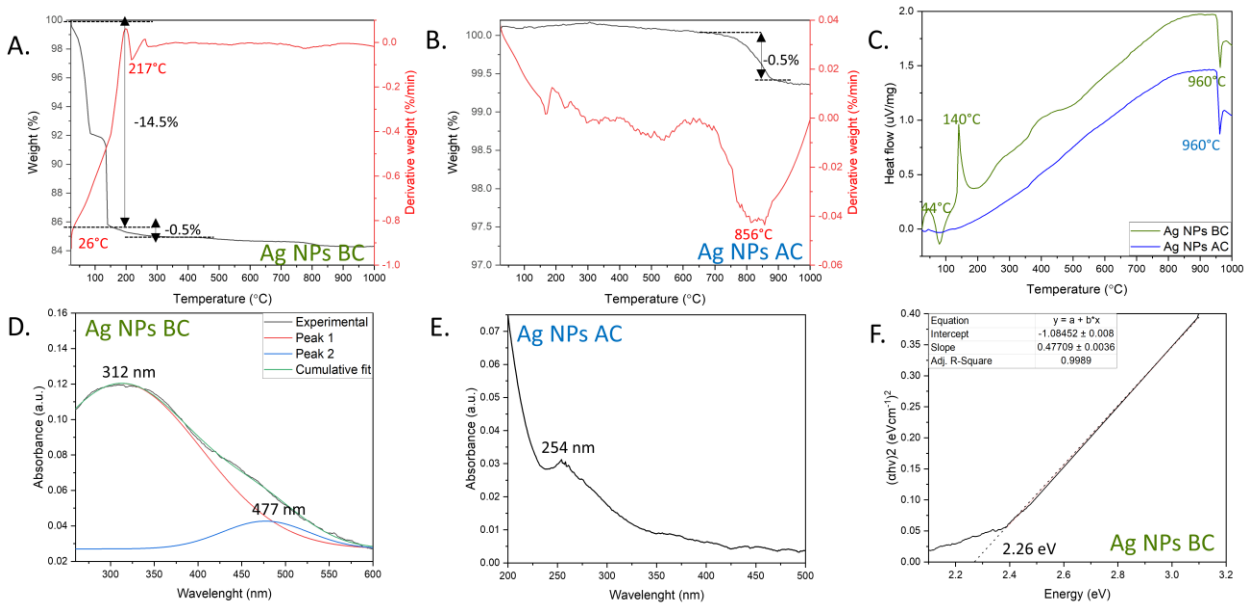

Figure 35 Thermal and optical properties of Ag NPs, (A) TG and DTG of Ag NPs BC, (B) TG and DTG of Ag NPs AC, (C) DTA of Ag NPs BC and Ag NPs AC, (D) UV-Vis spectrum of Ag NPs BC, (E) UV-Vis spectrum of Ag NPs AC, (F) Tauc plot of Ag NPs BC.

The obtained Ag NPs AC showed high thermal stability with the only weight decrease of 0.5% at 700 - 900°C range with low intensity DTG peak at 856°C. The decrease is probably connected with decarbonization from Ag NPs AC structure [19]. The DTA analysis displays the peak at 960°C attributed to the endothermic melting point of silver [18]. The results show that most organic compounds on Ag NPs BC surface are temperature-sensitive which might play an important role while designing the synthesis methodology of Ag NPs using *H. pluvialis* extract. While temperature is considered beneficial for the reduction process of metal ions [20], it might also negatively impact stability of the metabolites during the biological synthesis.

The optical properties of the obtained Ag NPs were assessed by UV-Vis spectroscopy (Fig. 35D-E). The electrons in the conduction band of Ag NPs undergo a collective oscillation when excited by the specific light wavelength, which is known as a surface plasmon resonance. As a result, the light can be strongly scattered and absorbed which might be a predictor of the photocatalytic activity of the tested material. The Ag NPs BC exhibit a broad absorbance band which after deconvolution can be attributed to two peaks. The peak at 312 nm probably originates from the metabolites present on the surface of Ag NPs BC. Similar pattern has been reported before as a

result of the synthesis using plant extract [21]. The second peak at 477 nm can be attributed to the specific surface plasmon resonance of Ag NPs typically occurring in the 400 – 500 nm range [22]. The results also show the potential of Ag NPs BC to be photoactivated in the visible light spectrum.

Due to calcination, the optical characteristic of Ag NPs AC changed with only one peak present at 254 nm. The high temperature might have caused structural defects and a change in the electronic state which affected plasmonic properties. The observed peak can be attributed to the electronic transition to metallic Ag [23] which is in line with the XRD findings. Furthermore, the introduced defects decreased the photocatalytic potential of Ag NPs AC.

Another important parameter describing optical properties is a band gap energy. It is defined as an energy difference between electrons in the highest occupied energy state in the valence band and lowest unoccupied state in the conduction band. Moreover, it can determine the ability of the material to absorb light, generate electron-hole pairs, and initiate photocatalytic processes. Based on the UV-Vis spectrum, the band gap energy of Ag NPs BC was calculated at 2.26 eV (Fig. 35F). The same band gap value was previously reported for Ag NPs synthesized using plant *Cynara cardunculus* extract [24].

5.2.3.2 Photocatalytic activity

5.2.3.2.1 Influence of light

The BBR dye degradation activity of Ag NPs BC was first assessed in the dark conditions (Fig. 36). During the initial 30 min the concentration slightly decreases then it stabilizes and reaches equilibrium. The interactions between dye and Ag NPs BC are the result of the weak van der Waals forces associated with physisorption, and no strong bonds were formed [25]. After 120 min, around 18.5% of the dye was degraded and k value was recorded at 0.00208 min^{-1}. After the results from the initial experiment, the subsequent experiments were carried out under dark conditions for the first 30 min to ensure that the reaction had reached equilibrium. By conducting the experiments in this manner, the effect of the various factors on the catalytic performance of Ag NPs can be accurately analyzed.

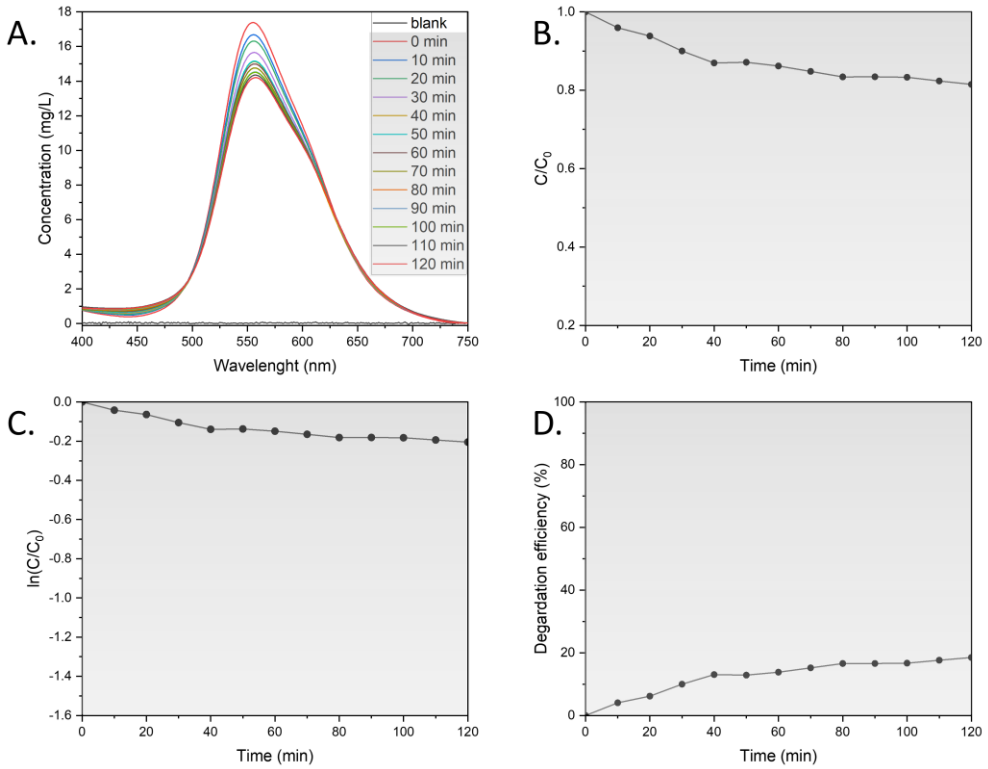

Figure 36 Degradation of BBR dye in the dark (A) UV–Vis spectral changes for the degradation of dye, (B) changes in dye concentration, (C) pseudo-first-order kinetic plot, (D) percentage degradation efficiency.

The photocatalytic activity of Ag NPs BC was first tested by varying light intensities (Fig. 37). The efficacy of photocatalytic degradation reactions depends critically on the intensity of light, which directly impacts the rate of electron-hole pair formation and subsequent recombination [26]. This, in turn, influences the production of active hydroxyl radicals playing an important role in the degradation of organic molecules. The concentration of BBR dye was tested in the varying light intensities of 75, 150, and 300 µmol/m^2/s.

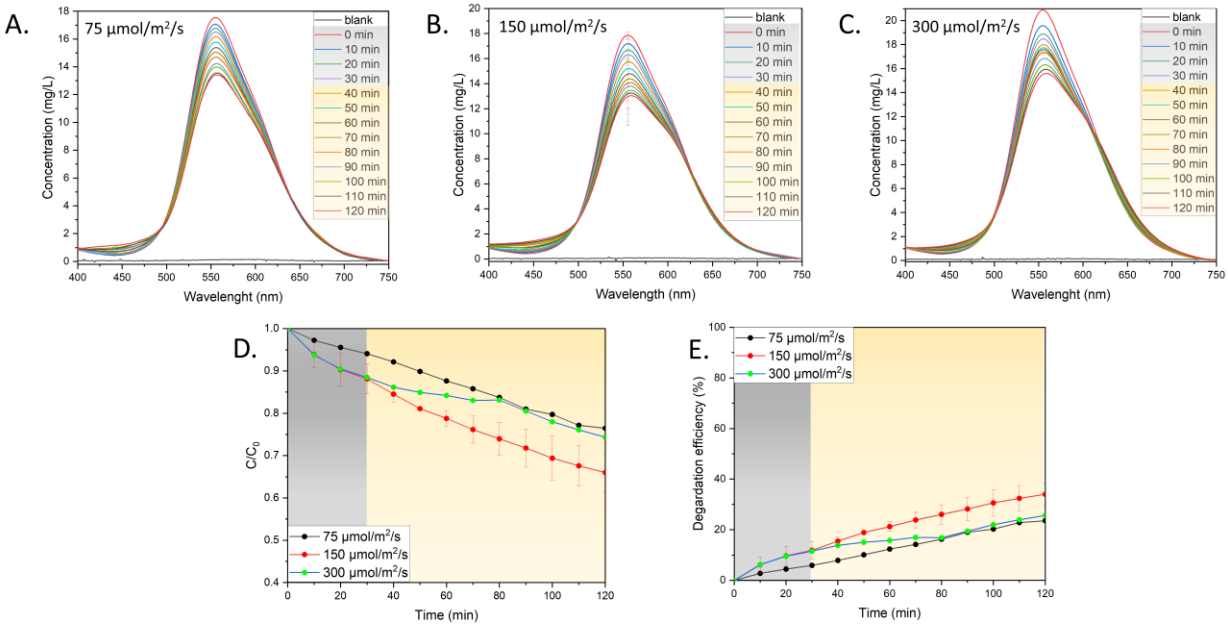

Figure 37 Influence of light on the photocatalytic activity (A-C) UV–Vis spectral changes in the varying light irradiation, (D) changes in dye concentration, (E) percentage degradation efficiency.

The light intensity of 75 µmol/m^2/s resulted in the lowest decrease in the dye concentration with degradation efficiency around 23.5% and k value of 0.00238 min^{-1}. Doubling the light intensity resulted in a further dye concentration decrease with degradation efficiency recorded at around 34% and k value at 0.00280 min^{-1}. However, the light intensity of 300 µmol/m^2/s decreased the photocatalytic efficiency to around 25.6% with k value of 0.00176 min^{-1}. The difference in light intensity in heterogenous catalysis was previously described in the context of quantum efficiency detailing the number of photons transformed relative to the number absorbed [27]. Thus, the higher quantum efficiency the higher the likelihood of photocatalytic degradation which can describe the behavior of Ag NPs BC in 75 and 150 µmol/m^2/s. Higher light intensity could have increased the temperature of the solution, which enhances kinetic energy of the BBR dye molecules allowing them to escape from the active sites on the surface of Ag NPs BC without being subjected to photodegradation [28]. Nevertheless, the light intensity is an important parameter to evaluate for photocatalytic degradation and its role should be evaluated more carefully.

5.2.3.2.2 Influence of dye concentration

The light availability can also be indirectly affected by the concentration of the BBR dye in the solution. Part of the light illumination can be absorbed by the dye molecules, limiting the number of photons reaching catalyst surface resulting in decreased radical production. The influence of the varying BBR dye in the 8-30 mg/L range on the photocatalytic action of Ag NPs BC is shown in Fig. 38. The lowest tested BBR dye concentration of 8 mg/L resulted in the highest decrease in the concentration with degradation efficiency around 65.8% and k value of 0.00544 min^{-1}. However, the further increase of dye concentration decreased the degradation efficiency to the similar values around 34% and 27% with k values of 0.00280 min^{-1} and 0.00208 min^{-1} for 18 mg/l and 30 mg/L, respectively. In addition to the easier light scattering, the low concentration of the dye molecules allows easier access to the active sites on the catalyst surface and prevents the competing action of the molecules and their agglomeration. Considering the usual low concentration of the dye present in the wastewater due to the multiple washings [29], obtained Ag NPs BC show potential to be used for effective BBR dye removal.

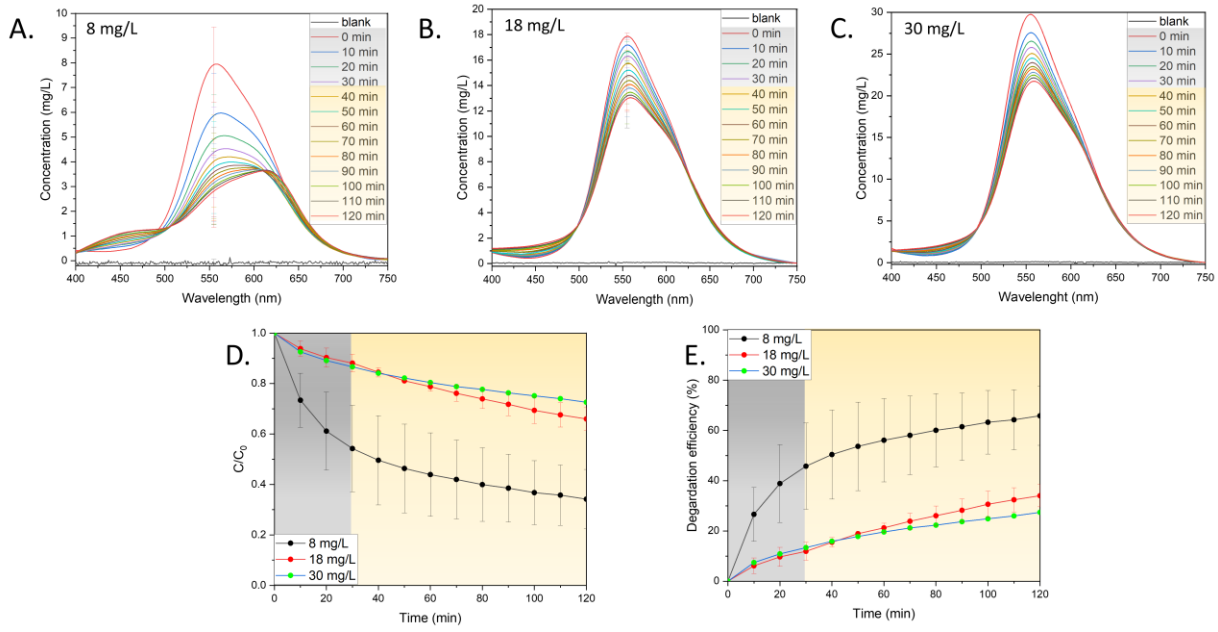

Figure 38 Influence of dye concentration on the photocatalytic activity (A-C) UV–Vis spectral changes in the varying dye concentration, (D) changes in dye concentration, (E) percentage degradation efficiency.

5.2.3.2.3 Influence of catalyst dosage

The availability of the active sites on Ag NPs BC was tested by varying the catalyst dosage in the range 125-500 mg/L (Fig. 39). The lowest tested catalyst dosage exhibited the lowest decrease in the dye concentration with degradation efficiency around 16.9% and k value of 0.00175 min^{-1}. The increase in the Ag NPs BC concentration increased the degradation efficiency to around 34% with k value of 0.00280 min^{-1}. Further catalyst dosage increase showed a significant increase in the degradation efficiency of around 65.9% with k value of 0.00947 min^{-1}. The results confirm the important role of the availability of active sites on Ag NPs BC surface to enhance the photocatalytic degradation of BBR dye. However, it has been reported that excess amount of the catalyst might cause high turbidity which can impair the light penetration [30].

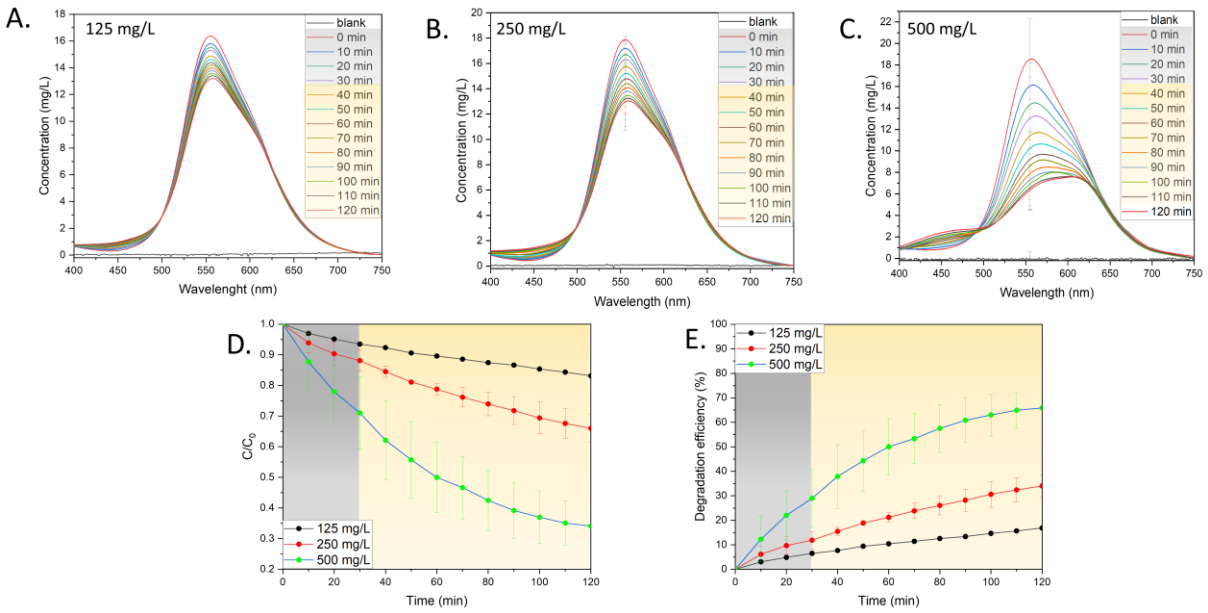

Figure 39 Influence of catalyst concentration on the photocatalytic activity (A-C) UV–Vis spectral changes in the varying catalyst concentration, (D) changes in dye concentration, (E) percentage degradation efficiency.

5.2.3.2.4 Influence of pH

Another tested factor for the photocatalytic activity of Ag NPs BC was pH of the solution in the range 3-11 (Fig. 40). In the acidic environment, the lowest decrease in BBR dye concentration was recorded with degradation efficiency of 23.6% and k value of 0.00144 min^{-1}. The neutral pH revealed slightly improved degradation efficiency of around 34% with k value 0.00280 min^{-1} while

alkaline medium further increased the degradation efficiency to around 44.4% with k value 0.00377 min^{-1}. The precise description of the role of pH is challenging owning to pH-dependency of many processes in the solution such as electrostatic interactions of the catalyst surface with other substances, such as solvent molecules, substrate molecules, and charged radicals produced during photodegradation [31]. In the present study, the alkaline medium might have provided more accessible hydroxyl anions which after interactions with positive holes in the catalyst, could form hydroxyl radicals degrading BBR dye [32]. However, the effect might continue up to a specific pH which can trigger Coulomb repulsion between the negatively charged surface of the catalyst and hydroxyl anions decreasing the radicals rate formation [33].

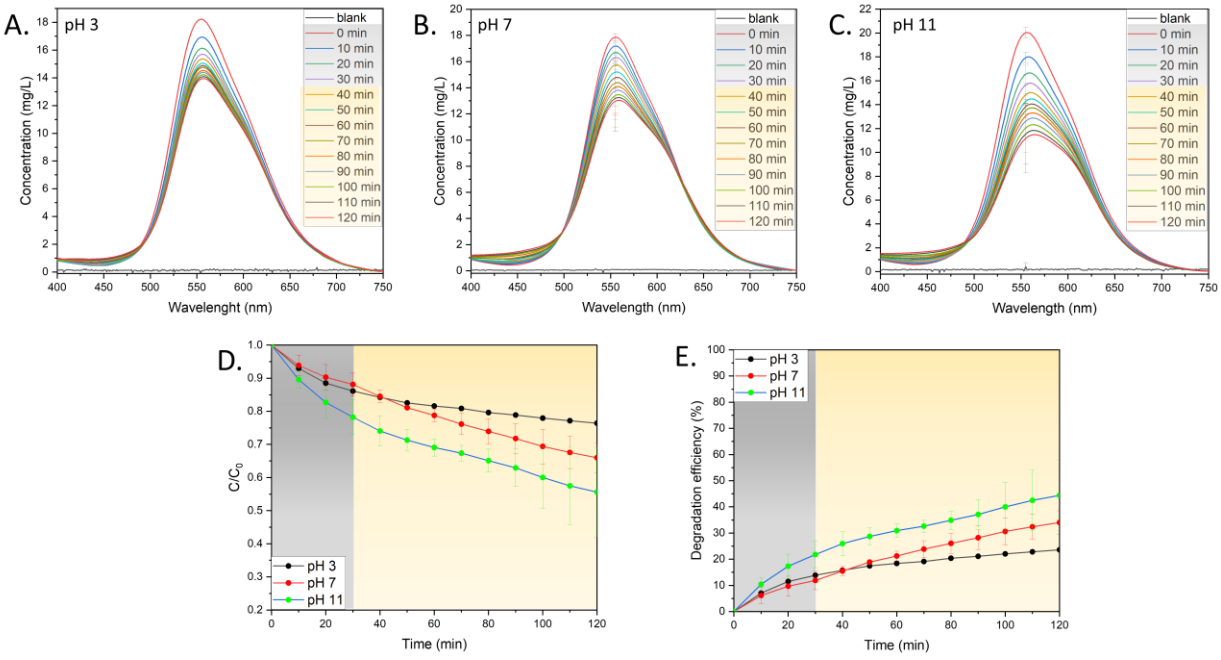

Figure 40 Influence of pH on the photocatalytic activity (A-C) UV–Vis spectral changes in the varying pH, (D) changes in dye concentration, (E) percentage degradation efficiency.

5.2.3.2.5 Influence of calcination

Finally, the influence of the calcination and the removal of the organic content was tested for the photocatalytic activity (Fig. 41). The Ag NPs AC showed only a slight decrease in the BBR dye concentration with degradation efficiency of 10.7% and k value of 0.00079 min^{-1}. In the same conditions, Ag NPs BC revealed a degradation efficiency around 34% with k value of 0.00280 min^{-1}. The BBR dye without any catalyst exhibits the degradation around 6.5% and k value of 0.00049

min^{-1}. Although calcination might cause morphology changes [34], it might also cause structural defects which might change the optical properties as shown in the UV-Vis findings. The photocatalytic activity of Ag/Ag_2O NPs after calcination was reported in the UVA spectrum, however, it might significantly increase the removal cost [35].

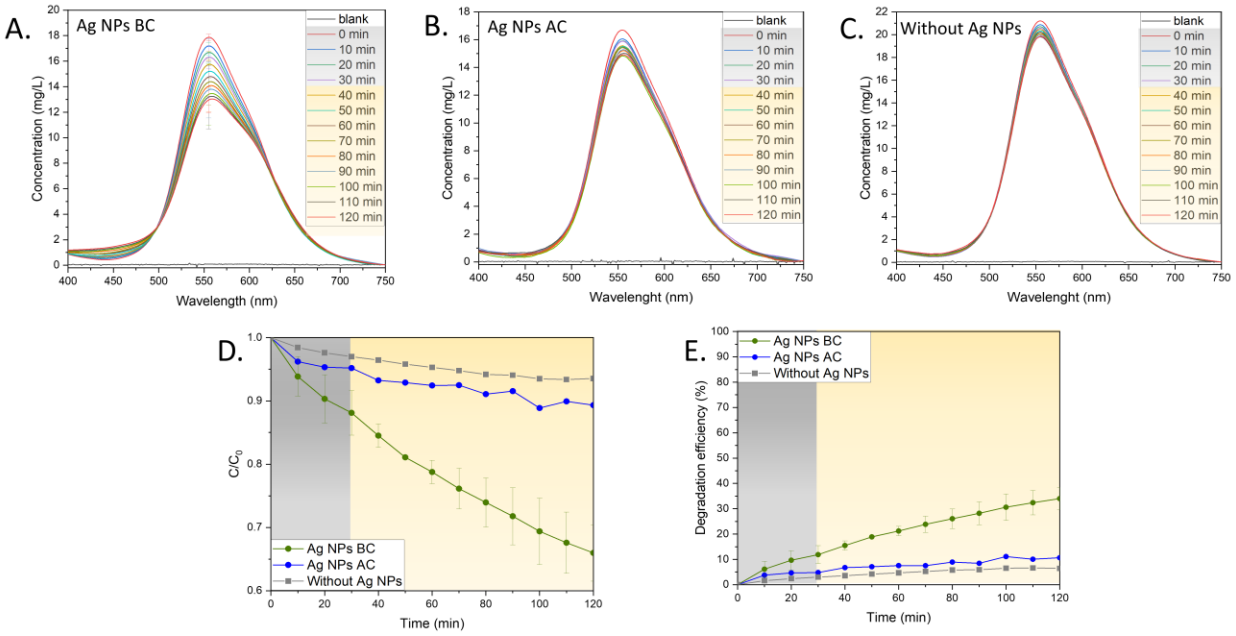

Figure 41 Influence of calcination on the photocatalytic activity (A) UV–Vis spectral changes before calcination, (B) UV–Vis spectral changes after calcination, (C) UV–Vis spectral changes without catalyst, (D) changes in dye concentration, (E) percentage degradation efficiency.

5.2.3.2.6 Mechanism of dye degradation

The mechanism of the BBR dye degradation is based on the photocatalytic action of Ag NPs BC [26,32,36]. First, light irradiation excites electrons (e^-) in the valence band to conduction band leaving behind positively charged holes (h^+) (4). Then, water molecules react with holes generating H^+ and •OH radical (5). The electrons transform molecular oxygen into $•O_2^-$(6), reacting with water molecules to produce •OOH (7). After rearrangement into H_2O_2 (8), it reacts with $•O_2^-$, producing •OH (9) which can be also produced after hydroxyl ions interact with holes (10). The above reactions are depicted below (4-10).

Photocatalyst surface + hv → electron (e^-) + hole (h^+) (4)

$h^+ + H_2O \rightarrow H^+ + \bullet OH$ (5)

$e^- + O_2 \rightarrow \bullet O_2^-$ (6)

$\bullet O_2^- + H_2O \rightarrow \bullet OOH + OH^-$ (7)

$2\bullet OOH \rightarrow H_2O_2 + O_2$ (8)

$H_2O_2 + \bullet O_2- \rightarrow \bullet OH + O_2 + OH^-$ (9)

$OH^- + h^+ \rightarrow \bullet OH$ (10)

The BBR dye degradation pathway was studied previously by LC-Q-TOF-MS analysis using another AOP method, ultrasound-based, which also involves generation of hydroxyl radicals [37]. Two degradation pathways were proposed, when first intermediates are a result of either OH addition or hydrogen abstraction followed by disproportionation/hydroxylation reaction [37]. The next products are a result of many occurring reactions such as bond breakage, oxidative cleavage, or demethylation. In total, 13 transformed products were identified which could undergo further ring opening and other oxidative cleavages resulting in the mineralization reaction [37]. The majority of aliphatic and aromatic substances undergo a process of conversion whereby they are ultimately transformed into inorganic ions, carbon dioxide, and water. Moreover, the degradation pathway was also tested in river water and revealed that it does not depend on the presence of inorganic ions [38].

5.2.4 Conclusions

Efficient and economical photocatalysts are crucial for high-performance reaction systems that combat water pollution. Ongoing research focuses on finding effective photoactive materials for photocatalytic dye removal reactions. This work presents sustainable production of Ag NPs BC and Ag NPs AC using methanolic extract of *H. pluvialis*. The XRD analysis displayed the Ag_2O and Ag phases in Ag NPs BC with crystalline size of 14.27 nm while only Ag phase was present in Ag NPs AC with crystalline size of 34.78 nm. The FTIR analysis showed an abundance of functional groups on Ag NPs BC surface. Irregular morphologies were observed in SEM analysis while elemental analysis confirmed the involvement of metabolites from the extract. Organic content

was further examined by TGA analysis showing decrease after calcination. The optical properties analyzed by UV-Vis revealed visible light activation of Ag NPs BC with band gap energy of 2.26 eV.

The Ag NPs BC were tested for the photocatalytic removal of BBR dye in the visible light tested the influence of light intensity, dye concentration, catalyst dosage, pH, and calcination. The highest degradation efficiency of 65.9% with k value of 0.00947 min^{-1} was achieved in the increased catalyst dosage. The mechanism of BBR dye degradation was proposed based on the obtained results. The work shows the potential of *H. pluvialis* as a source of metabolites which can be used to obtain highly valuable products.

5.2.5 References

1. T. Islam, M.R. Repon, T. Islam, Z. Sarwar, M.M. Rahman, Impact of textile dyes on health and ecosystem: a review of structure, causes, and potential solutions, Environ. Sci. Pollut. Res. 2022 304. 30 (2022) 9207–9242. https://doi.org/10.1007/S11356-022-24398-3.

2. R. Al-Tohamy, S.S. Ali, F. Li, K.M. Okasha, Y.A.G. Mahmoud, T. Elsamahy, H. Jiao, Y. Fu, J. Sun, A critical review on the treatment of dye-containing wastewater: Ecotoxicological and health concerns of textile dyes and possible remediation approaches for environmental safety, Ecotoxicol. Environ. Saf. 231 (2022) 113160. https://doi.org/10.1016/J.ECOENV.2021.113160.

3. J. Zhao, Q.X. Wu, X. Du Cheng, T. Su, X.H. Wang, W.N. Zhang, Y.M. Lu, Y. Chen, Biodegradation and detoxification of the triphenylmethane dye coomassie brilliant blue by the extracellular enzymes from mycelia of Lactarius deliciosus, Front. Chem. Sci. Eng. 15 (2021) 421–436. https://doi.org/10.1007/s11705-020-1952-7.

4. S. Rodríguez-Couto, Production of laccase and decolouration of the textile dye Remazol Brilliant Blue R in temporary immersion bioreactors, J. Hazard. Mater. 194 (2011) 297–302. https://doi.org/10.1016/J.JHAZMAT.2011.07.098.

5. S. Sarkar, A. Banerjee, U. Halder, R. Biswas, R. Bandopadhyay, Degradation of Synthetic Azo Dyes of Textile Industry: a Sustainable Approach Using Microbial Enzymes, Water Conserv. Sci. Eng. 2 (2017) 121–131. https://doi.org/10.1007/s41101-017-0031-5.

6. A. Iqbal, A. Yusaf, M. Usman, T. Hussain Bokhari, A. Mansha, Insight into the degradation of different classes of dyes by advanced oxidation processes; a detailed review, Int. J. Environ. Anal. Chem. (2023). https://doi.org/10.1080/03067319.2022.2125312.

7. M. Saeed, M. Muneer, A. ul Haq, N. Akram, Photocatalysis: an effective tool for photodegradation of dyes—a review, Environ. Sci. Pollut. Res. 2021 291. 29 (2021) 293–311. https://doi.org/10.1007/S11356-021-16389-7.

8. A. Naganthran, G. Verasoundarapandian, F.E. Khalid, M.J. Masarudin, A. Zulkharnain, N.M. Nawawi, M. Karim, C.A.C. Abdullah, S.A. Ahmad, Synthesis, Characterization and Biomedical

Application of Silver Nanoparticles, Mater. 2022, Vol. 15, Page 427. 15 (2022) 427. https://doi.org/10.3390/MA15020427.

9. A. Sidorowicz, T. Szymański, J.D. Rybka, Photodegradation of biohazardous dye brilliant blue r using organometallic silver nanoparticles synthesized through a green chemistry method, Biology (Basel). 10 (2021) 784. https://doi.org/10.3390/biology10080784.

10. V. Seerangaraj, S. Sathiyavimal, S.N. Shankar, J.G.T. Nandagopal, P. Balashanmugam, F.A. Al-Misned, M. Shanmugavel, P. Senthilkumar, A. Pugazhendhi, Cytotoxic effects of silver nanoparticles on Ruellia tuberosa: Photocatalytic degradation properties against crystal violet and coomassie brilliant blue, J. Environ. Chem. Eng. 9 (2021) 105088. https://doi.org/10.1016/J.JECE.2021.105088.

11. T. Thomas, A.K. Thalla, Synthesis of silver nanoparticles using Myristica fragrans seed shell: Assessment of antibacterial, antioxidant properties and photocatalytic degradation of dyes, J. Environ. Chem. Eng. 11 (2023) 109585. https://doi.org/10.1016/J.JECE.2023.109585.

12. S.N.H. Oslan, N.F. Shoparwe, A.H. Yusoff, A.A. Rahim, C.S. Chang, J.S. Tan, S.N. Oslan, K. Arumugam, A. Bin Ariff, A.Z. Sulaiman, M.S. Mohamed, A Review on Haematococcus pluvialis Bioprocess Optimization of Green and Red Stage Culture Conditions for the Production of Natural Astaxanthin, Biomol. 2021, Vol. 11, Page 256. 11 (2021) 256. https://doi.org/10.3390/BIOM11020256.

13. M.M.R. Shah, Y. Liang, J.J. Cheng, M. Daroch, Astaxanthin-producing green microalga Haematococcus pluvialis: From single cell to high value commercial products, Front. Plant Sci. 7 (2016) 172296. https://doi.org/10.3389/fpls.2016.00531.

14. M. Mecozzi, M. Pietroletti, M. Scarpiniti, R. Acquistucci, M.E. Conti, Monitoring of marine mucilage formation in Italian seas investigated by infrared spectroscopy and independent component analysis, Environ. Monit. Assess. 184 (2012) 6025–6036. https://doi.org/10.1007/s10661-011-2400-4.

15. S.J. Parikh, J. Chorover, Infrared spectroscopy studies of cation effects on lipopolysaccharides in aqueous solution, Colloids Surfaces B Biointerfaces. 55 (2007) 241–250. https://doi.org/10.1016/J.COLSURFB.2006.12.014.

16. Z. Gong, P. Fang, Z. Wang, X. Li, Z. Wang, F. Meng, Pyrolysis characteristics and products distribution of haematococcus pluvialis microalgae and its extraction residue, Renew. Energy. 146 (2020) 2134–2141. https://doi.org/10.1016/J.RENENE.2019.06.080.

17. C. Keskin, A. Ölçekçi, A. Baran, M.F. Baran, A. Eftekhari, S. Omarova, R. Khalilov, E. Aliyev, A. Sufianov, A. Beilerli, I. Gareev, Green synthesis of silver nanoparticles mediated Diospyros kaki L. (Persimmon): determination of chemical composition and evaluation of their antimicrobials and anticancer activities, Front. Chem. 11 (2023) 1187808. https://doi.org/10.3389/FCHEM.2023.1187808/BIBTEX.

18. B. Kis, E.A. Moacă, L.B. Tudoran, D. Muntean, I.Z. Magyari-Pavel, D.I. Minda, A. Lombrea, Z. Diaconeasa, C.A. Dehelean, Ștefania Dinu, C. Danciu, Green Synthesis of Silver Nanoparticles Using Populi gemmae Extract: Preparation, Physicochemical Characterization, Antimicrobial Potential and In Vitro Antiproliferative Assessment, Mater. 2022, Vol. 15, Page 5006. 15 (2022) 5006. https://doi.org/10.3390/MA15145006.

19. M.E.E. Zin, P. Moolkaew, T. Junyusen, W. Sutapun, Preparation of hybrid particles of Ag nanoparticles and eggshell calcium carbonate and their antimicrobial efficiency against beef-extracted bacteria, R. Soc. Open Sci. 10 (2023). https://doi.org/10.1098/RSOS.221197.

20. F. Khan, A. Shahid, H. Zhu, N. Wang, M.R. Javed, N. Ahmad, J. Xu, M.A. Alam, M.A. Mehmood, Prospects of algae-based green synthesis of nanoparticles for environmental applications, Chemosphere. 293 (2022) 133571. https://doi.org/10.1016/J.CHEMOSPHERE.2022.133571.

21. S. Pirtarighat, M. Ghannadnia, S. Baghshahi, Green synthesis of silver nanoparticles using the plant extract of Salvia spinosa grown in vitro and their antibacterial activity assessment, J. Nanostructure Chem. 9 (2019) 1–9. https://doi.org/10.1007/s40097-018-0291-4.

22. Z. Ma, J. Liu, Y. Liu, X. Zheng, K. Tang, Green synthesis of silver nanoparticles using soluble soybean polysaccharide and their application in antibacterial coatings, Int. J. Biol. Macromol. 166 (2021) 567–577. https://doi.org/10.1016/J.IJBIOMAC.2020.10.214.

23. L. Baia, S. Simon, UV-VIS and TEM assessment of morphological features of silver nanoparticles from phosphate glass matrices, Mod. Res. Educ. Top. …. (2007) 576–583. http://www.formatex.org/microscopy3/pdf/pp576-583.pdf (accessed August 11, 2023).

24. M.A.; Malik, M.G.; Batterjee, M.R.; Kamli, K.A.; Alzahrani, E.Y.; Danish, A. Nabi, M.A. Malik, M.G. Batterjee, M.R. Kamli, K.A. Alzahrani, E.Y. Danish, A. Nabi, Polyphenol-Capped Biogenic Synthesis of Noble Metallic Silver Nanoparticles for Antifungal Activity against Candida auris, J. Fungi 2022, Vol. 8, Page 639. 8 (2022) 639. https://doi.org/10.3390/JOF8060639.

25. G. Ohemeng-Boahen, D.D. Sewu, H.N. Tran, S.H. Woo, Enhanced adsorption of congo red from aqueous solution using chitosan/hematite nanocomposite hydrogel capsule fabricated via anionic surfactant gelation, Colloids Surfaces A Physicochem. Eng. Asp. 625 (2021) 126911. https://doi.org/10.1016/J.COLSURFA.2021.126911.

26. I. Groeneveld, M. Kanelli, F. Ariese, M.R. van Bommel, Parameters that affect the photodegradation of dyes and pigments in solution and on substrate – An overview, Dye. Pigment. 210 (2023) 110999. https://doi.org/10.1016/J.DYEPIG.2022.110999.

27. D.F. Ollis, E. Pelizzetti, N. Serpone, Destruction of water contaminants, Environ. Sci. Technol. 25 (1991) 1522–1529. https://doi.org/10.1021/es00021a001.

28. N.A.M. Barakat, M.A. Kanjwal, I.S. Chronakis, H.Y. Kim, Influence of temperature on the photodegradation process using Ag-doped TiO2 nanostructures: Negative impact with the nanofibers, J. Mol. Catal. A Chem. 366 (2013) 333–340. https://doi.org/10.1016/J.MOLCATA.2012.10.012.

29. R. Kishor, D. Purchase, G.D. Saratale, R.G. Saratale, L.F.R. Ferreira, M. Bilal, R. Chandra, R.N. Bharagava, Ecotoxicological and health concerns of persistent coloring pollutants of textile

industry wastewater and treatment approaches for environmental safety, J. Environ. Chem. Eng. 9 (2021) 105012. https://doi.org/10.1016/J.JECE.2020.105012.

30. A. Nawaz, M. Atif, A. Khan, M. Siddique, N. Ali, F. Naz, M. Bilal, T.H. Kim, M. Momotko, H.U. Haq, G. Boczkaj, Solar light driven degradation of textile dye contaminants for wastewater treatment – studies of novel polycationic selenide photocatalyst and process optimization by response surface methodology desirability factor, Chemosphere. 328 (2023) 138476. https://doi.org/10.1016/J.CHEMOSPHERE.2023.138476.

31. V. Javanbakht, M. Mohammadian, Photo-assisted advanced oxidation processes for efficient removal of anionic and cationic dyes using Bentonite/TiO2 nano-photocatalyst immobilized with silver nanoparticles, J. Mol. Struct. 1239 (2021) 130496. https://doi.org/10.1016/J.MOLSTRUC.2021.130496.

32. Q. Lin, X. Huang, L. Lu, D. Tang, Snowflake-like CdS@ZnIn2S4 heterojunction-based photocatalyst-electrolyte effect: An innovative mode for photoelectrochemical immunoassay, Biosens. Bioelectron. 216 (2022) 114679. https://doi.org/10.1016/J.BIOS.2022.114679.

33. H.B. Uma, S. Ananda, M.B. Nandaprakash, High efficient photocatalytic treatment of textile dye and antibacterial activity via electrochemically synthesized Ni-doped ZnO nano photocatalysts, Chem. Data Collect. 24 (2019) 100301. https://doi.org/10.1016/J.CDC.2019.100301.

34. X. Yang, Y. Liu, J. Li, Y. Zhang, Effects of calcination temperature on morphology and structure of CeO2 nanofibers and their photocatalytic activity, Mater. Lett. 241 (2019) 76–79. https://doi.org/10.1016/J.MATLET.2019.01.006.

35. N. Khandan Nasab, Z. Sabouri, S. Ghazal, M. Darroudi, Green-based synthesis of mixed-phase silver nanoparticles as an effective photocatalyst and investigation of their antibacterial properties, J. Mol. Struct. 1203 (2020) 127411. https://doi.org/10.1016/J.MOLSTRUC.2019.127411.

36. A. Ahmed, M. Usman, B. Yu, X. Ding, Q. Peng, Y. Shen, H. Cong, Efficient photocatalytic degradation of toxic Alizarin yellow R dye from industrial wastewater using biosynthesized Fe nanoparticle and study of factors affecting the degradation rate, J. Photochem. Photobiol. B Biol. 202 (2020) 111682. https://doi.org/10.1016/J.JPHOTOBIOL.2019.111682.

37. M.P. Rayaroth, U.K. Aravind, C.T. Aravindakumar, Sonochemical degradation of Coomassie Brilliant Blue: Effect of frequency, power density, pH and various additives, Chemosphere. 119 (2015) 848–855. https://doi.org/10.1016/J.CHEMOSPHERE.2014.08.037.

38. M.P. Rayaroth, U.K. Aravind, C.T. Aravindakumar, Ultrasound based AOP for emerging pollutants: from degradation to mechanism, Environ. Sci. Pollut. Res. 24 (2017) 6261–6269. https://doi.org/10.1007/s11356-016-6606-4.

5.3 Investigating eco-friendly photocatalysis of Brilliant Blue R using silver nanoparticles derived from *S. platensis*

5.3.1 Introduction

While industrialization has improved standards of living, it has also had a negative impact on the environment by producing hazardous chemical species. The produced contaminants are mostly organic dyes, which are waste products of the tanneries, paint, and textile industries [1]. Subsequently, their discharge into water bodies without proper treatment can be a major source of water pollution. Due to their complex aromatic structure, they can maintain toxicity and stability over a prolonged time, ultimately damaging aquatic life and human health [2]. Their engineered ability to resist degradation hinders biodegradability [3]; therefore, the research focuses on the development of various techniques to combat this issue.

One of the most efficient methods used for wastewater treatment is the advanced oxidation process (AOP), such as photocatalysis. The mechanism behind it relies on the absorption of light energy higher than the band gap energy of the catalyst, which results in the excitation of the electron in the valence band to the conduction band, leaving behind the holes [4]. The electron-hole pairs participate in redox reactions generating reactive oxygen species (ROS), such as hydroxyl radicals, which oxidize the dye into lower molecular weight products [5]. The efficiency of the process relies on the properties of the used catalyst, such as band gap energy or electron transfer [6]; thus, various synthesis techniques were studied to obtain highly valuable products.

Considering many synthesis routes, the biological approach has emerged as an alternative way to decrease high operating costs and the generation of toxic by-products [7]. Various organisms have been utilized due to the abundance of metabolites in their structure that can act as reducing and stabilizing agents during the synthesis of nanoparticles [7]. Recently, microalgae typically studied for their nutritional value, are gaining more attention also as a source of metabolites that can participate in the synthesis of nanoparticles [8]. Other advantages of microalgae include rapid growth and ease of cultivation, which shows their potential to prepare a variety of materials for a wide range of applications.

Among many microalgae, *Spirulina platensis* has a significantly increased protein content besides a high concentration of vitamins, essential fatty acids, and minerals [9]. The *S. platensis* biomass has been utilized in the past for the synthesis of silver nanoparticles (Ag NPs) tested against malachite green biosorption from wastewater [10]. Moreover, the Ag NPs photocatalytic activity was studied against methylene blue and eosin y, showing excellent dye degradation properties [11,12]. However, to the best of our knowledge, Ag NPs synthesized using *S. platensis* have not been studied for the degradation of Brilliant Blue R (BBR), a common laboratory dye used mainly for protein staining.

In the current work, the methanolic extract from *S. platensis* was utilized for the synthesis of Ag NPs. The product was also calcined to determine the influence of organic capping agents on the structure and activity. The material was characterized and applied for the photocatalytic degradation of BBR in the varying parameters of light intensity, dye concentration, catalyst concentration, pH, or presence or absence of organic content. The photocatalytic mechanism was studied to develop a better understanding of the degradation pathway, which might aid in optimization of the conditions for the removal of hazardous BBR dye from the environment.

5.3.2 Materials and methods

5.3.2.1 Preparation of photocatalyst

The *Spirulina platensis* (courtesy of TOLO Green, Arborea, Italy) was cultivated in modified Zarrouk Medium. The medium was prepared while K_2SO_4 and $MgSO_4$ were added aseptic after setting pH to 9 and autoclaving. The culture was cultivated under continuous illumination of 58W fluorescent lamps (Osram®) with a photon flux of 30 µmol/m^{-2}/s^{-1} and stirring for 30 days to obtain a suitable amount of biomass. Then, it was centrifuged at 1500 RPM at 4°C (Heraeus® Megafuge® 1.0R) and the algal biomass was dried at room temperature.

In the next step, 4.3 g of dried residue was combined with 260 mL of methanol (Merck® LiChrosolv® hypergrade). The flask was sonicated for 30 min (Soltec® Sonica® 2400 ETH S3) and stirred at 250 RPM (IKA® RH Digital Magnetic Stirrer) for the next 30 min to release the cell content into the solvent. In order to remove the cell debris, the suspension was filtered using standard filtration paper (Whatman®) and then evaporated using rotary evaporator (BUCHI

Rotavapor™ R-210 Rotary Evaporator System) to remove about 70% of methanol. The concentrated extract was then diluted with MiliQ H_2O (Millipore®, Milan, Italy) to the final volume of 520 mL and used for the synthesis of nanoparticles.

The flask containing *S. platensis* extract was heated to 85°C and stirred at 250 RPM (IKA® RH Digital Magnetic Stirrer). Then, 0.1 M of silver nitrate (Carlo Erba®) was added, and after 15 min the pH was raised to 8 by using 1.25 M NaOH. From the moment of adding the salt, the reaction continued for 1.5 h and then it was left for maturation in room temperature. Subsequently, the liquid was centrifuged at 4000 RPM at 8°C (Heraeus® Megafuge® 1.0R) and the residue was repeatedly washed with MiliQ H_2O (Millipore®, Milan, Italy) in the two washing cycles. Then, the residue was dried at 80°C for 24 h, ground using mortar and pestle and divided into two parts. One part was stored in Eppendorf tube in absence of light and the other was calcined in muffle furnace (Gelman Instrument®) for 2 h at 600°C. After calcination, the samples were stored in the same conditions as the samples before calcination.

5.3.2.2 Characterization

The X-Ray Diffraction (XRD) analysis of Ag NPs was performed using X-Ray Diffractometer (Phillips®, PW1830/00, Nederlands and D8 Advance, Bruker AXS®). The scanning was conducted with a diffraction angle between 12° and 90° at 0.1° per 10 s, at 40 kV and 30 mA using CuKα (λ =1.54 Å) radiation. Phase identification was obtained by using Diffrac.Eva software v.6.1.0.4 according to the COD database. The crystallite size was calculated after baseline correction using Debye-Scherrer's formula.

Functional groups present on Ag NPs were analyzed using Fourier Transform Infrared Spectroscopy (FT/IR-6700, Jasco, Tokyo, Japan) in the range 500-4000 cm^{-1}.

Scanning Electron Microscopy (SEM) analysis was conducted using Hitachi S4000 FEG HRSEM (Hitachi Ltd., Tokyo, Japan) operated at 20 kV with image acquisition software Quartz PCI (Quartz Imaging Corporation, Vancouver, Canada). Before the analysis, the samples were coated with 2 nm of platinum to enhance the contrast. EDX analysis was obtained using UltraDry EDX Detector (Thermo Fisher Scientific®, Madison, Wisconsin, USA), and NSS3 software (Thermo Fisher Scientific®, Madison, Wisconsin, USA).

Thermal properties were examined by Thermogravimetric Analysis (TGA using Differential Thermal Analyzer TG/DSC (NETZSCH® STA 409 PC) in a heating range 25 – 1000°C at 10°C/min with airflow 100 mL/min.

UV-Vis absorption measurements were carried out using CARY 50 spectrophotometer (Varian Inc., Australia) with a cell path length of 10 mm. UV-Vis spectra of Ag NPs were recorded in the wavelength range of 200–750 nm. The direct bandgap energy was calculated from the Tauc relation (Equation 1):

$$(\alpha h\nu)^2 = (h\nu - E_g) \quad (1)$$

Where α is the molar extinction coefficient, h is the Plank's constant, ν is the light frequency, and E_g is the band gap energy. The bandgap energy was calculated by linear fit extrapolation of the plot of $(\alpha h\nu)^2$ against energy.

5.3.2.3 In-situ photocatalysis

First, calibration line was obtained by assessing the correlation between absorbance and concentration of the dye. Before each photocatalytic experiment, 50 mL of ddH2O was mixed with Ag NPs and sonicated for 15 min in a sonication bath (Soltec® Sonica® 2400 ETH S3) to ensure even dispersion. Firstly, the baseline of the solution of dispersed Ag NPs was generated. Then, the reaction sample was mixed with various concentrations of BBR (Sigma-Aldrich®) dye in ethanol (500 mg/L). The flask was constantly stirred for 30 min in the dark to ensure that equilibrium was reached. Next, the solution was irradiated by a warm white 10.5 W LED bulb (Phillips), and the irradiation intensity was monitored by a luxmeter (HD2302.0 Delta-Ohm, Padua, Italy). The emission spectrum as provided by the manufacturer is shown in Fig. 42. The peristaltic pump (Keenso DC) was used to circulate the liquid between the flask and a 10 mm flow-through cuvette attached to the UV-Vis Spectrophotometer (Cary 50, Varian®) operating in the range of 400-750 nm. The UV-Vis measurements were conducted every 10 min. The experiments with the highest degradation efficiency were performed in triplicate.

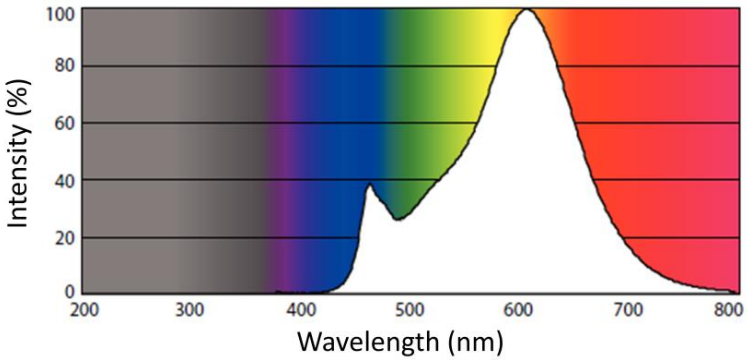

Figure 42 Emission spectrum of the light source provided by manufacturer.

The efficiency of the photocatalysis by the synthesized Ag NPs was calculated using Equation 2 as:

$$Degradation\ efficiency\ (\%) = 100 - \left({}^{C}/_{C_0} \cdot 100\right) \quad (2)$$

where C_0 is the initial concentration of the BBR dye and C is the final concentration of the pollutant at the end of the degradation period.

The obtained data were fit using OriginPro 2021© 9.8 according to the pseudo-first order reaction model according to the Equation 3:

$$C = C_0 * e^{-{}^{k}/_{t}} \quad (3)$$

Where t is time and k (min^{-1}) is the reaction constant.

5.3.3 Results and discussion

5.3.3.1 Characterization

The XRD analysis has proven to be an effective method for revealing the crystal structure of Ag NPs to determine their atomic arrangement, providing valuable insights into their physical and chemical properties (Fig. 43). The XRD spectrum of Ag NPs BC revealed the presence of mainly AgCl (COD 9011666 and COD 9011673) and Ag (COD 1100136) phases with organic capping agents at 20°. After calcination, only Ag (COD 1509146) phase was identified in Ag NPs AC. The average crystalline size was determined after measuring full width at half maximum (FWHM)

values and using Debye-Scherrer's formula with 15.22 nm for AgCl and 9.72 nm for Ag with average of 13.02 nm for Ag NPs BC. The calcination increased the crystalline size to 24.35 nm for Ag NPs AC.

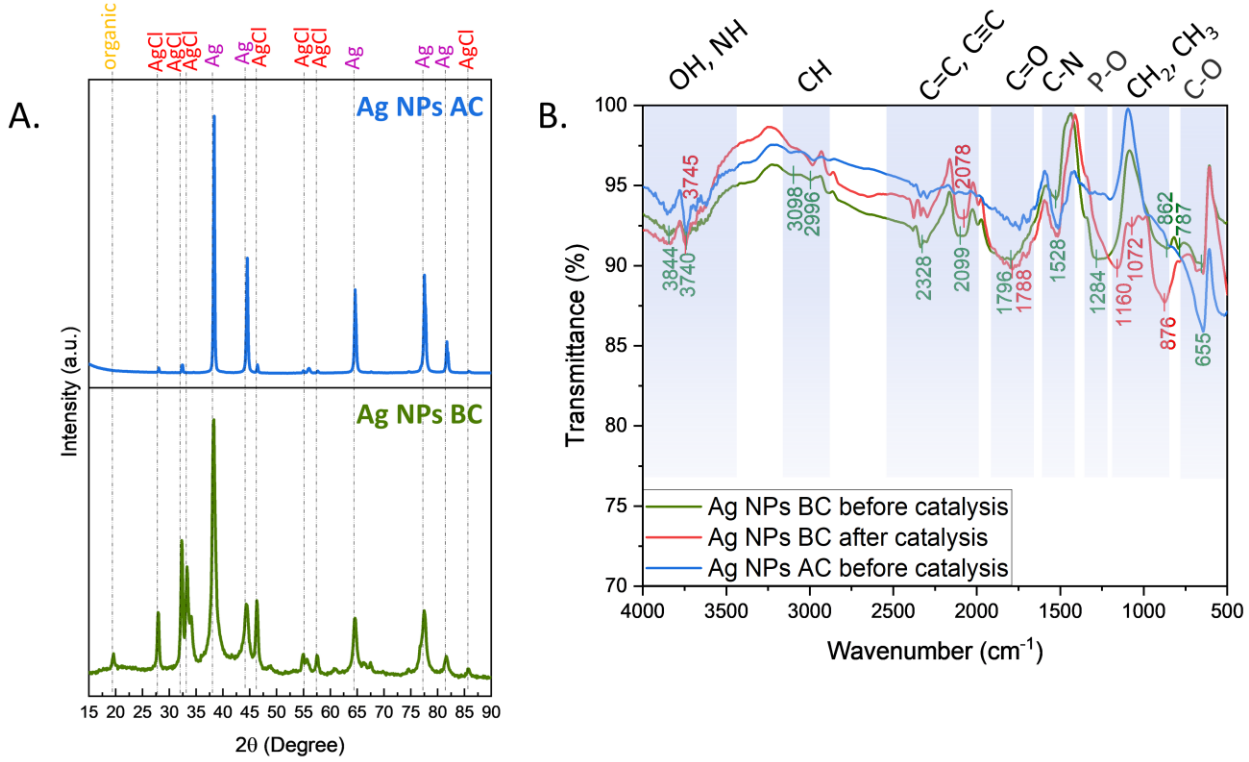

Figure 43 Crystallographic and spectroscopic analyses (A) XRD, (B) FTIR, BC – before calcination, AC – after calcination.

The synthesis mechanism of Ag NPs was studied previously and revealed the involvement of methylamine, diethanolamine, and ethanamine as reducing and stabilizing agents [13]. The phase transition and increase in the crystalline size signify the important role of metabolites in stabilizing the structure. Both AgCl and Ag phases in Ag NPs have been reported as a result of intracellular synthesis using *Dunaliella salina* and *Scenedesmus sp*. [14,15]. In the current study, the metabolites from the cell were successfully released during extract preparation and the synthesis occurred extracellularly which decreased the time needed to obtain the product. The organic coating on the surface of Ag NPs was further examined by FTIR analysis.

The FTIR technique showed an abundance of functional groups on the surface of Ag NPs such as OH, NH, C=C, C≡C, C=O, C-N, P-O, CH_2, CH_3, and C-O originating from the *S. pluvialis* extract used for the synthesis [13,16]. The spectra of Ag NPs BC before and after catalysis display the difference in intensity mainly in the wavenumber areas attributed to C=C, C≡C and CH_2, CH_3 groups which confirms their involvement in the photocatalytic generation of radicals. The Ag NPs AC exhibit a higher transmittance intensity compared with Ag NPs BC, which proves partial removal of the organic content due to the calcination.

The morphological properties of the obtained Ag NPs were studied using SEM and EDX analyses (Fig. 44). The obtained Ag NPs BC are spherical or quasi-spherical in shape with silver, chlorine, oxygen, carbon, phosphorus, and sulfur in their structure with homogeneous distributions. The Ag NPs AC are more agglomerated or coalescent while maintaining the tendency towards spherical or quasi-spherical shape. In the elemental analysis of Ag NPs AC only silver, oxygen, carbon, and phosphorous were detected with homogenous distributions. Due to calcination, the organic content was partially removed which decreased the Ag NPs stability and caused the agglomeration of the material.

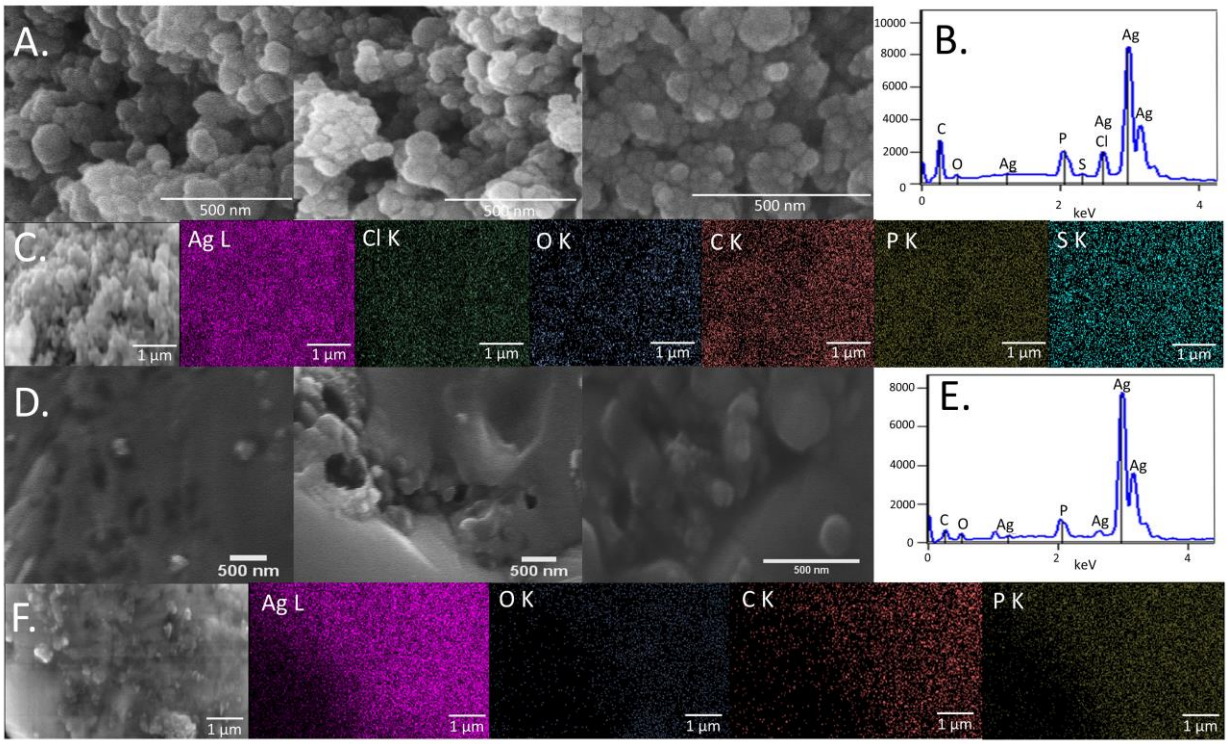

Figure 44 Microscopy analysis, (A) SEM of Ag NPs BC, (B) EDX spectrum of Ag NPs BC, (C) EDX mappings of Ag NPs BC, (D) SEM of Ag NPs AC, (E) EDX spectrum of Ag NPs AC, (F) EDX mappings of Ag NPs AC.

Thermal behavior of the obtained products was examined by TGA technique (Fig. 45A-C). The Ag NPs BC show three stages of mass loss at the ranges 25 - 250°C, 250 - 550°C, and 550 - 1000°C. The first decrease with 7.5% weight loss and DTG peak at 182°C can be attributed to the loss of physically adsorbed water molecules or decomposition of temperature-sensitive organic compounds [17]. The removal of organic compounds progresses in the next stage, with 4.9% weight loss and DTG peak at 380°C when phenolic compounds decompose on the surface [18]. Then, the weight decreased by 5.7% with the DTG peak close to 1000°C signifying the decomposition of higher molecular weight compounds or molecular oxygen removal [13,17]. The final weight of Ag NPs BC was recorded at around 80%. In addition, DTA analysis provided information about the exothermic nature of the organic content decomposition with various peaks at 25 - 600°C signifying the presence of the abundance of compounds on the surface of Ag NPs BC. The endothermic peak at 960°C is attributed to the melting point of silver present in the structure [19].

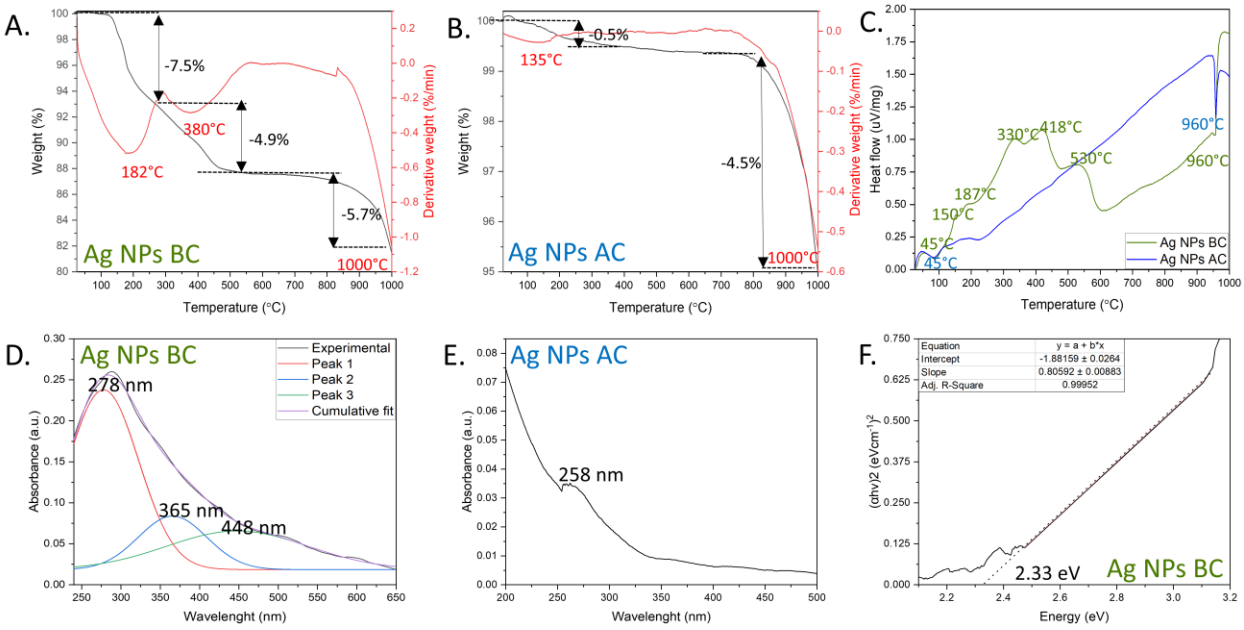

Figure 45 Thermal and optical properties of Ag NPs, (A) TG and DTG of Ag NPs BC, (B) TG and DTG of Ag NPs AC, (C) DTA of Ag NPs BC and Ag NPs AC, (D) UV-Vis spectrum of Ag NPs BC, (E) UV-Vis spectrum of Ag NPs AC, (F) Tauc plot of Ag NPs BC.

Thermal properties of Ag NPs AC were also assessed. The slight weight loss of 0.5% with the DTG peak at 135°C can relate to the water loss or oxidation of the remaining organic content. The most significant weight loss of 4.5% with DTG peak at around 1000°C is similar to Ag NPs BC. The weight at the end of the measurement was recorded at around 95%. The DTA analysis revealed a low intensity exothermic peak at around 45°C and endothermic peak at 960°C which represent melting point of silver. The TGA analysis confirmed the difference in the amount of organic content in Ag NPs BC and Ag NPs AC. Moreover, the metabolites showed different thermal behavior manifesting itself in the presence of many peaks especially in DTA analysis which proves the abundance of molecules as observed in the FTIR analysis.

The optical properties of Ag NPs BC and Ag NPs AC were analyzed using UV-Vis spectroscopy (Fig. 45D-E). Plasmonic nanoparticles such as Ag NPs can exhibit surface plasmon resonance when electrons in the conductive band excited at specific wavelength undergo a collective oscillation. The effect enables strong light scattering and absorption which are important for the photocatalytic activity. The Ag NPs BC display broad absorption band which after deconvolution

can be divided into three separate peaks. The peaks at 278 nm and 365 nm can be attributed to the organic molecules present on the surface. In the literature, the metabolites present in the extract were previously detected in similar range [20]. Moreover, the peak at 448 nm can be assigned to characteristic Ag NPs surface plasmon resonance typically in the 400 – 500 nm range [21]. The results show the potential of Ag NPs BC to be photoactivated in the visible light spectrum.

Obtained Ag NPs AC display one peak at 258 nm which might be a result of structural defects and change in the electronic state due to the calcination procedure [22]. A similar behavior has been reported before as a result of electronic transition to metallic Ag [22] which is correlated with the XRD findings. Consequently, the calcination procedure might have impaired the photocatalytic activity of Ag NPs AC.

The optical properties were also characterized by the calculation of band gap energy. The parameter is defined as an energy difference between the highest occupied energy state in the valence band and the lowest unoccupied energy state in conduction band. Low band gap value facilities the ability of the material to absorb light, generate electron-hole pairs, and initiate photocatalytic reactions. Based on the UV-Vis absorption, the band gap energy for Ag NPs BC was calculated at 2.33 eV (Fig. 45F). A similar band gap value has been reported for Ag NPs synthesized using plant *Hagenia abyssinica (Brace) JF. Gmel.* extract [23].

5.3.3.2 Photocatalytic activity

5.3.3.2.1 Influence of light

The BBR dye degradation activity of Ag NPs BC was first analyzed in dark conditions (Fig. 46). The highest decrease in dye concentration was recorded at around 30 min with following further slight concentration reduction. The interplay between dye and Ag NPs BC can be described as physisorption mainly connected with weak van der Waals forces [24]. At the end of the measurement around 33% of the dye molecules were degraded and the k value was recorded as 0.00380 min^{-1}. In the next experiments, the reaction was subjected to 30 min in the dark at the beginning to allow more precise evaluation of the tested factors on the photocatalytic activity of Ag NPs BC.

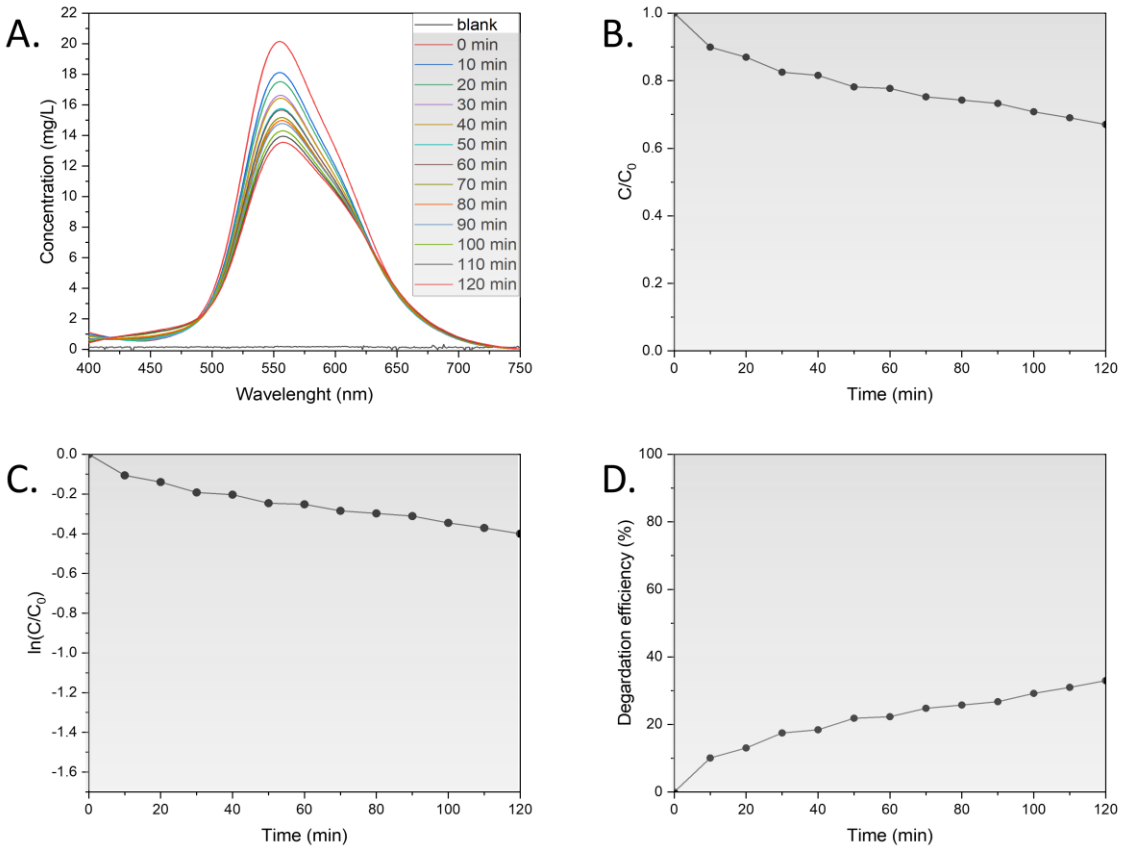

Figure 46 Degradation of BBR dye in the dark (A) UV–Vis spectral changes for the degradation of dye, (B) changes in dye concentration, (C) pseudo-first-order kinetic plot, (D) percentage degradation efficiency.

The initial evaluation of photocatalytic activity of Ag NPs BC involved the assessment of various levels of light intensities of 75, 150, and 300 µmol/m^2/s (Fig. 47). In photocatalysis, electron-hole pairs production relies on light exposure intensity and is a crucial step for creating active radicals to degrade pollutants [25]. As light intensity increases, more electrons transition from valence to conduction bands, resulting in the generation of hydroxyl or oxygen radicals [26]. In the series of experiments, the concentration of BBR dye was measured with time to evaluate the performance of Ag NPs BC.

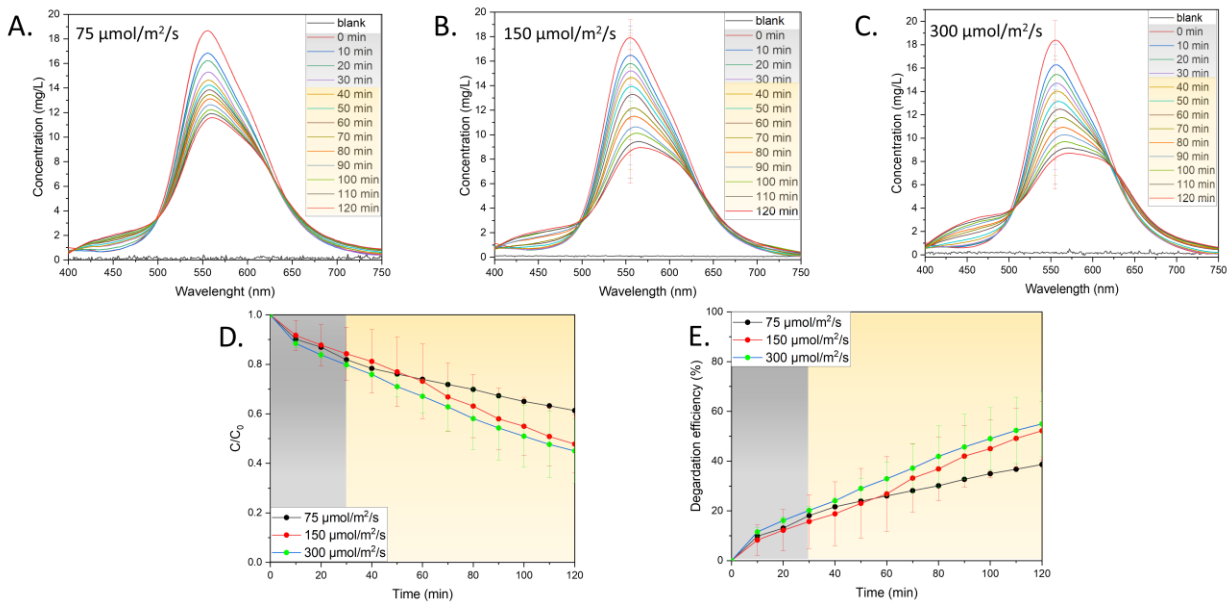

Figure 47 Influence of light on the photocatalytic activity (A-C) UV–Vis spectral changes in the varying light irradiation, (D) changes in dye concentration, (E) percentage degradation efficiency.

The lowest tested light intensity resulted in the lowest decrease in the BBR dye concentration with degradation efficiency of around 39% and k value of 0.00326 min^{-1}. The increase in light intensity to 150 µmol/m^2/s revealed significant increase in degradation efficiency to around 52.2% and k value of 0.00595 min^{-1}. Further increase in light intensity to 300 µmol/m^2/s showed only a slight increase in degradation efficiency to around 55% with k value of 0.00632 min^{-1}. The results can be explained in the context of the quantum yield of photodegradation which is described as the ratio of absorbed photons that result in a molecular reaction to the total number of absorbed photons [26]. High quantum yield increases the likelihood of the molecular reaction while the energy in low quantum yield can be converted to heat or fluorescence [26]. Overall, the results show the important role of light intensity for the photocatalytic activity of Ag NPs BC.

5.3.3.2.2 Influence of dye concentration

The light intensity can also be influenced by the concentration of the BBR dye in the solution. The light illuminating the system can also be absorbed by the BBR dye molecules which decreases the number of photons reaching catalyst surface and leading to generation of fewer radicals. The effect of various BBR dye concentrations in the range 4-26 mg/L on the photocatalytic activity of

Ag NPs BC is presented in Fig. 48. As expected, the lowest concentration of the BBR dye resulted in the highest decrease in the concentration with time with degradation efficiency around 73.8% and k value of 0.00986 min^{-1}. The increase in the concentration to 18 mg/L showed a decrease in the degradation efficiency at around 52.2% with k value of 0.00595 min^{-1}. The highest tested BBR dye concentration revealed the degradation efficiency around 31% with k value 0.00276 min^{-1}. The high concentration of the BBR dye in the solution might not only impart light scattering, but also it can result in the competing action of the molecules for access to the active sites on catalyst surface resulting in agglomeration [27]. However, usually the BBR dye concentration in the wastewater is low due to the multiple washings [28] which shows the potential of Ag NPs BC for the removal of BBR dye.

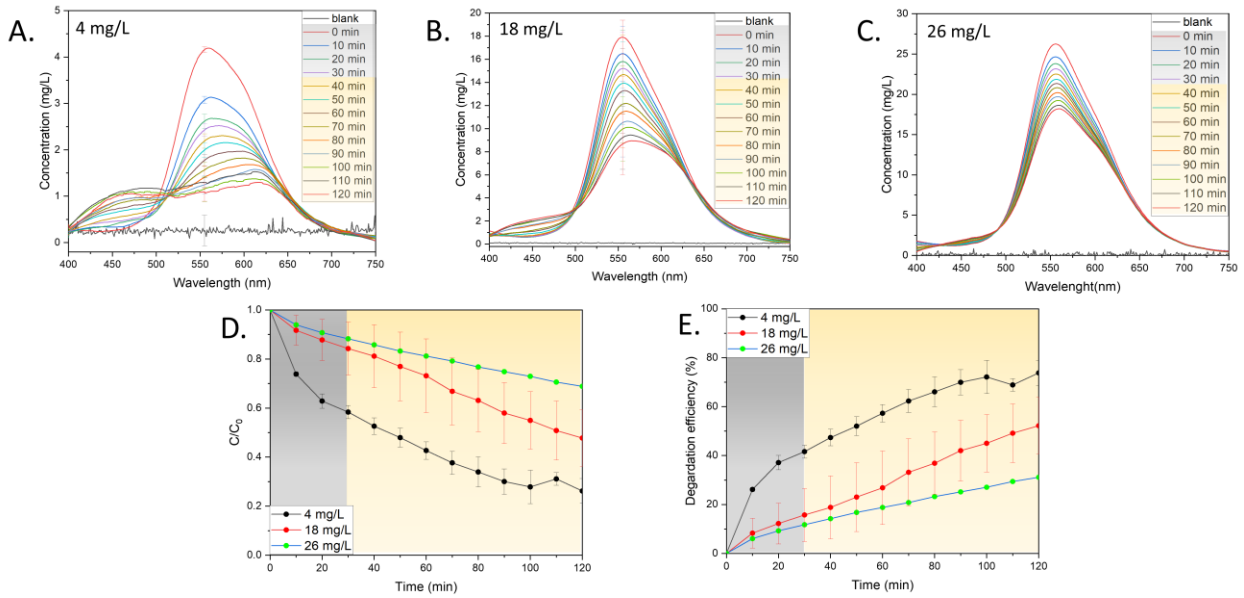

Figure 48 Influence of dye concentration on the photocatalytic activity (A-C) UV–Vis spectral changes in the varying dye concentration, (D) changes in dye concentration, (E) percentage degradation efficiency.

5.3.3.2.3 Influence of catalyst dosage

The access to the active sites on the surface of Ag NPs BC was tested by measuring the BBR dye concentration in the presence of various catalyst concentrations in the range 500-2000 mg/L (Fig. 49). As expected, the tested lowest catalyst dosage of 500 mg/L resulted in the lowest decrease in the BBR dye concentration with degradation efficiency of 36.7% and k value of 0.00272 min^{-1}. Further increase in the catalyst dosage raised the degradation efficiency to around 52.2% and

71.9% with k values of 0.00595 min^{-1} and 0.00933 min^{-1} for 1000 mg/L and 2000 mg/L respectively. The results showed the important role of active sites on Ag NPs BC surface to improve the photocatalytic degradation of BBR dye [27]. However, it has been reported that the trend is only up to certain limits as the excess amount of added catalyst might increase turbidity which renders the light scattering [29].

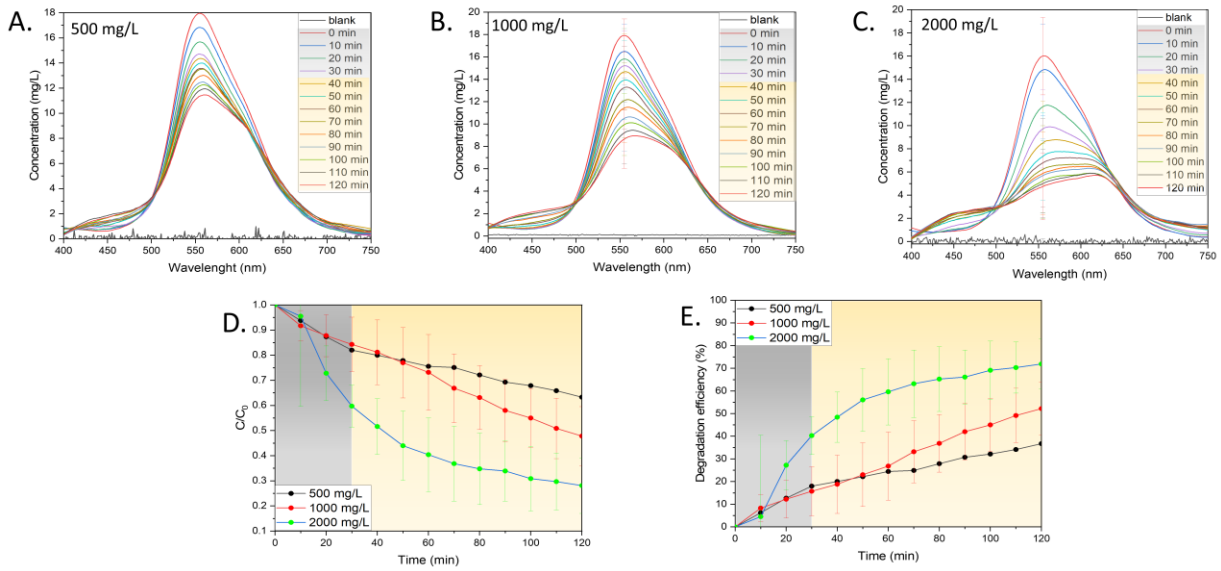

Figure 49 Influence of catalyst concentration on the photocatalytic activity (A-C) UV–Vis spectral changes in the varying catalyst concentration, (D) changes in dye concentration, (E) percentage degradation efficiency.

5.3.3.2.4 Influence of pH

The next tested factor for the photocatalytic activity of Ag NPs BC was pH of the solution in the range 3-11 (Fig. 50). In acidic conditions, the decrease in the BBR dye was the least prominent and degradation efficiency was recorded at around 47.3% with k value of 0.00443 min^{-1}. The neutral pH showed a degradation efficiency of around 52.2% with k value of 0.00595 min^{-1}. The alkaline conditions resulted in the degradation efficiency of 81.9% and k constant of 0.01496 min^{-1}. The description of the pH role can be challenging, primarily due to the pH-dependence of many processes such as electrostatic interactions of the catalyst surface with other molecules, such as solvent, substrate, and generated charged radicals [30]. In the present study, increased BBR removal with increasing pH could relate to higher accessibility of hydroxyl anions which after interactions with positive holes on the catalyst can result in the elevated concentration of

hydroxyl radicals [31]. The effect might persist until a certain pH when the radical rate formation is decreased due to Coulomb repulsion between the negatively charged surface of the catalyst and hydroxyl anions [32].

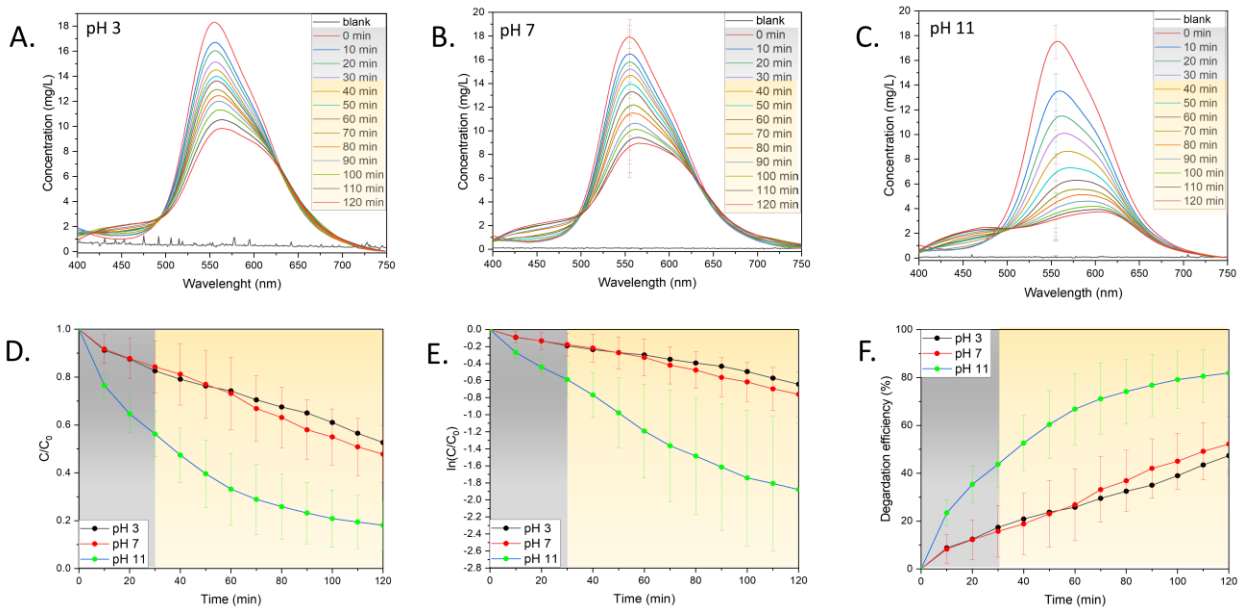

Figure 50 Influence of pH on the photocatalytic activity (A-C) UV–Vis spectral changes in the varying pH, (D) changes in dye concentration, (E) pseudo-first-order kinetic plot, (F) percentage degradation efficiency.

5.3.3.2.5 Influence of calcination

In the final set of experiments, the influence of calcination and the resulting removal of organic content was tested for photocatalytic activity (Fig. 51). The Ag NPs AC showed a minimal decrease in BBR dye concentration with degradation efficiency around 10.7% and k value of 0.00009 min^{-1}. Moreover, before the treatment the degradation efficiency was recorded around 52.2% with k value of 0.00595 min^{-1}. The BBR dye without any catalyst was degraded by around 6.5% with k value of 0.00049 min^{-1}. In the previous study, the calcination at 150°C managed to reduce the antifungal activity of Ag NPs synthesized using *S. platensis* extract [13]. The increased calcination temperature might cause more structural defects which can result in different properties of the material as shown in the UV-Vis findings. In addition, Ag/Ag_2O calcined at 600°C exhibited the photocatalytic activity in the UVA spectrum which might increase the cost of the photocatalytic removal [33].

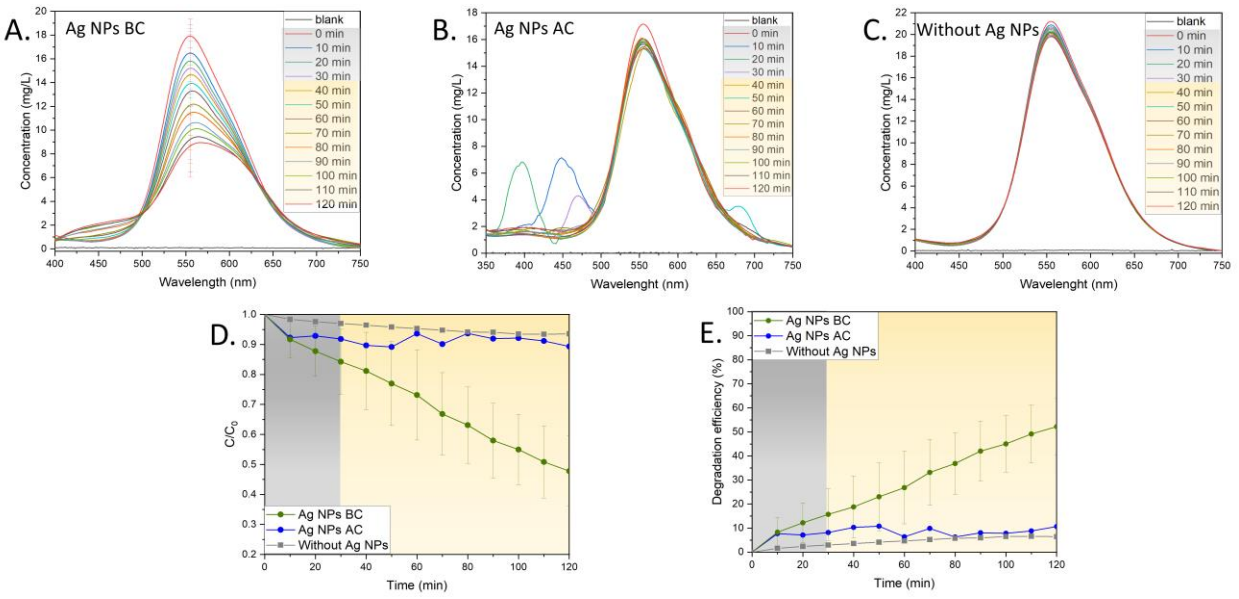

Figure 51 Influence of calcination on the photocatalytic activity (A) UV–Vis spectral changes before calcination, (B) UV–Vis spectral changes after calcination, (C) UV–Vis spectral changes without catalyst, (D) changes in dye concentration, (E) percentage degradation efficiency.

5.3.3.2.6 Mechanism of dye degradation

It is widely acknowledged that photocatalysis entails a sequence of reactions between the catalyst and pollutant [26,31,34]. The scheme of the BBR dye degradation process is shown in Fig. 52. First, the electrons from the valence band are excited into conduction band upon light irradiation (Eq. 4) which generates positively charged holes (h^+). Then, holes react with water molecules producing H^+ and •OH radical (5). The electrons after excitation convert molecular oxygen in the solution into $•O_2^-$ (6) reacting with water molecules to produce •OOH (7). After rearrangement to H_2O_2 (8), it reacts with $•O_2^-$ to produce •OH (9) which can also be generated after reaction of hydroxyl ions with holes (10). The above reactions are described below (Eq. 4-10).

Photocatalyst surface + hv → electron (e^-) + hole (h^+) (4)

$h^+ + H_2O \rightarrow H^+ + •OH$ (5)

$e^- + O_2 \rightarrow •O_2^-$ (6)

$•O_2^- + H_2O \rightarrow •OOH + OH^-$ (7)

$2 \bullet OOH \rightarrow H_2O_2 + O2$ (8)

$H_2O_2 + \bullet O_2^- \rightarrow \bullet OH + O_2 + OH^-$ (9)

$OH^- + h^+ \rightarrow \bullet OH$ (10)

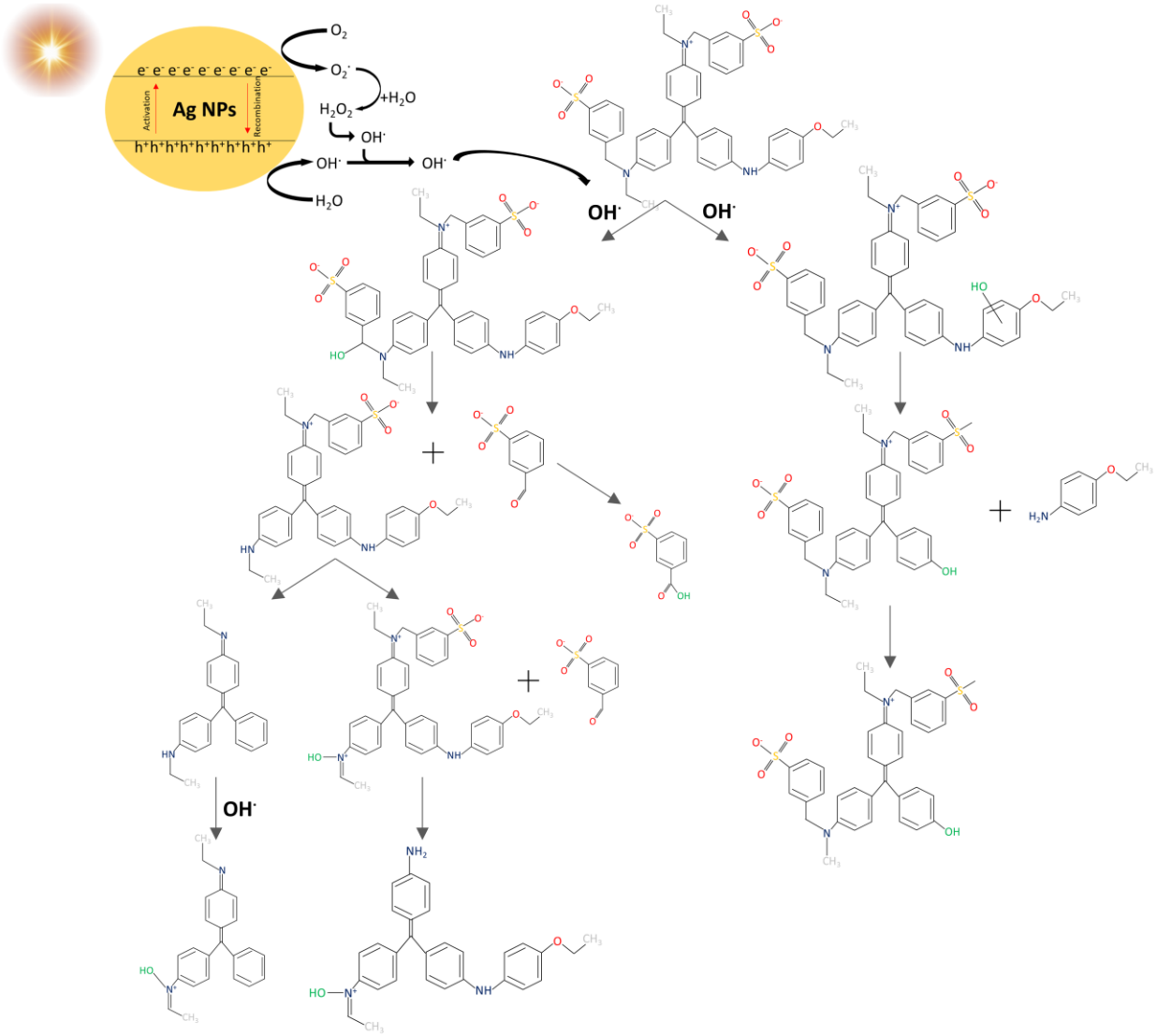

Figure 52 Mechanism of BBR dye degradation, adapted from [39].

BBR is a synthetic dye designed for its color stability and longevity which possesses a challenge to degradation. It belongs to the class of triphenylmethane dyes containing three phenyl rings linked to a central carbon atom [35]. The presence of conjugated double bonds in the aromatic

rings leads to electron delocalization with resonance stabilization which allows electronic charge distribution and prevents the formation of reactive sites [36,37]. Moreover, BBR dye does not contain highly labile functional groups which could be easily cleaved which reduces its susceptibility to chemical breakdown [38]. Thus, AOP is considered a promising method to degrade the BBR dye.

The BBR degradation pathway was studied based on the ultrasound treatment which also includes generation of hydroxyl radicals [39]. Based on the LC-Q-TOF-MS analysis, two degradation pathways were proposed, one involving OH addition or other with hydrogen abstraction followed by disproportionation/hydroxylation reaction [39]. Then, the molecules undergo a series of reactions such as bond breakage, oxidative cleavage, or demethylation. In total, 13 transformed products were identified, however, the molecules could be further transformed by ring opening and other oxidative cleavages resulting in formation of inorganic ions, carbon dioxide, and water as part of the mineralization process [39]. The degradation pathway was also studied in river water revealing its independence from presence of inorganic ions [40].

5.3.4 Conclusions

The production of efficient and stable photocatalysts is of utmost importance for the successful remediation of water pollution. Achieving this goal requires a comprehensive understanding of the underlying chemical processes, as well as an analysis of the various factors that can influence the performance of photocatalytic systems. In the present study, methanolic extract of *S. platensis* was used to obtain Ag NPs BC and Ag NPs AC. The XRD analysis displayed the AgCl and Ag phases in Ag NPs BC with crystalline size of 13.02 nm while only Ag phase was observed for Ag NPs AC with crystalline size of 24.35 nm. The FTIR analysis showed an abundance of functional groups from the extract present on the surface of Ag NPs BC. The SEM analysis showed spherical or quasi-spherical morphologies while EDX confirmed the involvement of extract confirming FTIR findings. The organic content was further examined by TGA analysis with different thermal stability of Ag NPs BC and Ag NPs AC. The UV-Vis study revealed the visible light activation of Ag NPs BC with band gap energy of 2.33 eV.

The photocatalytic properties of Ag NPs were tested in the visible light against BBR dye. The influence of various factors was observed such as light intensity, dye concentration, catalyst dosage, pH, and calcination. The highest average dye degradation efficiency of 81.9% was achieved in alkaline conditions. The mechanism of the BBR dye was proposed involving the generation of hydroxyl radicals. The work shows the potential of *S. platensis* as a source of metabolites to synthesize products with efficient photocatalytic activity.

5.3.5 References

1. T. Islam, M.R. Repon, T. Islam, Z. Sarwar, M.M. Rahman, Impact of textile dyes on health and ecosystem: a review of structure, causes, and potential solutions, Environ. Sci. Pollut. Res. 2022 304. 30 (2022) 9207–9242. https://doi.org/10.1007/S11356-022-24398-3.

2. T. Tomar, N. Kahandawala, J. Kaur, L. Thounaojam, I. Choudhary, S. Bera, Bioremediation of synthetic dyes from wastewater by using microbial nanocomposites: An emerging field for water pollution management, Biocatal. Agric. Biotechnol. 51 (2023) 102767. https://doi.org/10.1016/j.bcab.2023.102767.

3. M. Ahmadian, M. Jaymand, Interpenetrating polymer network hydrogels for removal of synthetic dyes: A comprehensive review, Coord. Chem. Rev. 486 (2023) 215152. https://doi.org/10.1016/j.ccr.2023.215152.

4. A. Iqbal, A. Yusaf, M. Usman, T. Hussain Bokhari, A. Mansha, Insight into the degradation of different classes of dyes by advanced oxidation processes; a detailed review, Int. J. Environ. Anal. Chem. (2023). https://doi.org/10.1080/03067319.2022.2125312.

5. A. V. Mohod, M. Momotko, N.S. Shah, M. Marchel, M. Imran, L. Kong, G. Boczkaj, Degradation of Rhodamine dyes by Advanced Oxidation Processes (AOPs) – Focus on cavitation and photocatalysis - A critical review, Water Resour. Ind. 30 (2023) 100220. https://doi.org/10.1016/j.wri.2023.100220.

6. S. Park, Y. Keum, J. Park, Ti-Based porous materials for reactive oxygen species-mediated photocatalytic reactions, Chem. Commun. 58 (2022) 607–618. https://doi.org/10.1039/D1CC04858A.

7. N. Vidyasagar, R.R. Patel, S.K. Singh, M. Singh, Green synthesis of silver nanoparticles: methods, biological applications, delivery and toxicity, Mater. Adv. 4 (2023) 1831–1849. https://doi.org/10.1039/D2MA01105K.

8. A. Sidorowicz, G. Fais, M. Casula, M. Borselli, G. Giannaccare, A.M. Locci, N. Lai, R. Orrù, G. Cao, A. Concas, Nanoparticles from Microalgae and Their Biomedical Applications, Mar. Drugs. 21 (2023) 352. https://doi.org/10.3390/md21060352.

9. G. Gentscheva, K. Nikolova, V. Panayotova, K. Peycheva, L. Makedonski, P. Slavov, P. Radusheva, P. Petrova, I. Yotkovska, Application of Arthrospira platensis for Medicinal Purposes and the Food Industry: A Review of the Literature, Life. 13 (2023) 845. https://doi.org/10.3390/life13030845.

10. G.A. Ismail, N.G. Allam, W.M. El-Gemizy, M.A. Salem, The role of silver nanoparticles biosynthesized by Anabaena variabilis and Spirulina platensis cyanobacteria for malachite green removal from wastewater, Environ. Technol. (United Kingdom). 42 (2021) 4475–4489. https://doi.org/10.1080/09593330.2020.1766576.

11. K. Roja, P. Mehta, M. Premalatha, K. Jeyadheepan, C. Gopalakrishnan, N. Meenakshisundaram, K. Sankaranarayanan, Biosynthesized silver nanoparticles as antimicrobial agents and photocatalytic degradation of methylene blue, Desalin. Water Treat. 156 (2019) 292–302. https://doi.org/10.5004/dwt.2019.23605.

12. A. Gul, D. Ahmed, M.M. Fazil, T. Aslam, M.A. Rashid, H. Khan, A. Ali, S. Ali, Biofabrication of silver nanoparticles using Spirulina platensis: In vitro anti-coagulant, thrombolytic and catalytic dye degradation activity, Microsc. Res. Tech. 86 (2023) 823–833. https://doi.org/10.1002/JEMT.24344.

13. A. Sidorowicz, V. Margarita, G. Fais, A. Pantaleo, A. Manca, A. Concas, P. Rappelli, P.L. Fiori, G. Cao, Characterization of nanomaterials synthesized from Spirulina platensis extract and their potential antifungal activity, PLoS One. 17 (2022) e0274753. https://doi.org/10.1371/JOURNAL.PONE.0274753.

14. L. Cepoi, I. Zinicovscaia, L. Rudi, T. Chiriac, V. Turchenko, Changes in the Dunaliella salina biomass composition during silver nanoparticles formation, Nanotechnol. Environ. Eng. 7 (2022) 235–243. https://doi.org/10.1007/s41204-022-00218-4.

15. M. Kashyap, K. Samadhiya, A. Ghosh, V. Anand, H. Lee, N. Sawamoto, A. Ogura, Y. Ohshita, P.M. Shirage, K. Bala, Synthesis, characterization and application of intracellular Ag/AgCl nanohybrids biosynthesized in Scenedesmus sp. as neutral lipid inducer and antibacterial agent, Environ. Res. 201 (2021) 111499. https://doi.org/10.1016/J.ENVRES.2021.111499.

16. M. Mecozzi, M. Pietroletti, M. Scarpiniti, R. Acquistucci, M.E. Conti, Monitoring of marine mucilage formation in Italian seas investigated by infrared spectroscopy and independent component analysis, Environ. Monit. Assess. 184 (2012) 6025–6036. https://doi.org/10.1007/s10661-011-2400-4.

17. E.A. Alzahrani, A. Nabi, M.R. Kamli, S.M. Albukhari, S.A. Althabaiti, S.A. Al-Harbi, I. Khan, M.A. Malik, Facile Green Synthesis of ZnO NPs and Plasmonic Ag-Supported ZnO Nanocomposite for Photocatalytic Degradation of Methylene Blue, Water (Switzerland). 15 (2023) 384. https://doi.org/10.3390/w15030384.

18. J. Vera, W. Herrera, E. Hermosilla, M. Díaz, J. Parada, A.B. Seabra, G. Tortella, H. Pesenti, G. Ciudad, O. Rubilar, Antioxidant Activity as an Indicator of the Efficiency of Plant Extract-Mediated Synthesis of Zinc Oxide Nanoparticles, Antioxidants. 12 (2023) 784. https://doi.org/10.3390/antiox12040784.

19. B. Kis, E.A. Moacă, L.B. Tudoran, D. Muntean, I.Z. Magyari-Pavel, D.I. Minda, A. Lombrea, Z. Diaconeasa, C.A. Dehelean, Ștefania Dinu, C. Danciu, Green Synthesis of Silver Nanoparticles Using Populi gemmae Extract: Preparation, Physicochemical Characterization, Antimicrobial Potential and In Vitro Antiproliferative Assessment, Materials (Basel). 15 (2022) 5006. https://doi.org/10.3390/ma15145006.

20. M.C. Lite, R.R. Constantinescu, E.C. Tănăsescu, A. Kuncser, C. Romaniţan, I. Lăcătuşu, N. Badea, Design of Green Silver Nanoparticles Based on Primula Officinalis Extract for Textile Preservation, Mater. 2022, Vol. 15, Page 7695. 15 (2022) 7695. https://doi.org/10.3390/MA15217695.

21. Z. Ma, J. Liu, Y. Liu, X. Zheng, K. Tang, Green synthesis of silver nanoparticles using soluble soybean polysaccharide and their application in antibacterial coatings, Int. J. Biol. Macromol. 166 (2021) 567–577. https://doi.org/10.1016/j.ijbiomac.2020.10.214.

22. L. Baia, S. Simon, UV-VIS and TEM assessment of morphological features of silver nanoparticles from phosphate glass matrices, Mod. Res. Educ. Top. …. (2007) 576–583. http://www.formatex.org/microscopy3/pdf/pp576-583.pdf (accessed August 11, 2023).

23. H.C. Ananda Murthy, T. Desalegn Zeleke, C.R. Ravikumar, M.R. Anil Kumar, H.P. Nagaswarupa, Electrochemical properties of biogenic silver nanoparticles synthesized using Hagenia abyssinica (Brace) JF. Gmel. medicinal plant leaf extract, Mater. Res. Express. 7 (2020) 055016. https://doi.org/10.1088/2053-1591/ab9252.

24. V.S. Munagapati, H.Y. Wen, A.R.K. Gollakota, J.C. Wen, K.Y.A. Lin, C.M. Shu, V. Yarramuthi, P.K. Basivi, G.M. Reddy, G. V. Zyryanov, Magnetic Fe3O4 nanoparticles loaded guava leaves powder impregnated into calcium alginate hydrogel beads (Fe3O4-GLP@CAB) for efficient removal of methylene blue dye from aqueous environment: Synthesis, characterization, and its adsorption performance, Int. J. Biol. Macromol. 246 (2023) 125675. https://doi.org/10.1016/J.IJBIOMAC.2023.125675.

25. S.A. Heredia Deba, B.A. Wols, D.R. Yntema, R.G.H. Lammertink, Photocatalytic ceramic membrane: Effect of the illumination intensity and distribution, J. Photochem. Photobiol. A Chem. 437 (2023) 114469. https://doi.org/10.1016/j.jphotochem.2022.114469.

26. I. Groeneveld, M. Kanelli, F. Ariese, M.R. van Bommel, Parameters that affect the photodegradation of dyes and pigments in solution and on substrate – An overview, Dye. Pigment. 210 (2023) 110999. https://doi.org/10.1016/J.DYEPIG.2022.110999.

27. M. Saeed, M. Muneer, A. ul Haq, N. Akram, Photocatalysis: an effective tool for photodegradation of dyes—a review, Environ. Sci. Pollut. Res. 2021 291. 29 (2021) 293–311. https://doi.org/10.1007/S11356-021-16389-7.

28. L.M. Chiarello, M. Mittersteiner, P.C. de Jesus, J. Andreaus, I.O. Barcellos, Reuse of enzymatically treated reactive dyeing baths: Evaluation of the number of reuse cycles, J. Clean. Prod. 267 (2020) 122033. https://doi.org/10.1016/J.JCLEPRO.2020.122033.

29. A. Nawaz, M. Atif, A. Khan, M. Siddique, N. Ali, F. Naz, M. Bilal, T.H. Kim, M. Momotko, H.U. Haq, G. Boczkaj, Solar light driven degradation of textile dye contaminants for wastewater treatment – studies of novel polycationic selenide photocatalyst and process optimization by response surface methodology desirability factor, Chemosphere. 328 (2023) 138476. https://doi.org/10.1016/J.CHEMOSPHERE.2023.138476.

30. V. Javanbakht, M. Mohammadian, Photo-assisted advanced oxidation processes for efficient removal of anionic and cationic dyes using Bentonite/TiO2 nano-photocatalyst immobilized with silver nanoparticles, J. Mol. Struct. 1239 (2021) 130496. https://doi.org/10.1016/J.MOLSTRUC.2021.130496.

31. Q. Lin, X. Huang, L. Lu, D. Tang, Snowflake-like CdS@ZnIn2S4 heterojunction-based photocatalyst-electrolyte effect: An innovative mode for photoelectrochemical immunoassay, Biosens. Bioelectron. 216 (2022) 114679. https://doi.org/10.1016/J.BIOS.2022.114679.

32. H.B. Uma, S. Ananda, M.B. Nandaprakash, High efficient photocatalytic treatment of textile dye and antibacterial activity via electrochemically synthesized Ni-doped ZnO nano photocatalysts, Chem. Data Collect. 24 (2019) 100301. https://doi.org/10.1016/J.CDC.2019.100301.

33. N. Khandan Nasab, Z. Sabouri, S. Ghazal, M. Darroudi, Green-based synthesis of mixed-phase silver nanoparticles as an effective photocatalyst and investigation of their antibacterial properties, J. Mol. Struct. 1203 (2020) 127411. https://doi.org/10.1016/J.MOLSTRUC.2019.127411.

34. A. Ahmed, M. Usman, B. Yu, X. Ding, Q. Peng, Y. Shen, H. Cong, Efficient photocatalytic degradation of toxic Alizarin yellow R dye from industrial wastewater using biosynthesized Fe nanoparticle and study of factors affecting the degradation rate, J. Photochem. Photobiol. B Biol. 202 (2020) 111682. https://doi.org/10.1016/J.JPHOTOBIOL.2019.111682.

35. J. Zhao, Q.X. Wu, X. Du Cheng, T. Su, X.H. Wang, W.N. Zhang, Y.M. Lu, Y. Chen, Biodegradation and detoxification of the triphenylmethane dye coomassie brilliant blue by the extracellular enzymes from mycelia of Lactarius deliciosus, Front. Chem. Sci. Eng. 15 (2021) 421–436. https://doi.org/10.1007/s11705-020-1952-7.

36. S.B. Bukallah, M.A. Rauf, S.S. Ashraf, Photocatalytic decoloration of Coomassie Brilliant Blue with titanium oxide, Dye. Pigment. 72 (2007) 353–356. https://doi.org/10.1016/j.dyepig.2005.09.016.

37. M.S. Salem, A.R. Wassel, M. Fedawy, A. Shaker, A.H. Al-Bagawia, G.M. Aleid, A.M. El-Mahalawy, Integration of biocompatible Coomassie Brilliant Blue dye on silicon in organic/Inorganic heterojunction for photodetection applications, J. Phys. Chem. Solids. 169 (2022) 110890. https://doi.org/10.1016/j.jpcs.2022.110890.

38. A.R. Khataee, M.B. Kasiri, Photocatalytic degradation of organic dyes in the presence of nanostructured titanium dioxide: Influence of the chemical structure of dyes, J. Mol. Catal. A Chem. 328 (2010) 8–26. https://doi.org/10.1016/j.molcata.2010.05.023.

39. M.P. Rayaroth, U.K. Aravind, C.T. Aravindakumar, Sonochemical degradation of Coomassie Brilliant Blue: Effect of frequency, power density, pH and various additives, Chemosphere. 119 (2015) 848–855. https://doi.org/10.1016/J.CHEMOSPHERE.2014.08.037.

40. M.P. Rayaroth, U.K. Aravind, C.T. Aravindakumar, Ultrasound based AOP for emerging pollutants: from degradation to mechanism, Environ. Sci. Pollut. Res. 24 (2017) 6261–6269. https://doi.org/10.1007/s11356-016-6606-4.

Chapter 6

Conclusions

Microalgae have emerged as a valuable resource to produce useful compounds with applications ranging from food and dietary supplements to environmentally friendly nanoparticle synthesis. The recent focus on global health threats has shed light on the potential medicinal and environmental applications of microalgae-derived secondary metabolites in nanoparticle-based therapeutics. Microalgae are promising candidates for synthesizing various nanoparticles because of their rich secondary metabolites, which serve as capping and reducing agents. Microalgae-derived nanoparticles have shown significant potential in the biomedical sector, but further research is needed to address issues related to kinetics, cell viability, and yield, impacting NP properties in both conventional and microalgae-based synthesis methods. Employing various extraction techniques or conditions during the synthesis process of nanoparticles might result in a variety of nanoparticles with different properties which can be applied in many sectors.

The study on the synthesis of silver nanoparticles, titanium dioxide nanoparticles, cobalt (II) hydroxide nanomaterials, and cobalt (II,III) oxide from *S. platensis* methanolic extract demonstrated their potential as novel antifungal agents. The synthesis mechanism, characterized using GCMS and FTIR, confirmed the involvement of secondary metabolites, particularly amines. Various analytical techniques, such as XRD, SEM, TGA, and zeta potential, provided valuable insights into the properties of these nanomaterials. Notably, silver nanoparticles exhibited exceptional thermal stability and water dispersion properties among all the prepared structures. When tested against different *Candida* species, silver nanoparticles and cobalt (II) hydroxide nanomaterials displayed robust antifungal activity at a concentration of 50 µg/mL, with low minimum inhibitory concentration (MIC) values. Interestingly, exposure to light had a differential impact on MIC values, with a decrease observed for *C. krusei* and an increase for *C. albicans* and *C. glabrata*. These findings underscore the potential of these nanomaterials for the development

of effective antifungal agents, offering a promising avenue for addressing the increasing challenge of fungal infections in contemporary healthcare. Further research is warranted to explore their clinical applicability and safety in treating fungal infections.

Another tested application of nanomaterials synthesized using microalgae was related to their catalytic oxidation of carbon monoxide. The research has demonstrated the potential of utilizing extracts from microalgae such as *S. platensis, C. vulgaris*, and *H. pluvialis* for the sustainable synthesis of nanosized Co_3O_4 catalysts with distinct properties. By varying the calcination temperatures and leveraging the metabolites present in the extracts, Co_3O_4 catalysts with octahedral, nanosheet, and spherical morphologies, accompanied by structural defects and surface segregation of phosphorous and potassium, were successfully synthesized. Notably, the presence of phosphorous and potassium originating from the extracts significantly enhanced the catalytic activity of Co_3O_4, particularly when normalized by the specific surface area. In situ studies of carbon monoxide oxidation unveiled differences in oxygen mobility and carbonate formation, shedding new light on the catalytic mechanisms. These novel insights hold promise for the development of innovative synthesis strategies to manufacture highly active Co_3O_4 catalysts, contributing to more efficient carbon monoxide oxidation, reduced environmental and health impacts, enhanced internal combustion engine efficiency, and sustainable catalyst synthesis for a greener future. Further exploration and optimization of these catalysts are warranted to unlock their full potential in various applications.

The catalytic activity was further explored by studying the photocatalytic activity of microalgae-derived silver nanoparticles against Brilliant Blue R dye commonly used in the laboratory for protein staining. The methanolic extract of *C. vulgaris* resulted in the successful synthesis of silver nanoparticles. Moreover, the results revealed valuable insights into the influence of calcination on their characteristics. XRD analysis indicated a crystalline nature of the products, with the presence of Ag_2O and Ag phases and an average crystalline size of 16.07 nm before calcination, which transformed into a pure Ag phase with a larger crystalline size of 24.61 nm after calcination. FTIR highlighted capping functional groups on Ag NPs, while SEM showed irregular morphology and agglomeration following calcination. EDX and TGA analyses further confirmed

the involvement of metabolites in the organic coating. UV-Vis analysis demonstrated alterations in optical properties due to calcination. Importantly, the synthesized silver nanoparticles exhibited remarkable photocatalytic activity, with the highest degradation efficiency of 90.6% and a calculated k value of 0.04402 min^{-1} achieved under increased catalyst dosage after 90 minutes of visible light irradiation.

Similarly, methanolic extract of *H. pluvialis* was used for synthesis of silver nanoparticles and their photocatalytic activity against Brilliant Blue R dye. XRD analysis demonstrated the crystalline nature of the product before calcination, with the presence of Ag_2O and Ag phases and a crystalline size of 14.27 nm. Post-calcination, only the Ag phase was observed, with an increased crystalline size of 34.78 nm. Similar profile to silver nanoparticles from *C. vulgaris* of FTIR, SEM, EDX, and TGA was obtained. In addition, UV-Vis analysis also demonstrated changes in optical properties due to calcination. Importantly, the Ag NPs exhibited significant photocatalytic activity, with the highest degradation efficiency of 65.9% achieved under increased catalyst dosage after 90 minutes of visible light irradiation, with a calculated k value of 0.00947 min^{-1}.

Another methanolic extract used to synthesize silver nanoparticles for photocatalytic activity was obtained from *S. platensis*. XRD analysis showed the presence of AgCl and Ag phases with a crystalline size of 13.02 nm before calcination, which transformed into pure Ag with an increased crystalline size of 24.35 nm after calcination. FTIR confirmed the role of metabolites from the extract in capping the Ag NPs. SEM provided visual evidence of spherical or quasi-spherical morphologies with some agglomeration attributed to calcination. EDX and TGA analyses further substantiated the involvement of metabolites in the synthesis process. UV-Vis analysis demonstrated optical changes in the products. Notably, the obtained silver nanoparticles exhibited commendable photocatalytic activity, with the highest degradation efficiency of approximately 81.9% achieved under alkaline conditions after 90 minutes of light irradiation. These findings prove the potential of silver nanoparticles synthesized from microalgal extract for eco-friendly and efficient photocatalytic applications, particularly in addressing water pollution concerns and the removal of organic dyes from wastewater. Further research and optimization

efforts are warranted to harness their full potential in practical environmental remediation applications.

List of figures

List of tables